An Introduction to Scientific Computing

Twelve Computational Projects Solved with MATLAB

Ionut Danaila
Pascal Joly
Sidi Mahmoud Kaber
Marie Postel

Springer

An Introduction to Scientific Computing

Ionut Danaila
Pascal Joly
Sidi Mahmoud Kaber
Marie Postel

An Introduction to Scientific Computing

Twelve Computational Projects Solved
with MATLAB

Springer

Ionut Danaila
Laboratoire Jacques-Louis Lions
Université Pierre et Marie Curie
Paris 75252
FRANCE
danaila@ann.jussieu.fr

Pascal Joly
Laboratoire Jacques-Louis Lions
Université Pierre et Marie Curie
Paris 75252
FRANCE
joly@ann.jussieu.fr

Sidi Mahmoud Kaber
Laboratoire Jacques-Louis Lions
Université Pierre et Marie Curie
Paris 75252
FRANCE
kaber@ann.jussieu.fr

Marie Postel
Laboratoire Jacques-Louis Lions
Université Pierre et Marie Curie
Paris 75252
FRANCE
postel@ann.jussieu.fr

Library of Congress Control Number: 2006931780

ISBN-10: 0-387-30889-X
ISBN-13: 978-0-387-30889-0

Printed on acid-free paper.

9 8 7 6 5 4 3 2 1

springer.com

Ionut Danaila
Pascal Joly
Sidi Mahmoud Kaber
Marie Postel

An Introduction to Scientific Computing: Twelve Computational Projects Solved with MATLAB

SPIN Springer's internal project number, if known

– Monograph –

October 13, 2006

Springer
Berlin Heidelberg New York
Hong Kong London
Milan Paris Tokyo

To *Alice*, *Luminita*
Romain, *Sylvain*
Sarah, *Thomas*
Camille, *Paul*

Preface

Teaching or learning numerical methods in applied mathematics cannot be conceived nowadays without numerical experimentation on computers. There is a vast literature devoted either to theoretical numerical methods or numerical programming of basic algorithms, but there are few texts offering a complete discussion of numerical issues involved in the solution of concrete and relatively complex problems. This book is an attempt to fill this need. It is our belief that advantages and drawbacks of a numerical method cannot be accounted for without one's experiencing all the steps of scientific computing, from physical and mathematical description of the problem to numerical formulation and programming and, finally, to critical discussion of numerical results.

The book provides twelve *computational projects* aimed at numerically solving problems selected to cover a broad spectrum of applications, from fluid mechanics, chemistry, elasticity, thermal science, computer-aided design, signal and image processing, etc. Even though the main volume of this text concerns the numerical analysis of computational methods and their implementation, we have tried to start, when possible, from realistic problems of practical interest for researchers and engineers.

For each project, an introductory record card summarizes the mathematical and numerical topics explained and the fields of application of the approach. A level of difficulty, scaling from 1 to 3, is assigned to each project. Most of the projects are of level 1 or 2 and can be easily tackled; the reader will no doubt realize that projects of level 3 require a solid background in both numerical analysis and computational techniques.

Excepting projects 1 and 3, which are more theoretical, all projects follow the typical steps of scientific computing: physical and mathematical modeling of the problem, numerical discretization, construction of a numerical algorithm, and, finally, programming. We have placed considerable emphasis on practical issues of computational methods that are not usually available in basic textbooks. Numerical checking of accuracy or stability, the choice of boundary conditions, the effective solving of linear systems, and comparison to exact solutions when available are only a few examples of problems en-

countered in the application of numerical methods. The last section of each project contains solutions of all proposed exercises and guides the reader in using the MATLAB scripts that can be accessed via the publisher's web site `www.springer.com`. Programming techniques such as vectorial programming and memory storage optimization are also addressed. We finally discuss the physical meaning of the obtained results. The complementary references given at the end of each chapter form a guide for further, more specialized, reading.

The text offers two levels of interest. The mathematical framework provides a basic grounding in the subject of numerical analysis of partial differential equations and main discretization techniques (finite differences, finite elements, spectral methods, wavelets). Meanwhile, we hope that the information contained herein and the wide range of topics covered by the book will allow the reader to select the appropriate numerical method to solve his or her particular problem.

The book is based on material offered by the authors in courses at *Université Pierre et Marie Curie (Paris, France)* and different engineering schools. It is primarily intended as a graduate-level text in applied mathematics, but it may also be used by students in engineering or physical sciences. It will also be a useful reference for researchers and practicing engineers. Since different possible developments of the projects are suggested, the text can be used to propose assignments at different graduate levels.

Despite our efforts to avoid typing, spelling, or other errors, the reader will no doubt find some remaining. We shall appreciate all feedback notifying us of any mistakes, as well as comments and suggestions that will help us to improve the text. Please use the e-mail addresses given below for this purpose.

We conclude by saying a few words about the programs provided with this book. They are written in MATLAB, a widely used software environment for scientific computing produced by The MathWorks Inc. We consider that an interpreted language (such as MATLAB, SCILAB, OCTAVE) is the ideal framework to start a scientific programming activity. Debugging is very simple and the wide variety of available numerical tools (for solving linear systems, integrating ordinary differential equations, etc.) allows one to concentrate on the main features of the resolution algorithm. The highly versatile graphical interface is also very important to easy visualization of the obtained results.

Our programs are written with a general concern for simplicity and efficiency on ordinary personal computers; program lines are commented in what we hope is sufficient detail for the reader to follow mathematical developments. Programming tricks are discussed in the text when they seem to be of general interest. Projects 11 and 12 are also provided with more elaborate versions of the programs, using interactive graphical user interfaces. The reader should try to modify these programs to test different suggested run cases or extensions of the projects. We believe that experience with these simple programs will be valuable in writing numerical codes using compiled languages (such as Fortran, C, or C++) to solve real industrial problems on mainframe computers.

Paris, October 2005

Ionut Danaila (danaila@ann.jussieu.fr)
Pascal Joly (joly@ann.jussieu.fr)
Sidi Mahmoud Kaber (kaber@ann.jussieu.fr)
Marie Postel (postel@ann.jussieu.fr)

Laboratoire Jacques-Louis Lions
Université Pierre et Marie Curie (Paris 6) and
Centre National de la Recherche Scientifique (CNRS)

Contents

1 Numerical Approximation of Model Partial Differential Equations 1
1.1 Discrete Integration Methods for Ordinary Differential Equations 1
1.1.1 Construction of Numerical Integration Schemes 2
1.1.2 General Form of Numerical Schemes 6
1.1.3 Application to the Absorption Equation 8
1.1.4 Stability of a Numerical Scheme 9
1.2 Model Partial Differential Equations 11
1.2.1 The Convection Equation 11
1.2.2 The Wave Equation 14
1.2.3 The Heat Equation 17
1.3 Solutions and Programs 19
Chapter References 30

2 Nonlinear Differential Equations: Application to Chemical Kinetics 33
2.1 Physical Problem and Mathematical Modeling 33
2.2 Stability of the System 34
2.3 Model for the Maintained Reaction 36
2.3.1 Existence of a Critical Point and Stability 36
2.3.2 Numerical Solution 37
2.4 Model of Reaction with a Delay Term 37
2.5 Solutions and Programs 41
Chapter References 48

3 Polynomial Approximation 49
3.1 Introduction 49
3.2 Polynomial Interpolation 50
3.2.1 Lagrange Interpolation 51
3.2.2 Hermite Interpolation 57

3.3 Best Polynomial Approximation 59
3.3.1 Best Uniform Approximation 59
3.3.2 Best Hilbertian Approximation 61
3.3.3 Discrete Least Squares Approximation 64
3.4 Piecewise Polynomial Approximation 65
3.4.1 Piecewise Constant Approximation 66
3.4.2 Piecewise Affine Approximation 67
3.4.3 Piecewise Cubic Approximation 68
3.5 Further Reading 69
3.6 Solutions and Programs 70
Chapter References 83

4 Solving an Advection–Diffusion Equation by a Finite Element Method 85
4.1 Variational Formulation of the Problem 85
4.2 A $P1$ Finite Element Method 87
4.3 A $P2$ Finite Element Method 90
4.4 A Stabilization Method 93
4.4.1 Computation of the Solution at the Endpoints of the Intervals 93
4.4.2 Analysis of the Stabilized Method 95
4.5 The Case of a Variable Source Term 97
4.6 Solutions and Programs 97
Chapter References 108

5 Solving a Differential Equation by a Spectral Method 111
5.1 Some Properties of the Legendre Polynomials 112
5.2 Gauss–Legendre Quadrature 113
5.3 Legendre Expansions 115
5.4 A Spectral Discretization 117
5.5 Possible Extensions 119
5.6 Solutions and Programs 120
Chapter References 125

6 Signal Processing: Multiresolution Analysis 127
6.1 Introduction 127
6.2 Approximation of a Function: Theoretical Aspect 127
6.2.1 Piecewise Constant Functions 127
6.2.2 Decomposition of the Space V_J 129
6.2.3 Decomposition and Reconstruction Algorithms 132
6.2.4 Importance of Multiresolution Analysis 133
6.3 Multiresolution Analysis: Practical Aspect 134
6.4 Multiresolution Analysis: Implementation 135
6.5 Introduction to Wavelet Theory 137
6.5.1 Scaling Functions and Wavelets 137

6.5.2 The Schauder Wavelet . . . 139
6.5.3 Implementation of the Schauder Wavelet . . . 141
6.5.4 The Daubechies Wavelet . . . 142
6.5.5 Implementation of the Daubechies Wavelet D4 . . . 144
6.6 Generalization: Image Processing . . . 146
6.6.1 Image Processing: Implementation . . . 147
6.7 Solutions and Programs . . . 148
Chapter References . . . 150

7 Elasticity: Elastic Deformation of a Thin Plate . . . 151
7.1 Introduction . . . 151
7.2 Modeling Elastic Deformations (Linear Problem) . . . 152
7.3 Modeling Electrostatic Forces (Nonlinear Problem) . . . 153
7.4 Numerical Discretization of the Problem . . . 154
7.5 Programming Tips . . . 157
7.5.1 Modular Programming . . . 157
7.5.2 Program Validation . . . 158
7.6 Solving the Linear Problem . . . 159
7.7 Solving the Nonlinear Problem . . . 159
7.7.1 A Fixed-Point Algorithm . . . 159
7.7.2 Numerical Solution . . . 160
7.8 Solutions and Programs . . . 162
7.8.1 Further Comments . . . 162
Chapter References . . . 164

8 Domain Decomposition Using a Schwarz Method . . . 165
8.1 Principle and Application Field of Domain Decomposition . . . 165
8.2 One-Dimensional Finite Difference Solution . . . 166
8.3 Schwarz Method in One Dimension . . . 167
8.3.1 Discretization . . . 168
8.4 Extension to the Two-Dimensional Case . . . 171
8.4.1 Finite Difference Solution . . . 171
8.4.2 Domain Decomposition in the Two-Dimensional Case . . . 175
8.4.3 Implementation of Realistic Boundary Conditions . . . 178
8.4.4 Possible Extensions . . . 180
8.5 Solutions and Programs . . . 181
Chapter References . . . 190

9 Geometrical Design: Bézier Curves and Surfaces . . . 193
9.1 Introduction . . . 193
9.2 Bézier Curves . . . 193
9.3 Basic Properties of Bézier Curves . . . 195
9.3.1 Convex Hull of the Control Points . . . 195
9.3.2 Multiple Control Points . . . 196
9.3.3 Tangent Vector to a Bézier Curve . . . 197

9.3.4 Junction of Bézier Curves . . . 197
9.3.5 Generation of the Point $P(t)$ . . . 198
9.4 Generation of Bézier Curves . . . 200
9.5 Splitting Bézier Curves . . . 201
9.6 Intersection of Bézier Curves . . . 203
9.6.1 Implementation . . . 205
9.7 Bézier Surfaces . . . 206
9.8 Basic properties of Bézier Surfaces . . . 206
9.8.1 Convex Hull . . . 206
9.8.2 Tangent Vector . . . 207
9.8.3 Junction of Bézier Patches . . . 207
9.8.4 Construction of the Point $P(t)$ . . . 208
9.9 Construction of Bézier Surfaces . . . 209
9.10 Solutions and Programs . . . 210
Chapter References . . . 212

10 Gas Dynamics: The Riemann Problem and Discontinuous Solutions: Application to the Shock Tube Problem . . . 213
10.1 Physical Description of the Shock Tube Problem . . . 213
10.2 Euler Equations of Gas Dynamics . . . 215
10.2.1 Dimensionless Equations . . . 218
10.2.2 Exact Solution . . . 218
10.3 Numerical Solution . . . 222
10.3.1 Lax–Wendroff and MacCormack Centered Schemes . . . 222
10.3.2 Upwind Schemes (Roe's Approximate Solver) . . . 227
10.4 Solutions and Programs . . . 232
Chapter References . . . 233

11 Thermal Engineering: Optimization of an Industrial Furnace . . . 235
11.1 Introduction . . . 235
11.2 Formulation of the Problem . . . 236
11.3 Finite Element Discretization . . . 237
11.4 Implementation . . . 239
11.5 Boundary Conditions . . . 241
11.5.1 Modular Implementation . . . 242
11.5.2 Numerical Solution of the Problem . . . 242
11.6 Inverse Problem Formulation . . . 244
11.7 Implementation of the Inverse Problem . . . 245
11.8 Solutions and Programs . . . 248
11.8.1 Further Comments . . . 249
Chapter References . . . 250

12 Fluid Dynamics: Solving the Two-Dimensional Navier–Stokes Equations 251
12.1 Introduction 251
12.2 The Incompressible Navier–Stokes Equations 252
12.3 Numerical Algorithm 253
12.4 Computational Domain, Staggered Grids, and Boundary Conditions 255
12.5 Finite Difference Discretization 256
12.6 Flow Visualization 264
12.7 Initial Condition 265
12.8 Step-by-Step Implementation 268
12.8.1 Solving a Linear System with Tridiagonal, Periodic Matrix 268
12.8.2 Solving the Unsteady Heat Equation 271
12.8.3 Solving the Steady Heat Equation Using FFTs 275
12.8.4 Solving the 2D Navier–Stokes Equations 275
12.9 Solutions and Programs 277
Chapter References 284
Bibliography 285
Index 289
Index of Programs 293

1

Numerical Approximation of Model Partial Differential Equations

Project Summary

Level of difficulty:	1
Keywords:	Linear differential equations; numerical integration methods; finite difference schemes: Euler schemes, Runge–Kutta schemes
Application fields:	Transport phenomena, diffusion, wave propagation

This first chapter is intended as a quick introduction to basic discretization techniques of time-dependent partial differential equations (PDEs). We consider it important that the reader, before tackling the complex problems of the next chapters, have some understanding of the mathematical and physical properties of the following model PDEs: the convection equation, the wave equation, and the heat equation. This chapter is therefore organized as a collection of several short exercises in which model PDEs are theoretically analyzed and numerically solved using the simplest discretization methods. The essential features of numerical methods are presented, with emphasis on fundamental ideas of accuracy, stability, convergence, and numerical dissipation. Particular care is devoted to the validation of numerical procedures by comparing to exact solutions available for these simple cases.

1.1 Discrete Integration Methods for Ordinary Differential Equations

We generally define a partial differential equation (PDE) as a relation between a function of several variables and its partial derivatives. In this section, we consider the simplest case of ordinary differential equations (ODE), which depend on a single independent variable (time variable here) and present discrete methods for their numerical integration. These methods (or numerical

schemes) will prove useful in the following sections when we discuss PDEs depending both on time and space variables.

Let us consider the following problem: find a differentiable function $u : [0,T] \mapsto \mathbb{R}^m$ that is a solution of the ODE

$$u'(t) = f(t, u(t)), \tag{1.1}$$

where T is a nonnegative scalar and $f : [0,T] \times \mathbb{R}^m \mapsto \mathbb{R}^m$ a continuous function. This problem is not completely specified by its equation: for its integration we need to know the initial value (at $t = 0$) of the unknown function.

Definition 1.1. *A Cauchy (or initial value) problem is the coupling of the ODE (1.1) with an initial condition*

$$u(0) = u_0, \tag{1.2}$$

where u_0 is a given vector in $\mathbb{R}^m$.

Theoretical results on existence and uniqueness of the solution of the problem (1.1)–(1.2) go back to Cauchy in 1824. The reader interested in a more mathematical approach to the problem will want to refer to many existing books on ODEs (see, for instance, the references at the end of this chapter). We adopt here a more practical point of view, and we start directly by presenting simple numerical methods to compute approximations of the solution in the scalar case, or one-dimensional case, $m = 1$.

Since the computer can deal only with a finite number of discrete values, the numerical algorithm to solve the Cauchy problem (1.1)–(1.2) starts by setting the points $t_0, t_1, \ldots, t_N$ at which the solution will be computed. The points $t_n, n = 0, \ldots, N$, define a *discretization* (or a grid) of the interval $I = [0,T]$. The equidistant or *regular* distribution of the grid points is the simplest and will be used in this chapter. We set (see Fig. 1.1) $t_n = nh$, with $h = T/N$ the constant discretization step (or time step if t is regarded as a time variable) and define the subintervals $I_n = [t_n, t_{n+1}], n = 0, \ldots, N-1$ (notice that $t_0 = 0$ and $t_N = T$).

The numerical approximation of the Cauchy problem consists in building a sequence of numbers (depending on N) $u_0^{(N)}, \ldots, u_N^{(N)}$ that approximate the values $u(t_0), \ldots, u(t_N)$ of the exact solution $u(t)$ at the same computation points. We always start with $u_0^{(N)} = u_0$ in order to satisfy the initial value condition $u(t_0) = u_0$. In order to simplify notation, we will refer, when possible, to $u_n^{(N)}$ by u_n.

1.1.1 Construction of Numerical Integration Schemes

Having discretized the definition interval I, we must find a formula to compute values u_n, for $n = 1, \ldots, N$. Such a formula, which is usually called a *numerical*

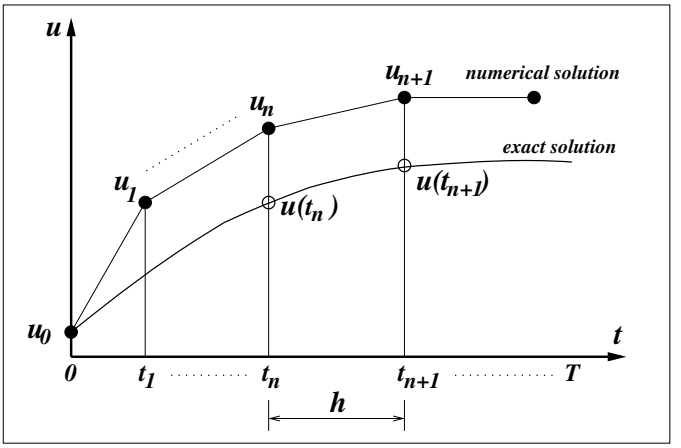

Fig. 1.1. Regular grid and numerical approximation of an ODE.

scheme, is obtained by *discretizing* the differential operator in the ODE. We present here two types of methods that can be used to build numerical schemes for the ODE (1.1). Remember that any integration scheme will start from the value u_0 imposed by the initial condition.

Methods Based on Finite Differences

This type of method consists in writing the equation (1.1) at time $t = t_n$ and replacing $u'(t_n)$ by a finite difference approximation. For this purpose we use a Taylor series expansion to approximate the values of the unknown u for t close to t_n. We consider, for instance, the example of the first derivative.

Definition 1.2. *The discretization step h being fixed, we define the following finite difference operators:*

- *forward or progressive*

$$D^+u(t) = \frac{u(t+h) - u(t)}{h}, \tag{1.3}$$

- *backward or regressive*

$$D^-u(t) = \frac{u(t) - u(t-h)}{h}, \tag{1.4}$$

- *central*

$$D^0u(t) = \frac{u(t+h) - u(t-h)}{2h}. \tag{1.5}$$

Let us assume that the function u is twice continuously differentiable. Then there exists $\theta_n^+ \in [0, h]$ such that

$$u(t_{n+1}) = u(t_n) + hu'(t_n) + \frac{h^2}{2}u''(t_n + \theta_n^+). \tag{1.6}$$

We can derive from this expansion an approximation of $u'(t_n)$:

$$u'(t_n) = \frac{u(t_{n+1}) - u(t_n)}{h} - \frac{h}{2}u''(t_n + \theta_n^+) \approx D^+u(t_n), \tag{1.7}$$

and calculate the approximation (or truncation) error

$$\varepsilon_n = \left|u'(t_n) - D^+u(t_n)\right| \leq \frac{h}{2}\max_{t\in I_n}|u''(t)|. \tag{1.8}$$

Assuming that $|u''|$ is bounded, we infer that the truncation error decays to 0 with h. We conventionally denote the approximation error by $\mathcal{O}(h)$ and write: $u'(t_n) = D^+u(t_n) + \mathcal{O}(h)$.

Definition 1.3. *We say that $D^+u(t_n)$ is a first-order approximation of $u'(t_n)$. We generally define the order of accuracy of the difference approximation as the power of h with which the approximation error tends to zero.*

It is easy to see that $D^-u(t_n) = [u(t_n) - u(t_{n-1})]/h$ is also a first-order approximation of $u'(t_n)$, while $D^0u(t_n) = [u(t_{n+1}) - u(t_{n-1})]/(2h)$ is a second-order (i.e., the order of accuracy is two) approximation of $u'(t_n)$.

More generally, it is possible to use linear combinations of several finite difference operators to find approximations of $u'(t_n)$. For instance, we can approach

$$u'(t_n) \approx \alpha D^-u(t_n) + \beta D^0u(t_n) + \gamma D^+u(t_n), \tag{1.9}$$

with parameters α, β, and γ chosen such that the approximation has the highest possible order of accuracy.

Taylor series expansion remains the basic tool for building approximations of higher-order derivatives. For the second derivative, for instance, the simplest recipe is the following: continue the expansion (1.6) to the fourth-order, write a similar expansion for $u(t_{n-1})$, and sum the two relationships. A centered second-order approximation of the second derivative is thus obtained:

$$u''(t_n) \approx D^-D^+u(t_n) = \frac{u(t_{n+1}) - 2u(t_n) + u(t_{n-1})}{h^2}. \tag{1.10}$$

We address now the problem of building numerical schemes for the ODE (1.1) using the previous finite difference approximations. Considering the ODE at time t_n and replacing $u'(t_n)$ by $D^+u(t_n)$, we obtain the scheme

$$u_{n+1} = u_n + hf(t_n, u_n). \tag{1.11}$$

We recall that u_{n+1}, respectively u_n, are numerical approximations of $u(t_{n+1})$, respectively $u(t_n)$.

The scheme (1.11) is called the *explicit* Euler scheme, or simply the Euler scheme. This method is said to be explicit because u_{n+1} depends explicitly on t_n and the old value u_n. More generally, a numerical scheme is explicit if u_{n+1} can be calculated explicitly from quantities that are already known (i.e., values of the solution at previous times).

Consider now the ODE (1.1) at time t_{n+1} and replace $u'(t_{n+1})$ by $D^- u(t_{n+1})$; we obtain the *implicit* Euler scheme

$$u_{n+1} = u_n + hf(t_{n+1}, u_{n+1}). \tag{1.12}$$

This time, u_{n+1} is computed as the solution (if it exists!) of an implicit equation. This requires more work, in particular when the function $u \mapsto f(t, u)$ is nonlinear with respect to u.

The approximation $u'(t_n) \approx D^0 u(t_n)$ in (1.1), written at time t_n, leads to the scheme

$$u_{n+1} = u_{n-1} + 2hf(t_n, u_n), \tag{1.13}$$

called the leapfrog (or midpoint) scheme.

Methods Based on Quadrature Formulas

Another way to build a numerical scheme is based on quadrature formulas (numerical integration is also called quadrature). Integrating the ODE (1.1) on the interval $I_n = [t_n, t_{n+1}]$, we obtain

$$u(t_{n+1}) - u(t_n) = \int_{t_n}^{t_{n+1}} f(s, u(s))ds = \mathcal{I}_n. \tag{1.14}$$

We can hence compute $u(t_{n+1})$ starting from the old value $u(t_n)$ if we are able to approximate the integral $\mathcal{I}_n$. We go back to a quadrature problem.

Several quadrature rules can be used to estimate the integral in (1.14):

- *the left endpoint rule*
$$\mathcal{I}_n \approx hf(t_n, u_n), \tag{1.15}$$
leading to the explicit Euler scheme (1.11);
- *the right endpoint rule*
$$\mathcal{I}_n \approx hf(t_{n+1}, u_{n+1}), \tag{1.16}$$
defining the implicit Euler scheme (1.12);
- *the midpoint (or rectangle) rule*
$$\mathcal{I}_n \approx hf(t_n + h/2, u(t_n + h/2)), \tag{1.17}$$
leading, using the approximation

$$u(t_n + h/2) \approx u(t_n) + \frac{h}{2}u'(t_n) = u(t_n) + \frac{h}{2}f(t_n, u(t_n)), \tag{1.18}$$

to the modified explicit Euler scheme:

$$u_{n+1} - u_n = hf\left(t_n + \frac{h}{2}, u_n + \frac{h}{2}f(t_n, u_n)\right). \tag{1.19}$$

- *the trapezoid rule*

$$\mathcal{I}_n \approx \frac{h}{2}\left[f(t_n, u_n) + f(t_{n+1}, u_{n+1})\right], \tag{1.20}$$

yielding the *semi-implicit* Crank–Nicolson scheme.

1.1.2 General Form of Numerical Schemes

The general form of a numerical scheme for the ODE (1.1) is

$$u_{n+1} = F(h; t_{n+1}, u_{n+1}; t_n, u_n; \ldots). \tag{1.21}$$

If F depends on q previous values u_{n-j}, $j = 0, \ldots, q-1$, the scheme is said to be a q-step scheme. For instance, the leapfrog scheme is a two-step scheme. If F does not depend on the solution at time level t_{n+1}, the scheme is said to be explicit. Otherwise, the scheme is implicit.

Remark 1.1. To start a one-step scheme, a single value is needed; this is u_0, which is always set by the initial condition $u(0)$. It goes differently in the case of a $(q > 1)$-step scheme; this scheme can be used to compute values u_n for $n \geq q$, once the first q values $u_0, \ldots, u_{q-1}$ are known. Since only the initial condition u_0 is provided, the missing intermediate values can be computed using lower-step schemes. For example, a one-step scheme can be used to compute u_1, a two-step scheme to compute u_2, and a $(q-1)$-step scheme to compute u_{q-1}.

Definition 1.4. *For the numerical scheme (1.21) we define the formal local truncation error as*

$$e_n = u(t_{n+1}) - F\left(h; t_{n+1}, u(t_{n+1}); t_n, u(t_n); \ldots\right), \tag{1.22}$$

where $u(t)$ is the solution of the ODE (1.1). The scheme has order of accuracy p if $e_n = \mathcal{O}(h^{p+1})$ as $h \to 0$. The scheme is said consistent if it has order of accuracy $p \geq 1$.

The idea behind this definition is that the discretized equation should tend to the exact ODE when $h \to 0$. In other words, when applying the numerical scheme to the exact solution function $u(t)$ one should recover (by Taylor series expansions) the original ODE plus a reminder representing the truncation error. Let us illustrate this by the example of the leapfrog scheme (1.13), for

Explicit Euler (first order)	$u_{n+1} = u_n + hf(t_n, u_n)$
Implicit Euler (first order)	$u_{n+1} = u_n + hf(t_{n+1}, u_{n+1})$
leapfrog (second order)	$u_{n+1} = u_{n-1} + 2hf(t_n, u_n)$
Modified Euler (second order)	$u_{n+1} = u_n + hf(t_n + \frac{h}{2}, u_n + \frac{h}{2} f(t_n, u_n))$
Crank–Nicolson (second order)	$u_{n+1} = u_n + \frac{h}{2}[f(t_n, u_n) + f(t_{n+1}, u_{n+1})]$
Adams–Bashforth (second order)	$u_{n+1} = u_n + h[\frac{3}{2} f(t_n, u_n) - \frac{1}{2} f(t_{n-1}, u_{n-1})]$
Adams–Bashforth (third order)	$u_{n+1} = u_n + h[\frac{23}{12} f(t_n, u_n) - \frac{16}{12} f(t_{n-1}, u_{n-1}) + \frac{5}{12} f(t_{n-2}, u_{n-2})]$
Adams–Moulton (third order)	$u_{n+1} = u_n + h[\frac{5}{12} f(t_{n+1}, u_{n+1}) + \frac{8}{12} f(t_n, u_n) - \frac{1}{12} f(t_{n-1}, u_{n-1})]$
Runge–Kutta (Heun) (second order)	$\begin{cases} k_1 = hf(t_n, u_n), \\ k_2 = hf(t_n + h, u_n + k_1), \\ u_{n+1} = u_n + \frac{1}{2}(k_1 + k_2) \end{cases}$
Runge–Kutta (fourth order)	$\begin{cases} k_1 = hf(t_n, u_n), \\ k_2 = hf(t_n + h/2, u_n + k_1/2), \\ k_3 = hf(t_n + h/2, u_n + k_2/2), \\ k_4 = hf(t_n + h, u_n + k_3), \\ u_{n+1} = u_n + \frac{1}{6}(k_1 + 2k_2 + 2k_3 + k_4) \end{cases}$

Table 1.1. Numerical schemes for the ODE $u'(t) = f(t, u)$.

which $F = u_{n-1} + 2hf(t_n, u_n)$. Using Taylor series expansions about $t = t_n$, we obtain for the truncation error (1.22) the expression

$$e_n = 2h\,[u'(t_n) - f(t_n, u(t_n))] + \frac{h^3}{3} u''(t_n) + \cdots. \tag{1.23}$$

Since $u'(t_n) = f(t_n, u(t_n))$, we conclude that the leap-frog scheme is a second-order scheme, i.e., the order of accuracy is two. Some numerical schemes commonly used in practice are summarized in Table 1.1.

1.1.3 Application to the Absorption Equation

The model equation that describes an absorption (or production) phenomenon is the following: find a function $u : \mathbb{R}^+ \to \mathbb{R}$ that is a solution of the Cauchy problem

$$\begin{cases} u'(t) + \alpha u(t) = f(t), \quad \forall t > 0, \\ u(0) = u_0, \end{cases} \tag{1.24}$$

where $\alpha \in \mathbb{R}$ is a given physical constant and the source term f takes into account the production in time of the quantity u.

Example 1.1. The intensity of the radiation emitted by a radioactive body is estimated by measuring the concentration $u(t)$ of an unstable isotope. This concentration decays by a factor of two during a time interval T (called the half-life) according to the law

$$u'(t) = \alpha u(t), \quad \text{with} \quad \alpha = -\frac{\ln 2}{T}.$$

Exercise 1.1. Consider the Cauchy problem (1.24).

1. We set $u(t) = e^{-\alpha t} v(t)$. Write the ordinary differential equation satisfied by v. Solve analytically this equation and verify that

$$u(t) = e^{-\alpha t} \left(u_0 + \int_0^t e^{\alpha s} f(s) ds \right). \tag{1.25}$$

2. Derive the exact solution in the case of α depending on t.
3. Assuming that α and f are constants, derive an expression for u and calculate $\lim_{t \to +\infty} u(t)$.
4. Consider $f = 0$, and a more general coefficient $\alpha \in \mathbb{C}$, with real part $\alpha_r > 0$. Show that $\lim_{t \to +\infty} u(t) = 0$.
5. Write a MATLAB function to implement the explicit Euler scheme (1.11). The definition header of the function will be as follows

```
function u=PDE_EulerExp(fun,u0,t0,t1,n)
% Input arguments:
%      fun  the name of the right-hand-side EDO function
%      t0   the initial time
%      u0   the initial condition at  t0
%      t1   the final time
%      n    the number of time steps between t0 and t1
% Output arguments:
%      u    the dimension (n+1) vector containing the numerical
%              solution at times  t0+i*h, with h=(t1-t0)/n
```

Hint: use the MATLAB built-in function `feval` to evaluate the parameter function `fun` within the `PDE_EulerExp` function.
In a MATLAB program (or script), call the `PDE_EulerExp` function to solve the ODE $u'(t) + 4u(t) = 0$ with the initial condition $u(0) = 1$. Set $t_0 = 0, t_1 = 3$, and $n = 24$ ($h = 1/8$). Plot the results, both exact and numerical solutions superimposed on a single graph, and comment on them. Perform the same computation for $n = 6$ ($h = 1/2$). Comment on the results.

6. Use instead of the explicit Euler scheme the fourth-order Runge–Kutta scheme (write a function `PDE_RKutta4` using as model `PDE_EulerExp`). Comment on the results obtained for $h = 1/2$.

A solution of this exercise is proposed in Sect. 1.3 at page 19.

1.1.4 Stability of a Numerical Scheme

We consider here the absorption equation for $f = 0$ and $\alpha \in \mathbb{R}^+$. The exact solution is then $u(t) = e^{-\alpha t}u_0$ with the property $\lim_{t\to+\infty} u(t) = 0$. Assume that we want to compute this solution using the explicit Euler scheme (1.11). We obtain a sequence of values $u_n = (1 - \alpha h)^n u_0$. It is easy to see that

- if $h > 2/\alpha$, then $1 - \alpha h \leq -1$ and the sequence (u_n) diverges;
- if $0 < h < 2/\alpha$, then $|1 - \alpha h| < 1$ and the sequence (u_n) decays to 0 as $t \to \infty$, reproducing the behavior of the exact solution.

Let us assume at this point that the reader, pushed by curiosity, has already answered question 5 of Exercise 1.1. The above analysis explains the *strange* behavior of the numerical solution obtained for a discretization step $h = 1/2$ and $\alpha = 4$ (the solution takes alternatively the values $+1$ and -1, see Fig. 1.3). The real question behind this observation is how to be sure that the numerical scheme gives the right solution. Part of the answer is related to the accuracy of the scheme: if the scheme is consistent (see Definition 1.4), we know that the discrete scheme commits local (at a given time) errors that vanish when $h \to 0$. Unfortunately, as can be seen from our example, consistency is not sufficient to achieve convergence to the exact solution. The stability of the numerical scheme is also required for a successful numerical computation. Intuitively, we can say that a numerical scheme will be stable if it does not magnify the errors appearing during the computation.

The fundamental concept of stability can be mathematically addressed in several ways (see, for example, Richtmyer and Morton, 1967; LeVeque, 1992; Hirsch, 1988; Trefethen, 1996). The widely used definition of the stability (also known as *zero-stability*, or Lax–Richtmyer stability for PDEs) requires that the computed values remain bounded when $h \to 0$ for a fixed integration interval $[0, T]$. This is an important concept since, as stated from the well-known equivalence theorem (due to Dahlquist for ODEs and to Lax and Richtmyer for PDEs, see Trefethen (1996)), the zero-stability is a necessary and sufficient condition for a consistent scheme to be convergent.

In some practical applications, it is not always possible to take h small enough for the zero-stability to apply. This is the case of *stiff* ODEs, i.e., involving different varying time scales (see Chap. 2). For this type of ODEs, we generally use the concept of *absolute stability* which considers the behavior of the numerical scheme when the time step h is held fixed and $t \to \infty$.

We illustrate in the following the concept of absolute stability by the example of the absorption equation ($u'(t) = -\alpha u$).[1] We consider the simplest case of one-step schemes in Table 1.1. We can recast these numerical schemes into the general form

$$u_{n+1} = G(-\alpha h)u_n = \ldots = [G(-\alpha h)]^{n+1} u_0. \tag{1.26}$$

G is called the amplification function[2] and is supposed to reflect the behavior of the exact solution, since this satisfies the relationship

$$u(t_{n+1}) = e^{-\alpha h} u(t_n). \tag{1.27}$$

The reader is invited to derive the following expressions for the amplification function (we denote $z = -\alpha h$):

Explicit Euler:	$G(z) = 1 + z$,
Implicit Euler:	$G(z) = 1/(1 - z)$,
Modified Euler:	$G(z) = (2 + z)/(2 - z)$,
Runge–Kutta (second order):	$G(z) = 1 + z + z^2/2$,
Runge–Kutta (fourth order):	$G(z) = 1 + z + z^2/2 + z^3/6 + z^4/24$.

A sufficient condition for stability is now $|G(-\alpha h)| < 1$. This stability condition ensures that the numerical solution has the same behavior as the exact solution when $t \to \infty$, since

$$\lim_{n \to +\infty} |u_n| \leq \lim_{n \to +\infty} |u_0| \, |G(-\alpha h)|^n = 0.$$

Definition 1.5. *The locus $\mathcal{S}$ of points $z \in \mathbb{C}$ for which $|G(z)| < 1$ is called the (absolute) stability region of the scheme.*

For example, the stability region $\mathcal{S}$ of the explicit Euler scheme is the open disk of radius 1, centered at the point $(-1, 0)$. The scheme will hence be absolutely stable if the discretization step h is chosen such that $|1 - \alpha h| < 1$.

[1] The linear ODE $u'(t) = au(t)$ for some constant $a \in \mathbb{C}$ is generally used as model equation to investigate the absolute stability of a numerical scheme. For nonlinear systems of ODEs, a similar analysis can be applied after linearization and diagonalization (see Chap. 2) – this type of stability is often reffered to as the *eigenvalue stability*.

[2] For multistep schemes, G becomes a matrix; for the analysis of the absolute stability of multistep schemes, see, for instance, Trefethen (1996).

Remark 1.2. According to Definition 1.5, the absolute stability region $\mathcal{S}$ contains the points for which $|u_n| \to 0$ as $t \to \infty$. It is interesting to note that in some textbooks (e.g. Trefethen (1996)) the absolute stability region is defined as the locus $\bar{\mathcal{S}}$ of points $z \in \mathbb{C}$ for which $|G(z)| \leq 1$, i.e., we ask that the numerical solution u_n be bounded as $t \to \infty$. In general, if $\mathcal{S}$ is not empty, $\bar{\mathcal{S}}$ is the closure of $\mathcal{S}$. But there are some special cases, as the leapfrog scheme for which $\mathcal{S}$ is empty and $\bar{\mathcal{S}} = [-\mathrm{i}, \mathrm{i}]$.

This second definition of the absolute stability is important since it makes the link with the zero-stability: a numerical scheme is zero-stable if and only if the origin $z = 0$ belongs to $\bar{\mathcal{S}}$ (see Trefethen, 1996, for more details).

Exercise 1.2. Plot in the same figure the bounds of the stability regions of the following schemes: explicit Euler, second-order Runge–Kutta, and fourth-order Runge–Kutta. Hint: define a complex variable $z = (x, y)$ covering the rectangle $[-4, 1] \times [-4, 4]$ (use the MATLAB built-in function `meshgrid`) and plot the contour line corresponding to $|G(z)| = 1$ (function `contour`).
A solution of this exercise is proposed in Sect. 1.3 at page 19.

1.2 Model Partial Differential Equations

The PDEs presented in this chapter model elementary physical phenomena: convection, wave propagation, and diffusion. For each of these problems, we present one or several model equations, derive an exact solution in particular cases, and compute approximate solutions using appropriate numerical schemes. We consider in this section the following PDEs:

- the convection equation: $\partial_t u(x,t) + c\partial_x u(x,t) = f(x,t)$,
- the wave equation: $\partial_{tt}^2 u(x,t) - c^2 \partial_{xx}^2 u(x,t) = 0$,
- the heat equation: $\partial_t u(x,t) - \kappa \partial_{xx}^2 u(x,t) = f(x,t)$.

1.2.1 The Convection Equation

The PDE describing the convection (or transport) of a quantity $u(x,t)$ at velocity c (assumed constant in the following) is

$$\partial_t u(x,t) + c\partial_x u(x,t) = f(x,t), \quad \forall x \in \mathbb{R}, \quad \forall t > 0, \tag{1.28}$$

with the initial condition

$$u(x,0) = u_0(x), \quad \forall x \in \mathbb{R}. \tag{1.29}$$

The source term $f(x,t)$ generally models the production in time of u.

Example 1.2. The transport of a pollutant in the atmosphere is modeled by the PDE $\partial_t u + \partial_x(cu) = 0$, where $u(x,t)$ is the concentration of the pollutant and c the wind velocity. If c is assumed constant, we retrieve the form (1.28) of the PDE. Note that $f = 0$ corresponds to the case that there is no further production of pollutant at times $t > 0$.

Exercise 1.3. We consider the convection equation (1.28) with the initial condition (1.29) in the case $f(x,t) = 0$ (no sources).

1. In order to compute the exact solution we introduce the change of variables

$$X = \alpha x + \beta t, \quad T = \gamma x + \mu t \qquad (\alpha, \beta, \gamma, \mu \in \mathbb{R}), \tag{1.30}$$

and define the function U by $U(X,T) = u(x,t)$. Is this change of variables a bijection? Write the PDE satisfied by U. What happens to this equation if $\beta = -c\alpha$? Solve this last equation analytically. Deduce that the solution is constant along the lines (C_ξ) defined in the (x,t) plane by

$$x = \xi + ct, \qquad \xi \in \mathbb{R}. \tag{1.31}$$

Definition 1.6. *The lines (1.31) are called characteristic curves of the convection equation (1.28).*

2. We now want to find the exact solution of (1.28)–(1.29) on a finite real interval $[a,b]$. We assume that $c > 0$ and proceed geometrically. After drawing in the (x,t) plane the characteristic curves C_ξ for $\xi \in [a,b]$, show that the solution $u(x,t)$ for all $x \in [a,b]$ and all $t > 0$ is completely determined by the initial condition u_0 and an additional boundary condition

$$u(a,t) = \varphi(t), \qquad \forall t > 0. \tag{1.32}$$

Show that for a given T the exact solution is

$$u(x,t) = \begin{cases} u_0(x - cT) & \text{if } \ x - cT > a, \\ \varphi\left(T - \dfrac{x-a}{c}\right) & \text{if } \ x - cT < a. \end{cases} \tag{1.33}$$

Note that in the case $u_0(a) \neq \varphi(0)$, the solution is discontinuous along the characteristic curve $x - cT = a$. Find the value of T after which the initial condition u_0 has completely left the interval $[a,b]$, i.e., $u(x,t)$ can be written as a function of $\varphi(t)$ only. Determine the boundary condition necessary to calculate u in the case of $c < 0$.

3. For the numerical solution of the convection equation (1.28) we define a regular space discretization

$$x_j = a + j\delta x, \quad \delta x = \frac{b-a}{J}, \quad j = 0, 1, \ldots, J \geq 2, \tag{1.34}$$

and a time discretization ($T > 0$ is fixed)

$$t_n = n\delta t, \quad \delta t = \frac{T}{N}, \quad n = 0, 1, \ldots, N \geq 2. \tag{1.35}$$

Write a MATLAB function to compute the exact solution (1.33) following the model:

```
function uex=PDE_conv_exact_sol(a,b,x,T,fun_ci,fun_cl)
% Input arguments:
%      a,b  the interval [a,b]
%      c>0  the convection speed
%      x    the vector x(j)=a+j*delta x, j=0,1,...,J
%      T    the time at which the solution is computed
%      fun_in(x)  the initial condition for t=0
%      fun_bc(x) the  boundary condition for x=a
% Output argument:
%      uex   the vector of length J+1 containing the
%      exact solution
```

4. We assume that $c > 0$ and denote by u_j^n an approximation of $u(x_j, t_n)$. The following numerical scheme is proposed to compute u_j^n:
   - For $n = 0$ the initial condition is imposed: $u_j^0 = u_0(x_j), j = 0, 1, \ldots, J$.
   - For $n = 0, \ldots, N-1$ (loop in time to compute u^{n+1}):
     - For $j = 1, \ldots, J$ (the interior of the domain)

$$u_j^{n+1} = u_j^n - \frac{c\delta t}{\delta x}(u_j^n - u_{j-1}^n). \tag{1.36}$$

     - Set boundary value: $u_0^{n+1} = \varphi(t_{n+1})$.

   (a) Justify geometrically (draw the characteristic starting from point u_j^{n+1}) that the previous algorithm is well defined if

$$\sigma = \frac{c\delta t}{\delta x} \leq 1. \tag{1.37}$$

   Definition 1.7. *The inequality (1.37) gives a sufficient condition for the stability of the upwind scheme (1.36) for the convection equation and is called the CFL (Courant–Friedrichs–Lewy) condition.*

   (b) Write a program using this algorithm to solve the convection equation for the following data:

$$a = 0, \quad b = 1, \quad c = 4, \quad f = 0,$$

$$u_0(x) = x, \quad \varphi(t) = \sin(10\pi t).$$

   Choose $J = 40$ and compute δt from (1.37) with $\sigma = 0.8$.
   Plot the solutions obtained after $n = 10, 20, 30, 40, 50$ time steps. Compare to the exact solution.
   What happens if $\sigma = 1$, or $\sigma = 1.1$? Comment on the influence of the value of σ on the stability of the scheme.

A solution of this exercise is proposed in Sect. 1.3 at page 21.

1.2.2 The Wave Equation

Acoustic (or elastic, or seismic) wave propagation is modeled by the following second-order PDE:

$$\partial_{tt}^2 u(x,t) - c^2 \partial_{xx}^2 u(x,t) = 0, \quad t > 0, \tag{1.38}$$

where c is the wave propagation velocity. The corresponding Cauchy problem requires two initial conditions:

$$u(x,0) = u_0(x), \quad \partial_t u(x,0) = u_1(x). \tag{1.39}$$

Example 1.3. The oscillations of an elastic string are described by the equation (1.38), where the function $u(x,t)$ represents the displacement of the string in the vertical plane. The propagation speed depends on the tension τ in the string and on its linear density ρ according to the law $c = \sqrt{\tau/\rho}$. Relations (1.39) provide the initial position and velocity of the string.

If the string is considered infinite, the equation is defined on the whole set $\mathbb{R}$. For a string of finite length ℓ, boundary conditions must be imposed in addition. For instance, if the string is fixed at both ends, the corresponding boundary conditions will be

$$u(0,t) = u(\ell,t) = 0, \quad \forall t > 0. \tag{1.40}$$

Definition 1.8. *The boundary conditions (1.40) are called Dirichlet conditions (the values of the solution are imposed at the boundary of the computational domain). When the imposed values are null, the boundary conditions are said to be homogeneous.*

Infinite string. We first consider the case of an infinite vibrating string.

Exercise 1.4. *Exact solution for the infinite string.* Using the change of variables (1.30), we define the function $U(X,T) = u(x,t)$ and attempt to derive the exact solution:

- Write $\partial_{tt}^2 v$ and $\partial_{xx}^2 u$ as functions of the derivatives of U. Derive the PDE satisfied by U.
- Write this PDE for $\mu = c\gamma$ and $\beta = -c\alpha$. Show that there exist two functions $F(X)$ and $G(T)$ such that $U(X,T) = F(X) + G(T)$.
- Conclude that the general solution of the wave equation can be written as

$$u(x,t) = f(x - ct) + g(x + ct). \tag{1.41}$$

- Using the initial conditions (1.39) show that

$$u(x,t) = \frac{u_0(x - ct) + u_0(x + ct)}{2} + \frac{1}{2c} \int_{x-ct}^{x+ct} u_1(s) ds. \tag{1.42}$$

A solution of this exercise is proposed in Sect. 1.3 at page 25.

Domain of dependence, CFL condition. The expression (1.42) shows that the value of $u(x,t)$ depends only on the initial values u_0 and u_1 restricted to the interval $[x-ct, x+ct]$ (see Fig. 1.2).

Definition 1.9. *The lines of equations $x-ct=\xi$ and $x+ct=\xi$, with $\xi \in \mathbb{R}$ a given constant, are the characteristic curves of the wave equation (1.38).*

We now intend to use a numerical scheme to solve the wave equation. At time $t_{n+1} = (n+1)\delta t$, the value of the solution u_j^{n+1} at point $x_j = j\delta x$ is defined by the information transported from the level t_n along the two characteristics starting from the point (x_j, t_{n+1}) (see Fig. 1.2). The region located between the two characteristics is called the domain of dependence of the wave equation.

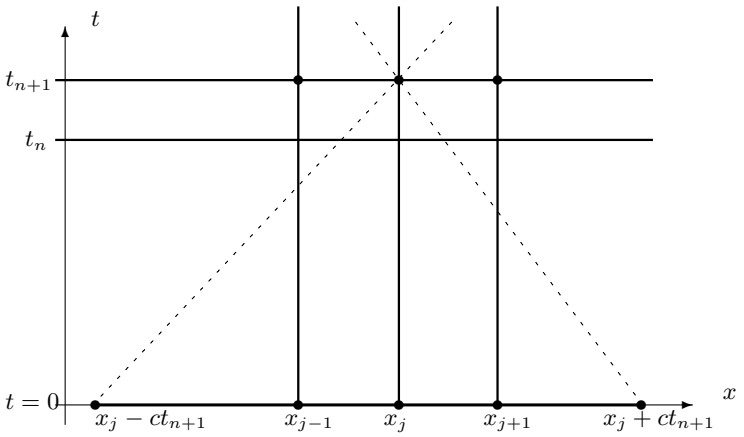

Fig. 1.2. Domain of dependence for the wave equation.

Exercise 1.5. Justify the following numerical scheme for the wave equation:

$$\frac{u_j^{n+1} - 2u_j^n + u_j^{n-1}}{\delta t^2} = c^2 \frac{u_{j+1}^n - 2u_j^n + u_{j-1}^n}{\delta x^2}. \tag{1.43}$$

Show that this scheme is second-order accurate in time and space (use (1.10)) and that the stability (CFL) condition is the same as that found for the convection equation:

$$\sigma = |c| \frac{\delta t}{\delta x} \leq 1. \tag{1.44}$$

A solution of this exercise is proposed in Sect. 1.3 at page 26.

Exercise 1.6. *Periodic initial conditions.* Let us now assume that the initial conditions $u_0(x)$ and $u_1(x)$ are periodic (with the same period τ). Show that the solution $u(x,t)$ of the wave equation is periodic in space (with period τ) and in time (with period τ/c).

1. Justify the following algorithm:
   - for given initial conditions $u_0(x_j)$ and $u_1(x_j)$, compute u_j^0, u_j^1 as
   $$u_j^0 = u_0(x_j), \quad u_j^1 = u_j^0 + \delta t\, u_1(x_j), \tag{1.45}$$
   - for $n \geq 1$, compute
   $$u_j^{n+1} = 2(1-\sigma^2)u_j^n + \sigma^2(u_{j-1}^n + u_{j+1}^n) - u_j^{n-1}. \tag{1.46}$$
2. Write a program to implement this algorithm.
3. Test the program for a string of length $\ell = 1$ and wave velocity $c = 2$. The initial data are $u_0(x) = \sin(2\pi x) + \sin(10\pi x)/4$ and $u_1(x) = 0$, corresponding to a string initially at rest. What is the time period of the solution?
4. Using $nx = 50$ points for the space discretization and $nt = 50$ points to discretize one period of time, superimpose on a single graph the exact and numerical solutions corresponding to one and two time periods. Verify that the numerical scheme preserves the periodicity of the solution. Same question for $nx = 51$. Comment on the results.

A solution of this exercise is proposed in Sect. 1.3 at page 26.

Finite-length vibrating string. Consider the wave equation (1.38) with initial conditions (1.39) and boundary conditions (1.40). We seek a solution of the following form (also called the Fourier or elementary waves expansion):

$$u(x,t) = \sum_{k\in\mathbb{N}^*} \hat{u}_k(t)\phi_k(x), \quad \phi_k(x) = \sin\left(\frac{k\pi}{\ell}x\right). \tag{1.47}$$

For each wave ϕ_k, k is the wave number and $\hat{u}_k$ the wave amplitude.

Exercise 1.7.

1. Derive and solve the PDE satisfied by a function $\hat{u}_k$.
2. Show that the exact solution for the finite-length vibrating string is
   $$u(x,t) = \sum_{k\in\mathbb{N}^*} \left[A_k \cos\left(\frac{k\pi}{\ell}ct\right) + B_k \sin\left(\frac{k\pi}{\ell}ct\right)\right]\phi_k(x), \tag{1.48}$$
   with
   $$A_k = \frac{2}{\ell}\int_0^\ell u_0(x)\phi_k(x)dx, \qquad B_k = \frac{2}{k\pi c}\int_0^\ell u_1(x)\phi_k(x)dx. \tag{1.49}$$
   Find the time and space periods of the solution.

3. Write a program to solve the finite-length vibrating string problem, using the centered scheme (1.43). Hint: start from the program previously implemented and modify the boundary conditions.
   Find the exact solution corresponding to the following initial conditions:

$$u_0(x) = \sin\left(\frac{\pi}{\ell}x\right) + \frac{1}{4}\sin\left(10\frac{\pi}{\ell}x\right), \quad u_1(x) = 0. \tag{1.50}$$

   Plot the exact and numerical solutions at several times over one spatial period. Use the following numerical values: $c = 2$, $\ell = 1$, $nx = 50$, $nt = 125$.

A solution of this exercise is proposed in Sect. 1.3 at page 27.

1.2.3 The Heat Equation

Diffusion phenomena such as molecular and heat diffusion can be described mathematically using the heat equation model

$$\partial_t u - \kappa \partial^2_{xx} u = f(x,t), \quad \forall t > 0, \tag{1.51}$$

with the initial condition

$$u(x,0) = u_0(x). \tag{1.52}$$

Example 1.4. The temperature θ of a heated body is a solution of the equation

$$\partial_t \theta - \partial_x(\kappa \partial_x \theta) = f(x,t), \tag{1.53}$$

where κ is the thermal diffusivity of the material and the function f models the heat source. In a homogeneous medium, κ does not depend on the space position x and we retrieve the model equation (1.51).

Consider the problem of a wall of thickness ℓ, initially at uniform temperature θ_0 (the room temperature). At time $t = 0$, the outside temperature (at $x = 0$) suddenly rises to the value $\theta_s > \theta_0$, which is afterwards maintained constant by an external heat source. The temperature at $x = \ell$ is kept at its initial value θ_0. The heat propagation within the wall is described by the heat equation (1.51), with the unknown $u(x,t) = \theta(x,t) - \theta_0$, $f(x,t) = 0$, the initial condition $u_0(x) = 0$, and Dirichlet boundary conditions

$$u(0,t) = \theta_s - \theta_0 = u_s, \quad u(\ell,t) = 0, \quad \forall t > 0. \tag{1.54}$$

Infinite domain. For an infinitely thick wall ($\ell \to \infty$) we look for a solution of the form

$$u(x,t) = f(\eta), \quad \text{with} \quad \eta = \frac{x}{2\sqrt{\kappa t}}. \tag{1.55}$$

Exercise 1.8. Show that the function f defined above satisfies the following PDE:

$$\frac{d^2 f}{d\eta^2} + 2\eta \frac{df}{d\eta} = 0. \tag{1.56}$$

We introduce the following function, called the *error function*:

$$\mathrm{erf}(z) = \frac{2}{\sqrt{\pi}} \int_0^z e^{-\zeta^2} d\zeta, \tag{1.57}$$

which satisfies $\mathrm{erf}(0) = 0$ and $\mathrm{erf}(\infty) = 1$. Find that the solution of the heat equation for $\ell \to \infty$ is

$$u(x,t) = \left[1 - \mathrm{erf}\left(\frac{x}{2\sqrt{\kappa t}}\right)\right] u(0,t). \tag{1.58}$$

A solution of this exercise is proposed in Sect. 1.3 at page 28.

Remark 1.3. A change in the value of the initial condition at point $x = 0$ has as consequence the modification of the solution everywhere in the domain. In other words, the perturbation introduced at $x = 0$ is instantaneously propagated in the computation domain ($u(x,t) > 0, \forall x$ in formula (1.58)). The propagation speed is said to be infinite. We can also prove that the solution at any point depends on all initial values $u_0(x)$. This implies that the domain of dependence for the heat equation is the whole domain of definition. We recall, for comparison, that for the wave equation the domain of dependence is restricted to the area bounded by the characteristics and that the propagation speed of the solution is finite.

Finite domain. For a wall of finite thickness ℓ, the elementary waves expansion (1.47) is used.

Exercise 1.9. Write and solve the equation satisfied by the functions $\hat{u}_k$ in the case of the heat equation. Verify that the solution of the heat equation with boundary conditions (1.54) is

$$u(x,t) = \left(1 - \frac{x}{\ell}\right) u_s + \sum_{k \in \mathbb{N}^*} A_k \exp\left(-\left(\frac{k\pi}{\ell}\right)^2 \kappa t\right) \phi_k(x). \tag{1.59}$$

Show that $A_k = -2u_s/(k\pi)$.
A solution of this exercise is proposed in Sect. 1.3 at page 29.

Remark 1.4. Let us compare the exact solution (1.59) to the exact solution of the wave equation (1.48). The wave equation describes the transport in time of the initial condition. The amplitude of each spatial wave $\phi_k(x)$ oscillates over one time period without damping. The diffusion phenomenon described by the heat equation is characterized by a fast decrease in time of the amplitude of each wave $\phi_k(x)$ due to the presence of the exponential factor in (1.59). This *smoothing* effect of the heat operator increases as the wave number k becomes larger.

Exercise 1.10. *Numerical solution.* Consider first the following explicit centered scheme for the heat equation:

$$\frac{u_j^{n+1} - u_j^n}{\delta t} - \kappa \frac{u_{j+1}^n - 2u_j^n + u_{j-1}^n}{\delta x^2} = 0. \tag{1.60}$$

The stability condition for this scheme is:

$$\kappa \frac{\delta t}{\delta x^2} \leq \frac{1}{2}. \tag{1.61}$$

1. Write a program to solve the problem of the heat propagation in a finite thickness wall. Set $\kappa = 1$, $\ell = 1$, $u_s = 1$, and take $nx = 50$ discretization points in space. The time step δt is calculated using (1.61). Plot the numerical solution for different times and compare to the exact solution (1.59). Compare also to the solution obtained for an infinite domain (1.58). Comment on the results for small t and then for large t.
   Hint: the exact solution is computed to a fair degree of approximation by considering the first 20 wave numbers k in the expansion (1.59).
2. *Smoothing effect.* Run the previous program for $u_s = 0$ and the initial condition defined by

$$u_0(x) = u(x, 0) = \sin\left(\frac{\pi}{\ell} x\right) + \frac{1}{4} \sin\left(10 \frac{\pi}{\ell} x\right). \tag{1.62}$$

   Compare the numerical solution to the exact solution (1.59). Comment on the results by comparing to those obtained for the wave equation with the same initial condition. Describe the damping of the waves defining the initial condition.

A solution of this exercise is proposed in Sect. 1.3 at page 29.

1.3 Solutions and Programs

Solution of Exercises 1.1 and 1.2 (the Absorption Equation)

1. Inserting $u(t) = e^{-\alpha t} v(t)$ in (1.24) gives the differential equation $v'(t) = e^{\alpha t} f(t)$ with the initial condition $v(0) = u(0) = u_0$. It is easy to integrate this ODE to obtain the solution (1.25).
2. If $\alpha = \alpha(t)$ we obtain

$$u(t) = e^{-\int_0^t \alpha(s) ds} \left[u_0 + \int_0^t e^{-\int_0^z \alpha(s) ds} f(z) dz \right].$$

3. Let us assume that the function $f(t) = f$ is constant. The expression (1.25) becomes

$$u(t) = \frac{f}{\alpha} + e^{-\alpha t} \left(u_0 - \frac{f}{\alpha} \right).$$

If $u_0 = f/\alpha$, the solution is constant: $u(t) = u_0,\ \forall t$.
For $\alpha > 0$, $u(t) \to f/\alpha$ for $t \to \infty$.
For $\alpha < 0$, $u(t) \to +\infty \times \text{sign}(u_0 - f/\alpha)$.

4. If $\alpha = \alpha_r + \mathrm{i}\alpha_i$, we obtain

$$|u(t)| = |e^{-\alpha t} u_0| = |e^{-(\alpha_r + \mathrm{i}\alpha_i)t} u_0| = |e^{-\alpha_r t} u_0| \to 0.$$

5. The script *PDE_EulerExp.m* (respectively *PDE_RKutta4.m*) implements the explicit Euler scheme (respectively the fourth-order Runge–Kutta scheme) to integrate the ODE $u'(t) = f(t, u)$. The right-hand side $f(t, u)$ is identified by the generic name `fun` inside these functions; the real name of this function is specified by the user when the functions are called. The two functions return a vector holding the numerical values u_k, computed at discrete times uniformly distributed between t_0 and t_1.

The MATLAB program *PDE_absorption.m* calls the functions `PDE_EulerExp` and `PDE_RKutta4`, sending as input argument the name `PDE_absorption_source` which represents the function implementing the right-hand side of the absorption equation. The results are displayed in two separate figures (Fig. 1.3). The program also plots (Fig. 1.4) the bounds of the stability regions for the considered numerical schemes (Exercise 1.2).

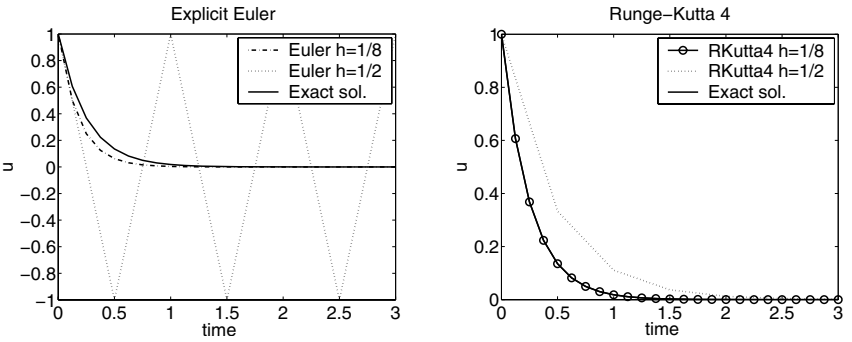

Fig. 1.3. Numerical solution of the ODE $u'(t) + 4u(t) = 0$, obtained using the explicit Euler scheme (left) and the fourth-order Runge–Kutta scheme (right). Solid line represents the exact solution.

Let us comment on the results displayed in Fig. 1.3. Everything goes well for $h = \frac{1}{8} < \frac{2}{\alpha} = \frac{1}{2}$: the numerical solution approaches the exact solution with a better approximation for the Runge–Kutta scheme (in this last case the exact and numerical solutions are not distinguishable in the graph). On the other hand, for $h = \frac{1}{2} = \frac{2}{\alpha}$ the stability limit of the explicit Euler scheme is reached. The numerical solution remains bounded (which is no longer true when $h > \frac{1}{2}$, a case to be tested) but does not converge.

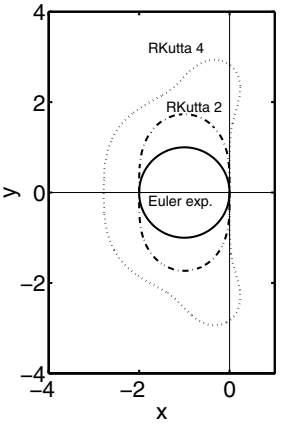

Fig. 1.4. stability region for different numerical schemes.

The fourth-order Runge–Kutta (*RKutta4*) scheme has a wider stability region and remains stable for the two values of the discretization step h considered in this computation. Figure 1.4 shows that the stability region of the *RKutta4* scheme includes both regions of stability of the explicit Euler scheme and *RKutta2*.

In light of these results, the *RKutta4* scheme seems to be the best choice, offering the best stability and accuracy. In fact, the choice of one scheme or another for a practical application is motivated by a compromise between its characteristics (accuracy, stability) and its computational costs (the *RKutta4* scheme is approximately four times as expensive as the explicit Euler scheme for the same discretization step).

Solution of Exercise 1.3 (the Convection Equation)

1. The change of variables can be written as

$$\begin{pmatrix} X \\ T \end{pmatrix} = \begin{pmatrix} \alpha & \beta \\ \gamma & \mu \end{pmatrix} \begin{pmatrix} x \\ t \end{pmatrix},$$

and it is one-to-one and onto (i.e. bijective) if $\alpha\mu \neq \beta\gamma$. Differentiation with respect to the new variables gives

$$\partial_t u = \beta \partial_X U + \mu \partial_T U, \quad \partial_x u = \alpha \partial_X U + \gamma \partial_T U, \tag{1.63}$$

and we find that U is the solution of the PDE:

$$(\beta + c\alpha)\, \partial_X U + (\mu + c\gamma)\, \partial_T U = 0.$$

For $\beta = -c\alpha$, we get $(\mu + c\gamma)\, \partial_T U = 0$, and, consequently, $\partial_T U = 0$. This last equation has $U(X, T) = F(X)$ as a solution, where F is an arbitrary smooth

function. Therefore we can put $u(x,t) = F(X) = F(\alpha x+\beta t) = F(\alpha x-\alpha ct) = G(x-ct)$, where G is again an arbitrary function. Finally, imposing the initial condition (1.29) we get $u(x,t) = u_0(x-ct)$. This implies in particular that the solution remains unchanged along the characteristic lines, that is

$$\text{if} \quad (x,t) \in C_\xi \Longrightarrow u(x,t) = u_0(\xi), \quad \xi = x - ct.$$

In the plane (x,t), the characteristic curves C_ξ are straight lines of positive slopes $1/c$ (see Fig. 1.5).

2. To derive the solution $u(x,T)$ for $x \in [a,b]$ and $T < T^* = (b-a)/c$, we draw the characteristics through the points (x,T) and use the fact that the solution $u(x,t)$ is constant along a characteristic line. Two cases are possible (see Fig. 1.5):

- the characteristic (C_ξ in the figure) crosses the segment $[a,b]$; this is the case for points located at $x \geq x_T$, with $x_T = a + cT$. The solution will be therefore determined by the initial condition:

$$u(x,T) = u_0(\xi) = u_0(x - cT).$$

- the characteristic (C_μ in the figure) does not cross the segment $[a,b]$; in this case a boundary condition is needed. If we impose $u(a,t) = \varphi(t)$, since the information will be searched through the characteristics back to this boundary condition, the solution is calculated as

$$u(x,T) = \varphi(t_\mu) = \varphi\left(T - \frac{x-a}{c}\right).$$

Note that the initial condition u_0 is completely "evacuated" from the domain $[a,b]$ after a time value $T^* = (b-a)/c$.

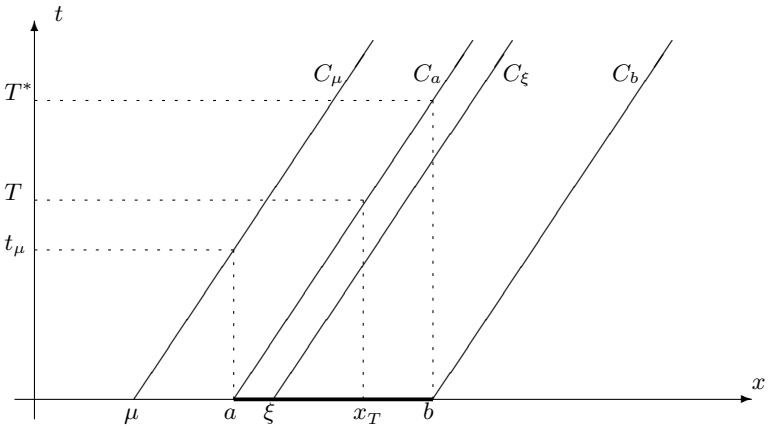

Fig. 1.5. Using characteristics to calculate the solution of the convection equation.

For $c < 0$, the boundary condition must be imposed on the right-hand side of the domain by setting $u(b,t) = \varphi(t)$.

3. The function *PDE_conv_exact_sol.m* computes the exact solution for a given time T. Note in particular the use of the MATLAB command `find` to implement the formula (1.33).

4. We recognize a discretization of equation (1.28) where the time derivative $\partial_t u$ is approximated by $D^+u(t_n)$ and the space derivative $\partial_x u$ by $D^-u(x_j)$. The choice of the upwind approximation for $\partial_x u$ is imposed by the fact that $c > 0$ and therefore the information comes from the left.

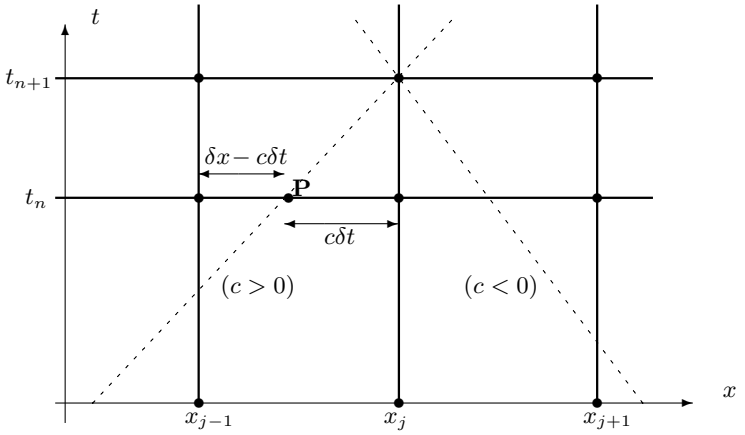

Fig. 1.6. Geometrical interpretation of the CFL condition for the upwind scheme.

The characteristic going through the point u_j^{n+1} is drawn in Fig. 1.6. This line cuts the horizontal line $t = t_n$ at a point P located between x_{j-1} and x_j, at a distance $c\delta t$ from x_j and $\delta x - c\delta t$ from x_{j-1}. Since the solution is constant along a characteristic, necessarily $u_j^{n+1} = u_P^n$.

It is interesting to note from these geometrical considerations that the scheme (1.36) is nothing else but a linear interpolation between the values of the solution at points x_{j-1} and x_j:

$$u_j^{n+1} = \frac{\delta x - c\delta t}{\delta x} u_j^n + \frac{c\delta t}{\delta x} u_{j-1}^n.$$

The CFL condition $c\delta t \leq \delta x$ can be thus regarded as a criterion imposing the positivity of the interpolation coefficients; in other words, the point P must lie within the interval $[x_{j-1}, x_j]$.

Some computing tips may be useful at this point. First of all, we must be careful and make all array indices start from 1 (and not 0 as in mathematical expressions). Then, the solution at time t_{n+1} will be computed according to

$$u_j^{n+1} = (1-\sigma)u_j^n + \sigma u_{j-1}^n, \quad \sigma = \frac{c\delta t}{\delta x}.$$

Since we seek a solution for $n = N$, we save storage memory by using a single array u for the calculation. If the solution is needed at intermediate times, it will be either written to a file or graphically displayed. With this programming trick, the previous relation becomes

$$u(j) = (1 - \sigma)u(j) + \sigma u(j - 1),$$

and the values at time t_n will be replaced by new values at time t_{n+1}. We also must be careful to use in the numerical scheme the values u_{j-1} before they are modified (i.e., at previous time t_n). This is achieved by using an inverse loop ($j = J + 1, J, \ldots, 2$); for $j = 1$ the boundary condition is imposed.

This algorithm is implemented in the program *PDE_convection.m*. This program calls the functions `PDE_conv_bound_cond` and `PDE_conv_init_cond`, which define, in separate files, the initial condition and, respectively, the boundary condition.

The solution for chosen intermediate times is represented in Fig. 1.7 and compared to the exact solution (computed by the function `PDE_conv_exact`). Note that starting from time $T^* = \frac{1}{4}$, the initial data leaves the computation domain, and the solution depends only on the boundary condition.

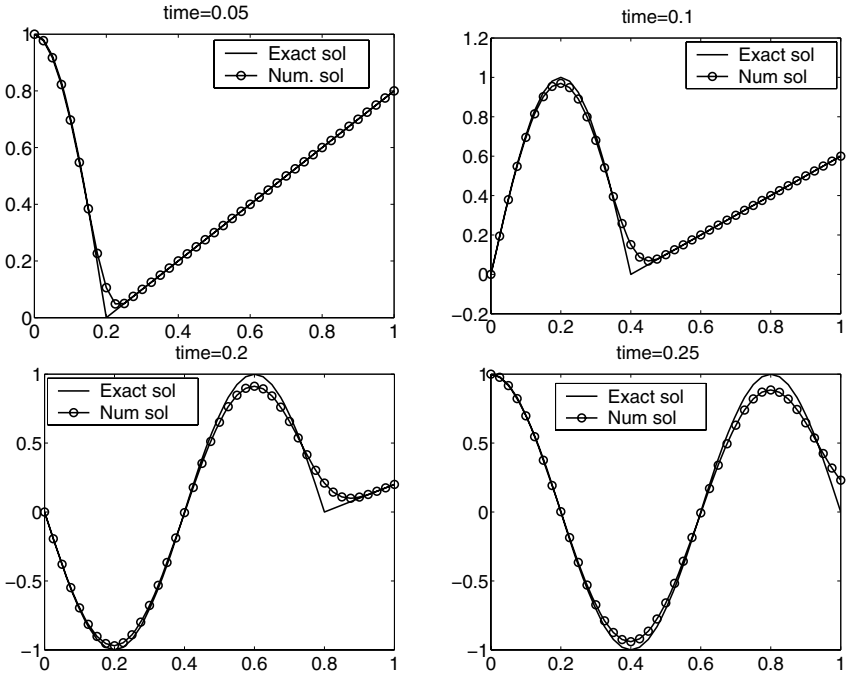

Fig. 1.7. Computation of the solution of the convection equation using the upwind scheme (CFL= 0.8). Solid line represents the exact solution.

An interesting phenomenon can be observed when one looks closer at the solution in the region where the derivative of the exact solution is discontinuous (i.e., where the part of the solution depending on the initial condition is connected to that depending on the boundary condition). There is a numerical *smoothing* of this sharp transition. What is interesting here is that this observed dissipation has no physical meaning and is exclusively due to the numerical scheme. The upwind scheme is therefore said to be *dissipative*. We shall discuss in detail dissipation effects, in a more physical context, when analyzing the heat equation.

A computation performed for $\sigma = 1$ (or CFL = 1) gives results that are perfectly superimposed on the exact solution. This is not surprising, since the upwind scheme becomes in this case an exact relation: $u_j^{n+1} = u_{j-1}^n$. In practice, the convection speed c and the space discretization step δx are generally not constant, making impossible a computation with $\sigma = 1$.

The computation for $\sigma = 1.1$ illustrates the loss of stability of the upwind scheme when $\sigma > 1$.

Solution of Exercise 1.4 (the Wave Equation)

Starting from (1.63), we obtain for the second derivatives

$$\begin{cases} \partial_{tt}^2 u &= \beta^2 \partial_{XX}^2 U + \mu^2 \partial_{TT}^2 U + 2\beta\mu \partial_{TX}^2 U, \\ \partial_{xx}^2 u &= \alpha^2 \partial_{XX}^2 U + \gamma^2 \partial_{TT}^2 U + 2\alpha\gamma \partial_{TX}^2 U, \end{cases}$$

and conclude that U is solution of the PDE:

$$\left(\mu^2 - c^2\gamma^2\right) \partial_{TT}^2 U + \left(\beta^2 - c^2\alpha^2\right) \partial_{XX}^2 U + 2\left(\beta\mu - c^2\alpha\gamma\right) \partial_{XT}^2 U = 0.$$

For $\mu = c\gamma$ and $\beta = -c\alpha$, the equation becomes $-4c^2\alpha\gamma\partial_{XT}^2 U = 0$, which implies that $\partial_{XT}^2 U = 0$, or again $\partial_T(\partial_X U) = 0$. From the previous relationship we infer that there exist two functions $F(X)$ and $G(T)$ such that $U(X,T) = F(X) + G(T)$. Since $X = \alpha(x - ct)$ and $T = \gamma(x + ct)$, we can choose $\alpha = \gamma = 1$, and the solution becomes

$$u(x,t) = f(x - ct) + g(x + ct).$$

Imposing initial conditions for $u(x,t)$ and $\partial_t u(x,t) = -cf'(x-ct)+cg'(x+ct)$, we obtain the system of equations

$$\begin{cases} f'(x) + g'(x) &= u_0'(x), \\ -f'(x) + g'(x) &= (1/c)u_1(x), \end{cases}$$

giving expressions for f' and g' and finally the formula (1.42) for u.

Solution of Exercise 1.5

In the discretization proposed for the wave equation, the second partial derivatives $\partial^2_{xx}u$ and $\partial^2_{tt}u$ are approximated by centered finite differences (see equation (1.10)). One can easily show that the scheme (1.43) is of second order in space and also in time.

The stability condition (1.44) expresses that the domain of dependence (see Fig. 1.2) bounded by the two characteristics starting from the point (x_j, t_{n+1}) must lie inside the triangle $\{(x_j, t_{n+1}), (x_{j-1}, t_n), (x_{j+1}, t_n)\}$ defined by the three-point stencil used by the numerical scheme. In other words, if the time step is larger that the critical value $\delta x/c$, the information searched for by the characteristics will be found outside the interval $[x_{j-1}, x_{j+1}]$ used by the scheme. This is not in accord with the physical phenomenon described by the wave equation and therefore results in instability of the numerical scheme.

From the formula (1.42), it can be easily checked that $u(x+\tau, t) = u(x, t)$ and $u(x, t+\tau/c) = u(x, t)$. The solution $u(x, t)$ is hence periodic in time and space, with period τ in space and τ/c in time.

Solution of Exercise 1.6

In the proposed algorithm, the scheme (1.43) is used together with the computation of the solution for the first time step based on the approximation $\partial_t u(x, t) \approx u_1(x)$.

This algorithm is implemented in the program *PDE_wave_infstring.m* and the initial conditions in files *PDE_wave_infstring_u0.m* and, respectively, *PDE_wave_infstring_u1.m*.

It is worth explaining some programming tricks used in this program. The periodicity condition (also satisfied by the initial condition $u_0(x) = u_0(x+\tau)$ with $\tau = 1$!) is translated in discrete form by $u_{nx+1} = u_1$, since the spatial discretization is built such that $x_1 = 0$ and $x_{nx+1} = 1$. In order to fully exploit the capabilities of MATLAB in terms of vectorial programming, we define the arrays jp and jm corresponding to indices $j+1$, respectively $j-1$, for all discretization points. The periodicity is expressed then by setting $jp(nx) = 1$, $jm(1) = nx$, and the numerical scheme (1.46) is written within a single line of code:

```
u2=-u0+coeff*u1+sigma2*(u1(jm)+u1(jp)).
```

Here $u2$ corresponds to the array $(u^{n+1})_j$, $u1$ to $(u^n)_j$, and $u0$ to $(u^{n-1})_j$. The advantage of this compact programming is to avoid loops interrupted by specific treatments of the points on the boundaries. We shall use this simple programming tip in a more complicated project (Chap. 12).

The numerical results are displayed in Fig. 1.8. The period of the solution in time is $1/c = 0.5$. For $nx = nt = 50$, the CFL number is $\sigma = 1$. The numerical scheme propagates the initial condition correctly and preserves the periodicity in time. The solution after one time period coincides with the exact solution (which is in fact the initial condition u_0). Unlike the upwind scheme

used for the convection equation, this centered scheme does not generate any numerical diffusion (even for smaller nx corresponding to CFL < 1). For $nx = 51$ the scheme becomes unstable because CFL > 1. It is also interesting to note that the instability of the scheme appears only after some time (here after one time period).

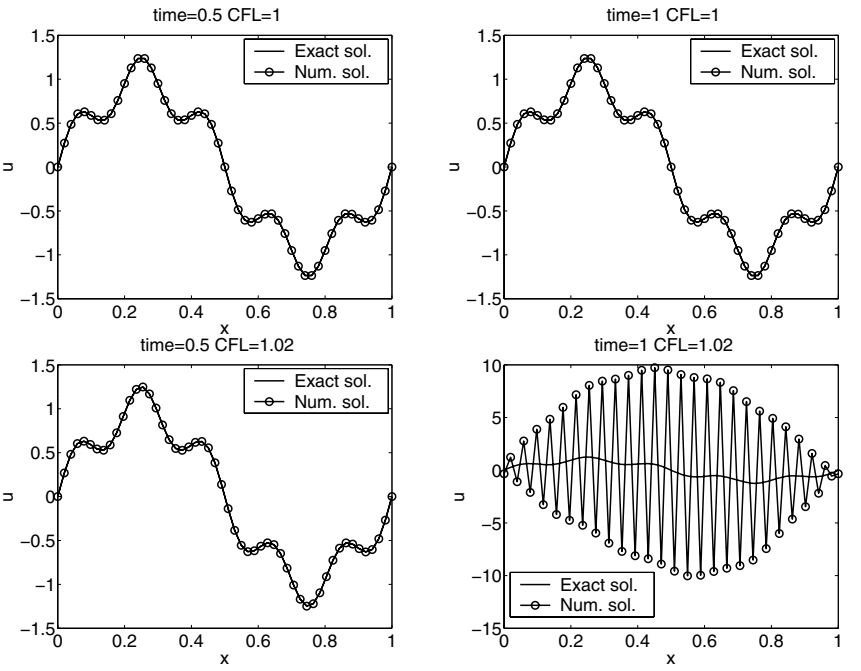

Fig. 1.8. Numerical solution of the wave equation for the infinite vibrating string (periodicity conditions). Initial condition: $u(x,0) = \sin(2\pi x) + \sin(10\pi x)/4$ and $\partial_t u(x,0) = 0$. Comparison with the exact solution for CFL $= 1$ (top) and CFL > 1 (bottom) after one period in time (left) and two periods in time (right).

Solution of Exercise 1.7

The amplitude $\hat{u}_k$ satisfies the PDE

$$\frac{d^2}{dt^2}\hat{u}_k + c^2\left(\frac{k\pi}{\ell}\right)^2 \hat{u}_k = 0, \tag{1.64}$$

which is often encountered in physics. It models in particular the oscillations of a pendulum. The general solution of this PDE being

$$\hat{u}_k(t) = A_k \cos\left(\frac{k\pi}{\ell}ct\right) + B_k \sin\left(\frac{k\pi}{\ell}ct\right), \tag{1.65}$$

the expression (1.48) is straightforward. The coefficients A_k, B_k are computed using the orthogonality of the trigonometric functions ϕ_k on $[0, \ell]$.

We observe that the solution is periodic, of period 2ℓ in space and $2\ell/c$ in time. The initial condition (1.50) corresponds to a decomposition in elementary waves with

$$k = \{1, 10\}, \quad A_k = \{1, 1/4\}, \quad B_k = \{0, 0\}.$$

The exact solution is given by (1.48) with these values.

The program *PDE_wave_fstring.m* computes the solution for the finite-length string. The initial condition is computed in *PDE_wave_fstring_in.m* and the exact solution in *PDE_wave_fstring_exact.m*.

Note that once again, we use vector notation (avoiding `for` loops) for the centered scheme. The computation points corresponding to the boundaries are not modified during the loop in time, and preserve their initial values (which respect the imposed boundary conditions). Figure 1.9 displays a comparison between the exact solution and the numerical solution for two different time instants.

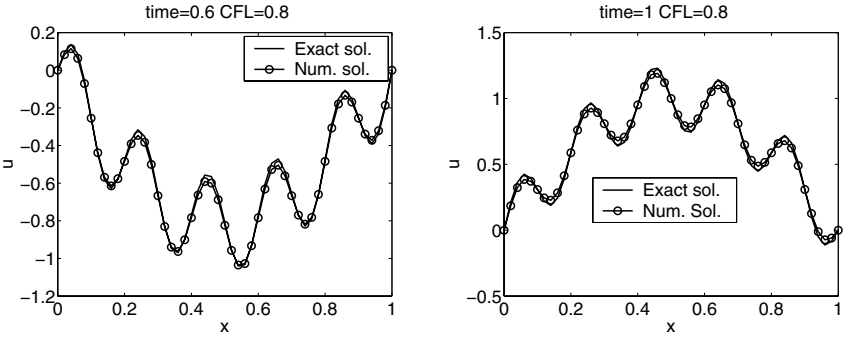

Fig. 1.9. Numerical solution of the wave equation for the finite-length string. Initial condition: $u(x, 0) = \sin(\pi x) + \sin(10\pi x)/4$ and $\partial_t u(x, 0) = 0$. Comparison with the exact solution (one time period corresponds to $t = 1$).

Solution of Exercise 1.8

The partial derivatives can be written in terms of f as

$$\frac{\partial u}{\partial t} = -\frac{\eta}{2t}\frac{df}{d\eta}, \quad \frac{\partial^2 u}{\partial x^2} = \frac{1}{4kt}\frac{d^2 f}{d\eta^2};$$

hence the PDE (1.56) is satisfied by f. After integration, we obtain

$$\frac{df}{d\eta} = Ae^{-\eta^2} \Longrightarrow u(x, t) = f(\eta) = B + A\,\mathrm{erf}(\eta).$$

Taking into account the properties of the function erf when imposing boundary conditions, we can easily obtain the formula (1.58).

Solution of Exercise 1.9

The amplitude $\hat{u}_k$ is solution of the ODE:

$$\frac{d\hat{u}_k}{dt} + \kappa \left(\frac{k\pi}{\ell}\right)^2 \hat{u}_k = 0,$$

and has the analytical form

$$\hat{u}_k(t) = A_k \exp\left(-\left(\frac{k\pi}{\ell}\right)^2 \kappa t\right).$$

We can easily check that any elementary wave $\hat{u}_k(t)\phi_k(x)$ is a solution of the heat equation, but it does not satisfy the boundary conditions (1.54). This is the reason why a linear function of x (which is a also a solution of the heat equation) has been added to obtain the final form of the exact solution (1.59). We note that this is allowed by the linearity of the heat equation.

Finally, the coefficients A_k are calculated using the orthogonality of ϕ_k functions:

$$A_k = -\frac{2u_s}{\ell}\int_0^l \left(1 - \frac{x}{\ell}\right)\sin\left(\frac{k\pi}{\ell}x\right)dx = -\frac{2u_s}{k\pi}.$$

Solution of Exercise 1.10

The MATLAB program *PDE_heat.m* answers questions 1 and 2. The initial condition is computed in *PDE_heat_u0.m* and the exact solution in *PDE_heat_uex.m* (the `erf` function is already available in the standard MATLAB package). Numerical results (see Fig. 1.10) confirm the fact that the erf-solution (1.58) obtained for an infinite domain is a good approximation for small times t (this is the main reason why it is often used in practice by engineers). For longer times t, the exact solution (and hopefully the numerical one as well) converges to the *steady-state* solution (i.e., independent of time) $u(x) = (1 - \frac{x}{\ell})u_s$.

The diffusion phenomenon described by the heat equation is characterized by a time scale $t_0 = \ell^2/\kappa$ (see the expression of η in (1.55)). Consequently, the effective speed of propagation $c_0 = \ell/t_0 = \kappa/\ell$ of a thermal perturbation decreases with the distance to the source. This accounts for the poor efficiency of diffusion systems to propagate heat for large distances or time!

Let us imagine a domestic heating system based on diffusion only. The thermal diffusivity of air being $\kappa \approx 20$ [mm^2/s], the heating effect will be felt at a distance of 1 cm after 5 seconds and at 1 meter after $5{\cdot}10^4$ s ≈ 14 hours!

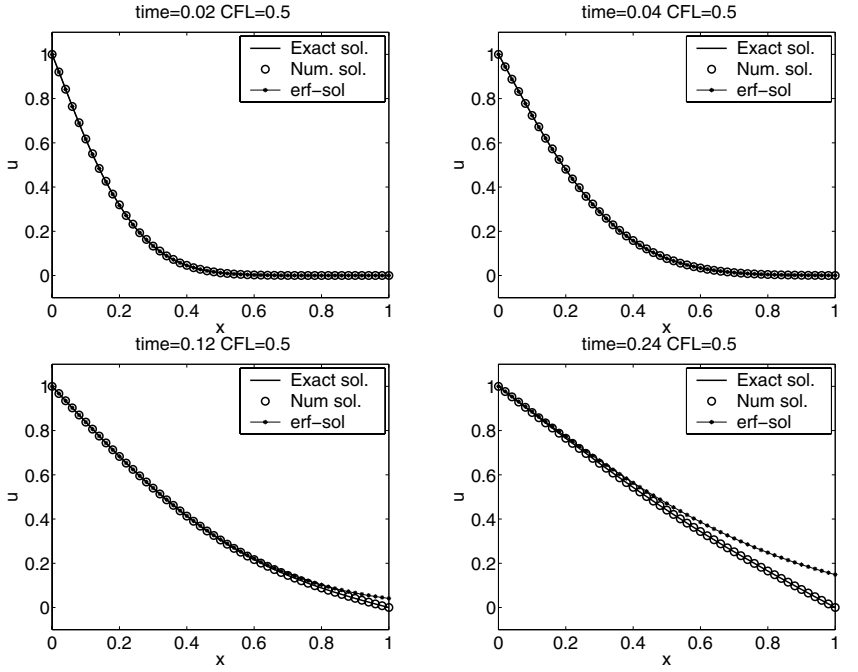

Fig. 1.10. Numerical solution of the heat equation for $x \in [0, \ell]$, $\kappa = 1$, and boundary conditions $u(0,t) = 1, u(\ell,t) = 0$. Initial condition $u(0,0) = 1, u(x,0) = 0, x > 0$. Comparison with the exact solution (1.59) and the erf-solution (1.58) for an infinite domain.

Fortunately, real heating systems are more efficient due to other phenomena (such as air convection and radiation).

For the next question, it is easy to return to the previous program (*PDE_heat.m*) to implement the new initial condition (1.62). The lines to modify are written as comments. The results (see Fig. 1.11) clearly show that the wave of highest wave number, equivalent to highest frequency ($k = 10$ in our case), is first damped. The solution tends to the constant steady-state solution $u(x) = 0$. Recall, for comparison, the behavior of the wave equation, for which the same initial condition was transported without damping of the wave amplitudes (see Fig. 1.9).

Chapter References

Extensive analysis of numerical methods for solving ODEs or PDEs can be found in a large number of books, ranging from the classic text by Richtmyer and Morton (1967), to Lambert (1973), John (1978), Mitchell and Griffiths (1980), Butcher (1987), and more recently Trefethen (1996). Introductions to

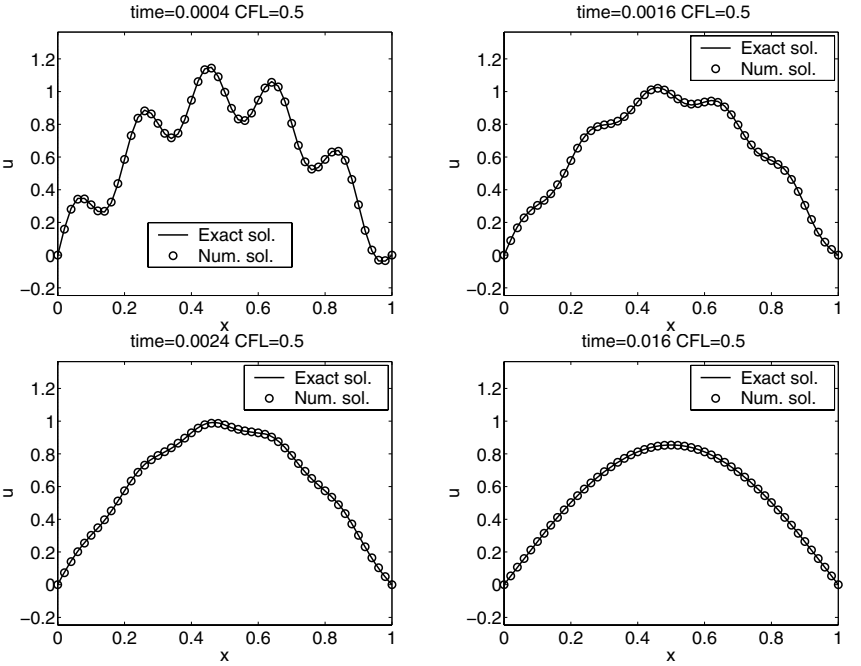

Fig. 1.11. Numerical solution of the heat equation for $x \in [0, \ell]$, $\kappa = 1$, and boundary conditions $u(0,t) = 0, u(\ell,t) = 0$. Initial condition: $u(x,0) = \sin(\pi x) + \sin(10\pi x)/4$. Comparison to the exact solution (1.59). Note the early damping of high frequency waves.

finite difference methods can be found in Strikwerda (1989) or several texts on computational fluid dynamics, such as Hirsch (1988), LeVeque (1992).

The reader acquainted with French literature may refer to Crouzeix and Mignot (1989), Delabrière and Postel (2004), Demailly (1996) for the numerical analysis of ODEs and Lucquin (2004), Mohammadi and Saïac (2003) for PDEs; the implementation of numerical schemes using object-oriented programming is discussed in Danaila, Hecht, and Pironneau (2003).

J. C. Butcher, *The Numerical Analysis of Ordinary Differential Equations*, Wiley, 1987.

M. Crouzeix and A. Mignot, *Analyse numérique des équations différentielles*, Masson, Paris, 1989.

I. Danaila, F. Hecht and O. Pironneau, *Simulation numérique en C++*, Dunod, Paris, 2003.

S. Delabrière and M. Postel, *Méthodes d'approximation, Equations différentielles, Applications Scilab*, Ellipses, Paris, 2004.

J. P. Demailly, *Analyse numérique et équations différentielles*, Presses Universitaires de Grenoble, 1996.

C. Hirsch, *Numerical Computation of Internal and External Flows*, John Wiley & Sons, 1988.
F. John, *Partial Differential Equations*, SpringerVerlag, 1978.
J. D. Lambert, *Computational Methods in Ordinary Differential Equations*, Wiley, 1973.
R. LeVeque, *Numerical Methods for Conservation Laws*, Birkhäuser, 1992.
B. Lucquin, *Équations aux dérivées partielles et leurs approximations*, Ellipses, Paris, 2004.
A. R. Mitchell and D. F. Griffiths, *Computational Methods in Partial Differential Equations*, Wiley, 1980.
B. Mohammadi and J.-H. Saïac, *Pratique de la simulation numérique*, Dunod, 2003.
R. D. Richtmyer and K. W. Morton, *Difference Methods for Initial Value Problems*, 2nd ed., WileyInterscience, 1967.
J. C. Strikwerda, *Finite Difference schemes and Partial Differential Equations*, Wadsworth and Brooks/Cole, 1989.
L. N. Trefethen, *Finite Difference and Spectral Methods for Ordinary and Partial Differential Equations*, unpublished text, available at http//web.comlab.ox.ac.uk/oucl/work/nick.trefethen/pdetext.html, 1996.

2

Nonlinear Differential Equations: Application to Chemical Kinetics

Project Summary

Level of difficulty:	1
Keywords:	Nonlinear system of differential equations, stability, integration schemes, Euler explicit scheme, Runge–Kutta scheme, delayed differential equation
Application fields:	Chemical kinetics, biology

2.1 Physical Problem and Mathematical Modeling

The laws governing chemical kinetics can be written as systems of ordinary differential equations. In the case of complex reactions with several different participating molecules, these equations are nonlinear and present interesting mathematical properties (stability, periodicity, bifurcation, etc.). The numerical solution of this type of system is a domain of study in itself with a flourishing literature. Very efficient numerical methods to solve systems of ODEs are implemented in MATLAB, as in most such software. The first model of reaction that we shall study in this chapter can be completely solved using such a standard package. We will therefore use the ode solvers provided by MATLAB , assuming that the user masters the underlying theory and the basic concepts such as convergence, stability, and precision (see Chap. 1).

The other model includes a delay term. We choose here not to use the delay equation solver dde23 and describe a specific numerical treatment. Both are examples of models presented in Hairer, Norsett, and Wanner (1987).

We first study the so-called *Brusselator* model, which involves six reactants and products A, B, D, E, X, and Y:

$$\begin{cases} A \xrightarrow{v_1} X, & \\ B + X \xrightarrow{v_2} Y + D, & \text{bimolecular reaction,} \\ 2X + Y \xrightarrow{v_3} 3X, & \text{trimolecular autocatalytic reaction,} \\ X \xrightarrow{v_4} E, & \end{cases} \tag{2.1}$$

where v_i are the constant chemical reaction rates. The concentrations of the species as functions of time t are denoted by $A(t)$, $B(t)$, $D(t)$, $E(t)$, $X(t)$, and $Y(t)$. Mass conservation in the chemical reactions leads to the following differential equations:

$$\begin{cases} A' = -v_1 A, \\ B' = -v_2 BX, \\ D' = v_2 BX, \\ E' = v_4 X, \\ X' = v_1 A - v_2 BX + v_3 X^2 Y - v_4 X, \\ Y' = v_2 BX - v_3 X^2 Y. \end{cases}$$

We start by eliminating the two equations governing the production of species D and E, since they are independent of the four others:

$$\begin{cases} A' = -v_1 A, \\ B' = -v_2 BX, \\ X' = v_1 A - v_2 BX + v_3 X^2 Y - v_4 X, \\ Y' = v_2 BX - v_3 X^2 Y. \end{cases}$$

The system can be furthermore simplified by assuming that A and B are kept constant and by taking all reactions rates equal to 1. The resulting system of two equations with two unknowns can be written as the initial value problem

$$\begin{cases} U'(t) = F(U(t)), \\ U(0) = U_0 = (X_0, Y_0)^T, \end{cases} \tag{2.2}$$

where $U(t) = (X(t), Y(t))^T$ is the vector modeling the variations of concentration of substances X and Y, and

$$F(U) = \begin{pmatrix} A - (B+1)X + X^2 Y \\ BX - X^2 Y \end{pmatrix}.$$

2.2 Stability of the System

The stability of the system is its propensity to evolve toward a *constant* or *steady* solution. This steady solution $U(t) = U_c$, if it exists, satisfies $U'(t) = 0$, and can therefore be calculated by solving $F(U_c) = 0$. The solution U_c is called a *critical point*. In the above example it is easy to compute: $U_c = (A, B/A)^T$. The stability of the system can also be regarded as its ability to relax in finite

time to the steady state when a perturbation $\Delta(t) = U(t) - U_c$ is applied to the solution. In order to study the influence of variations $\Delta(t)$, the right-hand side of the system is linearized around the critical point using a Taylor expansion:

$$U'(t) = F(U) = F(U_c) + \nabla F_{U=U_c}(U - U_c) + \mathcal{O}(\|U - U_c\|^2),$$

where

$$\nabla F = \begin{pmatrix} \dfrac{\partial F_1}{\partial X} & \dfrac{\partial F_1}{\partial Y} \\ \dfrac{\partial F_2}{\partial X} & \dfrac{\partial F_2}{\partial Y} \end{pmatrix} = \begin{pmatrix} 2XY - (B+1) & X^2 \\ B - 2XY & -X^2 \end{pmatrix}.$$

Assuming small variations $\Delta(t)$, the term $\mathcal{O}(\|U - U_c\|^2)$ can be neglected, leading to the linear differential system

$$\begin{cases} \Delta'(t) = J\Delta(t), \\ \Delta(0) = \Delta_0, \end{cases} \tag{2.3}$$

where the Jacobian matrix $J = \nabla F_{U=U_c}$ is in this case

$$J = \begin{pmatrix} B - 1 & A^2 \\ -B & -A^2 \end{pmatrix}.$$

In the case that J is diagonalizable, it can be decomposed as $J = MDM^{-1}$, where $D_{ij} = \lambda_i \delta_{ij}$ and its integer powers are $J^n = MD^nM^{-1}$ for $n > 0$. We recall the definition of the exponential of a matrix J (see for instance Allaire and Kaber (2006)):

$$e^J = \sum_{n=0}^{\infty} \frac{1}{n!} J^n = \sum_{n=0}^{\infty} \frac{1}{n!} MD^nM^{-1} = M \left(\sum_{n=0}^{\infty} \frac{1}{n!} D^n \right) M^{-1} = Me^DM^{-1},$$

where e^D is the diagonal matrix $(e^D)_{ij} = \delta_{ij} e^{\lambda_i}$, formed out of the exponential of the eigenvalues of the matrix J. With this definition, the differential system (2.3) can be directly integrated:

$$\Delta(t) = e^{tJ}\Delta_0. \tag{2.4}$$

The long-time behavior is obtained by making $t \longrightarrow +\infty$ in the exact solution (2.4) of the linearized system (2.3). If all eigenvalues λ of J have negative real part, then $e^{\lambda t} \to 0$ as $t \to +\infty$. Therefore the matrix $e^{Jt} = Me^{Dt}M^{-1} \to 0$ as $t \to +\infty$ and the solution $\Delta(t)$ goes to 0. The Taylor expansion around the critical point is valid in this case, and the solution of the nonlinear system (2.2) tends toward the critical point.

In this very simple example, the eigenvalues of the matrix J can be explicitly calculated as the roots of the characteristic polynomial. The reader can easily verify that they are

$$\lambda_{\pm} = \frac{B - A^2 - 1 \pm \sqrt{\Delta}}{2}, \quad \text{with } \Delta = (A^2 - B + 1)^2 - 4A^2,$$

and that their real part is negative if $B < A^2 + 1$.
The numerical method described in the following exercise can also be used to provide a stability criterion. This can be useful in a more general case when the eigenvalues cannot be calculated explicitly.

Exercise 2.1. Write a program to display, as a function of B, the maximum of the real part of the eigenvalues of the matrix J. The parameter A is kept constant. Mark out the value of the stability criterion, which is the abscissa at which the curve crosses the horizontal axis.
A solution of this exercise is proposed in Sect. 2.5 at page 41.

In order to solve the system of differential equations (2.2), we could implement one of the numerical integration schemes proposed in Table 1.1, Chap. 1. Another possibility is to use already available programs, for instance one of the ODE solvers proposed in MATLAB.

Exercise 2.2. Compute the approximated solutions for different choices of parameter A corresponding to stability and instability. In each case display graphically the solutions X and Y as a function of time and in another figure, Y as a function of X, that is, the parametric curve $(X(t), Y(t))_t$.
A solution of this exercise is proposed in Sect. 2.5 at page 42.

2.3 Model for the Maintained Reaction

Consider now the system (2.1) with the hypothesis that component B is injected in the mixture at rate v. The concentration of B as a function of time is denoted by $Z(t)$. The system of chemical reactions reduces to a new system of three equations:

$$\begin{cases} X' = A - (Z+1)X + X^2Y, \\ Y' = XZ - X^2Y, \\ Z' = -XZ + v. \end{cases} \tag{2.5}$$

2.3.1 Existence of a Critical Point and Stability

The problem (2.5) now admits a steady solution corresponding to the critical point $U_c = (A, v/A^2, v/A)^T$. The Jacobian matrix of the right-hand-side function of the system (2.5) is

$$\nabla F = \begin{pmatrix} -(Z+1) + 2XY & Z - 2XY & -Z \\ X^2 & -X^2 & 0 \\ -X & X & -X \end{pmatrix}.$$

In order to study the stability of the system, this matrix is evaluated at the critical point

$$J = \begin{pmatrix} v/A - 1 & 1 & -1 \\ -v & -1 & 1 \\ -v & 0 & -1 \end{pmatrix}.$$

Exercise 2.3. Find numerical values of v corresponding to stable or unstable behavior of the system. Hint: the numerical method proposed in Exercise (2.1) can be used again.
A solution of this exercise is proposed in Sect. 2.5 at page 43.

2.3.2 Numerical Solution

Exercise 2.4. Solve the system (2.5) numerically for the following values of v: 0.9, 1.3, and 1.52.
For each case, display in separate figures the three concentrations versus time and concentrations Y and Z versus X.
A solution of this exercise is proposed in Sect. 2.5 at page 44.

2.4 Model of Reaction with a Delay Term

An example of a more complicated chemical reaction is proposed in Hairer, Norsett, and Wanner (1987). An additional component I is introduced at a constant rate into the system, initiating a chain reaction.

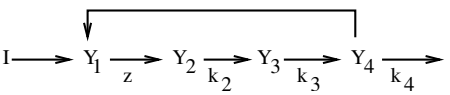

The quantity of final product Y_4 slows down the first step of the reaction $Y_1 \to Y_2$. A fine modeling of this process, taking into account the transport time and diffusion properties of molecules, leads to a *delayed* ODE system:

$$\begin{cases} y_1'(t) = I - z(t)y_1(t), \\ y_2'(t) = z(t)y_1(t) - y_2(t), \\ y_3'(t) = y_2(t) - y_3(t), \\ y_4'(t) = y_3(t) - 0.5y_4(t), \\ z(t) \ = \dfrac{1}{1 + \alpha y_4(t - t_d)^3}, \end{cases} \tag{2.6}$$

where t_d is the time delay parameter. This system has a critical point Y_c, which is, once again, determined by solving $y'(t) = 0$:

$$Y_c = \begin{pmatrix} I(1+8\alpha I^3) \\ I \\ I \\ 2I \end{pmatrix}. \tag{2.7}$$

As in the previous section, the system can be linearized around this point. The stability of the resulting system can then be studied by introducing a fifth variable $y_5(t) = y_4(t - t_d)$. The Jacobian of the right-hand-side function

$$F(y) = \begin{pmatrix} I - \dfrac{y_1}{1+\alpha y_5^3} \\ \dfrac{y_1}{1+\alpha y_5^3} - y_2 \\ y_2 - y_3 \\ y_3 - 0.5 y_4 \end{pmatrix}$$

can then be easily calculated at the critical point

$$\nabla F(Y_c) = \begin{pmatrix} -\bar{z} & 0 & 0 & 0 & 12\alpha I^3 \bar{z} \\ \bar{z} & -1 & 0 & 0 & -12\alpha I^3 \bar{z} \\ 0 & 1 & -1 & 0 & 0 \\ 0 & 0 & 1 & -0.5 & 0 \end{pmatrix},$$

where

$$\bar{z} = \frac{1}{1+8\alpha I^3}.$$

The small variations $\Delta(t)$ around the critical point Y_c satisfy to a first-order approximation the linear system of ODEs

$$\begin{aligned} \Delta_1'(t) &= -\bar{z}\Delta_1(t) + 12\alpha I^3 \bar{z}\Delta_4(t - t_d), \\ \Delta_2'(t) &= \bar{z}\Delta_1(t) - \Delta_2(t) - 12\alpha I^3 \bar{z}\Delta_4(t - t_d), \\ \Delta_3'(t) &= \Delta_2(t) - \Delta_3(t), \\ \Delta_4'(t) &= \Delta_3(t) - 0.5\Delta_4(t). \end{aligned} \tag{2.8}$$

An expression for $\Delta(t)$ is sought of the form $\Delta(t) = Ve^{xt}$, where V is a constant vector of $\mathbb{R}^4$. Plugging this ansatz into (2.8) leads to the characteristic equation

$$(x+1)^2(x+0.5)(x+\bar{z}) + 12\alpha\bar{z}I^3 x e^{-xt_d} = 0. \tag{2.9}$$

The corresponding system is stable if all roots have a negative real part.

Exercise 2.5. Set $\alpha = 0.0005$, $t_d = 4$, and solve numerically the characteristic equation for $x \in \mathbb{C}$ for different values of I between 0 and 20. Estimate a minimum value of the parameter I beyond which unstable equilibrium solutions can be obtained.
A solution of this exercise is proposed in Sect. 2.5 at page 45.

In order to illustrate numerically the instability phenomenon, the full system (2.6) has to be integrated. Standard solvers for ODE cannot be used, since they assume the generic form

$$\begin{cases} y'(t) = F(t, y(t)), \\ y(0) = u_0, \end{cases} \tag{2.10}$$

whereas in our case the right-hand side depends on the solution at a previous time,

$$\begin{cases} y'(t) = G(t, y(t), y(t - t_d)), \\ y(t) = u_0, \quad \text{for} \quad t \leq 0. \end{cases} \tag{2.11}$$

In this example the function G is the vector function

$$G : \mathbb{R} \times \mathbb{R}^4 \times \mathbb{R}^4 \longrightarrow \mathbb{R}^4,$$

$$(t, u, v) \longmapsto G(t, u, v) = \begin{pmatrix} I - \dfrac{u_1}{1 + \alpha v_4^3} \\ \dfrac{u_1}{1 + \alpha v_4^3} - u_2 \\ u_2 - u_3 \\ u_3 - 0.5u_4 \end{pmatrix}. \tag{2.12}$$

Numerical schemes well adapted to systems of standard type (2.10) have to be modified to handle the time delay. We start with the simplest case of the explicit Euler scheme:

$$\left\| \begin{array}{l} \text{initialization :} \quad y_0 = u_0 \\ \text{for} \quad i = 0, 1, \ldots, n-1 \quad \text{do} \\ \qquad y_{i+1} = y_i + hF(t_i, y_i) \\ \text{end} \end{array} \right. \tag{2.13}$$

This scheme provides a first-order approximation $y_n \approx y(t_n)$, with $t_n = nh$ for h sufficiently small (see Butcher (1987)). It can be easily adapted to the system with delay term (2.11) if the time delay t_d (here $t_d = 4$) is an integer multiple of the time step h, *i.e.*, $t_d = dh$ with $d \in \mathbb{N}$,

$$\left\| \begin{array}{l} \text{initialization :} \quad y_0 = u_0 \\ \text{for} \quad i = 0, 1, \ldots, n-1 \quad \text{do} \\ \qquad \gamma_i = \begin{cases} u_0 & \text{if} \quad i < d \\ y_{i-d} & \text{elsewhere} \end{cases} \\ \qquad y_{i+1} = y_i + hG(t_i, y_i, \gamma_i) \\ \text{end} \end{array} \right. \tag{2.14}$$

Exercise 2.6. 1. The solution is supposed to be constant and equal to y_0 for all $t \leq 0$. Write a function `ODE_DelayEnzyme(t,Y,h,y0)` returning the value $G(t, y(t), y(t - t_d))$ given by (2.12). Hints: the values of y are discretized with the time step $h = t_{\max}/n$ and stored in an array Y. The delay parameter t_d is a `global` variable set equal to 4 in the calling script.

2. Write a function `ODE_EulerDelay(fdelay,tmax,nmax,y0)` implementing the algorithm (2.14) to compute an approximation of the solution at time `tmax` in `nmax` time steps. The name of the right-hand-side function `ODE_DelayEnzyme` is passed as input argument `fdelay`.
3. Write a main script to integrate the system using the algorithm (2.14) up to $t_{\max} = 160$. The value of α is fixed at 0.0005 and I is chosen in the range corresponding to instability. The initial condition u_0 should be chosen close to the equilibrium solution Y_c. Display graphically the four components of the solution versus time in one figure and the components $y_i,\ i = 2, \ldots, 4$, versus the component y_1 in another figure.
A solution of this exercise is proposed in Sect. 2.5 at page 46.

In the case of a Runge–Kutta-type scheme, intermediate values needed for the computation of y_{i+1} must be stored. The standard fourth-order Runge–Kutta scheme presented in Chap. 1 will be adapted to our problem. We start by rewriting the scheme such as to compute explicitly the intermediate parameters of the right-hand-side function instead of the values of the function itself:

$$
\begin{aligned}
&\text{initialization:} \quad y_0 = u_0 \\
&\text{for} \quad i = 0, 1, \ldots, n-1 \quad \text{do} \\
&\qquad g^1 = y_i, \\
&\qquad g^2 = y_i + \frac{h}{2} F(t_i, g^1), \\
&\qquad g^3 = y_i + \frac{h}{2} F(t_i, g^2), \\
&\qquad g^4 = y_i + h F(t_i, g^3), \\
&\qquad y_{i+1} = y_i + \frac{h}{6} \left(F(t_i, g^1) + 2F\left(t_i + \frac{h}{2}, g^2\right) \right. \\
&\qquad\qquad \left. + 2F\left(t_i + \frac{h}{2}, g^3\right) + F\left(t_i + h, g^4\right) \right). \\
&\text{end}
\end{aligned}
\tag{2.15}
$$

To adapt this algorithm to the case (2.11) the values g^k, $k = 1, \ldots, 4$, should be stored as functions of time. They are needed to compute the intermediate values for the third input argument of the system function G, which holds the values of the solution at the delayed time $t - t_d$. This leads to the following algorithm:

$$
\begin{array}{l}
\text{initialization:} \quad y_0 = u_0 \\
\text{for} \quad i = 0, 1, \ldots, n-1 \quad \text{do} \\
\quad g_i^1 = y_i, \\
\quad g_i^2 = y_i + \dfrac{h}{2} G(t_i, g_i^1, \gamma_i^1), \\
\quad g_i^3 = y_i + \dfrac{h}{2} G(t_i, g_i^2, \gamma_i^2), \\
\quad g_i^4 = y_i + h G(t_i, g_i^3, \gamma_i^3), \\
\quad y_{i+1} = y_i + \dfrac{h}{6} \left(G(t_i, g_i^1, \gamma_i^1) + 2G\left(t_i + \dfrac{h}{2}, g_i^2, \gamma_i^2\right) \right. \\
\qquad\qquad \left. + 2G\left(t_i + \dfrac{h}{2}, g_i^3, \gamma_i^3\right) + G(t_i + h, g_i^4, \gamma_i^4) \right), \\
\qquad \text{where} \quad \gamma_i^k = \begin{cases} u_0 & \text{if} \quad i + c_k \le d, \\ g_{i-d}^k & \text{otherwise,} \end{cases} \\
\qquad \text{with} \quad c = (\,0 \quad 0.5 \quad 0.5 \quad 1\,)^T . \\
\text{end}
\end{array}
\tag{2.16}
$$

Exercise 2.7. 1. Write a function `ODE_DelayRungeKutta` with input arguments `fdelay,tmax,nmax`, and `y0` implementing the algorithm (2.16) to compute an approximation of the solution at time `tmax` in `nmax` time steps.
2. Compare graphically the solutions obtained using respectively the Euler and Runge–Kutta schemes. For $t_{\max} = 16$, plot the two solutions obtained using $n_{\max} = 100$ and $n_{\max} = 1000$. Compute the solution for $n_{\max} = 5000$ and store it as reference solution. Compute the error in L^∞ norm, as a function of h, by performing several calculations for different values of $n_{\max}$ varying between 100 and 2000.
3. Study the influence of the initial condition: plot the trajectories y_i, $i = 2, \ldots, 4$, as functions of y_1 with different colors for different initial conditions.

A solution of this exercise is proposed in Sect. 2.5 at page 46.

2.5 Solutions and Programs

Solution of Exercise 2.1
To illustrate graphically the stability criterion, the script *ODE_stab2comp.m* computes the eigenvalues of the Jacobian matrix of F at the critical point, using the MATLAB built-in function `eigen`. The maximum value of the real part of these eigenvalues is computed and stored for different values of the parameter B, the parameter A remaining fixed. An approximation of the stability criterion is the abscissa where the maximum value of the real part

changes sign.

Solution of Exercise 2.2
The script *ODE_Chemistry2.m* uses the ODE solver `ode45` available in MATLAB main distribution to integrate numerically the system of ODEs (2.2):

```
global A
global B
fun='ODE_fun2' ;
A=1;
B=0.9;
%
U0=[2;1]; % Initial condition
t0=0;     % initial time
t1=10;   % final time
[timeS1,solS1]=ode45(fun,[t0,t1],U0);
```

The above example corresponds to a stable case. The MATLAB function `ode45` requires as input the following parameters:

- the right-hand-side vector function of the differential system (written in *ODE_fun2.m*),
- the time interval [`t0,t1`] over which the system is integrated,
- the solution `U0` at initial time `t0`.

It returns as output the array `timeS1` of discrete intermediate times at which the solver has computed the corresponding solution `solS1`.
The `A` and `B` parameters of the differential system are declared as `global` in the main script and in the right-hand-side function `ODE_fun2`. Therefore they do not need to be included in the list of input parameters of `fun2` when calling `ode45`. We first run the script with parameters corresponding to stability ($A = 1$ and $B = 0.9$), then with parameters corresponding to instability ($A = 1$ and $B = 3.2$). In the first run case, the concentrations tend, for large times, to a constant value, which is the critical point. This behavior is illustrated in Fig. 2.1. In the left figure, (a), the trend of concentrations versus time is represented, showing that they rapidly stabilize to their critical values. The right figure, (b), shows the behavior of component Y versus the component X for two different initial conditions. The two trajectories converge toward the same critical point of coordinates $(A, B/A) = (1, 0.9)$.

The second choice of parameters, corresponding to instability, is illustrated in Fig. 2.2. In the left figure (a) the concentrations are displayed as functions of time. They remain bounded but exhibit periodic behavior. If the simulation is run over a long enough time, the graph of Y versus X represents the limit cycle. Figure 2.2 (b) numerically illustrates that this cycle does not depend on initial conditions but only on the parameters A and B. As they get closer to the instability limit ($B = A^2 + 1$), the limit cycle becomes smaller and eventually collapses into the critical point. This phenomenon is called *Hopf*

bifurcation (see Hairer, Norsett, and Wanner (1987) for details).

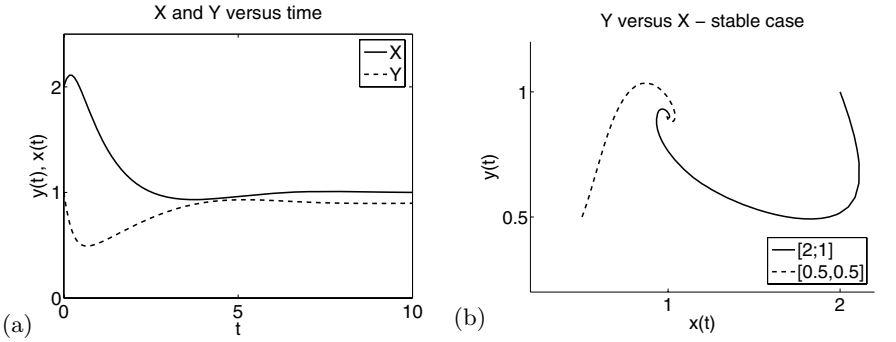

Fig. 2.1. Simplified Brusselator model, stable case $A = 1$, $B = 0.9$. (a) Concentrations X and Y as a function of time. (b) Parametric curves $(X, Y)_t$ for two different initial conditions, $(2, 1)^T$ and $(0.5, 0.5)^T$.

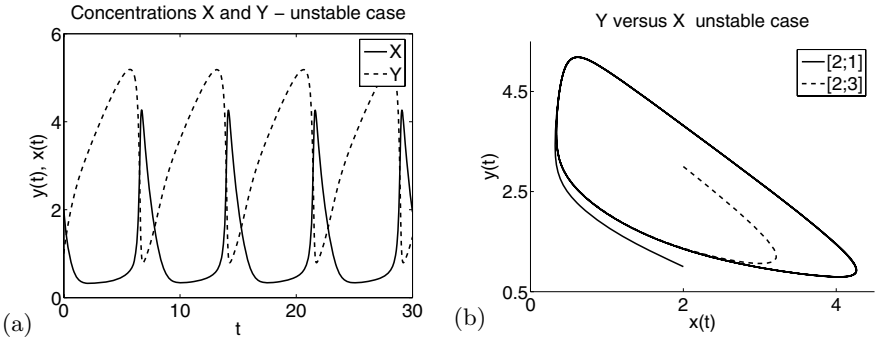

Fig. 2.2. Simplified Brusselator model, unstable case $A = 1$, $B = 3.2$. (a) Concentrations X and Y as a function of time. (b) Parametric curves $(X, Y)_t$ for two different initial conditions, $(2, 1)^T$ and $(2, 3)^T$.

Solution of Exercise 2.3

The script *ODE_stab2comp.m* that was written to answer Exercise 2.1 is modified in order to find the values of the parameter v for which all eigenvalues of the Jacobian matrix J have a negative real part. From the figure displayed by the script *ODE_stab3comp.m* we find that only the first value $v = 0.9$ proposed in Exercise 2.4 corresponds to a stable case. For the values $v = 1.3$ and 1.52 some of the eigenvalues have a positive real part.

Solution of Exercise 2.4

The integration of the full system with three equations is performed in the script *ODE_Chemistry3.m*. The right-hand-side function is defined in *ODE_fun3.m*. For $v = 0.9$, the system is stable; therefore all three concentrations tend toward their equilibrium value ($U_c = (1, 0.9, 0.9)^T$) as shown in Fig. 2.3 (a). The right figure (b), which shows the variations of Y as a function of X, also points out the convergence toward the critical point, starting from several different initial conditions.

For $v = 1.3$, the system is unstable, but the concentrations remain bounded. Their variation as a function of time is periodic and tends toward a limit cycle as displayed in Fig. 2.4.

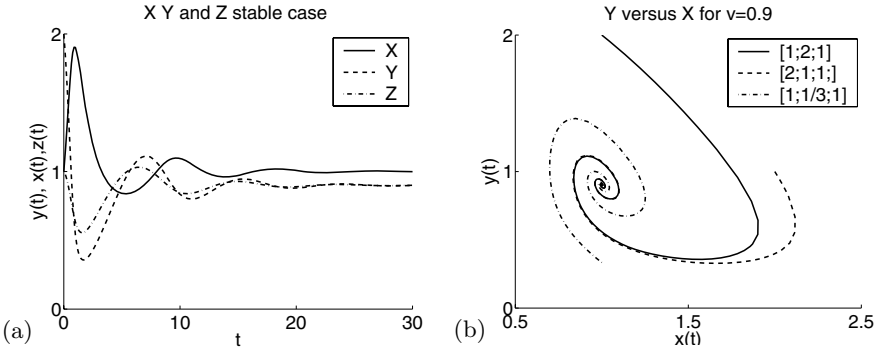

Fig. 2.3. Brusselator model, stable case $v = 0.9$. (a) Concentrations X, Y, and Z as a function of time. (b) Parametric curves $(X, Y)_t$ for two different initial conditions, $(1, 2, 1)^T$ and $(2, 2, 2)^T$.

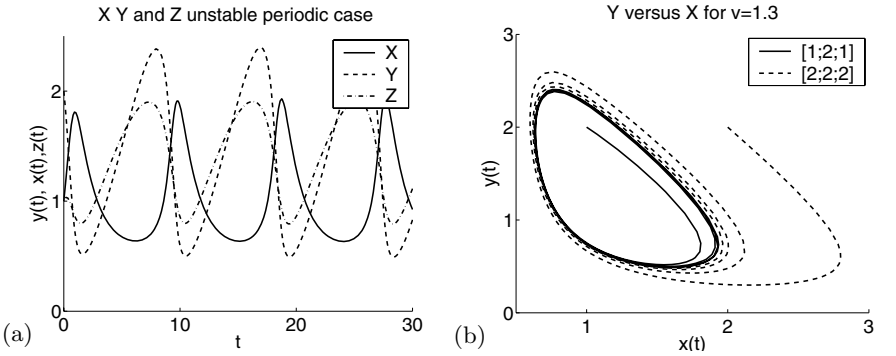

Fig. 2.4. Brusselator model, unstable periodic case $v = 1.3$. (a) Concentrations X, Y, and Z as a function of time. (b) Parametric curves $(X, Y)_t$ for two different initial conditions, $(1, 2, 1)^T$ and $(2, 2, 2)^T$.

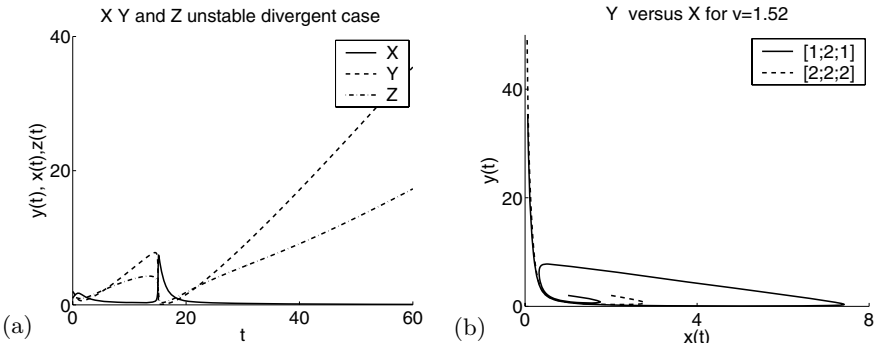

Fig. 2.5. Brusselator model, unstable divergent case $v = 1.52$. (a) Concentrations X, Y, and Z as a function of time. (b) Parametric curves $(X, Y)_t$ for two different initial conditions, $(1, 2, 1)^T$ and $(2, 2, 2)^T$.

Eventually, for $v > 1.5$, the system is unstable and divergent and the values of the concentrations y and z are unbounded for large times while the concentration x goes to 0. The global behavior is completely different from the previous case. In particular, there is no limit cycle of y as a function of x or of z as a function of x.

Solution of Exercise 2.5
This nonlinear equation can be solved numerically using the MATLAB built-in function `fsolve`, as proposed in the script *ODE_StabDelay.m* displayed below:

```
clear %important to reinitialize the Matlab  square root of (-1)
td=4;
alpha=0.0005;
for  I=0:20
 bz=1/(1+8*alpha*I^3);
 funtext='(x+1)^2*(x+0.5)*(x+bz)+12 *alpha*I^3*bz*x*exp(-td*x)';
 funequi=inline(funtext,'x','bz','I','alpha','td');
 guess=i/2;
 x0=fsolve(funequi,guess,optimset('Display','off'),bz,I,alpha,td);
 fprintf('I=%f x0=%f+i%f n',I,real(x0),imag(x0))
end
```

Running the script with a real value as initial guess for the `fsolve` function (`guess=2` for instance) will provide a negative real solution. This corresponds to a stable equilibrium, since deviations from the critical point decay exponentially to zero. Conversely, if we run the script with a pure imaginary initial guess, the root found by the solver is complex, with a nonzero imaginary part. Choose `guess=i/2` as in the above example, and let I vary to obtain a solution with a real part that will be positive for values of $I > 9$. The equilibrium for this parameter choice is unstable, since the deviations increase exponentially.

On the other hand, stability is not ensured for $I < 9$, since not all the roots of equation (2.9) necessarily have a negative real part.

Solution of Exercise 2.6

The main script *ODE_Enzyme.m* calls the function `ODE_EulerDelay`, which implements the Euler scheme (2.14) adapted to the delayed equation. The right-hand-side function $G(t, y, \gamma)$ is programmed in the file *ODE_DelayEnzyme.m*. The selected value `I=10` corresponds to an instability. The initial condition is fixed by adding a small deviation to the unstable equilibrium solution (2.7). In Fig. 2.6 (b) the trajectories are superimposed, which indicates the periodic character of the solution. The length of the period can be graphically estimated in Fig. 2.6 (a) to a value close to 13, which roughly corresponds to one of the phases obtained in solving the characteristic equation (2.9).

In contrast, setting `I=5`, which is a value for which no unstable linear equilibrium could be found by running the script `ODE_StabDelay`, we observe that the solutions tend to equilibrium.

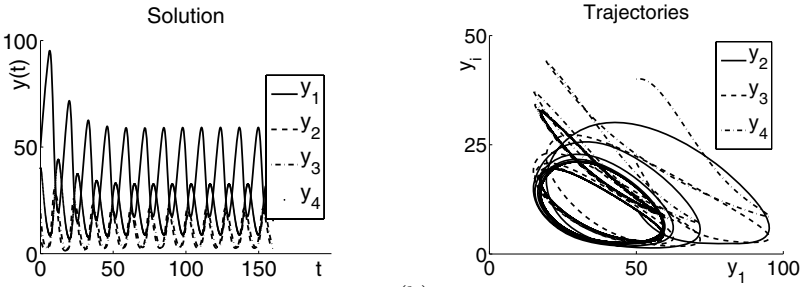

Fig. 2.6. Solutions of the system (2.6) obtained using the Euler scheme. (a) $y(t)$ versus t. (b) Trajectories y_i, $i = 2, \ldots, 4$, versus y_1.

Solution of Exercise 2.7

The delayed system of equations is now integrated with the fourth-order Runge–Kutta scheme programmed in the function `ODE_RungeKuttaDelay`. Calls to `ODE_EulerDelay` should be replaced by `ODE_RungeKuttaDelay` in the script *ODE_Enzyme.m*. This is done by changing the assigment of the variable `scheme`. In order to implement the Runge–Kutta scheme for delayed ODEs (2.16), we introduce a triple-index array `g(:,n,k)` for $k = 1, \ldots, 4$. It is used to store the four intermediate values $(g^k)_{k=1}^4$ as a function of time, so that it can be passed as input parameter to the right-hand-side function `ODE_DelayEnzyme`.

A more detailed study of the convergence order of the two schemes is proposed in the script *ODE_ErrorEnzyme.m*. Reference solutions for each scheme are computed with a very fine discretization, here `nmax=5000`. They are used as exact solutions to evaluate the error on the solution at the final time $t_{\max} = 50$ when coarser discretizations are used. In Fig. 2.7, the variations of the error with the discretization parameter h are represented in logarithmic scale, along with the theoretical convergence orders $\mathcal{O}(h)$ and $\mathcal{O}(h^4)$ for comparison.

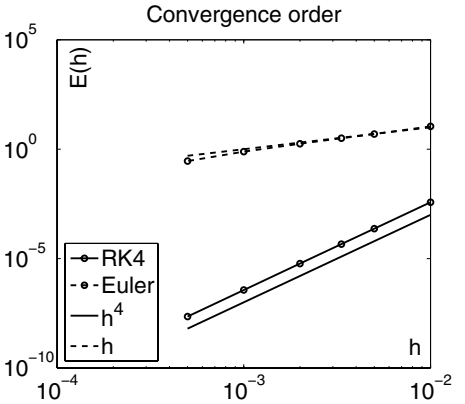

Fig. 2.7. Error in L^∞ norm as a function of the time step at time $t = 50$ for Euler and fourth-order Runge–Kutta schemes.

Finally, the influence of the initial condition is investigated by the script `ODE_EnzymeCondIni`. We display in the same figure the trajectories starting from different initial conditions, randomly chosen in the vicinity of the unstable equilibrium. Figure 2.8 shows that after an initial phase (of different lengths), they all converge to the same periodic trajectory.

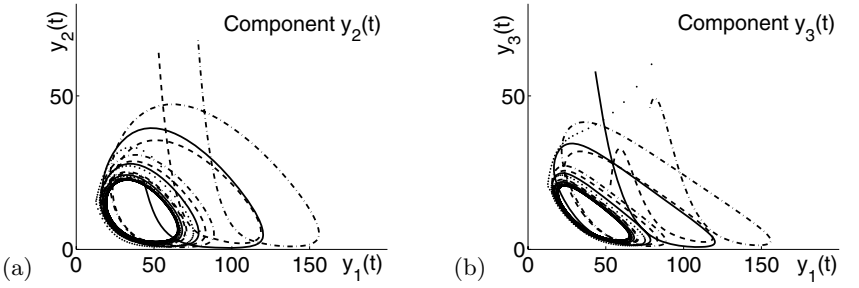

Fig. 2.8. Solutions of system (2.6) obtained for four different initial conditions using the Runge–Kutta scheme. (a) Trajectories y_2 versus y_1. (b) y_3 versus y_1.

Chapter References

Numerous references for solving ODEs have already been cited in the previous chapter. The numerical examples treated in this project are directly selected from Hairer, Norsett, and Wanner (1987) and we also recommand the book by Bellen and Zennaro (2003) for advanced reading on delay equations.

G. Allaire and S. M. Kaber, *Numerical Linear Algebra*, Springer, New York, forthcoming, 2007.

A. Bellen and M. Zennaro, *Numerical Methods for Delay Differential Equations*, Numerical Mathematics and Scientific Computation, The Clarendon Press, Oxford University Press, New York, 2003.

J. C. Butcher, *The Numerical Analysis of Ordinary Differential Equations*, Wiley, 1987.

E. Hairer, S. P. Norsett, and G. Wanner, *Solving Ordinary Differential Equations I, Nonstiff Problems*, Springer series in computational mathematics, 8, Springer-Verlag, 1987.

A. Iserles, *A First Course in the Numerical Analysis of Differential Equations*, Cambridge Texts in Applied Mathematics, Cambridge University Press, Cambridge, 1996.

L. N. Trefethen and D. Bau III, *Numerical Linear Algebra*, Society for Industrial and Applied Mathematics (SIAM), Philadelphia, 1997.

3

Polynomial Approximation

Project Summary

Level of difficulty:	1
Keywords:	Polynomial approximation, splines, best approximations, interpolation
Application fields:	Approximation of functions

This chapter is devoted to the approximation of a given real function by a simpler one that belongs, for example, to $\mathbb{P}_n$, the set of polynomials of degree less than or equal to n. We also consider approximation by piecewise polynomial functions, that is, functions whose restrictions to some prescribed intervals are polynomials. The definitions and results of this chapter, given without proofs, are widely used in the rest of the book. We refer the reader to books on polynomial approximation theory, for instance Crouzeix and Mignot (1989), DeVore and Lorentz (1993), and Rivlin (1981).

3.1 Introduction

The approximation of a given function by a polynomial is an efficient tool in many problems arising in applied mathematics. In the following examples, f is the function to be approximated by a polynomial p_n. The precise meaning of the word "approximated" will be explained later.

1. *Visualization of some computational results.* Given the values of a function f and some points x_i, we want to draw this function on the interval $[a, b]$. This is the interpolation problem if $[a, b] \subset [\min_i x_i, \max_i x_i]$; otherwise, it is an extrapolation problem. The following approximation is often made:

$$\forall x \in [a, b]\,, \qquad f(x) \approx p_n(x).$$

2. *Numerical quadrature:* to compute an integral involving the function f, the following approximation is used:

$$\int_a^b f(x)dx \approx \int_a^b p_n(x)dx,$$

since the computation of the last integral is easy.
3. *Differential equations:* in spectral methods, the solution of an ordinary or partial differential equation is approximated by a polynomial. See Chap. 5.

To approximate f by $p_n \in \mathbb{P}_n$ means:

1. *Interpolation.* The polynomial p_n and the function f coincide at $n+1$ points $x_0, \ldots, x_n$ of the interval $[a, b]$. These points can be prescribed or be some unknowns of the problem.
2. *Best approximation.* The polynomial p_n is the element (or one element) of $\mathbb{P}_n$ (if it exists) that is closest to f with respect to some given norm $\|.\|$. More precisely,

$$\|f - p_n\| = \inf_{q \in \mathbb{P}_n} \|f - q\|.$$

If the norm is

$$\|\varphi\|_2 = \sqrt{\int_a^b |\varphi(x)|^2 dx},$$

the approximation is called least squares approximation or approximation in the L^2 sense or Hilbertian approximation. The norm of the uniform convergence (the supremum norm), which we denote by

$$\|\varphi\|_\infty = \sup_{x \in [a,b]} |\varphi(x)|,$$

leads to the approximation in the uniform sense or approximation in the L^∞ sense or Chebyshev approximation.

3.2 Polynomial Interpolation

In this section $f : [a, b] \longrightarrow \mathbb{R}$ is a continuous function, $(x_i)_{i=0}^k$ a set of $k+1$ *distinct* points in the interval $[a, b]$, and $(\alpha_i)_{i=0}^k$ a set of $(k+1)$ integers. We define $n = k + \alpha_0 + \cdots + \alpha_k$. We are interested in the following problem: find a polynomial p that coincides with f and possibly with some derivatives of f at the points x_i. The integers α_i indicate the highest derivative of f to be interpolated at the point x_i.

3.2.1 Lagrange Interpolation

Lagrange polynomials correspond to the case that only the function f is interpolated and not its derivatives. In such a case $\alpha_i = 0$ for all i and thus $k = n$. We know from the theory of approximation the following important result.

Theorem 3.1. *Given $(n+1)$ distinct points $x_0, x_1, \ldots, x_n$ and a continuous function f, there exists a unique polynomial $p_n \in \mathbb{P}_n$ such that for all $i = 0, \ldots, n$,*

$$p_n(x_i) = f(x_i). \tag{3.1}$$

The polynomial p_n is called the Lagrange polynomial interpolant of f with respect to the points x_i. We denote it by $\mathcal{I}_n(f; x_0, \ldots, x_n)$ or simply $\mathcal{I}_n f$. We define the characteristic Lagrange polynomials associated with the points x_i as the $n+1$ polynomials $(\ell_i)_{i=0}^n$:

$$\ell_i \in \mathbb{P}_n \text{ and } \ell_i(x_j) = \delta_{i,j} \quad \text{for } j = 0, \ldots, n.$$

The Lagrange polynomials form a basis of $\mathbb{P}_n$ and are explicitly given by

$$\ell_i(x) = \prod_{j=0, j\neq i}^{n} \frac{x - x_j}{x_i - x_j}. \tag{3.2}$$

The four Lagrange polynomials associated with the four points -1, 0, 1, and 3 are displayed in Fig. 3.1. The Lagrange basis is mainly used to write in a

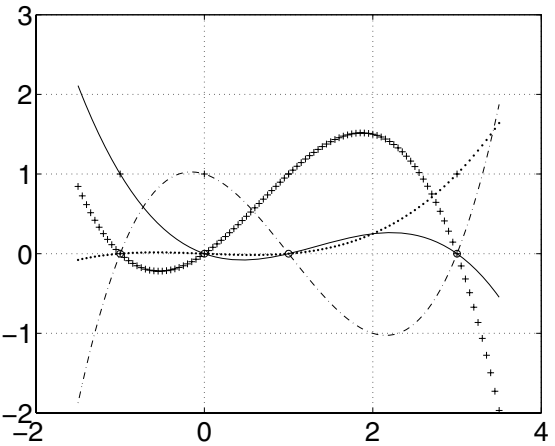

Fig. 3.1. Lagrange polynomials associated with the points -1, 0, 1, and 3.

very simple way the Lagrange polynomial interpolant:

$$\mathcal{I}_n f = \sum_{i=0}^{n} f(x_i)\ell_i. \tag{3.3}$$

A question arises naturally: what is the most appropriate basis of $\mathbb{P}_n$ for the computation of $\mathcal{I}_n f$? We compare three bases.

- *Basis 1.* The canonical basis of the monomials $1, x, \ldots, x^n$.
- *Basis 2.* The basis given by the Lagrange polynomials.
- *Basis 3.* The basis given by the polynomials

$$1, (x - x_0), (x - x_0)(x - x_1), \ldots, (x - x_0)(x - x_1) \cdots (x - x_{n-1}). \tag{3.4}$$

Exercise 3.1. Computations in the canonical basis.
Let $(a_k)_{k=0}^n$ be the coefficients of $\mathcal{I}_n f$ in the canonical basis,

$$\mathcal{I}_n f = \sum_{k=0}^{n} a_k x^k,$$

and $a = (a_0, \ldots, a_n)^T \in \mathbb{R}^{n+1}$.

1. Prove that the interpolation conditions (3.1) are equivalent to a linear system $Aa = b$, with matrix $A \in \mathbb{R}^{(n+1)\times(n+1)}$ and right-hand side $b \in \mathbb{R}^{n+1}$ to be determined.
2. For $n = 10$ (and 20) define an array x of $n + 1$ random numbers sorted in increasing order between 0 and 1. Write a program that computes the matrix A.
3. For $f(x) = \sin(10\, x \cos x)$, compute the coefficients of $\mathcal{I}_n f$ by solving the linear system $Aa = b$. Plot on the same figure $\mathcal{I}_n f$ and f evaluated at the points x_i. Use the MATLAB function `polyval` (warning: handle carefully the ordering of the coefficients α_i).
4. For $n = 10$, compute $\|Aa - b\|_2$, then the condition number of the matrix A (use the function `cond`) and its rank (use the function `rank`). Same questions for $n = 20$. Comment.

A solution of this exercise is proposed in Sect. 3.6 at page 70.

Exercise 3.2. For n going from 2 to 20 in steps of 2, compute the logarithm of the condition number of the matrix A (see the previous exercise) for $n + 1$ points x_i uniformly chosen between 0 and 1. Plot the logarithm of the condition number of the matrix as a function of n. Comment.
A solution of this exercise is proposed in Sect. 3.6 at page 71.

Exercise 3.3. Computations in the Lagrange basis.
For $n \in \{5, 10, 20\}$, define the points $x_i = i/n$ for $i = 0, \ldots, n$. Write a program (using n and k as input data) that computes the coefficients of the Lagrange polynomial ℓ_k. Use the function `polyfit`. Evaluate $\ell_{[n/2]}$ at 0. Comment.
A solution of this exercise is proposed in Sect. 3.6 at page 72.

Let us now consider Basis 3. This basis is related to what is called the divided difference. The divided difference of order k of the function f with respect to $k+1$ distinct points $x_0, \ldots, x_k$ is the real number denoted by $f[x_0, \ldots, x_k]$ and defined for $k = 0$ by $f[x_i] = f(x_i)$ and for $k \geq 1$ by

$$f[x_0, \ldots, x_k] = \frac{f[x_1, \ldots, x_k] - f[x_0, \ldots, x_{k-1}]}{x_k - x_0}.$$

The evaluation of the divided differences is computed by Newton's algorithm, described by the following "tree":

$$\begin{array}{lllll}
f[x_0] = f(x_0) & & & & \\
& \searrow & & & \\
& \nearrow & f[x_0, x_1] = \frac{f(x_1)-f(x_0)}{x_1-x_0} & & \\
f[x_1] = f(x_1) & & & \searrow & \\
& & & \nearrow & f[x_0, x_1, x_2] = \frac{f[x_1,x_2]-f[x_0,x_1]}{x_2-x_0} \ldots \\
& \searrow & f[x_1, x_2] = \frac{f(x_2)-f(x_1)}{x_2-x_1} & & \vdots \\
& \nearrow & & & \\
f[x_2] = f(x_2) & & \vdots & & \vdots \\
\vdots & & \vdots & & \vdots
\end{array}$$

The first column of the tree contains the divided differences of order 0, the second column contains the divided differences of order 1, and so on. The following proposition shows that the divided differences are the coefficients of $\mathcal{I}_n f$ in Basis 3:

Proposition 3.1.

$$\mathcal{I}_n f(x) = f[x_0] + \sum_{k=1}^{n} f[x_0, \ldots, x_k](x - x_0)(x - x_1) \cdots (x - x_{k-1}). \tag{3.5}$$

Let c be an array that contains the divided differences $c_i = f[x_0, \ldots, x_i]$. To evaluate the polynomial $\mathcal{I}_n f$ at a point x, we write

$$\mathcal{I}_n f(x) = c_0 + (x - x_0)\{c_1 + (x - x_1)\{c_2 + c_3(x - x_2) + \cdots.$$

This way of writing $\mathcal{I}_n f(x)$ is called the Horner form of the polynomial. It is a very efficient method since the computation of $\mathcal{I}_n f(x)$ in this form requires n multiplications, n subtractions, and n additions, while the form (3.5) requires $n(n+1)/2$ multiplications, $n(n+1)/2$ subtractions, and n additions. Here is Horner's algorithm for the evaluation of $\mathcal{I}_n f(x)$:

$y = c_n$
for $k = n - 1 \searrow 0$
    $y = (x - x_k)y + c_k u$
end

Exercise 3.4. Divided differences.

1. Write a program that computes the divided differences of order n of a function. Start from an array c that contains the $(n+1)$ values $f[x_i] = f(x_i)$. In the first step, $c_0 = f[x_0]$ is unchanged and all the other values c_k $(k \geq 1)$ are replaced by the divided differences of order 1. In the second step, $c_1 = f[x_0, x_1]$ is unchanged and the values c_k $(k \geq 2)$ are replaced by new ones, and so on. Here is the algorithm to implement:

```
for k = 0 ↗ n
        c_k ← f(x_k)
end
for p = 1 ↗ n
        for k = n ↘ p
                c_k ← (c_k − c_{k−1})/(x_k − x_{k−p})
        end
end
```

2. Use Horner's algorithm to evaluate $\mathcal{I}_n f$ on a fine grid of points in $[0, 1]$. Draw $\mathcal{I}_n f$ and f on the same figure. In the same figures, mark the interpolation points x_i.

A solution of this exercise is proposed in Sect. 3.6 at page 72.

We consider now the problem of the control of the Lagrange interpolation error. Given $x \in [a, b]$, the goal is to evaluate the *local error* or *pointwise error*

$$e_n(x) = f(x) - \mathcal{I}_n f(x). \tag{3.6}$$

Of course, if x is an interpolation point, there is no error, and $e_n(x) = 0$. Actually, the error is precisely known through the following result.

Proposition 3.2. *Assume $f \in \mathcal{C}^{n+1}([a, b])$. For all $x \in [a, b]$, there exists $\xi_x \in [a, b]$ such that*

$$e_n(x) = \frac{1}{(n+1)!} \Pi_n(x) f^{(n+1)}(\xi_x), \tag{3.7}$$

with $\Pi_n(x) = \prod_{i=0}^{n} (x - x_i)$.

For all $x \in [a, b]$, we deduce from (3.7) the upper bound

$$|e_n(x)| \leq \frac{1}{(n+1)!} \|\Pi_n\|_\infty \, \|f^{(n+1)}\|_\infty.$$

This suggests that a good way to choose the interpolation points consists in minimizing $\|\Pi_n\|_\infty$, since the term $\|f^{(n+1)}\|_\infty$ depends only on the function and not at all on the interpolation points. Suppose the interpolation points to be equidistant in the interval $[a, b]$:

$$x_i = a + i\frac{b-a}{n}, \qquad 0 \le i \le n.$$

In this case, there exists a constant c independent of n such that for n large enough,

$$\max_{a \le x \le b} |\Pi_n(x)| \ge c(b-a)^{n+1} e^{-n} n^{-5/2}. \tag{3.8}$$

Consider now the Chebyshev points. These are the n zeros of the Chebyshev polynomial T_n defined on the interval $[-1, 1]$ by

$$T_n(t) = \cos n\theta, \text{ with } \cos\theta = t. \tag{3.9}$$

Hence the Chebyshev points are

$$t_i = \cos(\theta_i), \quad \theta_i = \frac{\pi}{2n} + i\frac{\pi}{n}, \qquad 0 \le i \le n-1.$$

On an interval $[a, b]$, the Chebyshev points (see Fig. 3.2) are defined as the image of the previous points by the affine transformation φ that maps $[-1, 1]$ onto $[a, b]$:

$$x_i = \varphi(t_i) = \frac{a+b}{2} + \frac{b-a}{2}\cos(\theta_i), \qquad 0 \le i \le n-1.$$

Whatever the points x'_i in $[a, b]$, the following lower bound holds:

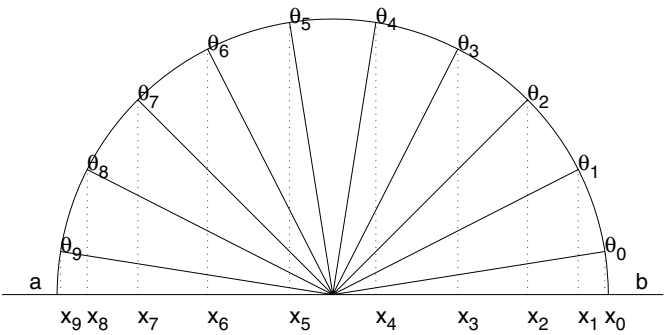

Fig. 3.2. The Chebyshev points on $[a, b]$, $n = 10$.

$$\max_{x\in[a,b]} \left| \prod_{i=0}^{n-1} (x - x'_i) \right| \ge \max_{x\in[a,b]} \left| \prod_{i=0}^{n-1} (x - x_i) \right| = \frac{(b-a)^n}{2^{2n-1}}. \tag{3.10}$$

Comparing the bounds in (3.8) and (3.10) favors the Chebyshev points. We will see in the next paragraph another reason to prefer these points to the equidistant points.

We introduce the Lebesgue constantassociated with the points $(x_i^n)_{i=0}^n$; it is the real number Λ_n defined by

$$\Lambda_n = \max_{x\in[a,b]} \sum_{i=0}^{n} |\ell_i(x)|. \tag{3.11}$$

It is important to notice that Λ_n does not depend on any function, but only on the points x_i. Let us suppose an error ε_i for each value $f(x_i)$. Let $\tilde{p}_n$ be the polynomial that interpolates the values $\tilde{f}_i = f_i + \varepsilon_i$. The interpolation error at the point x is $\mathcal{I}_n f(x) - \tilde{p}_n(x) = -\sum_{i=0}^n \varepsilon_i \ell_i(x)$. If $\varepsilon = \max_i |\varepsilon_i|$ is the maximal error on the values $f(x_i)$, we derive the upper bound

$$\|\mathcal{I}_n f - \tilde{p}_n\|_\infty \leq \varepsilon \Lambda_n,$$

which shows that the constant Λ_n is a measure of the amplification of the error in the Lagrange interpolation process. In other words, it is the stability measure of the Lagrange interpolation. The following negative result holds.

Proposition 3.3. *Whatever the interpolation points,*

$$\lim_{n\to+\infty} \Lambda_n = +\infty. \tag{3.12}$$

Hence small perturbations on the data (small ε) can lead to very big variations in the solution $(\mathcal{I}_n f)$. This is the typical case of an *ill-conditioned* problem.

Exercise 3.5. Computation of the Lebesgue constant.

1. Write a function that computes the Lebesgue constant associated with an array x of n real numbers (see (3.11)). Use the MATLAB functions `polyval` and `polyfit` to evaluate ℓ_i. Compute the maximum in (3.11) on a uniform grid of 100 points between $\min_i x_i$ and $\max_i x_i$.
2. The uniform case. Compute for n going from 10 to 30 in steps of 5 the Lebesgue constant $\Lambda_U(n)$ associated with $n+1$ equidistant points in the interval $[-1, 1]$. Draw the curve $n \mapsto \ln(\Lambda_U(n))$. Comment.
3. The Chebyshev points case. Compute for n going from 10 to 20 in steps of 5 the Lebesgue constant $\Lambda_T(n)$ associated with $n+1$ Chebyshev points on $[-1, 1]$. Draw the curve $\ln n \mapsto \Lambda_T(n)$. Comment.

A solution of this exercise is proposed in Sect. 3.6 at page 73.

Concerning a uniform bound of the error (3.6), we have the following result.

Proposition 3.4. *For any continuous function f defined on $[a, b]$,*

$$\|e_n\|_\infty \leq (1 + \Lambda_n) E_n(f),$$

with $E_n(f) = \inf_{q\in\mathbb{P}_n} \|f - q\|_\infty$ the error of best approximation of the function f by polynomials in $\mathbb{P}_n$, in the uniform norm.

Remark 3.1. Hence the global error $\|f - \mathcal{I}_n f\|_\infty$ is bounded by the product of two terms. One of them is Λ_n which always goes to $+\infty$; the other is $E_n(f)$, whose rate of convergence toward 0 increases with the smoothness of f. Hence the Lagrange interpolation process converges uniformly if the product $\Lambda_n E_n(f)$ goes to 0.

Exercise 3.6. Compute and draw (on a uniform grid of 100 points) the Lagrange polynomial interpolation of the function $f_1 : x \mapsto |\sin(\pi x)|$ at n Chebyshev points of the interval $[-1, 1]$. Take $n = 20$, 30, then 40. Do the same for the function $f_2 : x \mapsto x f_1(x)$. Comment on the results.
A solution of this exercise is proposed in Sect. 3.6 at page 75.

Exercise 3.7. Runge phenomenon.
Compute and draw on a uniform grid of 100 points the Lagrange polynomial interpolation of the function $f : x \mapsto 1/(x^2 + a^2)$ at the $n + 1$ points $x_i = -1 + 2i/n$ $(i = 0, \ldots, n)$. Take $a = 2/5$ and $n = 5$, 10, then 15. Note that the function to be interpolated is very regular on $\mathbb{R}$, in contrast to the functions considered in the previous exercise. Comment on the results.
A solution of this exercise is proposed in Sect. 3.6 at page 76.

3.2.2 Hermite Interpolation

We assume in this section that the function f has derivatives of order α_i at the point x_i. In this case there exists a unique polynomial $p_n \in \mathbb{P}_n$ such that for all $i = 0, \ldots, k$ and $j = 0, \ldots, \alpha_i$,

$$p_n^{(j)}(x_i) = f^{(j)}(x_i). \tag{3.13}$$

The polynomial p_n, which we denote by $\mathcal{I}_n(f; x_0, \ldots, x_k; \alpha_0, \ldots, \alpha_k)$, or simply $\mathcal{I}_n^H f$, is called the Hermite polynomial interpolation of f at the points x_i with respect to the indices α_i.

Theorem 3.2. *Suppose the function f is in $\mathcal{C}^{n+1}([a, b])$. For all $x \in [a, b]$, there exists $\xi_x \in [\min_i x_i, \max_i x_i]$ such that*

$$e_n^H(x) = f(x) - \mathcal{I}_n^H f(x) = \frac{1}{(n+1)!} \Pi_n^H(x) f^{(n+1)}(\xi_x), \tag{3.14}$$

with $\Pi_n^H(x) = \prod_{i=0}^k (x - x_i)^{1+\alpha_i}$.

Since the function f is of class $\mathcal{C}^{n+1}$ on the interval $[a, b]$, for all $n+1$ distinct points $x_0, \ldots, x_n$ in the interval $[a, b]$, there exists $\xi \in [a, b]$ such that

$$f^{(n)}(\xi) = n! f[x_0, \ldots, x_n].$$

This relation defines a link between the divided differences and the derivatives. More precisely, we make the following remark.

Remark 3.2. Letting each x_i go to x, we get an approximation of the nth derivative of f at x:

$$\frac{1}{n!} f^{(n)}(x) = \lim_{x_i \to x} f[x_0, \ldots, x_n].$$

This remark combined with the Newton algorithm allows the evaluation of the Hermite polynomial interpolation, as in the following example.

Example 3.1. Compute the polynomial interpolant p of minimal degree satisfying

$$p(0) = -1,\ p(1) = 0,\ p'(1) = \alpha \in \mathbb{R}. \tag{3.15}$$

Answer: compute the divided differences

$$\begin{array}{lll}
x_0 = 0 & f[x_0] = \boxed{-1} & \\
 & \searrow & \\
 & \nearrow f[x_0, x_1] = \boxed{1} & \\
x_1 = 1 \quad f[x_1] = 0 & & \searrow \\
 & & \nearrow f[x_0, x_1, x_2] = \frac{\alpha - 1}{1 - 0} = \boxed{\alpha - 1} \\
 & \searrow & \\
 & \nearrow \boxed{\boxed{f'(1)}} = \alpha & \\
x_2 = 1 \quad f[x_1] = 0 & &
\end{array}$$

We get

$$p(x) = \boxed{-1} + \boxed{1}x + \boxed{(\alpha - 1)}x(x - 1).$$

In these calculations, we wrote

$$x_2 = 1 + \varepsilon, \quad f[x_1, x_2] = (f(1 + \varepsilon) - f(1))/(1 + \varepsilon - 1),$$

and used the fact that $f[x_1, x_2]$ goes to $f'(1)$ as ε goes to 0.

Exercise 3.8. In this exercise, $f(x) = e^{-x}\cos(3\pi x)$.

1. Write a function based on the divided differences (as in Example 3.1) that computes the Hermite polynomial interpolant of a function (including the Lagrange case). The input data of this function are the interpolation points x_i, and for each point, the maximal derivative α_i to be interpolated at this point and the values $f^{(\ell)}(x_i)$ for $\ell = 0, \ldots, \alpha_i$.
2. Compute the Lagrange interpolation of f at the points $0, \frac{1}{4}, \frac{3}{4}$, and 1. Draw f and its polynomial interpolant on the interval $[0, 1]$.
3. Compute the Hermite interpolant of f at the same points (with $\alpha_i = 1$). Draw f and its Hermite polynomial on the interval $[0, 1]$. Compare to the previous results.
4. Answer the same questions in the case that f and f' are interpolated at the previous points and, in addition, the point $\frac{1}{2}$.

A solution of this exercise is proposed in Sect. 3.6 at page 76.

Exercise 3.9. Draw on $[0,1]$, and for several values of m, the polynomial of minimal degree p such that

$$p(0)=0,\ p(1)=1,\ \text{and } p^{(\ell)}(0)=p^{(\ell)}(1)=0,\ \text{for } \ell=1,\ldots,m.$$

A solution of this exercise is proposed in Sect. 3.6 at page 77.

3.3 Best Polynomial Approximation

In this section, we look for a polynomial that is nearest to f for a prescribed norm $\|.\|_{\mathcal{X}}$, $\mathcal{X}$ being a linear space that includes the polynomials. For $f\in\mathcal{X}$, we call a polynomial $p_n\in\mathbb{P}_n$ such that

$$\|f-p_n\|_{\mathcal{X}}=\inf_{q\in\mathbb{P}_n}\|f-q\|_{\mathcal{X}} \tag{3.16}$$

a best polynomial approximation of f in $\mathbb{P}_n$. The real number $\inf_{q\in\mathbb{P}_n}\|f-q\|_{\mathcal{X}}$ is called the best approximation error of f in $\mathbb{P}_n$, in the norm $\|\,.\,\|_{\mathcal{X}}$. We consider two spaces $\mathcal{X}$.

- *Case 1.* $I=[a,b]\,,\mathcal{X}=\mathcal{C}(I)$, the space of continuous functions equipped with the uniform norm, which we denote by $\|.\|_\infty$. The best uniform approximation error is denoted by

$$E_n(f)=\inf_{q\in\mathbb{P}_n}\|f-q\|_\infty\,.$$

- *Case 2.* $I=]a,b[,\mathcal{X}=L^2(I)$, the space of measurable functions defined on I such that the integral $\int_a^b|f(x)|^2dx$ is finite. $L^2(I)$ is equipped with the inner product and the norm

$$\langle f,g\rangle=\int_{-1}^{1}f(t)g(t)dt,\quad \|f\|=\sqrt{\langle f,f\rangle}.$$

3.3.1 Best Uniform Approximation

Here $I=[a,b]$ and $f\in\mathcal{X}=\mathcal{C}(I)$. We seek a polynomial $p_n\in\mathbb{P}_n$, solution of the problem

$$\|f-p_n\|_\infty=E_n(f)=\inf_{q\in\mathbb{P}_n}\|f-q\|_\infty\,.$$

The following definition enables the characterization of the polynomial of best uniform approximation.

Definition 3.1. *A continuous function φ is said to be equioscillatory on $n+1$ points of a real interval $[a,b]$ if φ takes alternately the values $\pm\|\varphi\|_\infty$ at $(n+1)$ points $x_0<x_1<\cdots<x_n$ of $[a,b]$ (see Fig. 3.3).*

The following theorem is known as the alternation theorem.

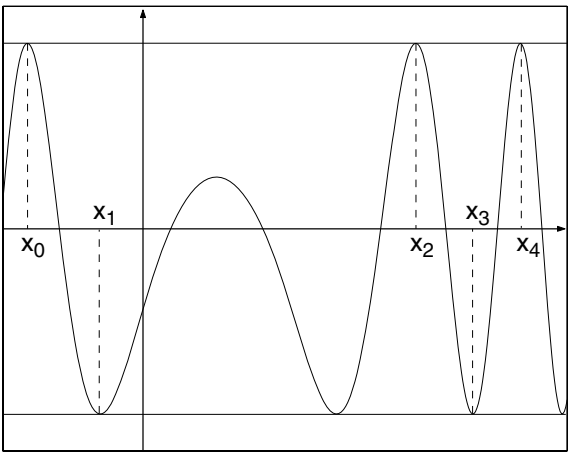

Fig. 3.3. Example of an equioscillatory function.

Theorem 3.3. *Let f be a continuous function defined on $I = [a, b]$. The polynomial p_n of best uniform approximation of f in $\mathbb{P}_n$ is the only polynomial in $\mathbb{P}_n$ for which the function $f - p_n$ is equioscillatory on (at least) $n+2$ distinct points of I.*

For example, the best uniform approximation of a continuous function f on $[a, b]$ by constants is

$$p_0 = \frac{1}{2}\left\{\min_{x\in[a,b]} f(x) + \max_{x\in[a,b]} f(x)\right\},$$

and there exist (at least) two points where the function $f - p_0$ equioscillates. These points are the two points where the continuous function reaches its extremal values on $[a, b]$.

Hence, to determine the best uniform approximation of a function f, it is sufficient to find a polynomial $p \in \mathbb{P}_n$ and $n + 2$ points such that $f - p$ equioscillates at these points. This is what the following algorithm (called the Remez algorithm) does.

The Remez algorithm

1. *Initialization.* Choose any $n + 2$ distinct points $x_0^0 < x_1^0 < \cdots < x_{n+1}^0$.
2. *Step k.* Suppose the $n + 2$ points $x_0^k < x_1^k < \cdots < x_{n+1}^k$ are known. Compute a polynomial $p_k \in \mathbb{P}_n$ (see Exercise 3.10) such that

$$f(x_i^k) - p_k(x_i^k) = (-1)^i\{f(x_0^k) - p_k(x_0^k)\}, \qquad i = 1, \ldots, n + 1.$$

   (a) If

$$\|f - p_k\|_\infty = |f(x_i^k) - p_k(x_i^k)|, \qquad i = 0, \ldots, n + 1, \tag{3.17}$$

the algorithm stops, since the function $f - p_k$ equioscillates at these points. Hence p_k is the polynomial of best uniform approximation of f.

(b) Otherwise, there exists $y \in [a, b]$ such that for all $i = 0, \ldots, n+1$,

$$\|f - p_k\|_\infty = |f(y) - p_k(y)| > |f(x_i^k) - p_k(x_i^k)|. \tag{3.18}$$

Design a new set of points $x_0^{k+1} < x_1^{k+1} < \cdots < x_{n+1}^{k+1}$ by replacing one of the points x_i^k by y in such a way that

$$\left(f(x_j^{k+1}) - p_k(x_j^{k+1})\right)\left(f(x_{j-1}^{k+1}) - p_k(x_{j-1}^{k+1})\right) \leq 0, \quad j = 1, \ldots, n+1.$$

Exercise 3.10. Prove the existence of a unique polynomial $p_k \in \mathbb{P}_n$ defined in step k of the Remez algorithm. Program a function that computes this polynomial (the input data are the $n+2$ points x_i and a function f).

Hint: write $p_k(t) = \sum_{j=0}^n a_j t^j$ and use MATLAB to solve the linear system whose solution is $(a_0, \ldots, a_n)^T$.

A solution of this exercise is proposed in Sect. 3.6 at page 78.

Exercise 3.11. Remez algorithm.

The goal is to compute the best uniform approximation of the function $x \mapsto \sin(2\pi \cos(\pi x))$ on $[0, 1]$ by the Remez algorithm. Discuss all the possible cases in point (b) (see the algorithm): $y < \min_i x_i$, $y > \max_i x_i$, $y \in \left]x_i^k, x_{i+1}^k\right[$, and $(f(x_i^k) - p_k(x_i^k))(f(y) - p_k(y)) \geq 0$ or $(f(x_i^k) - p_k(x_i^k))(f(y) - p_k(y)) < 0$. To check the inequality (3.18):

- compute $\|f - p_k\|_\infty$ on a uniform grid of 100 points in the interval $[0, 1]$,
- The equality (3.17) of the algorithm is supposed true if the absolute value of the difference between the two quantities is larger than a prescribed tolerance (10^{-8} for example).

Compare the results (in terms of the number of iterations required for the convergence of the algorithm) for the three choices of initialization points:

- equidistant points: $x_i = \frac{i}{n+1}$, $i = 0, \ldots, n+1$;
- Chebyshev points: $x_i = \frac{1}{2}(1 - \cos(i\frac{\pi}{n+1})$, $i = 0, \ldots, n+1$;
- random points: the x_i are $n+1$ points given by the function `rand` then sorted out.

A solution of this exercise is proposed in Sect. 3.6 at page 79.

3.3.2 Best Hilbertian Approximation

Here $I =]-1, 1[$ since every interval $]a, b[$ can be mapped to I by a simple affine transformation. The Hilbertian structure of $\mathcal{X} = L^2(I)$ extends to this infinite-dimensional space some very usual notions such as basis and orthogonal projection. See, for example, Schwartz (1980) for the definitions and results of this section. We are interested in the determination of the best approximation of a function in $L^2(I)$ by polynomials of a prescribed degree.

Hilbertian Basis

The Legendre polynomials are defined by the recurrence relation (see also Chap. 5)

$$(n+1)L_{n+1}(x) = (2n+1)xL_n(x) - nL_{n-1}(x) \qquad (\forall n \geq 1)$$

with $L_0(x) = 1$ and $L_1(x) = x$. The degree of L_n is n, and for all integers n and m,

$$\langle L_n, L_m \rangle = \begin{cases} 0 & \text{if } n \neq m, \\ 1/(n+1/2) & \text{if } n = m. \end{cases}$$

These polynomials are said to be orthogonal. We display in Fig. 3.4 some Legendre polynomials. The family $L_n^* = L_n/\|L_n\|$ forms a Hilbertian basis of

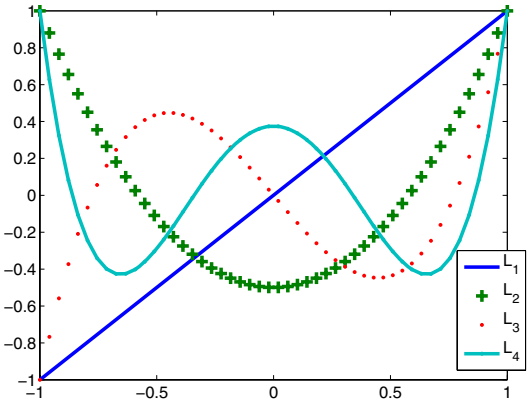

Fig. 3.4. Example of orthogonal polynomials: the Legendre polynomials.

$L^2(I)$, that is, $(L_n^*)_{n\geq 0}$ is orthonormal and the set of all finite linear combinations of the L_n^* is dense in $L^2(I)$. As in finite dimension, we can expand every function in $L^2(I)$ in the (infinite) Legendre basis.

Theorem 3.4. *Let $f \in L^2(I)$ and $n \in \mathbb{N}$.*

1. *f has a Legendre expansion: i.e., there exist real numbers $\hat{f}_k$ such that*

$$f = \sum_{k=0}^{\infty} \hat{f}_k L_k. \tag{3.19}$$

2. *There exists a unique polynomial in $\mathbb{P}_n$ (which we denote by $\pi_n f$) of best Hilbertian approximation of f in $\mathbb{P}_n$, i.e.,*

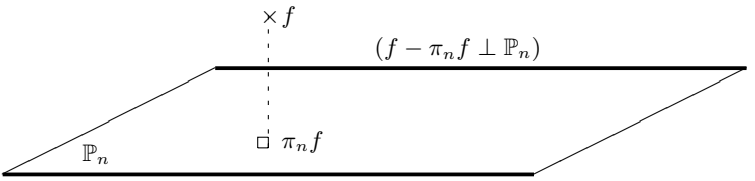

Fig. 3.5. The best Hilbertian approximation of f is its orthogonal projection on $\mathbb{P}_n$.

$$\|f - \pi_n f\| = \inf_{q \in \mathbb{P}_n} \|f - q\|.$$

Moreover, $\pi_n f$ is characterized by the orthogonality relations (see Fig. 3.5)

$$\langle f - \pi_n f, p \rangle = 0, \qquad \forall p \in \mathbb{P}_n, \tag{3.20}$$

which means that $\pi_n f$ is the orthogonal projection of f on $\mathbb{P}_n$.

The real numbers $\hat{f}_k$ in (3.19) are called the Legendre (or Fourier–Legendre) coefficients of the function f. We deduce from the orthogonality of the Legendre polynomials that

$$\hat{f}_k = \frac{\langle f, L_k \rangle}{\|L_k\|^2} = (k + \frac{1}{2}) \int_{-1}^{1} f(t) L_k(t) dt, \tag{3.21}$$

and $\pi_n f$ is the Legendre series of f, truncated to the order n:

$$\pi_n f = \sum_{k=0}^{n} \hat{f}_k L_k. \tag{3.22}$$

The computation of the best approximation of a function consists mainly in computing its Legendre coefficients. Since the integral in (3.21) can rarely be evaluated exactly, a numerical quadrature is required. See Chap. 5, where the Legendre polynomials are also used to solve a differential equation.

The convergence of the best Hilbertian approximation is stated in the following proposition.

Proposition 3.5. *For all $f \in L^2(I)$,*

$$\lim_{n \to +\infty} \|f - \pi_n f\| = 0. \tag{3.23}$$

3.3.3 Discrete Least Squares Approximation

In this section, we seek the best polynomial approximation of a function f with respect to a discrete norm. Given m distinct points $(x_i)_{i=1}^m$ and m values $(y_i)_{i=1}^m$, the goal is to determine a polynomial $p = \sum_{j=0}^{n-1} a_j x^j \in \mathbb{P}_{n-1}$ that minimizes the expression

$$E = \sum_{i=1}^{m} |y_i - p(x_i)|^2, \tag{3.24}$$

with m, in general, much larger than n. From a geometrical point of view, the problem is to find p such that its graph is as close as possible (in the Euclidean norm sense) to the points (x_i, y_i). The function E defined by (3.24) is a function of n variables $(a_0, a_1, \ldots, a_{n-1})$. To determine its minimum, we compute the partial derivatives

$$\frac{\partial E}{\partial a_j} = 0 \Longleftrightarrow -2\sum_{i=1}^{m} (y_i - p(x_i))\, x_i^j = 0 \Longleftrightarrow \sum_{k=0}^{n-1} \left(\sum_{i=1}^{m} x_i^{k+j} \right) a_k = \sum_{i=1}^{m} x_i^j y_i.$$

Hence the vector $a = (a_0, \ldots, a_{n-1})^T$ whose components are the coefficients of the polynomial where the minimum of E is reached is a solution of the linear system

$$\widetilde{A} a = \widetilde{b}, \tag{3.25}$$

with the matrix $\widetilde{A}$ and the right-hand side $\widetilde{b}$ defined by

$$\widetilde{A} = \begin{pmatrix} \sum_i 1 & \sum_i x_i & \cdots & \sum_i x_i^{n-1} \\ \sum_i x_i & \sum_i x_i^2 & \cdots & \sum_i x_i^n \\ \vdots & \vdots & \vdots & \vdots \\ \sum_i x_i^{n-1} & \sum_i x_i^n & \cdots & \sum_i x_i^{2n-1} \end{pmatrix} \in \mathbb{R}^{n \times n}, \quad \widetilde{b} = \begin{pmatrix} \sum_i y_i \\ \sum_i x_i y_i \\ \vdots \\ \sum_i x_i^{n-1} y_i \end{pmatrix}.$$

First of all, consider the case $n = 2$, corresponding to the determination of a straight line called the *regression line*. In this case the matrix $\tilde{A}$ and the vector $\widetilde{b}$ are

$$\widetilde{A} = \begin{pmatrix} m & \sum_i x_i \\ \sum_i x_i & \sum_i x_i^2 \end{pmatrix}, \quad \widetilde{b} = \begin{pmatrix} \sum_i y_i \\ \sum_i x_i y_i \end{pmatrix}. \tag{3.26}$$

The determinant of $\widetilde{A}$,

$$\Delta = m \left(\sum_{i=1}^{m} x_i^2 \right) - \left(\sum_{i=1}^{m} x_i \right)^2 = m \sum_{i=1}^{m} \left(x_i - \frac{1}{m} \sum_{j=1}^{m} x_j \right)^2$$

vanishes only if all the points x_i are identical. Hence the matrix $\widetilde{A}$ is invertible and the system (3.26) has a unique solution.
Let us go back to the general case. Noticing that the Vandermonde matrix

$$A = \begin{pmatrix} 1 & x_1 & \dots & x_1^{n-1} \\ \vdots & \vdots & & \vdots \\ 1 & x_m & \dots & x_m^{n-1} \end{pmatrix} \in \mathbb{R}^{m \times n}$$

is such that $\tilde{A} = A^T A$ and $\tilde{b} = A^T b$ with $b = (y_1, \dots, y_m)^T$, we can write the system (3.25) as

$$A^T A a = A^T b. \tag{3.27}$$

These equations are called normal equations. The following theorem tells us that the solutions of (3.27) are the solutions of the minimization problem: find $a \in \mathbb{R}^n$ such that

$$\|Aa - b\| = \inf_{x \in \mathbb{R}^n} \|Ax - b\|. \tag{3.28}$$

Theorem 3.5. *A vector $a \in \mathbb{R}^n$ is solution of the normal equations (3.27) if and only if a is solution of the minimization problem (3.28).*

Hence to solve the least squares problem, one can either solve the problem (3.28) by some optimization algorithms, or solve the problem (3.27) by some linear system solvers. See Allaire and Kaber (2006), for instance.

To compute a polynomial least squares approximation with MATLAB, use the instruction `polyfit(x,y,n)` with x a vector that contains the values x_i, y a vector that contains the y_i, and n the degree of the least squares polynomial.

Exercise 3.12. Compute the least squares approximation of the function $f(x) = \sin(2\pi \cos(\pi x))$ defined in Exercise 3.11. The optimal degree n could be determined in the following way. Starting from $n = 0$, one increases n in steps of 1 until the relative error $|e_n - e_{n-1}|/e_{n-1}$ becomes smaller than a prescribed value ($\frac{1}{2}$ for example). Here we set $e_n = \|x - p_n(x)\|_2$.
A solution of this exercise is proposed in Sect. 3.6 at page 80.

3.4 Piecewise Polynomial Approximation

We display in Fig. 3.6 some Lagrange polynomial interpolants of the function f, defined on $[0, 1]$ by

$$f(x) = \begin{cases} 1 & \text{for } 0 \le x \le 0.25, \\ 2 - 4x & \text{for } 0.25 \le x \le 0.5, \\ 0 & \text{for } 0.5 \le x \le 1, \end{cases}$$

at respectively 4, 6, 8, and 10 points. Obviously, there is a problem due to the lack of global regularity of f over the interval $I = [0, 1]$. However, this function has a very simple structure; it is affine on each interval $[0, \frac{1}{4}]$, $[\frac{1}{4}, \frac{1}{2}]$ and $[1/2, 1]$.

Let f be a continuous function defined on the interval $[0, 1]$. The goal is to approximate f by a piecewise polynomial function S. Such a function is called

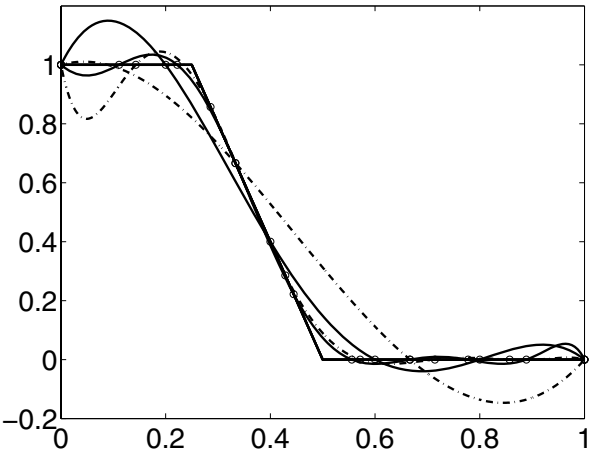

Fig. 3.6. Polynomial interpolation of a piecewise polynomial function.

a spline. The use of piecewise polynomials is a way to control the problems related to the lack of global regularity of f. Another practical reason is the stability of the numerical computations: it is better to use several polynomials of low degree than one polynomial with high degree.

The interval $I = [0, 1]$ is divided into subintervals $I_i = [x_i, x_{i+1}]$ for $i = 1, \ldots, n-1$. On each subinterval I_i, the function f is approximated by a polynomial $p_{k,i}$ of degree k. We denote by S_k the piecewise polynomial that coincides with $p_{k,i}$ on each interval I_i and satisfies some global regularity condition on the internal I: continuity, differentiability up to some order, etc.

3.4.1 Piecewise Constant Approximation

Let S_0 be a function that is constant on each interval I_i and interpolates f at the points $x_{i+1/2} = (x_i + x_{i+1})/2$:

$$S_{0|I_i}(x) = f(x_{i+1/2}).$$

Suppose the function f is in $\mathcal{C}^1(I)$. According to Proposition 3.2, for all $x \in I_i$, there exists $\xi_{x,i} \in I_i$ such that

$$f(x) - S_0(x) = (x - x_{i+1/2}) f'(\xi_{x,i}).$$

We deduce from this that if the points x_i are equidistant ($x_{i+1} - x_i = h = 1/n$) then

$$\|f - S_0\|_\infty \leq \frac{h}{2} M_1, \tag{3.29}$$

with M_1 an upper bound of f' on I. Hence, as h goes to 0, S_0 converges uniformly toward f.

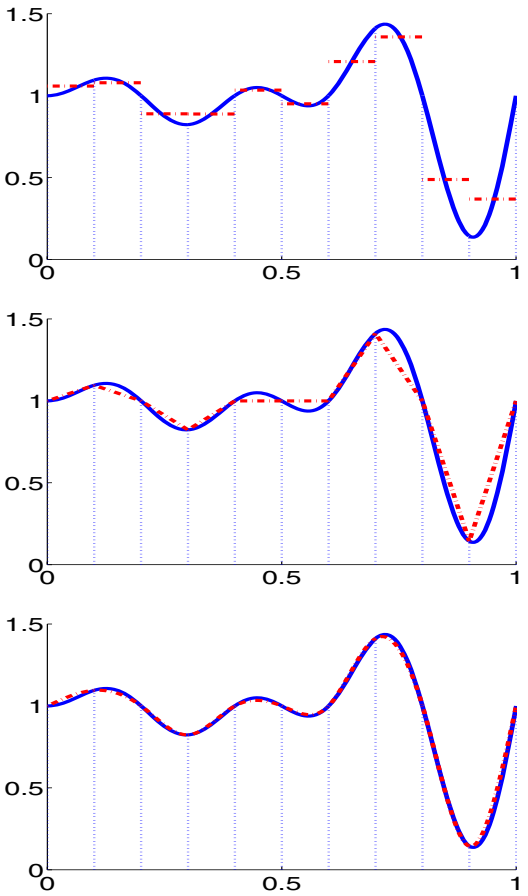

Fig. 3.7. From top to bottom: examples of piecewise constant, affine, and cubic approximations.

Remark 3.3. The power of h in (3.29) indicates that if the discretization parameter h is divided by a constant $c > 0$, the bound on the error $\|f - S_0\|_\infty$ is divided by the same constant c.

Exercise 3.13. Let $f : [0,1] \mapsto f(x) = \sin(4\pi x)$. Draw the curve $\ln n \mapsto \ln \|f - S_0\|_\infty$ and check (an approximation of) the estimate (3.29). Take the values $n = 10\,k$ with $k = 1, \ldots, 10$.
A solution of this exercise is proposed in Sect. 3.6 at page 80.

3.4.2 Piecewise Affine Approximation

This time, the approximation S_1 is affine on each interval I_i and coincides with f at the points x_i and x_{i+1}:

$$S_{1|I_i}(x) = \frac{f(x_{i+1}) - f(x_i)}{h}(x - x_i) + f(x_i).$$

First of all, suppose the function f is in $\mathcal{C}^2(I)$. According to Proposition 3.2, for all $x \in I_i$, there exists $\xi_{x,i} \in I_i$ such that

$$f(x) - S_1(x) = \frac{(x - x_i)(x - x_{i+1})}{2} f''(\xi_{x,i}).$$

We deduce from this

$$\|f - S_1\|_\infty \leq \frac{h^2}{8} M_2, \tag{3.30}$$

with M_2 an upper bound of f'' on I. Hence the uniform convergence of S_1 toward f.

Remark 3.4. The power of h in (3.30) indicates that if the discretization parameter h is divided by a constant $c > 0$, the bound on the error $\|f - S_1\|_\infty$ is divided by c^2. For example, changing h into $h/2$ divides the bound on the error by 4.

Exercise 3.14. Same questions as in the previous exercise to check the estimate (3.30).
A solution of this exercise is proposed in Sect. 3.6 at page 82.

If the function f is only in $\mathcal{C}^1$, convergence holds too. To prove it, write $f(x)$ as an integral,

$$f(x) = f(x_i) + \int_{x_i}^{x} f'(t)dt, \quad \text{and } S_1(x) = f(x_i) + \frac{x - x_i}{h} \int_{x_i}^{x_{i+1}} f'(t)dt,$$

and use the assumed bound on f',

$$\|f - S_1\|_\infty \leq 2hM_1.$$

That implies the convergence. Note that this estimate is less accurate than (3.30), but it requires less regularity on the function f.

3.4.3 Piecewise Cubic Approximation

Now we seek an approximation S_3 in $\mathcal{C}^2(I)$ that is cubic on each interval I_i and coincides with f at the points x_i and x_{i+1}. Let p_i be the restriction of S_3 to the interval I_i, for $i = 0, \ldots, n-1$:

$$p_i(x) = a_i(x - x_i)^3 + b_i(x - x_i)^2 + c_i(x - x_i) + d_i.$$

Obviously $d_i = f(x_i)$. The unknowns a_i, b_i, and c_i can be expressed in terms of the values of f and its second derivative at the points x_i. Setting $\alpha_i = p_i''(x_i)$ and using the continuity of the first and second derivatives of the approximation at the points x_i, we get for $i = 0, \ldots, n-1$,

$$b_i = \frac{1}{2}\alpha_i, \quad a_i = \frac{\alpha_{i+1} - \alpha_i}{6h}, \quad c_i = \frac{f_{i+1} - f_i}{h} - \frac{2\alpha_i + \alpha_{i+1}}{6}h$$

and a recurrence relation between the values α_{i-1}, α_i, and α_{i+1}:

$$h(\alpha_{i-1} + 4\alpha_i + \alpha_{i+1}) = \frac{6}{h}(f_{i-1} - 2f_i + f_{i+1}).$$

We have to add to these $n-1$ equations two other equations in order to close the system and compute the $n+1$ unknowns α_i. Several choices of these two equations exist. If α_0 and α_n are fixed, say

$$\alpha_0 = \alpha_n = 0, \tag{3.31}$$

the vector $\alpha = (\alpha_1, \ldots, \alpha_{n-1})^T$ is a solution of the linear tridiagonal system $Ax = b$, with

$$A = h\begin{pmatrix} 4 & 1 & 0 & \ldots & 0 \\ 1 & 4 & 1 & & \vdots \\ 0 & \ddots & \ddots & \ddots & 0 \\ \vdots & & 1 & 4 & 1 \\ 0 & \ldots & 0 & 1 & 4 \end{pmatrix} \quad \text{and} \quad b = \frac{6}{h}\begin{pmatrix} f_0 - 2f_1 + f_2 \\ \vdots \\ f_{i-1} - 2f_i + f_{i+1} \\ \vdots \\ f_{n-2} - 2f_{n-1} + f_n \end{pmatrix}. \tag{3.32}$$

The matrix A is invertible since its diagonal is strictly dominant.

Exercise 3.15. Write a program that computes the cubic spline with the conditions (3.31) and the $n+1$ points $(i/n)_{i=0}^n$. Test your program with the function $f(x) = \sin(4\pi x)$. Take $n = 5$, then $n = 10$. Draw on the same plot the function f and the spline. In order to see the behavior of the spline between two interpolation points, add ten or twenty points of representation in each interval I_i to get a very fine plot.
A solution of this exercise is proposed in Sect. 3.6 at page 82.

3.5 Further Reading

For the general theory of polynomial approximation, we refer the reader to Rivlin (1981) and DeVore and Lorentz (1993).

The Legendre polynomials are used in Chap. 5 to solve a differential equation. We refer the reader to Bernardi and Maday (1997) for the use of spectral methods in numerical analysis.

Related to the splines are the Bézier curves, which have many applications in computer-aided geometric design; see Chap. 9.

Wavelets are used in Chap. 6 for image processing purposes. See Cohen (2003) for the numerical analysis of wavelets.

We did not consider in this chapter trigonometric approximation. Of course, all the results stated here are valid with very minor modifications

to the approximation of periodic functions: existence and uniqueness of a best polynomial approximation, interpolation, etc. There exists a very efficient algorithm to compute the Fourier coefficients of a function from its pointwise values or the reverse; it is the famous fast Fourier transform. In Chap. 12, the trigonometric approximation is used to solve the Navier–Stokes equations.

3.6 Solutions and Programs

Solution of Exercise 3.1

1. $b = (f(x_0), \ldots, f(x_n))^T$ and $A = \begin{pmatrix} 1 & x_0 & x_0^2 & \ldots & x_0^n \\ 1 & x_1 & x_1^2 & \ldots & x_1^n \\ \vdots & \vdots & \vdots & \vdots & \\ 1 & x_n & x_n^2 & \ldots & x_n^n \end{pmatrix}$.

2.
```
n=10;x=sort(rand(n+1,1));
     A=ones(length(x),1);
     for k=1:length(x)-1
        A=[A x.^k];
     end;
```

3.
```
cf=A\test1(x);
%reordering of the coefficients
cf=cf(end:-1:1);
y=polyval(cf,x);
plot(x,test1(x),x,y,'r+');
```

   the function `test1` is defined by

```
test1=inline('sin(10.*x.*cos(x))');
```

4. A is a Vandermonde matrix, it is invertible if all the points are distinct. That is the case in this experiment. However, for MATLAB, $A\alpha - b$ is not zero. This is due to the very bad condition number of the matrix A. For large values of n (say $n = 20$), the matrix A becomes a singular matrix for MATLAB: the numerical rank of the matrix A computed by MATLAB is 18, while the right one is $n + 1$. Recall that the condition number of a matrix A measures the sensitivity of linear system $Ax = b$ to perturbations of the data A or b.

See the script in the file *APP_ApproxScript1.m*.

Solution of Exercise 3.2

The following script is written in the file *APP_ApproxScript2.m*. It uses the function `APP_condVanderMonde` defined below:

```
%Condition number of a Vandermonde matrix
N=2:2:20;cd=[ ];
for n=N
    cd=[cd APP_condVanderMonde(n)];
end;
plot(N,log(cd),'+-')
```

The function `APP_condVanderMonde` is defined as below:

```
function y=APP_condVanderMonde(n)
%compute the condition number of a Vandermonde matrix
%The n+1 points are uniformly chosen between 0 and 1.
x=(0:n)'/n;
A=ones(length(x),1);
for k=1:length(x)-1
    A=[A x.^k];
end;
y=cond(A);
```

We deduce from Fig. 3.8 that $\ln(\mathrm{cond}(A))$, as a function of n, is a straight line. Hence $\mathrm{cond}(A)$ grows exponentially with n.

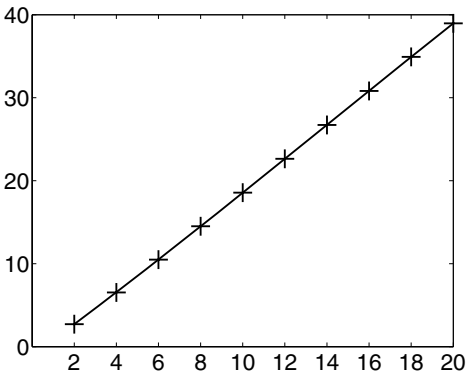

Fig. 3.8. Logarithm of the condition number of a Vandermonde matrix.

The reader is asked to compare the function `APP_condVanderMonde` to the following function in terms of numerical complexity

```
function c=APP_condVanderMondeBis(n)
```

```
%compute the condition number of a Vandermonde matrix
%The n+1 points are uniformly chosen between 0 and 1.
x=(0:n)'/n;
A=ones(length(x),1);y=x;
for k=1:length(x)-1
    A=[A y];y=y.*x;
end;
c=cond(A);
```

Solution of Exercise 3.3

```
%The Lagrange basis
n=10;x=(0:n)'/n;i=round(n/2);
twon=n;g=(0:twon)'/twon;
y=zeros(size(x));y(i)=1;cf=polyfit(x,y,n);
y0=polyval(cf,0);
```

For $n = 5$ or 10 everything goes well, since the program computes a value for $\ell_{n/2}(x_0)$ close to the exact value 0. But for $n = 20$, the computation of $\ell_{n/2}(x_0)$ gives -1.0460. This is again a consequence of the ill conditioning of the matrix. Note that in that case, MATLAB displays a warning message. See the script in *APP_ApproxScript3.m*.

Solution of Exercise 3.4

1. The function `APP_dd` defined below computes the divided differences.

```
function c=APP_dd(x)
% x contains the points xi
% c contains the divided differences
c=test1(x); %warning: "test1" is defined
            %either in another file or "inline"
n=length(x);
for p=1:n-1
    for k=n:-1:p+1
        c(k)=(c(k)-c(k-1))/(x(k)-x(k-p));
    end;
end;
```

It is sometimes useful to send the name of a function as an input parameter of `APP_dd`. This is possible up to a slight modification of the first two lines: see also section 5.6 of Chap. 5.

```
function c=APP_dd(x,f)
c=feval(f,x);
```

2. Running the script below produces Fig. 3.9. This script is available under the name *APP_ApproxScript4.m* as well as the functions `APP_dd` and `APP_interpol`:

```
function y=APP_interpol(c,x,g)
%compute the interpolation of the function f on the grid g
%knowing the divided differences c computed at the points x
n=length(c);
y=c(n)*ones(size(g));
for k=n-1:-1:1
    y=c(k)+y.*(g-x(k));
end;
```

```
n=20;x=(0:n)'/n;g=0:0.01:1;
c=APP_dd(x);y=APP_interpol(c,x,g);
yg=test1(g);plot(g,yg,g,y,'r+')
hold on;yx=test1(x);plot(x,yx,'O');hold off
```

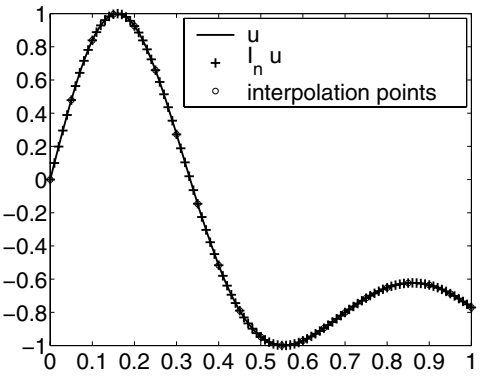

Fig. 3.9. Computation of a Lagrange interpolant.

Solution of Exercise 3.5

The script of this exercise is available under the name *APP_ApproxScript5.m* as well as the function `APP_Lebesgue`.

1. Computation of the Lebesgue constant:

```
function leb=APP_Lebesgue(x)
%Computation of the Lebesgue constant related
%to the points in the array x
n=length(x)-1;
```

```
xx=linspace(min(x),max(x),100);
%fine grid of 100 points
y=zeros(size(xx));
for i=1:n+1;
   %computation of ℓ_i(x)
   l=zeros(size(x));l(i)=1;cf=polyfit(x,l,n);
   y=y+abs(polyval(cf,xx));
end;
leb=max(y);
```

2. The uniform case:

```
ind=[ ];lebE=[ ];
for n=10:5:30
    x=(-n/2:n/2)/n*2;   %equidistant points
    l=APP_lebesgue(x)
    ind=[ind;n];lebE=[lebE;l];
end;
figure(1);plot(ind,log(lebE),'+-')
```

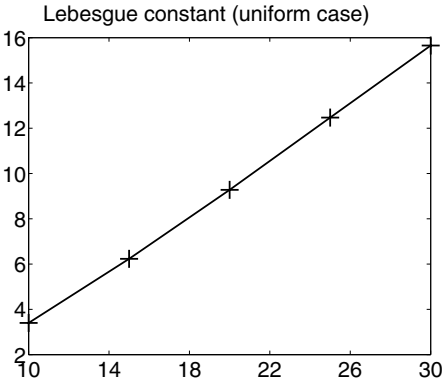

Fig. 3.10. The Lebesgue constant associated with equidistant points: $n \mapsto \ln(\Lambda(n))$.

We note in Fig. 3.10 that $\ln(\Lambda(n))$, as a function of n, is a straight line with slope (approximately) $\frac{1}{2}$. Hence $\Lambda(n) \approx e^{n/2}$.

3. The Chebyshev case:

```
ind=[ ];lebT=[ ];
for n=10:5:30
    x=cos(pi*(.5+n:-1:0)/(n+1)); %Chebyshev points
    l=APP_lebesgue(x);
    ind=[ind;n];lebT=[lebT;l];
```

```
end;
figure(2);plot(log(ind),lebT,'+-')
```

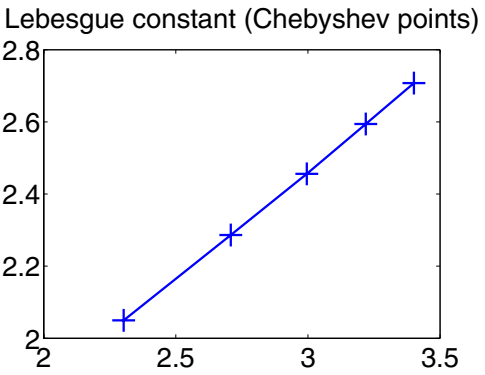

Fig. 3.11. The Lebesgue constant associated with the Chebyshev points: $\ln n \mapsto \Lambda(n)$.

We note in Fig. 3.11 that $e^{\Lambda_T(n)}$, as a function of n, is a straight line with slope (approximately) 0.6, hence $\Lambda_T(n) \approx 0.6 \ln(n)$. Indeed, one can prove rigorously that $\Lambda_T(n) \approx \frac{2}{\pi} \ln n$.

Solution of Exercise 3.6

For the function f_1, the results with $n = 30$ and $n = 40$ are shown in Fig. 3.12: the method converges slowly. For the function f_2, the results with $n = 10$ and

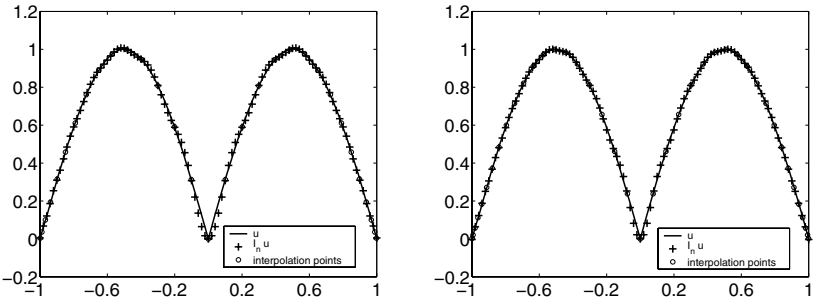

Fig. 3.12. Interpolation at the Chebyshev points: (a) $n = 30$ and (b) $n = 40$.

$n = 30$ are displayed in Fig. 3.13. It seems that the method converges, and

in fact it does. One can prove that the interpolation at the Chebyshev points converges for functions of class $\mathcal{C}^1$. This is the case for f_2, but not for f_1. See the script in *APP_Interpolation.m*.

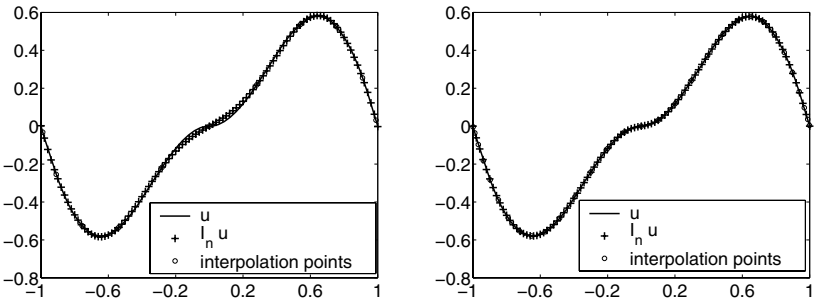

Fig. 3.13. Interpolation at the Chebyshev points: (a) $n = 10$ and (b) $n = 30$.

Solution of Exercise 3.7

See the script in *APP_Runge.m*. The results for $n = 10$, $n = 20$, and $n = 30$ are shown in Fig. 3.14: the method diverges at the boundaries. Note that in this case the function to be interpolated is very smooth, but its Lebesgue constant "explodes" (see Remark 3.1).

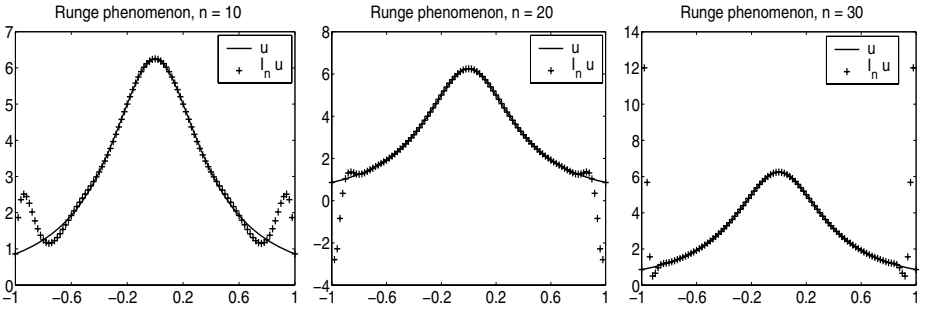

Fig. 3.14. Runge phenomenon. From left to right: interpolation at 11, 21, and 31 equidistant points.

Solution of Exercise 3.8

1. Computation of the Hermite interpolant using divided differences. See the function `APP_ddHermite`. The input data of this function is an array `Tab` whose first column contains the points x_i, and for each i:

- `Tab(i,1)` contains the points x_i.
- `Tab(i,2)` contains an integer α_i: the function and its derivatives up to α_i are interpolated.
- `Tab(i,3:Tab(i,2)+3)` contains the values of the function at point x_i and its derivatives up to order α_i.

The call `[xx,dd]=APP_ddHermite(Tab)` returns two vectors:

- the first vector contains the points x_i taking into account their "multiplicity": if the function and its α_i derivatives have to be interpolated at the point x_i, this point is copied $\alpha_i + 1$ times in `xx`.
- the vector `dd` contains the divided differences.

With the help of these two vectors, we can implement the Horner algorithm (see page 53) to evaluate $\mathcal{I}_n^H f(x)$.

2. This is done vectorwise as follows:

```
f=inline('cos(3*pi*x).*exp(-x)');
coll=[0 1/4 3/4 1]';
T=[coll zeros(size(coll)) f(coll)];
[xx,dd]=ddHermite(T);
%plot the function on a fine grid
x=linspace(0,1,100);n=length(dd);
y=dd(n)*ones(size(x));
for k=n-1:-1:1
   y=dd(k)+y.*(x-xx(k));
end;
plot(x,y,x,f(x),'r');hold on;plot(coll,f(coll),'+')
```

   See the script in *APP_ApproxScript8.m*. We see in Fig. 3.15 (a) that the curves intersect at only four points; they do not match at all, except at these points.
3. Imposing the matching of the derivatives forces the polynomial to fit the function more closely (see Fig. 3.15(b)). However, there is still a region of the interval $[0, 1]$ where the two curves are not close to each other.
4. By adding another interpolation point in this region, the approximation is much sharper, as shown in Fig. 3.15(b).

Solution of Exercise 3.9

The implementation is done in the script in *APP_scriptHermite.m*. For several values $m = 5(m' - 1)$ with $m' \in \{1, 2, 3, 4, 5\}$, we compute the corresponding polynomial p_m with the help of the function `APP_ddHermite`. The column m' of the matrix `Y` contains the values of p_m on a uniform fine grid of 100 points in $[0, 1]$. Figure 3.16 is generated by the script.

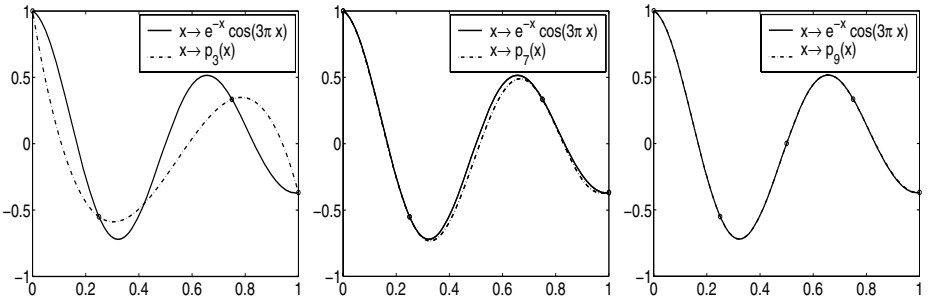

Fig. 3.15. (a) The Lagrange interpolation polynomial p_3 at the points 0, $\frac{1}{4}$, $\frac{3}{4}$, and 1, (b) the Hermite interpolation polynomial p_7 at the same points and (c) the Hermite interpolation polynomial p_9 at the points 0, $\frac{1}{4}$, $\frac{1}{2}$, $\frac{3}{4}$, and 1. The interpolation points are marked by circles.

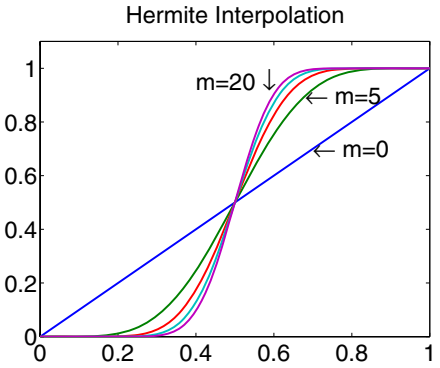

Fig. 3.16. Hermite polynomial interpolants.

Solution of Exercise 3.10

The equations form a linear system of $n+1$ equations and $n+1$ unknowns (the coefficients of the polynomial). This system has a unique solution if and only if the unique solution of the homogeneous problem (i.e., $f = 0$) is the null polynomial. This is the case since:

- The null polynomial is a trivial solution.
- If $p \in \mathbb{P}_n$ is a solution of the problem and if $p(x_0) = 0$, we deduce that $p(x_i) = 0$ for all $i = 1, \ldots, n$. Hence p is the null polynomial (a polynomial of $\mathbb{P}_n$ cannot have more than n distinct zeros). If $p(x_0) \neq 0$ then p has alternating signs between two successive x_i; hence it vanishes at $n+1$ distinct points and is again the null polynomial.

Writing $p(t) = \sum_{j=0}^{n} p_j t^j$, the equations become

$$p(x_i) - (-1)^i p(x_0) = f(x_i) - (-1)^i f(x_0)\}, \qquad i = 1, \ldots, n+1.$$

The vector $a = (p_0, \ldots, p_n)^T$ solves the system $Aa = b$ with

$$A_{i,j} = x_i^j - (-1)^i x_0^j, \quad b_i = f(x_i) - (-1)^i f(x_0) \qquad (1 \le i \le n+1, 0 \le j \le n).$$

The implementation is done in the function `APP_equiosc`. The input data of this function is a vector containing the values x_i. The function computes the matrix A and the vector b defined above and returns the coefficients p_j of the polynomial.

Solution of Exercise 3.11

The function `APP_Remez` computes for a given integer n the polynomial of best uniform approximation of a function f. Three cases are considered for the initialization of the algorithm: the Chebyshev points, equidistant points, and randomly chosen points. The parameter `tol` relaxes the equality constraint in step k of the algorithm (that is, a test of the form $a = b$ is replaced by the test $|a - b| <$ `Tol`). For $n = 5$, $n = 10$, and $n = 15$, the best uniform approximations on $[0, 1]$ of the function $x \mapsto \sin(2\pi \cos(\pi x))$ are displayed in Fig. 3.17.

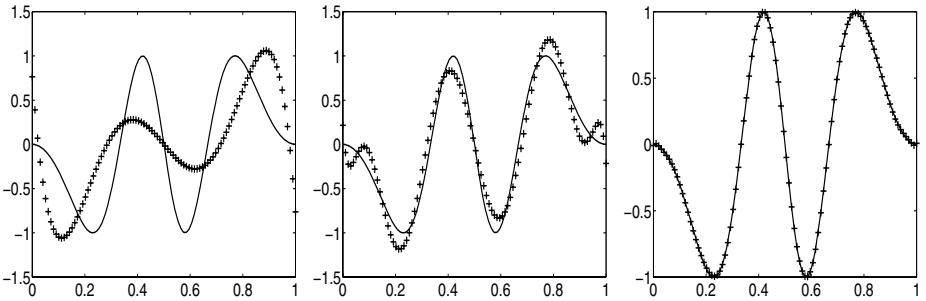

Fig. 3.17. Best uniform approximation in $\mathbb{P}_n$ of $f(x) = \sin(2\pi \cos(\pi x))$. From left to right: $n = 5$, $n = 10$, and $n = 15$. The function f is plotted with solid lines.

For $n = 15$, the algorithm initialized with the Chebyshev points converges in 21 iterations. Initialized with equidistant points, it converges in 28 iterations. Initialized with random points, it does not converge (in general) after 100 iterations.

The good result obtained with the Chebyshev points can be explained: since the function f has a Chebyshev expansion, analogous to the Legendre series in (3.19),

$$f = \sum_{k=0}^{\infty} \hat{f}_k T_k,$$

we can use the approximation

$$f - \sum_{k=0}^{n} \hat{f}_k T_k \approx \hat{f}_{n+1} T_{n+1}$$

by neglecting the remainder of the expansion. We remark that T_{n+1} equioscillates over $[-1, 1]$ at the $n+2$ points $t_i = \cos(i\frac{\pi}{n+1})$, $(i = 0, \ldots, n+1)$ since $T_{n+1}(t_i) = \cos(i\pi) = (-1)^i$. Hence $\sum_{k=0}^{n} \hat{f}_k T_k$ is close to the best uniform approximation of f in $\mathbb{P}_n$ (see Theorem 3.3). This is the reason why the Chebyshev points are good candidates for the initialization of the Remez algorithm.

Solution of Exercise 3.12

The script in *APP_ls.m* computes the least squares approximation on $[0, 1]$ of a given function. The instruction `p=polyfit(x,y,n)` returns an array `p` containing the coefficients of the polynomial with degree less than or equal to `n` that interpolates the values `y(i)` at the points `x(i)`. In order to evaluate this polynomial on a grid of points, we use the MATLAB function `polyval`. Running the script in *APP_ls.m* returns the value $n = 10$. The polynomial is displayed in Fig. 3.18 with the points (x_i, y_i) marked by the symbol $+$.

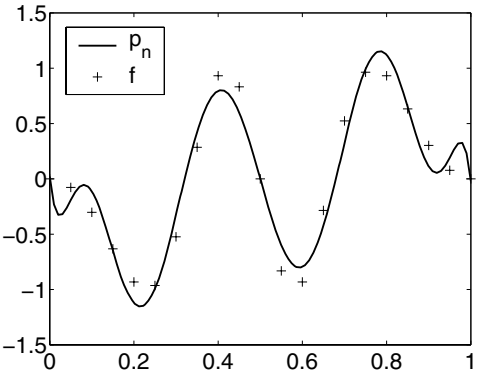

Fig. 3.18. Least squares approximation in $\mathbb{P}_{10}$: polynomial approximation (solid line) and the points $(x_i, f(x_i))$ $(+)$.

Solution of Exercise 3.13

We give only the results obtained with the piecewise constant spline, which can be found in *APP_spline0.m*:

```
% script spline0.m
n0=10;E=[ ];N=[ ];
for i=1:10,
    n=i*n0;E=[E;APP_errorS0(n)];N=[N;n];
end;
loglog(N,E,'-+');xlabel('log n');ylabel('log Error');
fprintf('slope of the straight line = %g ',...
log(E(end)/(E(1)))/log(N(end)/N(1)));
function y=APP_errorS0(n)
x=(0:n)'/n;h=1/n;fx=f(x);
%Evaluation of $p_i$ on each interval $[x_i,x_i+1]$
y=[ ];
for i=1:n
    Ii=linspace(x(i),x(i+1),20);
    fi=f(Ii);
    Si=f(.5*(x(i)+x(i+1)));
     y=[y norm(Si-fi,'inf')];
end
y=max(y);
function y=f(x)
y=sin(4*pi*x);
```

Running this script produces Fig. 3.19. The slope of the straight line is about -0.971325, which is a good approximation of the exact value -1 given by (3.29).

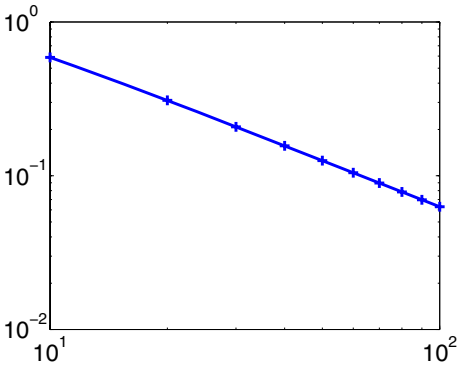

Fig. 3.19. Piecewise constant spline: curve $\ln n \mapsto \ln \|f - S_0\|_\infty$.

Solution of Exercise 3.14

The script in *APP_spline1.m* produces Fig. 3.20. The slope of the straight line is about -1.965, which is a good approximation of the exact value -2 given by (3.30).

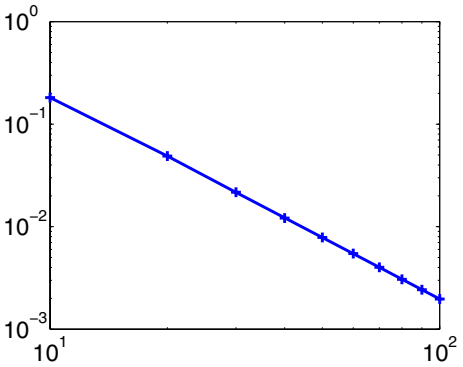

Fig. 3.20. Piecewise affine spline: curve $\ln n \mapsto \ln \|f - S_1\|_\infty$.

Solution of Exercise 3.15

See the script *APP_spline3.m*. The results obtained with $n = 5$ and $n = 10$ are displayed in Fig. 3.21.

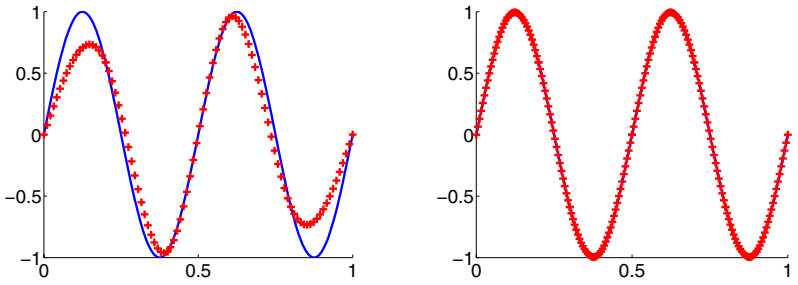

(a) (b)

Fig. 3.21. Cubic splines: (a) $n = 5$ and (b) $n = 10$.

Chapter References

G. Allaire and S.M. Kaber, *Numerical Linear Algebra*, Springer, New York, forthcoming, 2007.

C. Bernardi and Y. Maday, *Spectral Methods*, in Handbook of numerical analysis, Vol. V, North-Holland, Amsterdam, 1997.

A. Cohen, *Numerical Analysis of Wavelet Methods*, Studies in mathematics and its applications, North-Holland, Amsterdam, 2003.

M. Crouzeix and A. Mignot, *Analyse numérique des équations différentielles*, Masson, Paris, 1989.

R. A. DeVore and G. G. Lorentz, *Constructive Approximation*, Springer-Verlag, Berlin, 1993.

T. J. Rivlin, *An Introduction to the Approximation of Functions*, Dover Publications Inc., New York, 1981.

L. Schwartz, *Analyse, topologie générale et analyse fonctionnelle*, Hermann, Paris, 1980.

4

Solving an Advection–Diffusion Equation by a Finite Element Method

Project Summary

Level of difficulty:	1
Keywords:	Convection–diffusion equation, finite element method, stabilization of a numerical scheme.
Application fields:	Convection and diffusion phenomena.

In this project we seek a numerical approximation of the solution $u : [0,1] \longrightarrow \mathbb{R}$ of the following problem:

$$\begin{cases} -\varepsilon u''(x) + \lambda u'(x) = f(x), & x \in]0,1[\,, \\ u(0) = 0, \\ u(1) = 0. \end{cases} \tag{4.1}$$

The function f and the real numbers $\varepsilon > 0$ and λ are given in such a way that there exists a unique continuous solution of this problem. Our aim is to approximate the solution with a continuous piecewise polynomial function.

The differential equation in the problem (4.1) is an advection–diffusion equation. It models several phenomena, as, for example, the concentration of some chemical species transported in a fluid with speed λ; the parameter ε is the diffusivity of the chemical species. The ratio $\theta = \lambda/\varepsilon$ measures the importance of the advection compared to the diffusion. For large values of this ratio, the numerical solution of the problem (4.1) is delicate. The production and the vanishing of the chemical species are modeled by the function f, which in the general case depends on the unknown u. In this problem, we assume that f depends only on the position x and we consider λ and ε as constants.

4.1 Variational Formulation of the Problem

A solution u of the boundary value problem (4.1) is also a solution of the following problem:

$$\begin{cases} \text{Find } u \in H_0^1(0,1) \text{ such that} \\ \text{for all } v \in V: \qquad a(u,v) = \displaystyle\int_0^1 f(x)v(x)dx. \end{cases} \tag{4.2}$$

Here V denotes $H_0^1(0,1)$, the space of functions $v : [0,1] \to \mathbb{R}$ such that the integrals $\int_0^1 |v|^2$ and $\int_0^1 |v'|^2$ are bounded and $v(0) = v(1) = 0$. The bilinear form a is defined on $V \times V$ by

$$a(u,v) = \varepsilon \int_0^1 u'(x)v'(x)dx + \lambda \int_0^1 u'(x)v(x)dx. \tag{4.3}$$

Conversely, every regular solution of (4.2) is also a solution of (4.1). The problem (4.2) is a "variational formulation" of (4.1). The finite element method is based on the computation of the solution of the variational problem (4.2) rather than a direct discretization of equation (4.1) by a finite difference method (see Chaps. 1 and 2).

For a strictly positive integer n, we divide the interval $[0,1]$ into $n+1$ subintervals I_i. For a positive integer ℓ, we denote by $\mathbb{P}_\ell(I_i)$ the set of algebraic polynomials of degree less than or equal to ℓ on I_i and $\mathcal{V}_\ell^h$ the set of the continuous functions defined on $[0,1]$ whose restriction to each interval I_i belongs to $\mathbb{P}_\ell(I_i)$. Figure 4.1 displays two examples of functions of $\mathcal{V}_\ell^h$.

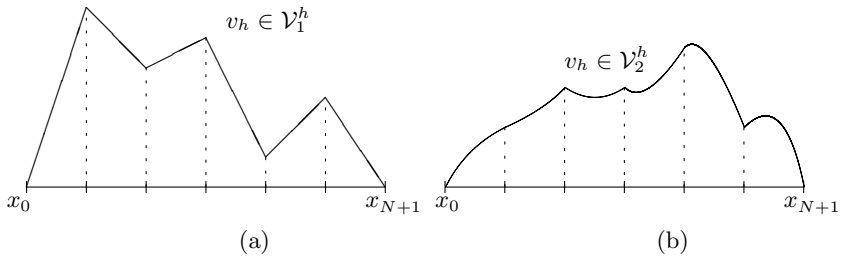

Fig. 4.1. Examples of functions of (a) $\mathcal{V}_1^h$ and (b) $\mathcal{V}_2^h$.

The finite element method consists in searching for an approximation $u_h \in \mathcal{V}_\ell^h$ of the function u, a solution of the following problem (compare to (4.2)):

$$\begin{cases} \text{Find } u_h \in \mathcal{V}_\ell^h \text{ such that} \\ \text{for all } v_h \in \mathcal{V}_\ell^h: \qquad a(u_h,v_h) = \displaystyle\int_0^1 f(x)v_h(x)dx. \end{cases} \tag{4.4}$$

The integrals in the left-hand side of (4.4) are easily computed since they involve products of polynomials. More difficult is the computation of the integral $\int_0^1 f(x)v_h(x)dx$, whose explicit calculation is rarely possible. In this case some quadrature rules are necessary. We will make use of two rules:

- the trapezoidal quadrature rule

$$\int_\alpha^\beta g(x)dx \approx (\beta-\alpha)\frac{g(\alpha)+g(\beta)}{2}.$$

This method is of order 1, that is, it is exact for all $g \in \mathbb{P}_1([\alpha,\beta])$.

- the Simpson quadrature rule

$$\int_\alpha^\beta g(x)dx \approx \frac{\beta-\alpha}{6}\left(g(\alpha)+4g(\frac{\alpha+\beta}{2})+g(\beta)\right). \tag{4.5}$$

This method is of order 3, i.e., it is exact for all $g \in \mathbb{P}_3([\alpha,\beta])$.

Using one of these basic quadrature formulas on each subinterval I_i, we get a quadrature formula on the whole interval $[0,1]$.

In this project, we compare two finite element methods (FEM) to solve the advection–diffusion problem. The first method is called $P1$ since it uses functions in $\mathcal{V}_1^h$; the second method is a $P2$ method since the approximation space for this method is $\mathcal{V}_2^h$.

To validate the computations, we have to compare the computed solution to the exact one. Generally, this can be done only in some special simple cases. The aim of the first exercise is to compute the exact solution of (4.1) in the case of constant source terms.

Exercise 4.1. The exact solution in the case of constant nonzero f.

1. Derive explicit formulas for the solution u of the problem (4.1).
2. Prove the existence of $x_\theta \in]0,1[$ depending only on the ratio $\theta = \lambda/\varepsilon$ such that the function $\frac{\lambda}{f}u$ is strictly increasing (respectively decreasing) over $]0,x_\theta[$ (respectively $]x_\theta,1[$). Calculate $\lim_{|\theta|\to+\infty} x_\theta$.
3. For $\lambda > 0$ fixed, we are interested in the behavior of the solution u for ε going to 0^+ (and thus $\theta \to +\infty$). Calculate $u(x_\theta)$ and $\lim_{\varepsilon\to0^+} u(x_\theta)$. Show that
$$\lim_{\varepsilon\to0^+}\lim_{x\to1} u(x) \neq \lim_{x\to1}\lim_{\varepsilon\to0^+} u(x).$$
Try to explain the meaning of the sentence, *for small values of ε, the solution of the differential problem (4.1) contains a thin boundary layer in a neighborhood of the point $x = 1$*'.
4. Write a program that computes the values of the solution u on a given set of points (an array). Plot u for $f = 1$, $\lambda \in \{-1,1\}$, and $\varepsilon \in \left\{1, \frac{1}{2}, 10^{-1}, 10^{-2}\right\}$. Comment the results.

A solution of this exercise is proposed in Sect. 4.6 at page 97.

4.2 A $P1$ Finite Element Method

For $n \in \mathbb{N}^*$, we define the points

$$x_k^{(1)} = kh, \qquad k = 0,\dots,n+1,$$

and the intervals

$$I_k = \left]x_k^{(1)}, x_{k+1}^{(1)}\right[, \qquad k = 0, \ldots, n,$$

with grid size $h = 1/(n+1)$. We also define k "hat functions" $\varphi_{h,k}^{(1)}$ ($k = 1, \ldots, n,$) (see Fig. 4.2), such that

$$\varphi_{h,k}^{(1)} \in \mathcal{V}_1^h \quad \text{and} \quad \varphi_{h,k}^{(1)}(x_j^{(1)}) = \delta_{j,k}, \quad \forall j = 1, \ldots, n,$$

with $\delta_{j,k}$ the Kronecker symbol. Note that the support of the function $\varphi_{h,k}^{(1)}$ is the union of two intervals I_{k-1} and I_k.

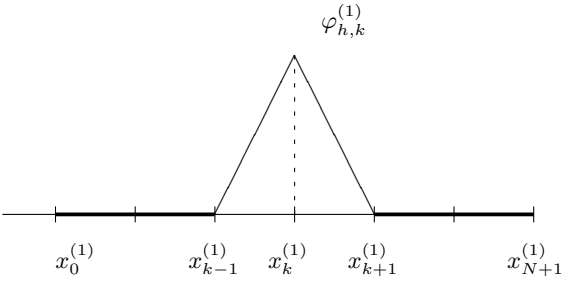

Fig. 4.2. A hat function $\varphi_{h,k}^{(1)}$ of $\mathcal{V}_1^h$.

In the finite element methods, the points $x_k^{(1)}$ are called *nodes* and the intervals I_k *cells*. We seek an approximation $u_h^{(1)} \in \mathcal{V}_1^h$ of the function u, a solution of the problem (4.4) with $\ell = 1$:

$$\begin{cases} \text{Find } u_h^{(1)} \in \mathcal{V}_1^h \text{ such that} \\ \text{for all } v_h \in \mathcal{V}_1^h : \qquad a\left(u_h^{(1)}, v_h\right) = \displaystyle\int_0^1 f(x) v_h(x) dx. \end{cases} \tag{4.6}$$

Exercise 4.2.

1. Prove that the functions $(\varphi_{h,k}^{(1)})_{k=1}^n$ form a basis of $\mathcal{V}_1^h$.
2. Deduce that problem (4.6) is equivalent to the following problem:

$$\begin{cases} \text{Find } u_h^{(1)} \in \mathcal{V}_1^h \text{ such that} \\ \text{for all } k = 1, \ldots, n : \qquad a\left(u_h^{(1)}, \varphi_{h,k}^{(1)}\right) = \displaystyle\int_0^1 f(x) \varphi_{h,k}^{(1)}(x) dx. \end{cases} \tag{4.7}$$

3. By expanding $u_h^{(1)}$ in the basis $\left(\varphi_{h,k}^{(1)}\right)_{k=1}^n$,

$$u_h^{(1)} = \sum_{m=1}^{n} \alpha_m \varphi_{h,m}^{(1)},$$

show that $\alpha_k = u_h\left(x_k^{(1)}\right)$ and that the vector $\tilde{u}_h^{(1)} = \left(u_h^{(1)}(x_1^{(1)}), \ldots, u_h^{(1)}(x_n^{(1)})\right)^T$ is a solution of the linear system

$$A_h^{(1)} \tilde{u}_h^{(1)} = b_h^{(1)}, \tag{4.8}$$

where $A_h^{(1)}$ is the real matrix of size $n \times n$ defined by

$$(A_h^{(1)})_{k,m} = a\left(\varphi_{h,m}^{(1)}, \varphi_{h,k}^{(1)}\right), \quad 1 \leq m, k \leq n,$$

and $b_h^{(1)}$ is the vector of $\mathbb{R}^n$

$$\left(b_h^{(1)}\right)_k = \int_0^1 f(x)\varphi_{h,k}^{(1)}(x)dx, \quad 1 \leq k \leq n.$$

Show that $A_h^{(1)} = \varepsilon B_h^{(1)} + \lambda C_h^{(1)}$, where $B_h^{(1)}$ is a tridiagonal symmetric matrix and $C_h^{(1)}$ a tridiagonal antisymmetric matrix.

4. Prove that the symmetric matrix $B_h^{(1)}$ is positive definite, i.e., for all $x \in \mathbb{R}^n$, $\langle B_h^{(1)} x, x\rangle \geq 0$, with equality if and only if x is the null vector ($\langle .,. \rangle$ denotes the Euler inner product). This property is very useful in the numerical analysis of linear problems. It implies, in particular, that the matrix is invertible.
5. Show that $\langle A_h^{(1)} x, x\rangle = \langle B_h^{(1)} x, x\rangle$. Conclude that $A_h^{(1)}$ is invertible.

A solution of this exercise is proposed in Sect. 4.6 at page 99.

Consequently, the system (4.7) has a unique solution that will be computed by solving the linear system (4.8).

Exercise 4.3. Computation of the $P1$ solution by solving (4.8).

1. Derive the following explicit formulas for $B_h^{(1)}$ and $C_h^{(1)}$:

$$B_h^{(1)} = \frac{1}{h}\begin{pmatrix} 2 & -1 & 0 & \ldots & \ldots & 0 \\ -1 & 2 & -1 & 0 & & \vdots \\ 0 & \ddots & \ddots & \ddots & & \vdots \\ \vdots & & \ddots & \ddots & \ddots & \vdots \\ \vdots & & 0 & -1 & 2 & -1 \\ 0 & \ldots & \ldots & 0 & -1 & 2 \end{pmatrix}, \quad C_h^{(1)} = \frac{1}{2}\begin{pmatrix} 0 & 1 & 0 & \ldots & \ldots & 0 \\ -1 & 0 & 1 & 0 & & \vdots \\ 0 & \ddots & \ddots & \ddots & & \vdots \\ \vdots & & \ddots & \ddots & \ddots & \vdots \\ \vdots & & 0 & -1 & 0 & 1 \\ 0 & \ldots & \ldots & 0 & -1 & 0 \end{pmatrix}.$$

2. Write a program that computes the matrix $A_h^{(1)}$ (with input data n, ε, and λ).
3. Write a program that computes the right-hand side $b_h^{(1)}$ (input data: n, and f). Use the trapezoidal rule to compute the components of the vector $b_h^{(1)}$.

4. For $\varepsilon = 0.1$, $\lambda = 1$, $f = 1$, and $n \in \{10, 20\}$, compute the solution $\tilde{u}_h$ of (4.8) and compare it to the exact solution.
5. Error analysis. Fix the parameters $\varepsilon = 0.1$, $\lambda = 1$ and $f = 1$. For n going from 10 to 100 in steps of 10, draw the curves $\log n \mapsto \log \|e_n^{(1)}\|_\infty$, with $e_n^{(1)} \in \mathbb{R}^n$ the error vector defined by $(e_n^{(1)})_k = \tilde{u}_h^{(1)}(k) - u(x_k^{(1)})$. Deduce a decreasing law for $\|e_n^{(1)}\|_\infty$ of the form

$$\|e_n^{(1)}\|_\infty \approx \text{constant}/n^{s_1} \qquad \text{for } n \to +\infty,$$

with $s_1 > 0$ to be determined.

A solution of this exercise is proposed in Sect. 4.6 at page 100.

The $P1$ finite element method seems to be well suited to solve the advection–diffusion problem. Unfortunately, things are not so simple. For $\lambda = 1$, $f = 1$, $\varepsilon = 0.01$, and $n = 10$ we obtain the results displayed in Fig. 4.3. The oscillatory behavior of $u_h^{(1)}$ shows that it is clearly not a good approximation of u, especially in the boundary layer. We investigate in the next section whether a high–order finite element method is able to suppress these oscillations.

The next exercise answers the following question: for a fixed ε, what is the minimum number of subintervals required to resolve the boundary layer?

Exercise 4.4. Fix $\lambda = 1$ and $f = 1$. For various "small" values of ε (for example in the range $[0.005, 0.02]$) determine the integer $n \equiv n(\varepsilon)$ from which the numerical solution seems to be a reasonable approximation of the exact solution in the boundary layer (i.e., the numerical approximation is not oscillating and is close to the exact solution in the boundary layer).
Hint: Use the following strategy: for fixed ε, run the program for $n = 10, 20, 30$, etc. For each value of n, plot the exact solution and the numerical approximation. From these graphs, decide whether the approximation is good. For each value of n, compute $P = \frac{|\lambda| h}{2\varepsilon}$, the Peclet number of the grid. What conclusion can be drawn from this?
A solution of this exercise is proposed in Sect. 4.6 at page 102.

4.3 A $P2$ Finite Element Method

For $n \in \mathbb{N}^*$, we set $h = 1/(n+1)$ and define the points $x_k^{(2)} = kh/2$ ($k = 0, \ldots, 2(n+1)$). Notice that $x_{2k}^{(2)} = x_k^{(1)}$ and the intervals $I_k = \left]x_{2k}^{(2)}, x_{2k+2}^{(2)}\right[$ ($k = 0, \ldots, n$) are those used in the previous section. In other words, we keep the same number of intervals and add to each interval a new node, namely the center of the element. To get a better approximation, we shall associate to each node of the mesh a piecewise quadratic function rather than a piecewise affine one.

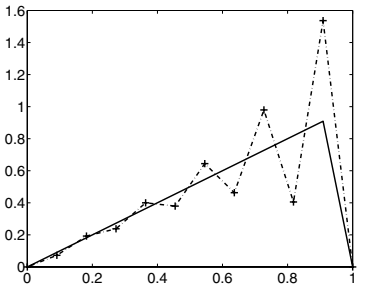

Fig. 4.3. Approximation of the solution of the advection–diffusion problem by a $P1$ finite element method, $\varepsilon = 0.01$, $\lambda = 1$, and $n = 10$.

We seek an approximation $u_h \in \mathcal{V}_2^h$ of the function u, a solution of problem (4.4) with $\ell = 2$:

$$\begin{cases} \text{Find } u_h^{(2)} \in \mathcal{V}_2^h \text{ such that} \\ \text{for all } v_h \in \mathcal{V}_2^h : \qquad a(u_h^{(2)}, v_h) = \displaystyle\int_0^1 f(x) v_h(x) dx. \end{cases} \tag{4.9}$$

As in the previous section, we begin by building a simple basis of $\mathcal{V}_2^h$. On each interval I_k, we define three quadratic Lagrange polynomials associated with the points $x_{2k}^{(2)}$, $x_{2k+1}^{(2)}$, and $x_{2k+2}^{(2)}$:

$$\begin{cases} \psi_{h,k}^{(-)}(x) = \quad 2(x - x_{2k+1}^{(2)})(x - x_{2k+2}^{(2)})/h^2, \\ \psi_{h,k}^{(0)}(x) = -4(x - x_{2k}^{(2)})(x - x_{2k+2}^{(2)})/h^2, \\ \psi_{h,k}^{(+)}(x) = \quad 2(x - x_{2k}^{(2)})(x - x_{2k+1}^{(2)})/h^2. \end{cases}$$

To each node $x_k^{(2)}$ of the mesh we associate the function $\varphi_{h,k}^{(2)} \in \mathcal{V}_2^h$ defined by (see also Fig. 4.4)

$$\varphi_{h,2k+1}^{(2)}(x) = \begin{cases} \psi_{h,k}^{(0)}(x) & \text{for } x \in I_k, \\ 0 & \text{otherwise,} \end{cases} \quad \text{and} \quad \varphi_{h,2k}^{(2)}(x) = \begin{cases} \psi_{h,k}^{(-)}(x) & \text{for } x \in I_k, \\ \psi_{h,k-1}^{(+)}(x) & \text{for } x \in I_{k-1}, \\ 0 & \text{otherwise.} \end{cases}$$

Notice that the support of the function $\varphi_{h,k}^{(2)}$ is either the interval I_k or the union of the two intervals I_{k-1} and I_k, according to the parity of k. Since the functions $(\varphi_{h,k}^{(2)})_{k=1}^{2n+1}$ form a basis of $\mathcal{V}_2^h$, problem (4.9) is equivalent to the problem

$$\begin{cases} \text{Find } u_h^{(2)} \in \mathcal{V}_2^h \text{ such that} \\ \text{for all } k = 1, \ldots, 2n+1 : \qquad a(u_h^{(2)}, \varphi_{h,k}^{(2)}) = \displaystyle\int_0^1 f(x) \varphi_{h,k}^{(2)}(x) dx. \end{cases} \tag{4.10}$$

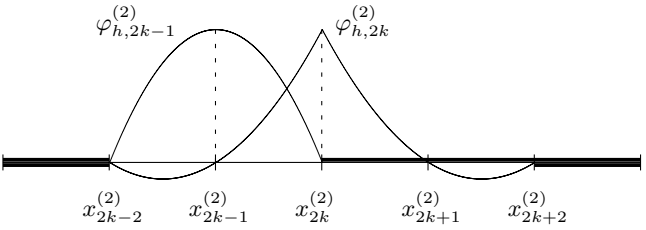

Fig. 4.4. Generic functions forming a basis of $\mathcal{V}_2^h$.

Expanding $u_h^{(2)}$ in the basis $\varphi_{h,k}^{(2)}$

$$u_h^{(2)} = \sum_{m=1}^{2n+1} \alpha_m \varphi_{h,m},$$

we prove, as in the $P1$ case, that $\alpha_m = u_h^{(2)}(x_m^{(2)})$ and the vector $\tilde{u}_h^{(2)} = (\alpha_1, \ldots, \alpha_{2n+1})^T$ solves a linear system

$$A_h^{(2)} \tilde{u}_h^{(2)} = b_h^{(2)}, \tag{4.11}$$

with $A_h^{(2)}$ the $(2n+1) \times (2n+1)$ matrix defined by

$$(A_h^{(2)})_{k,m} = a(\varphi_{h,m}^{(2)}, \varphi_{h,k}^{(2)}) \qquad 1 \le m, k \le 2n+1$$

and b_h the vector of $\mathbb{R}^{2n+1}$ defined by

$$(b_h^{(2)})_k = \int_0^1 f(x)\varphi_{h,k}^{(2)}(x)dx \qquad 1 \le k \le 2n+1.$$

Exercise 4.5. Put $A_h^{(2)} = \varepsilon B_h^{(2)} + \lambda C_h^{(2)}$. Is the matrix $B_h^{(2)}$ symmetric? tridiagonal? Is the matrix $C_h^{(2)}$ antisymmetric? tridiagonal? Prove the invertibility of the matrix $A_h^{(2)}$.
A solution of this exercise is proposed in Sect. 4.6 at page 103.

System (4.10) has thus a unique solution, which we compute by solving the linear system (4.11).

Exercise 4.6. Computation of the $P2$ solution.

1. Prove that $B_h^{(2)}$ and $C_h^{(2)}$ have the following pattern (given here for $n = 3$):

$$B_h^{(2)} = \frac{1}{3h} \begin{pmatrix} 16 & -8 & 0 & 0 & 0 & 0 & 0 \\ -8 & 14 & -8 & 1 & 0 & 0 & 0 \\ 0 & -8 & 16 & -8 & 0 & 0 & 0 \\ 0 & 1 & -8 & 14 & -8 & 1 & 0 \\ 0 & 0 & 0 & -8 & 16 & -8 & 0 \\ 0 & 0 & 0 & 1 & -8 & 14 & -8 \\ 0 & 0 & 0 & 0 & 0 & -8 & 16 \end{pmatrix},$$

$$C_h^{(2)} = \frac{1}{6}\begin{pmatrix} 0 & 4 & 0 & 0 & 0 & 0 & 0 \\ -4 & 0 & 4 & -1 & 0 & 0 & 0 \\ 0 & -4 & 0 & 4 & 0 & 0 & 0 \\ 0 & 1 & -4 & 0 & 4 & -1 & 0 \\ 0 & 0 & 0 & -4 & 0 & 4 & 0 \\ 0 & 0 & 0 & 1 & -4 & 0 & 4 \\ 0 & 0 & 0 & 0 & 0 & -4 & 0 \end{pmatrix}.$$

2. Write a program to compute the matrix $A_h^{(2)}$ (input data: n, ε, and λ).
3. Write a program to compute the right-hand side $b_h^{(2)}$ (input data: n and f). Use Simpson's rule to compute the components of the vector $b_h^{(2)}$.
4. Error analysis. Fix $\varepsilon = 0.1$, $\lambda = 1$, and $f = 1$. For n going from 10 to 100 in steps of 10, draw the curves $\log n \mapsto \log \|e_n^{(2)}\|_\infty$, with $e_n^{(2)} \in \mathbb{R}^{2n+1}$ the error vector defined by $(e_n^{(2)})_k = \tilde{u}_h^{(2)}(k) - u(x_k^{(2)})$. Deduce that the decreasing law for $\|e_n^{(2)}\|_\infty$ is of the form

$$e_n^{(2)} \approx \text{constant}/n^{s_2}, \qquad \text{for } n \to +\infty$$

with $s_2 > 0$ to be computed.

A solution of this exercise is proposed in Sect. 4.6 at page 103.

4.4 A Stabilization Method

In this section we propose a method for removing the oscillations that we have observed in Fig. 4.3. Running the $P2$ program with the same parameters ($\lambda = 1$, $f = 1$, $\varepsilon = 0.01$, and $n = 10$) we obtain Fig. 4.5. At first glance, the oscillations persist. However, if one is interested only in the values of the solution at the endpoints of the intervals (the points $x_{2k}^{(2)}$), one gets a nonoscillatory approximation of the exact solution. We propose to check this assertion and explain it. First of all, we define a way to compute the values of $u_h^{(2)}$ at the endpoints of the intervals, without computing the values at midpoints.

4.4.1 Computation of the Solution at the Endpoints of the Intervals

Let $\widehat{A}_h^{(2)}$ denote the matrix obtained after permutation of the rows of the matrix $A_h^{(2)}$ in order to put in the first places the rows with even indices (the same operation is performed for the columns). In the same way, we define the vector $\widehat{b}_h^{(2)}$ from the vector $b_h^{(2)}$. We also define the vector $\widehat{u}_h^{(2)}$ from the vector of unknowns $\tilde{u}_h^{(2)}$. The system (4.11) is equivalent to the system

$$\widehat{A}_h^{(2)} \widehat{u}_h^{(2)} = \widehat{b}_h^{(2)},$$

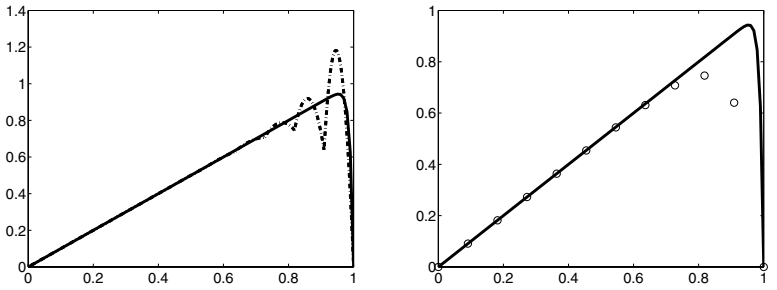

Fig. 4.5. Approximation of the solution of the advection–diffusion problem for $\varepsilon = 0.01$, $\lambda = 1$, and $n = 10$. (a) $P2$ finite element solution, (b) the same solution displayed only at the endpoints of the intervals.

which one could have obtained directly from the variational formulation by changing the numbering of the unknowns. Finally, we split $\widehat{A}_h^{(2)}$, $\widehat{b}_h^{(2)}$, and $\widehat{u}_h^{(2)}$ as

$$\widehat{A}_h^{(2)} = \begin{bmatrix} A & B \\ C & D \end{bmatrix}, \quad \widehat{b}_h^{(2)} = \begin{bmatrix} c \\ d \end{bmatrix}, \quad \widehat{u}_h^{(2)} = \begin{bmatrix} v \\ w \end{bmatrix},$$

where $A \in \mathbb{R}^{n\times n}$, $B \in \mathbb{R}^{n\times(n+1)}$, $C \in \mathbb{R}^{(n+1)\times n}$, $D \in \mathbb{R}^{(n+1)\times(n+1)}$, $c \in \mathbb{R}^n$, $d \in \mathbb{R}^{n+1}$, $v \in \mathbb{R}^n$, $w \in \mathbb{R}^{n+1}$, and

$$\begin{aligned} A_{i,j} &= a(\varphi_{h,2j}^{(2)}, \varphi_{h,2i}^{(2)}), & B_{i,j} &= a(\varphi_{h,2j}^{(2)}, \varphi_{h,2i-1}^{(2)}), \\ C_{i,j} &= a(\varphi_{h,2j-1}^{(2)}, \varphi_{h,2i}^{(2)}), & D_{i,j} &= a(\varphi_{h,2j-1}^{(2)}, \varphi_{h,2i-1}^{(2)}), \\ c_i &= \textstyle\int_0^1 f(x)\varphi_{h,2i}^{(2)}(x)dx, & d_i &= \textstyle\int_0^1 f(x)\varphi_{h,2i-1}^{(2)}(x)dx, \\ v_i &= u_h^{(2)}(x_{h,2i}^{(2)}), & w_i &= u_h^{(2)}(x_{h,2i-1}^{(2)}). \end{aligned}$$

It is easy to check that

- the matrix A is tridiagonal,
- the matrix B is upper triangular and bidiagonal,
- the matrix C is lower triangular and bidiagonal,
- the matrix D is diagonal.

The unknowns v and w are solutions of the linear system

$$\begin{cases} Av + Bw = c, \\ Cv + Dw = d. \end{cases} \tag{4.12}$$

The diagonal components of the matrix D are

$$D_{k,k} = a(\varphi_{h,2k-1}^{(2)}, \varphi_{h,2k-1}^{(2)}) = \varepsilon \int_{x_{h,2k-2}^{(2)}}^{x_{h,2k}^{(2)}} [\varphi_{h,2k-1}^{(2)}{}'(x)]^2 dx > 0,$$

and consequently the matrix is invertible. From the second equation of the system (4.12), we get $w = D^{-1}(d - Cv)$. Plugging this expression for w into the first equation, we obtain

$$(A - BD^{-1}C)v = c - BD^{-1}d. \tag{4.13}$$

This equation allows us to compute the vector v (i.e., the components of the $P2$ solution at the endpoints of the subintervals). Let us note that the matrix $A - BD^{-1}C$ is tridiagonal, whereas the matrix $A_h^{(2)}$ is pentadiagonal. This method, which consists in isolating, in a linear system, some of the unknowns that solve another simpler system, is called *condensation*. It is simply a Gaussian elimination of the unknowns associated with the centers of the subintervals.

Exercise 4.7.

1. Show that the matrix $A - BD^{-1}C$ is invertible.
2. Compute the matrices A, B, C, and D by extraction of rows and columns of the matrix $A_h^{(2)}$ computed in Exercise 4.6.
3. Fix $\lambda = 1$, $f = 1$, and $\varepsilon = 0.01$. For $n = 10$ and $n = 20$, solve the problem (4.13). In the same figure:
   - plot as a solid line the exact solution computed for 100 points in $[0, 1]$,
   - plot using some symbols the numerical solution, i.e., the components of the vector v.
4. For $n = 20$, compare to the $P1$ method. What is the minimum value n_0 starting from which the $P1$ method gives the same quality of approximation (a visual appreciation is enough)?

A solution of this exercise is proposed in Sect. 4.6 at page 105.

In conclusion, the $P2$ method, used only for the endpoints of the subintervals, provides good results. In the next section, we justify these observations.

4.4.2 Analysis of the Stabilized Method

Let us consider only the values $u_h^{(2)}(x_{h,2k}^{(2)})$, i.e., the values of $u_h^{(2)}$ on the grid of the $P1$ method. We prove that these values can be computed by a slightly modified $P1$ scheme. More precisely, setting

$$A_h^{(1S)} = A - BD^{-1}C,$$

the following result holds.

Proposition 4.1. *The matrix $A_h^{(1S)}$ equals the matrix $A_h^{(1)}$ in which ε is replaced by $\varepsilon' = \varepsilon + \lambda^2 h^2/(12\varepsilon)$.*

One could understand this result as an addition of a viscosity term to the original scheme that makes the solution smoother (less oscillatory). The remainder of the section is devoted to proving Proposition 4.1. In order to compute the matrix $A_h^{(1S)}$, we denote by $X = \text{Tridiag}(a, b, c; n, m)$ the tridiagonal $n \times m$ matrix X defined by

$$X_{i-1,i} = a, X_{i,i} = b, X_{i,i+1} = c, \quad \text{if these indices are defined.}$$

Notice that $\text{Tridiag}(a, b, c; n, m)$ is not necessarily a square matrix. The reader who enjoys long calculations will prove that

$$\begin{aligned}
A &= \frac{\varepsilon}{3h}\,\text{Tridiag}(1, 14, 1; n, n) + \frac{\lambda}{6}\,\text{Tridiag}(1, 0, -1; n, n),\\
B &= -\frac{8\varepsilon}{3h}\,\text{Tridiag}(0, 1, 1; n, n+1) - \frac{2\lambda}{3}\,\text{Tridiag}(0, 1, -1; n, n+1),\\
C &= -\frac{8\varepsilon}{3h}\,\text{Tridiag}(1, 1, 0; n+1, n) + \frac{2\lambda}{3}\,\text{Tridiag}(-1, 1, 0; n+1, n),\\
D &= \frac{16\varepsilon}{3h}\,\text{Tridiag}(0, 1, 0; n+1, n+1),
\end{aligned}$$

and that

$$\begin{aligned}
BC = &\frac{\sigma^2}{4}\,\text{Tridiag}(1, 2, 1; n, n) + \frac{\lambda\sigma}{3}\,\text{Tridiag}(2, 0, -2; n, n),\\
&-\frac{4}{9}\lambda^2\,\text{Tridiag}(-1, 2, -1; n, n),
\end{aligned}$$

where $\sigma = \frac{16\varepsilon}{3h}$. The reader may also calculate

$$A_h^{(1S)} = A - \frac{1}{\sigma}BC = \text{Tridiag}(\alpha, \beta, \gamma; n, n),$$

where

$$\begin{aligned}
\alpha &= -\frac{\varepsilon}{h} - \frac{\lambda}{2} - \frac{\lambda^2 h}{12\varepsilon} = -\frac{1}{h}\varepsilon' - \frac{\lambda}{2},\\
\beta &= 2\frac{\varepsilon}{h} + \frac{\lambda^2 h}{6\varepsilon} = \frac{2}{h}\varepsilon',\\
\gamma &= -\frac{\varepsilon}{h} + \frac{\lambda}{2} - \frac{\lambda^2 h}{12\varepsilon} = -\frac{1}{h}\varepsilon' + \frac{\lambda}{2}.
\end{aligned}$$

Finally

$$A_h^{(1S)} = \frac{\varepsilon'}{h}\,\text{Tridiag}(-1, 2, -1; n, n) + \frac{\lambda}{2}\,\text{Tridiag}(-1, 0, 1; n, n),$$

and the proposition follows since (see Exercise 4.3)

$$A_h^{(1)} = \frac{\varepsilon}{h}\,\text{Tridiag}(-1, 2, -1; n, n) + \frac{\lambda}{2}\,\text{Tridiag}(-1, 0, 1; n, n).$$

4.5 The Case of a Variable Source Term

We consider in this last section the advection–diffusion equation (4.1) with a nonconstant source term f in order to understand the effect of this term on the existence of a boundary layer.

Exercise 4.8.

1. Fix $\varepsilon = 0,01$, $\lambda = 1$, and $f(x) = \cos(a\pi x)$, $a \in \mathbb{R}$. For $a = 0$, we already know the existence of a boundary layer near the endpoint $x = 1$. We assume in this exercise that $a > 0$. For several values of $a = 1, 2, 3, \ldots$, compute (by any of the previous schemes) the solution of the equation (4.1). (Hint: take n large enough to avoid oscillations in the numerical solution.) Comment on the results. Same questions for $a = \frac{3}{2}$.
2. Calculation of the exact solution. Define for $x \in [0, 1]$,

$$F_\theta(x) = \int_0^x e^{\theta z} \left[\int_0^z f(y) e^{-\theta y} dy \right] dz.$$

   (a) Show that for all real numbers α and β, the function $\alpha + \beta e^{\theta x} - \frac{1}{\varepsilon} F_\theta$ is a solution of the differential equation (4.1).
   (b) Determine α and β such that $u = \alpha + \beta e^{\theta x} - \frac{1}{\varepsilon} F_\theta$ is a solution of problem (4.1) i.e., it satisfies the differential equation and the boundary conditions.
   (c) For $f(x) = \cos(a\pi x)$ with $a \in \mathbb{R}^*$, prove that

$$\lim_{\varepsilon \to 0^+} u(x) = \frac{1}{\lambda a \pi} \sin(a\pi x).$$

3. Explain the results obtained in question 1.

A solution of this exercise is proposed in Sect. 4.6 at page 106.

4.6 Solutions and Programs

Solution of Exercise 4.1

Computation of the exact solution.

1. For a constant function f, the solution of problem (4.1) is

$$u(x) = \frac{f}{\lambda} \left(x - \frac{e^{\lambda x/\varepsilon} - 1}{e^{\lambda/\varepsilon} - 1} \right).$$

2. With $\theta = \frac{\lambda}{\varepsilon}$, we rewrite u as

$$u(x) = \frac{f}{\lambda} \left(x - \frac{e^{\theta x} - 1}{e^{\theta} - 1} \right).$$

Hence

$$\frac{\lambda}{f}u'(x) = 0 \Longleftrightarrow 1 - \frac{\theta e^{\theta x}}{e^{\theta} - 1} = 0 \Longleftrightarrow \theta e^{\theta x} = e^{\theta} - 1 \Longleftrightarrow x = \frac{1}{\theta} \ln \frac{e^{\theta} - 1}{\theta}.$$

From this we deduce that $x_\theta = \frac{1}{\theta} \ln \frac{e^{\theta}-1}{\theta} = 1 + \frac{1}{\theta} \ln \frac{1-e^{-\theta}}{\theta} \in]0, 1[$ and

$$u'(x) > 0 \Longleftrightarrow e^{\theta} - 1 - \theta e^{\theta x} > 0 \Longleftrightarrow \theta e^{\theta x} < \theta e^{\theta x_\theta} \Longleftrightarrow x < x_\theta.$$

The limits are $\lim_{\theta \to +\infty} x_\theta = 1$ and $\lim_{\theta \to -\infty} x_\theta = 0$.

3. It is easy to check that

$$\lim_{\varepsilon \to 0^+} u(x_\theta) = \frac{f}{\lambda}, \quad \lim_{\varepsilon \to 0^+} \lim_{x \to 1} u(x) = 0, \quad \text{and} \quad \lim_{x \to 1} \lim_{\varepsilon \to 0^+} u(x) = \frac{f}{\lambda}.$$

The "boundary layer" is due to the strong variation of the solution (from f/λ to 0) over a small interval $[x_\theta, 1]$ whose length $1 - x_\theta = \frac{1}{\theta} \ln \frac{1-e^{-\theta}}{\theta}$ goes to 0 as θ goes to $+\infty$.

4. The following function `FEM_ConvecDiffSolExa` computes the exact solution of the problem:

```
function y=FEM_ConvecDiffSolExa(e,lambda,fc,x)
% solution of the convection--diffusion problem
% case ε, λ, and f constant
y=fc/lambda*(x-(1-exp(lambda*x/e))./(1-exp(lambda/e)));
```

We display in Fig. 4.6 the solutions for $f = 1$, $\varepsilon \in \{1, 1/2, 10^{-1}, 10^{-2}\}$, and (a) $\lambda = -1$ and (b) $\lambda = 1$. For small values of ε, we observe a small interval near $x = 1$ or $x = 0$ (according to the sign of λ) in which the solution suddenly changes from a value close to 1 to zero; this is the boundary layer.

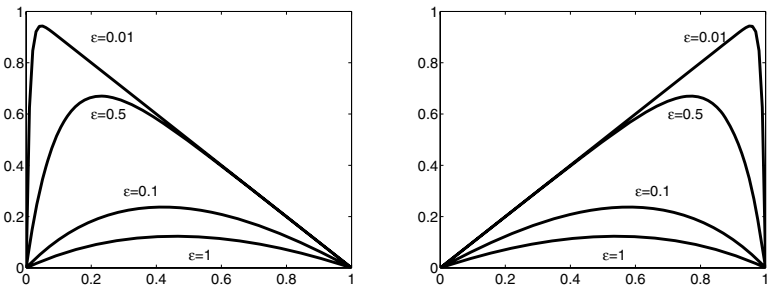

Fig. 4.6. Solution of the convection–diffusion problem for (a) $\lambda = -1$ and (b) $\lambda = 1$.

Solution of Exercise 4.2

1. The linear space $\mathcal{V}_1^h$ is of dimension n since there is an obvious isomorphism from this space onto $\mathbb{R}^n$: to each $u = (u_1, \ldots, u_n)^T \in \mathbb{R}^n$ corresponds a function $v \in \mathcal{V}_1^h$ defined by $v(x_i) = u_i$. From the identities $\varphi_{h,k}^{(1)}(x_j) = \delta_{j,k}$, we deduce that the functions $(\varphi_{h,k}^{(1)})_{k=1}^n$ are linearly independent:

$$\left(\sum_{k=1}^n c_k \varphi_{h,k}^{(1)}(x) = 0, \forall x\right) \Longrightarrow \left(\sum_{k=1}^n c_k \varphi_{h,k}^{(1)}(x_j) = 0, \forall j\right) \Longrightarrow (c_j = 0, \forall j)\,.$$

   Since $\mathcal{V}_1^h$ is of dimension n, the $(\varphi_{h,k}^{(1)})_{k=1}^n$ form a basis. Here are analytical expressions for $\varphi_{h,k}^{(1)}$ and its derivative
   - for $x \notin I_{k-1} \cup I_k$, $\varphi_{h,k}^{(1)}(x) = \varphi_{h,k}^{(1)\prime}(x) = 0$,
   - for $x \in I_{k-1}$, $\varphi_{h,k}^{(1)}(x) = (x - x_{k-1})/h$ and $\varphi_{h,k}^{(1)\prime}(x) = 1/h$,
   - for $x \in I_k$, $\varphi_{h,k}^{(1)}(x) = (x_{k+1} - x)/h$ and $\varphi_{h,k}^{(1)\prime}(x) = -1/h$.
2. Since $(\varphi_{h,j}^{(1)})_{j=1}^n$ form a basis of $\mathcal{V}_1^h$, we can replace in (4.6) $v_h \in \mathcal{V}_1^h$ by v_h any element of the basis $(\varphi_{h,j}^{(1)})_{j=1}^n$.
3. Using again the identities $\varphi_{h,k}^{(1)}(x_j) = \delta_{j,k}$, we get

$$u_h^{(1)}(x_j) = \sum_{k=1}^n \alpha f_k \varphi_{h,k}^{(1)}(x_j) = \alpha_j.$$

   Replacing in (4.7) u_h by its expansion in the basis $\varphi_{h,k}^{(1)}$, we get

$$\sum_{k=1}^n a(\varphi_{h,k}^{(1)}, \varphi_{h,j}^{(1)})\alpha_k = \int_0^1 f\varphi_{h,j} dx, \quad \forall j = 1, \ldots, n.$$

   Let $A_h^{(1)}$ be the $n \times n$ matrix and $b_h^{(1)}$ the vector of $\mathbb{R}^n$ defined by

$$(A_h^{(1)})_{j,k} = a(\varphi_{h,k}^{(1)}, \varphi_{h,j}^{(1)}), \quad (b_h^{(1)})_j = \int_0^1 f\varphi_{h,j}^{(1)} dx.$$

   The vector $\tilde{u}_h = (\alpha_1, \ldots, \alpha_n)^T$ solves the linear system $A_h^{(1)}\tilde{u}_h^{(1)} = b_h^{(1)}$. The matrix of this system can be split as $A_h^{(1)} = \varepsilon B_h^{(1)} + \lambda C_h^{(1)}$, where

$$(B_h^{(1)})_{j,k} = \int_0^1 \varphi_{h,k}^{(1)\prime}\varphi_{h,j}^{(1)\prime} dx, \quad \text{and} \quad (C_h^{(1)})_{j,k} = \int_0^1 \varphi_{h,k}^{(1)\prime}\varphi_{h,j}^{(1)} dx.$$

   Note the symmetry of the first matrix $(B_h^{(1)})_{j,k} = (B_h^{(1)})_{k,j}$. Using an integration by parts and the fact that the basis functions are null for $x = 0$ and $x = 1$ yields $(C_h^{(1)})_{j,k} = -(C_h^{(1)})_{k,j}$. The matrices are tridiagonal since the supports of any two functions $\varphi_{h,j}^{(1)}$ and $\varphi_{h,k}^{(1)}$ are disjoint for $|j-k| > 1$.

4. Consider $x \in \mathbb{R}^n$ with components $(x_k)_{k=1}^n$. We get

$$\begin{aligned}\langle B_h^{(1)} x, x\rangle &= \sum_{k=1}^n (B_h^{(1)} x)_k x_k = \sum_{k=1}^n \sum_{j=1}^n (B_h^{(1)})_{k,j} x_j x_k \\ &= \sum_{k=1}^n x_k \sum_{j=1}^n x_j \int_0^1 {\varphi_{h,k}^{(1)}}'(x) {\varphi_{h,j}^{(1)}}'(x) dx \\ &= \int_0^1 \left(\sum_{k=1}^n x_k {\varphi_{h,k}^{(1)}}'(x) \right)^2 dx \geq 0.\end{aligned}$$

   Moreover, $\langle B_h^{(1)} x, x\rangle = 0$ implies that

$$\sum_{k=1}^n x_k {\varphi_{h,k}^{(1)}}'(x) = 0$$

   for all $x \in [0,1]$; thus the x_k are all zero. Consequently, the symmetric matrix $B_h^{(1)}$ is positive definite.

5. From the antisymmetry of the matrix $C_h^{(1)}$, we get

$$\left\langle C_h^{(1)} x, x \right\rangle = \left\langle x, {C_h^{(1)}}^T x \right\rangle = - \left\langle x, C_h^{(1)} x \right\rangle = - \left\langle C_h^{(1)} x, x \right\rangle,$$

   that is, $\langle C_h^{(1)} x, x\rangle = 0$, and the result follows.

Solution of Exercise 4.3

Numerical computation of the $P1$ solution.

1. Computation of A_h. Recall that the supports of two sufficiently distant basis functions $\varphi_{h,j}^{(1)}$ and $\varphi_{h,k}^{(1)}$ are disjoint. More precisely, defining $b_{k,j} = \int_0^1 {\varphi_{h,k}^{(1)}}' {\varphi_{h,j}^{(1)}}'$ and $c_{j,k} = \int_0^1 {\varphi_{h,k}^{(1)}}' \varphi_{h,j}$, we get
   - for $|k-j| > 1$, $b_{k,j} = c_{k,j} = 0$,
   - for $k = j$,

$$\begin{aligned} b_{k,k} &= \int_0^1 ({\varphi_{h,k}^{(1)}}')^2 = \int_{I_{k-1}} ({\varphi_{h,k}^{(1)}}')^2 + \int_{I_k} ({\varphi_{h,k}^{(1)}}')^2 = \frac{2}{h}, \\ c_{k,k} &= \int_0^1 {\varphi_{h,k}^{(1)}}' \varphi_{h,k} = \int_{I_{k-1}} {\varphi_{h,k}^{(1)}}' \varphi_{h,k} + \int_{I_k} {\varphi_{h,k}^{(1)}}' \varphi_{h,k} = 0, \end{aligned}$$

   - for $k = j+1$,

$$\begin{aligned} b_{j+1,j} = \quad b_{j,j+1} &= \int_0^1 {\varphi_{h,j+1}^{(1)}}' {\varphi_{h,j}^{(1)}}' = -\frac{1}{h}, \\ c_{j+1,j} = -c_{j,j+1} &= \int_0^1 {\varphi_{h,j+1}^{(1)}}' \varphi_{h,j} = -\frac{1}{2}. \end{aligned}$$

2. See the function `FEM_ConvecDiffAP1`.
3. Using the trapezoidal rule, we get

$$\begin{aligned}(b_h^{(1)})_k &= \int_0^1 f\varphi_{h,k}^{(1)}dx = \int_{x_{k-1}^{(1)}}^{x_k^{(1)}} f\varphi_{h,k}^{(1)}dx + \int_{x_k^{(1)}}^{x_{k+1}^{(1)}} f\varphi_{h,k}^{(1)}dx \\ &\approx \frac{h}{2}\left[f(x_{k-1}^{(1)})\varphi_{h,k}^{(1)}(x_{k-1}^{(1)}) + 2f(x_k^{(1)})\varphi_{h,k}^{(1)}(x_k^{(1)}) + f(x_{k+1}^{(1)})\varphi_{h,k}^{(1)}(x_{k+1}^{(1)})\right] \\ &= hf(x_k^{(1)}).\end{aligned}$$

   See the function `FEM_ConvecDiffbP1`.
4. The following MATLAB script returns the results displayed in Fig. 4.7:

```
eps=0.1;lambda=1;      %physical parameters
f = inline('ones(size(x))');%right-hand side of the equation
n=10;
A=FEM_ConvecDiffAP1(eps,lambda,n);  %matrix of the linear system
b=FEM_ConvecDiffbP1(n,f);     %right-hand side of the linear system
u=A\b;      %FEM solution
u=[0;u;0];        %add to u the boundary values
x=(0:n+1)/(n+1);  %mesh
uexa=FEM_ConvecDiffSolExa(eps,lambda,1,x);%exact solution computed on x
plot(x,uexa,x,u,'+-r')
```

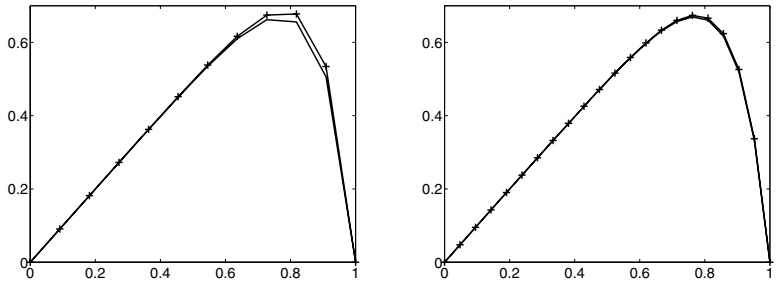

Fig. 4.7. Approximation of the convection–diffusion problem ($P1$ FEM), $\varepsilon = 0.1$, $\lambda = 1$, (a) $n = 10$ and (b) $n = 20$.

   For the tested values of λ and ε, we get a good approximation. This script is written in the file *FEM_ConvecDiffscript1.m*.
5. Analysis of the error. Figure 4.8 is generated by the following script

```
error=[ ];N=[ ];
for n=10:10:100
```

```
 A=FEM_ConvecDiffAP1(eps,lambda,n);
 b=FEM_ConvecDiffbP1(n,f);
 u=A\b;
 u=[0;u;0];
 x=(0:n+1)'/(n+1);
 uexa=FEM_ConvecDiffSolExa(eps,lambda,1,x);
 N=[N;n];error=[error; norm(uexa-u,'inf')];
end
plot(log(N),log(error),'+-');
```

We see in Fig. 4.8 a straight line of slope approximately -2. We deduce that $s_1 = 2$. If we refine the mesh twice, by changing h into $h/2$, the error is divided by $2^{s_1} = 4$.
See the script *FEM_ConvecDiffscript2.m*.

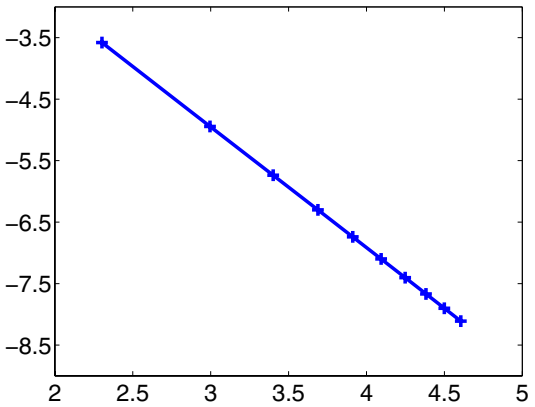

Fig. 4.8. Approximation of the convection–diffusion problem ($P1$ FEM). Logarithm of the error versus the logarithm of n ($\varepsilon = 0.1$, $\lambda = 1$).

Solution of Exercise 4.4

See the script *FEM_ConvecDiffscript3.m*.

```
eps=0.01;lambda=1;
f = inline('ones(size(x))');
yes=1;
while yes
    n=input('enter n : ');
    A=FEM_ConvecDiffAP1(eps,lambda,n);
    b=FEM_ConvecDiffbP1(n,f);
```

```
    u=A\b;
    u=[0;u;0];
    x=(0:n+1)/(n+1);
    uexa=FEM_ConvecDiffSolExa(eps,lambda,1,x);
    plot(x,uexa,x,u,'+-r')
    Peclet=abs(lambda)/2/eps/(n+1)
    yes=input('more ? yes=1, no=0 ')
end
```

Note that the approximation is good for a Peclet number $Pe < 1$.

Solution of Exercise 4.5

In the $P1$ method, the matrices $B_h^{(1)}$ and $C_h^{(1)}$ are tridiagonal. In the $P2$ method the supports of the basis functions are larger and the matrices $B_h^{(2)}$ and $C_h^{(2)}$ are pentadiagonal. As in the $P1$ case, we can prove that the matrix $B_h^{(2)}$ is symmetric, positive definite; the matrix $C_h^{(2)}$ is antisymmetric; and the matrix $A_h^{(2)}$ is invertible.

Solution of Exercise 4.6

The derivatives of the basis functions are

$$\varphi_{h,2k+1}^{(2)\,\prime}(x) = \begin{cases} -8(x - x_{2k+1}^{(2)})/h^2 & \text{for } x \in I_k, \\ 0 & \text{otherwise,} \end{cases}$$

and

$$\varphi_{h,2k}^{(2)\,\prime}(x) = \begin{cases} 4(x - x_{2k+3/2}^{(2)})/h^2 & \text{for } x \in I_k, \\ 4(x - x_{2k-1/2}^{(2)})/h^2 & \text{for } x \in I_{k-1}, \\ 0 & \text{otherwise.} \end{cases}$$

1. (a) Computation of $B_h^{(2)}$. Since the matrix is symmetric, only its upper triangular part is computed.
   - Rows with odd indices.
     - $(B_h^{(2)})_{2k+1,2k+1} = \int_0^1 [\varphi_{h,2k+1}^{(2)\,\prime}(x)]^2 dx = \int_{x_{2k}^{(2)}}^{x_{2k+2}^{(2)}} [\frac{8}{h^2}(x - x_{2k+1}^{(2)})]^2 dx = \frac{16}{3}\frac{1}{h}$,
     - $(B_h^{(2)})_{2k+1,2k+2} = -\frac{8}{3}\frac{1}{h}$,
     - $(B_h^{(2)})_{2k+1,m} = 0, \quad \forall m \geq 2k+3$.
   - Rows with even indices.
     - $(B_h^{(2)})_{2k,2k} = \frac{14}{3}\frac{1}{h}$,
     - $(B_h^{(2)})_{2k,2k+1} = -\frac{8}{3}\frac{1}{h}$,
     - $(B_h^{(2)})_{2k,2k+2} = \frac{1}{3}\frac{1}{h}$,
     - $(B_h^{(2)})_{2k,m} = 0, \quad \forall m \geq 2k+3$.

Thus, the upper triangular part of the matrix $B_h^{(2)}$ is

$$\frac{1}{3h}\begin{pmatrix} 16 & -8 & 0 & 0 & 0 & 0 & 0 \\ & 14 & -8 & 1 & 0 & 0 & 0 \\ & & 16 & -8 & 0 & 0 & 0 \\ & & & 14 & -8 & 1 & 0 \\ & & & & \ddots & \ddots & \ddots \\ & & & & & \ddots & \ddots \\ & & & & & & \ddots \end{pmatrix}.$$

(b) Computation of $C_h^{(2)}$. The matrix being antisymmetric, only its upper triangular part is computed.

- Rows with odd indices.
  - $(C_h^{(2)})_{2k+1,2k+1} = 0$,
  - $(C_h^{(2)})_{2k+1,2k+2} = \frac{2}{3}$,
  - $(C_h^{(2)})_{2k+1,m} = 0, \quad \forall m \geq 2k+3$.
- Rows with even indices.
  - $(C_h^{(2)})_{2k,2k} = 0$,
  - $(C_h^{(2)})_{2k,2k+1} = \frac{2}{3}$,
  - $(C_h^{(2)})_{2k,2k+2} = -\frac{1}{6}$,
  - $(C_h^{(2)})_{2k,m} = 0, \quad \forall m \geq 2k+3$.

Thus, the upper triangular part of the matrix $C_h^{(2)}$ is

$$\frac{1}{6}\begin{pmatrix} 0 & 4 & 0 & 0 & 0 & 0 & 0 \\ & 0 & 4 & -1 & 0 & 0 & 0 \\ & & 0 & 4 & 0 & 0 & 0 \\ & & & 0 & 4 & -1 & 0 \\ & & & & \ddots & \ddots & \ddots \\ & & & & & \ddots & \ddots \\ & & & & & & \ddots \end{pmatrix}.$$

2. See the function `FEM_ConvecDiffAP2` .
3. $(b_h^{(2)})_{2k+1} = \displaystyle\int_0^1 f\varphi_{h,2k+1}^{(2)} dx = \int_{x_{2k}^{(2)}}^{x_{2k+1}^{(2)}} f\varphi_{h,2k+1}^{(2)} dx + \int_{x_{2k+1}^{(2)}}^{x_{2k+2}^{(2)}} f\varphi_{h,2k+1}^{(2)} dx.$
Using Simpson's formula on each interval, we obtain

$$\left(b_h^{(2)}\right)_{2k+1} \approx \frac{2}{3} h f\left(x_{2k+1}^{(2)}\right).$$

In the same way, $\left(b_h^{(2)}\right)_{2k} \approx \frac{1}{3} h f\left(x_{2k}^{(2)}\right)$. See the function`FEM_ConvecDiffbP2`.

4. As for Exercise 4.3, we plot in Fig. 4.9 the logarithm of the error versus the logarithm of n. The curve is a straight line of slope approximately -3.3. The error decreases faster than in the $P1$ case.
Remark. For a more relevant comparison of the methods $P1$ and $P2$, consider the following quantity:

$$\int_0^1 |u_h'(x) - u'(x)|^2 dx = \sum_{\text{intervals } I_k} \int_{I_k} |u_h'(x) - u'(x)|^2 dx.$$

We refer the reader to the references at the end of this chapter.

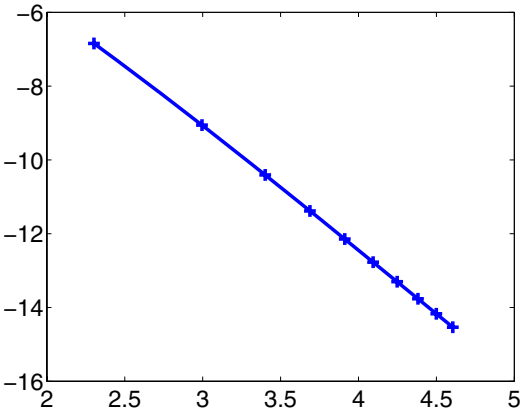

Fig. 4.9. Approximation of the convection–diffusion problem ($P2$ FEM). Logarithm of the error versus the logarithm of n ($\varepsilon = 0.1$, $\lambda = 1$).

Solution of Exercise 4.7

1. Let $x \in \mathbb{R}^n$ be a nonnull vector such that $(A - BD^{-1}C)x = 0$. The nonnull vector $y = (x^T, -(D^{-1}Cx)^T)^T \in \mathbb{R}^{2n+1}$ is such that $\widehat{A}_h^{(2)} y = 0$. However, the matrix $\widehat{A}^{(2)}$ is invertible. This leads to a contradiction. Hence the square matrix $A - BD^{-1}C$ is injective and consequently invertible.
2.

```
A=FEM_ConvecDiffAP2(eps,lambda,n);
a=A(2:2:2*n+1,2:2:2*n+1);b=A(2:2:2*n+1,1:2:2*n+1);
c=A(1:2:2*n+1,2:2:2*n+1);d=A(1:2:2*n+1,1:2:2*n+1);
```

3. The following script is written in the file *FEM_ConvecDiffscript4.m*:

```
n=10;eps=0.01;lambda=1;
f = inline(ones(size(x))');
sm=FEM_ConvecDiffbP2(n,f);
nsm=sm(2:2:2*n+1)-b*inv(d)*sm(1:2:2*n+1);
u=(a-b*inv(d)*c)\nsm;   %computation of v
x=linspace(0,1,100);
uexa=FEM_ConvecDiffSolExa(eps,lambda,1,x);
```

```
plot(x,uexa);hold on
plot((1:n)/(n+1),u,'+');hold off;
```

For $n = 10$ and $n = 20$, see Fig. 4.10.

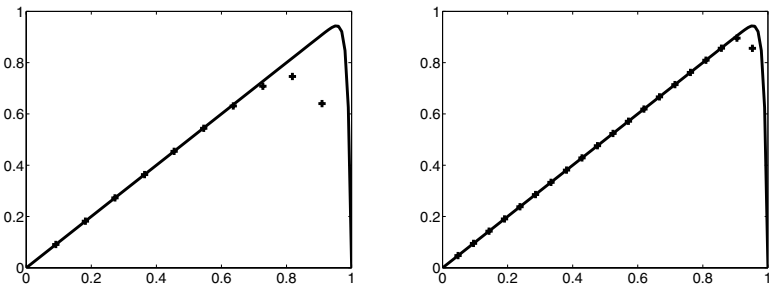

(a) (b)

Fig. 4.10. Stabilized solution of the convection–diffusion problem: $\lambda = 1$, $\varepsilon = 0.01$, and (a) $n = 10$ and (b) $n = 20$.

4. Figure 4.11 displays the stabilized solutions for $n = 20$ and the $P1$ solutions for $n \in \{20, 40, 60, 80\}$.

Solution of Exercise 4.8

1. With the same set of parameters and a constant f, we have observed a boundary layer. This is no longer true. We present some results in Fig. 4.12: the source term f transfers its oscillations to the solution u. Here is the script that produces Fig. 4.12. This script is written in the file *FEM_ConvecDiffscript5.m.*:

```
n=100;lambda=1;eps=0.01;
x=(0:(n+1))'/(n+1);
A=FEM_ConvecDiffAP1(eps,lambda,n);
X=[ ];Y=[ ];
h=1/(n+1);tab=(1:n)'*h;
for af=1:5
    b=h*cos(af*pi*tab);
    y=A\b;y=[0; y; 0];
     X=[X x];Y=[Y y];
end;
plot(X,Y);
```

For $a = \frac{3}{2}$, we observe a boundary layer; see Fig. 4.12. This observation is discussed in the next question.

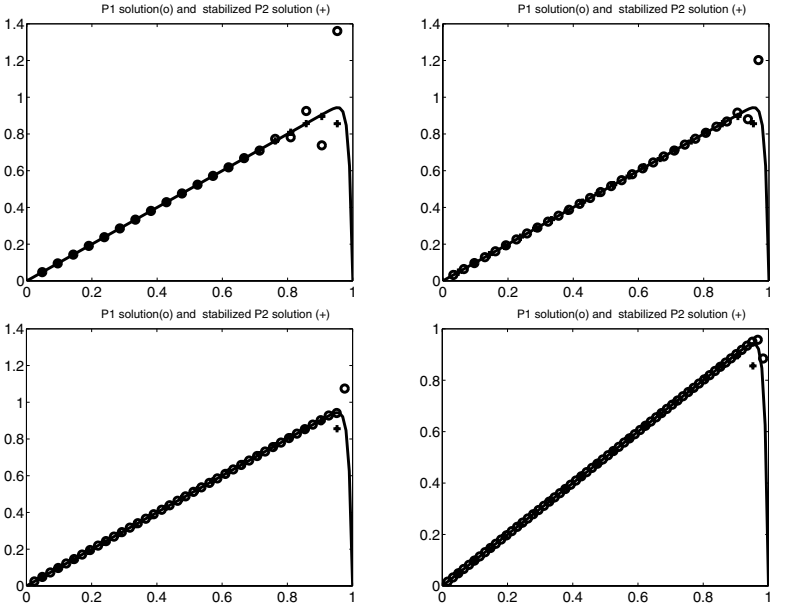

Fig. 4.11. Stabilized solution for $n = 20$ and the $P1$ solutions with $n = 20$ (top left), $n = 30$ (top right), $n = 40$ (bottom left), $n = 60$ (bottom right).

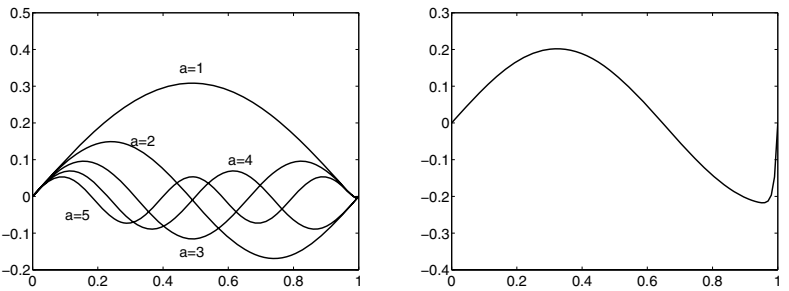

Fig. 4.12. Solution of the convection–diffusion equation: (a) $f(x) = \cos(a\pi x)$, for $a \in \{1, 2, 3, 4, 5\}$, (b) $f(x) = \cos(\frac{3}{2}\pi x)$.

2. Computation of the exact solution.
   (a) It is easy to check that $\alpha + \beta e^{\theta x} - \frac{1}{\varepsilon} F_\theta$ is a solution of the differential equation (4.1).
   (b) The boundary conditions $u(0) = 0$ and $u(1) = 0$ allow the determination of α and β,

$$\alpha = -\beta = \frac{1}{\varepsilon} \frac{F_\theta(1)}{1 - e^\theta},$$

and the solution is

$$u(x) = \frac{1}{\varepsilon(1-e^{\theta})}[(1-e^{\theta x})F_\theta(1) - (1-e^{\theta})F_\theta(x)]. \tag{4.14}$$

(c) $f(x) = \cos(a\pi x)$. Define $I = \int_0^z \cos(a\pi y)e^{-\theta y}dy$ and $J = \int_0^z \sin(a\pi y)e^{-\theta y}dy$. Computing the real part of $I + iJ$, we get

$$\int_0^z f(y)e^{-\theta y}dy = \frac{a\pi e^{-\theta z}\sin(a\pi z) + \theta - \theta e^{-\theta z}\cos(a\pi z)}{\theta^2 + \pi^2 a^2}$$

and deduce the identity

$$(\theta^2 + \pi^2 a^2)F_\theta(x) = e^{\theta x} - \cos(a\pi x) - \frac{\theta \sin(a\pi x)}{a\pi}.$$

The solution of the problem (4.1) is the sum of the two terms $-\frac{1}{\varepsilon}F_\theta(x)$ and $\alpha + \beta e^{\theta x}$.

- The first one can be split into three parts:
  - $\dfrac{1}{\varepsilon}\dfrac{\theta}{(\theta^2+\pi^2a^2)}\dfrac{\sin(a\pi x)}{a\pi}$, whose limit is $\dfrac{\lambda}{a\pi}\sin(a\pi x)$ for ε going to 0,
  - $\dfrac{1}{\varepsilon}\dfrac{\cos(a\pi x)}{(\theta^2+\pi^2a^2)}$, whose limit is 0,
  - and $\gamma_1 = -\dfrac{1}{\varepsilon}\dfrac{e^{\theta x}}{\theta^2+\pi^2a^2}$.
- The only term in $\alpha + \beta e^{\theta x}$ that does not go to 0 is $\gamma_2 = \dfrac{1}{\varepsilon}\dfrac{e^{\theta}}{\theta^2+\pi^2a^2}\dfrac{1-e^{\theta x}}{1-e^{\theta}}$.

Since the sum $\gamma_1 + \gamma_2$ goes to 0, we deduce that

$$\lim_{\varepsilon\to 0^+} u(x) = \frac{1}{\lambda a\pi}\sin(a\pi x).$$

3. The function u is continuous and satisfies the boundary condition $u(1) = 0$; hence

$$\lim_{\varepsilon\to 0^+}\lim_{x\to 1} u(x) = \lim_{\varepsilon\to 0^+} u(1) = 0.$$

In addition, $\lim_{x\to 1}\lim_{\varepsilon\to 0^+} u(x) = \frac{1}{\lambda a\pi}\sin(a\pi)$. Consequently, for an integer a, there is no boundary layer in the vicinity of $x = 1$ since $\lim_{x\to 1}\lim_{\varepsilon\to 0^+} u(x) = \lim_{\varepsilon\to 0^+}\lim_{x\to 1} u(x) = 0$. Conversely, for a noninteger value of a, there exists a boundary layer since $\lim_{x\to 1}\lim_{\varepsilon\to 0^+} u(x) \neq 0$.

Chapter References

K. Atkinson and W. Han, *Theoretical Numerical Analysis*, Springer, New York, 2001.

C. Bernardi, Y. Maday and F. Rapetti, *Discrétisations variationnelles de problèmes aux limites elliptiques, collection S.M.A.I. Mathématiques et Applications*, vol. 45, Springer, Paris, 2004.

F. Brezzi and A. Russo, *Choosing bubbles for advection-diffusion problems*, Math. Models and Meth. in Appl. Sci., vol. 4, no. 4, 1994.

I. Danaila, F. Hecht and O. Pironneau, *Simulation numérique en C++*, Dunod, Paris, 2003.

P. Joly, *Mise en œuvre de la méthode des éléments finis, collection S.M.A.I. Mathématiques et Applications*, Ellipses, Paris, 1990.

B. Lucquin and O. Pironneau, *Introduction to Scientific Computing*, Willey, Chichester, 1998.

5

Solving a Differential Equation by a Spectral Method

Project Summary

Level of difficulty:	2
Keywords:	Spectral method, polynomial approximation, Gauss quadrature, orthogonal polynomials, Legendre polynomials, variational formulation
Application fields:	Whenever high accuracy is required to compute smooth solutions of PDEs

Introduction

Spectral methods are approximation techniques for the computation of the solutions to ordinary and partial differential equations. They are based on a polynomial expansion of the solution. The precision of these methods is limited only by the regularity of the solution, in contrast to the finite difference method and the finite element methods. The approximation is based primarily on the variational formulation of the continuous problem. The test functions are polynomials and the integrals involved in the formulation are computed by suitable quadrature formulas. This project proposes to implement a spectral method to solve the following boundary value problem defined on the interval $\Omega = (-1, 1)$:

$$\begin{cases} -u'' + cu = f, \\ u(-1) = 0, \\ u(1) = 0, \end{cases} \tag{5.1}$$

with $f \in L^2(\Omega)$ and c a positive real number.

The first part of the project consists in pointing out some properties of the Legendre polynomials. These polynomials will be used to design a basis of the

approximation space. In the second part, we define the Legendre expansion of a function and compute the truncated Legendre expansion. To this end, we introduce a method to compute the integrals accurately, namely the Gauss quadrature formula. Finally, in the third part of the project, we implement the approximation of the differential equation (5.1) by a spectral method.

5.1 Some Properties of the Legendre Polynomials

Let $\mathbb{P}_n$ denote the set of all polynomials with degree less than or equal to a positive integer n and $(L_n)_{0\leq n}$ the family of Legendre polynomials. Note that these polynomials form an orthogonal basis on $]-1,1[$ since for all integers n and m,

$$\int_{-1}^{1} L_n(x)L_m(x)dx = \frac{2}{2n+1}\delta_{n,m}. \tag{5.2}$$

The Legendre polynomials are solutions of the differential equations

$$[(1-x^2)L_n'(x)]' + n(n+1)L_n(x) = 0, \qquad n \geq 0, \tag{5.3}$$

and they satisfy the following three-term recurrence formula

$$\begin{cases} L_0(x) = 1, \\ L_1(x) = x, \\ (n+1)L_{n+1}(x) = (2n+1)xL_n(x) - nL_{n-1}(x), \quad \text{for } n \geq 1, \end{cases} \tag{5.4}$$

from which we deduce the special values $L_n(\pm 1) = (\pm 1)^n$.

Exercise 5.1. 1. Write a function `y=SPE_LegLinComb(x,c)` that plots a linear combination of the Legendre polynomials of the form

$$y(x) = \sum_{k=1}^{p} c_k L_{k-1}(x). \tag{5.5}$$

The inputs of the program are:
- an array (a vector) `c` that contains the coefficients c_k,
- an array `x` that contains the points of the grid.

2. Write a script using `y=SPE_LegLinComb(x,c)` with `x` corresponding to a fine discretization of the interval $[-1,1]$ and `c` corresponding to the combination $L_0 - 2L_1 + 3L_5$. Plot `y` as a function of `x` as in Fig. 5.1.

A solution of this exercise is proposed in Sect. 5.6. at page 120.

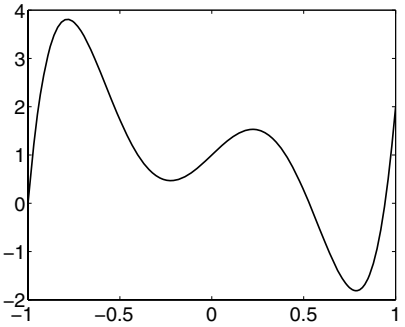

Fig. 5.1. Linear combination $L_0 - 2L_1 + 3L_5$.

5.2 Gauss–Legendre Quadrature

Numerical quadratures (or rules) are efficient tools for computing an approximation of an integral (see Krommer and Ueberhuber (1994)). In the general case, no antiderivative of the integrand is available, but the values of the integrand itself can be easily computed. Gauss quadrature is based on the following result, holding for smooth functions φ:

$$\int_{-1}^{1} \varphi(x)dx = \sum_{i=1}^{s} \varphi(x_i)\omega_i + R_s(\varphi), \tag{5.6}$$

where

1. the points x_i (called the *nodes* of the formula) are the zeros of the Legendre polynomial L_s,
2. the real numbers ω_i (called the *weights* of the formula) are given by

$$\omega_i = \frac{2}{(1 - x_i^2)[L_s'(x_i)]^2}. \tag{5.7}$$

3. The remainder is $R_s(\varphi) = \dfrac{2^{2s+1}(s!)^4}{(2s+1)[(2s)!]^3}\varphi^{(2s)}(\xi)$, for $\xi \in (-1, 1)$.

The Gauss–Legendre quadrature formula is the approximation

$$\int_{-1}^{1} \varphi(x)dx \approx \sum_{i=1}^{s} \varphi(x_i)\omega_i. \tag{5.8}$$

This formula is exact for $\varphi \in \mathbb{P}_{2s-1}$, since in such a case the remainder $R_s(\varphi)$ is null.

In order to use the Gauss quadrature formula, we explain an efficient way to compute its weights and nodes. For all x, the recurrence relations (5.4) for $j = 0, \ldots, s$ can be written in a compact matrix form,

$$Mu = xu + v, \tag{5.9}$$

where

$$M = \begin{pmatrix} 0 & 1 & & & \\ a_1 & 0 & b_1 & & \\ & \ddots & \ddots & \ddots & \\ & & a_{s-2} & 0 & b_{s-2} \\ & & & a_{s-1} & 0 \end{pmatrix}, \tag{5.10}$$

with $a_j = j/(2j+1)$, $b_j = (j+1)/(2j+1)$,

$$v = b_{s-1} L_s(x) \begin{pmatrix} 0 \\ \vdots \\ 0 \\ 1 \end{pmatrix}, \quad \text{and} \quad u = \begin{pmatrix} L_0(x) \\ \vdots \\ L_{s-1}(x) \end{pmatrix}. \tag{5.11}$$

Now let x be a zero of L_s; then $v = 0$ and the linear system (5.9) becomes

$$Mu = xu, \tag{5.12}$$

which means that *the zeros of L_s are the eigenvalues of the $s \times s$ tridiagonal matrix M*. To compute the weight ω_i with formula (5.7), the recurrence formula (5.4) can be combined with the following relation:

$$(1 - x^2) L_s'(x) = -sxL_s(x) + sL_{s-1}(x), \quad s \geq 1. \tag{5.13}$$

Since $L_s(x_i) = 0$, we get finally

$$\omega_i = \frac{2(1 - x_i^2)}{(sL_{s-1}(x_i))^2},$$

where $L_{s-1}(x_i)$ is computed by the recurrence formula (5.4).

Exercise 5.2.

1. Write a function `SPE_xwGauss` that computes the weights and nodes of a Gauss–Legendre quadrature formula. Compare your results for $s = 8$ with the table below:

x_i	w_i
±0.18343464249565	0.36268378337836
±0.52553240991633	0.31370664587789
±0.79666647741363	0.22238103445337
±0.96028985649754	0.10122853629036

2. Write a script to validate your function: test the quadrature formula on various integrals whose exact values are known. In particular, check the exactness of the formula for polynomials in $\mathbb{P}_{2s-1}$ and compare the exact and approximate values of the integral of e^x on $(-1, 1)$.

A solution of this exercise is proposed in Sect. 5.6. at page 121.

5.3 Legendre Expansions

We now associate to a function $f \in L^2(-1,1)$ its Legendre expansion

$$\mathcal{L}(f) = \sum_{j=0}^{\infty} \hat{f}_j L_j,$$

with the Legendre coefficients $\hat{f}_j$ defined by

$$\hat{f}_j = \frac{2j+1}{2} \int_{-1}^{1} f(x) L_j(x) dx. \tag{5.14}$$

We also define the truncated expansion (see Sect. 3.3 page 63)

$$\mathcal{L}_p(f) = \sum_{j=0}^{p} \hat{f}_j L_j.$$

This is an approximation of the function f, which is exact for polynomials in $\mathbb{P}_p$ since $(L_j)_{j=0}^p$ is an orthogonal basis of $\mathbb{P}_p$. The calculation of the coefficients $\hat{f}_j$ is done by a quadrature formula. The error induced by this approximation of $\hat{f}_j$ must be of the same order or negligible compared to the total error of the spectral method. Thus, it is necessary to use a high-order quadrature, and for this reason, the Gauss–Legendre quadrature is very suitable.

Exercise 5.3.

1. Write a script that computes the truncated Legendre expansion $\mathcal{L}_p(f)$ of a function f. The script includes the following steps:
   - Compute the nodes and weights of the Gauss–Legendre quadrature for a given s.
   - Compute the Legendre coefficients $(\hat{f}_k)_{k=0}^p$ (5.14) by the quadrature formula (5.8).
   - Plot the function and its truncated Legendre expansion $\mathcal{L}_p(f)$ on $[-1,1]$.
2. Compare with the example in Fig. 5.2.
3. Justify the choice of the Gauss quadrature parameter s as a function of the degree p of the truncated series.
4. Test the script with less-regular functions, namely the functions `abs(x)` and `sign(x)`.
5. Plot the error (computed in the supremum norm) between f and $\mathcal{L}_p(f)$ as a function of the truncation parameter p.

A solution of this exercise is proposed in Sect. 5.6. at page 122.

The choice of the number s of Gauss nodes is related to the degree p of the truncated expansion. The quadrature formula (5.8) with s nodes is exact

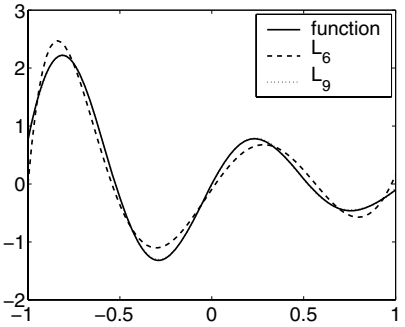

Fig. 5.2. Function $f(x) = \sin(6x)\exp(-x)$, $\mathcal{L}_6(f)$, and $\mathcal{L}_9(f)$.

on $\mathbb{P}_{2s-1}$. In addition, every polynomial $f \in \mathbb{P}_p$ is its own Legendre series $f = \mathcal{L}_p(f)$. In order to make the computation of the Legendre coefficients exact for $f \in \mathbb{P}_p$, it is necessary to take s such that $2s - 1 \geq 2p$, that is, $s \geq p + 1$. The reader will verify that for a very smooth function, let us say $f \in C^\infty(-1, 1)$, the error $f - \mathcal{L}_p(f)$ decreases to zero as p goes to infinity. This decreasing is faster than any power of $1/p$, as shown in Fig. 5.3. In this figure, the error stops decreasing from $p \approx 20$, since the computer accuracy is then reached. In contrast, running the same script for the nonsmooth function $|x|$

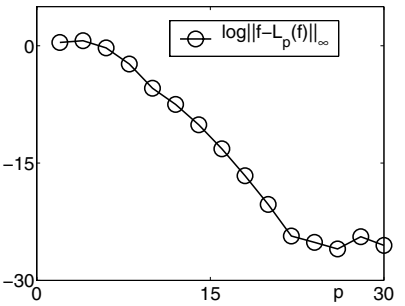

Fig. 5.3. Error $\|f - \mathcal{L}_p f\|_\infty$ for $f(x) = \sin(6x)\exp(-x)$.

exhibits a very slow convergence, displayed in Fig. 5.4. For the discontinuous function `sign`, the expansion does not converge to f in the norm L^∞, although it does converge in the L^2 norm. The truncated series $\mathcal{L}_p f$ has oscillations. As p increases, the size of the oscillations decreases slowly, except near the discontinuity $x = 0$, where the oscillations remain. This problem is known as the Gibbs phenomenon. The results for functions $|x|$ and $\text{sign}(x)$ are displayed in Fig. 5.5.

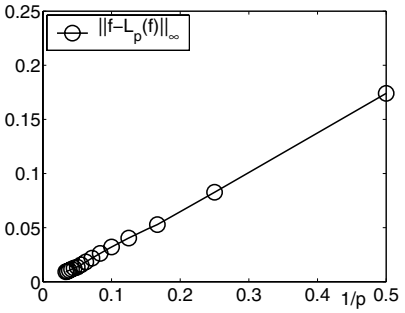

Fig. 5.4. Error $\|f - \mathcal{L}_p f\|_\infty$ for $f(x) = |x|$.

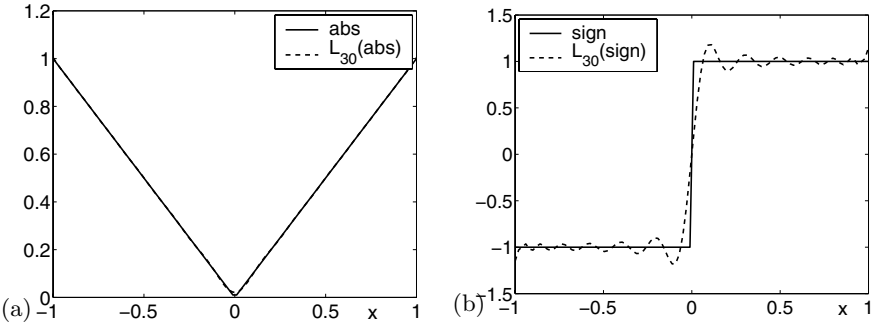

Fig. 5.5. Comparison of f with $\mathcal{L}_{30} f$. (a) $f(x) = |x|$; (b) $f(x) =$sign(x).

5.4 A Spectral Discretization

We consider a *variational formulation* of the problem (5.1) (see Chap. 4):

$$\begin{cases} \text{Find } u \in H_0^1(-1,1) \text{ such that for all } v \in H_0^1(-1,1): \\ \displaystyle\int_{-1}^{1} u'(x)v'(x)dx + c\int_{-1}^{1} u(x)v(x)dx = \int_{-1}^{1} f(x)v(x)dx. \end{cases} \tag{5.15}$$

Every regular solution of (5.15) is a solution to the problem (5.1). The space of test functions for this spectral method is the subset of $\mathbb{P}_m$ defined by

$$\mathbb{P}_m^0(\Omega) = \{p \in \mathbb{P}_m, p(-1) = p(1) = 0\}.$$

This linear space has dimension $m-1$ and can be rewritten as

$$\mathbb{P}_m^0(\Omega) = \{p = (1-x^2)q, \quad q \in \mathbb{P}_{m-2}\}.$$

Since $\mathbb{P}_m^0(\Omega)$ is included in $H_0^1(\Omega)$, we can easily define the variational approximation called the *spectral Galerkin method*:

$$\begin{cases} \text{Find } u_m \in \mathbb{P}_m^0(\Omega) \text{ such that for all } v_m \in \mathbb{P}_m^0(\Omega): \\ \displaystyle\int_{-1}^{1} u_m'(x)v_m'(x)dx + c\int_{-1}^{1} u_m(x)v_m(x)dx = \int_{-1}^{1} f(x)v_m(x)dx. \end{cases} \tag{5.16}$$

The functions $F_i = (1-x^2)L_i'$ for $i = 1, \ldots, m-1$ form a basis of $\mathbb{P}_m^0(\Omega)$. We denote this basis by $\mathcal{F}_m$. By linearity, the problem (5.16) is equivalent to the problem

$$\begin{cases} \text{Find } u_m \in \mathbb{P}_m^0(\Omega) \text{ such that for all } F_i \in \mathcal{F}_m : \\ \displaystyle\int_{-1}^{1} u_m'(x)F_i'(x)dx + c\int_{-1}^{1} u_m(x)F_i(x)dx = \int_{-1}^{1} f(x)F_i(x)dx. \end{cases} \tag{5.17}$$

Let $\bar{u}_m = (u_{m,1}, \ldots, u_{m,m-1})^T$ be the vector whose entries are the coefficients of u_m in the basis $\mathcal{F}_m$:

$$\bar{u}_m = \sum_{i=1}^{m-1} u_{m,i}F_i. \tag{5.18}$$

By plugging this expansion into (5.17), we get a linear system for $\bar{u}_m$, which we write in matrix form as

$$A_m\bar{u}_m = b_m, \tag{5.19}$$

where the $(m-1)\times(m-1)$ matrix A_m and the vector $b_m \in \mathbb{R}^{m-1}$ are defined by

$$\begin{aligned} (A_m)_{i,j} &= \frac{[i(i+1)]^2}{i+1/2}\delta_{i,j} \\ &\quad + c\frac{i(i+1)}{(2i+1)}\frac{j(j+1)}{(2j+1)}\left(\frac{4(2i+1)\delta_{i,j}}{(2i-1)(2i+3)} - \frac{2\delta_{i,j-2}}{2i+3} - \frac{2\delta_{i,j+2}}{2i-1}\right), \\ (b_m)_i &= \int_{-1}^{1} f(x)F_i(x)dx = \frac{2i(i+1)}{2i+1}\left(\frac{1}{2i-1}\hat{f}_{i-1} - \frac{1}{2i+3}\hat{f}_{i+1}\right). \end{aligned}$$

The terms $\hat{f}_i$ in the previous definition are the Legendre coefficients of the right-hand-side function f defined by (5.14).

Once the linear system is solved (*i.e.*, the coefficients of u_m in the basis $\mathcal{F}_m$ are known), the coefficients of u_m in the Legendre basis $(L_j)_{j=0}^m$ are computed using the identities

$$(1-x^2)L_i' = \frac{i(i+1)}{2i+1}\left(L_{i-1} - L_{i+1}\right). \tag{5.20}$$

Exercise 5.4.

1. Write a program including the following steps:
   - Compute the matrix A_m and the vector b_m. This step includes the computation of the Legendre coefficients $\hat{f}_k$ of the source term of the differential equation.
   - Solve the linear system (5.19).
   - Compute the Legendre coefficients $\hat{u}_{m_k}$ of the numerical solution u_m using (5.20).

- Plot on the same figure the function u and the numerical approximation u_m on $[-1, 1]$.

2. Construction of an exact solution: take any reasonable function $u_e(x)$ such that $u_e(-1) = u_e(1) = 0$ and compute $f(x)$ in such a way that u_e solves the problem (5.1) with a constant c. Program the two functions $u_e(x)$ and $f(x)$. The function u_e will be used as a benchmark to compare the spectral solution and the exact solution.
3. Advantages of the method: compare the spectral solution to a solution computed by a finite difference scheme leading to a linear system of identical dimension (see Section 8.2). Do you obtain the same precision? Compute the error between the exact solution and the spectral one. Increase the number of points in the finite difference discretization to get the same precision. Draw some conclusion on the respective advantages of the two methods.

A solution of this exercise is proposed in Sect. 5.6. at page 122.

5.5 Possible Extensions

The paragraph on the quadrature rules has several extensions. One can use a similar method to compute the nodes and weights of Gauss quadrature corresponding to other families of orthogonal polynomials. For example, the analogous formula to (5.6) for integrals on the real line $\mathbb{R}$ is

$$\int_{-\infty}^{+\infty} f(x)e^{-x^2}dx = \sum_{i=1}^{n} \omega_i f(x_i) + R_n(f). \tag{5.21}$$

Here the nodes x_i are the zeros of the Hermite polynomials (see below), the weights ω_i are given by (see (Davis, 1975; Szegő, 1975))

$$\omega_i = \frac{2^{n-1}n!\sqrt{\pi}}{\left(nH_{n-1}(x_i)\right)^2},$$

and the remainder is

$$R_n(f) = \frac{n!\sqrt{\pi}}{2^n(2n)!} f^{(2n)}(\xi).$$

The Hermite polynomials are defined by

$$\begin{cases} H_0(x) = 1, \\ H_1(x) = 2x, \\ 2xH_n(x) = H_{n+1}(x) + 2nH_{n-1}(x). \end{cases}$$

They are orthogonal for the inner product

$$\langle f, g \rangle = \int_{\mathbb{R}} f(x)g(x)e^{-x^2}dx.$$

Regarding the application of spectral methods to PDEs, one can think to generalize the example studied here in higher dimensions. Up to dimension two or three, the main feature of spectral methods is still the approximation by high-degree polynomials, using this time tensor products of polynomial bases. These objects have a high precision and turn out to be very efficient for simple geometries: rectangular prism or cylinder, for instance. The treatment of the Laplace equation in a square or cubic domain is thoroughly detailed in Bernardi, Dauge, and Maday (1999) and in the recent work by Bernardi, Maday, and Rapetti (2004) (in French), with several possible types of boundary conditions (Dirichlet, Neumann, and Fourier). For complicated geometries, a domain decomposition technique is required (see for instance Wohlmuth (2001)). Detailed problems are also proposed in Bernardi and Maday (1997) and Bernardi, Maday, and Rapetti (2004), which can be handled starting from the case treated in this project, such as for instance the spectral discretization of the Dirichlet problem in an axisymmetric domain or the heat equation in one dimension.

5.6 Solutions and Programs

Solution of Exercise 5.1
The computation of the linear combination (5.5) is performed by the function `SPE_LegLinComb`. In order to compute the values of the Legendre polynomial of degree p at points $x_1, \ldots, x_n$, there is no need to store all the values of the polynomials of degree less than p. Only the values corresponding to degrees $p-1$ and $p-2$, which come into play in the recurrence relation (5.4), must be stored in two arrays `pol1` and `pol2`, along with the current values that are stored in `pol`. The values of the linear combination are stored in an array `y` to which the terms $c_i p_i(x)$ are added as they are computed.

The graphical display of $L_0 - 2L_1 + 3L_5$ on the interval $[-1, 1]$ (see Fig. 5.1) is done in the script *SPE_PlotLegPol.m*. The function `SPE_LegLinComb` receives in its input argument the array $[0; -2; 0; 0; 0; 3]$ containing the coefficient values of the linear combination along with the points $x_i = -1 + (i-1)/250$ for $i = 1, \ldots, 501$ at which this function must be displayed.

The MATLAB built-in function `L=legendre(n,x)` computes an array `L` with $n+1$ rows, whose $(m+1)$th row holds the values of the Legendre function L_n^m defined by

$$L_n^m(x) = (-1)^m (1-x^2)^{m/2} \frac{d^m}{dx^m} L_n(x), \tag{5.22}$$

at points specified by the vector x. Therefore it is possible to compute the values of the Legendre polynomial with this function using only the first row of the computed array. Another method to compute the linear combination is to call the function `legendre` for all degrees from 0 up to p, to extract

for each degree the first row of the output array, and to multiply it by the corresponding coefficient.

The script `SPE_PlotLegPol` compares the computing times required by the two methods, by calling the function `tic` before the function `SPE_LegLinComb` and the function `toc` right afterward. The value returned by `toc` contains the computing time in seconds. The same thing is done again before and after the group of commands for the method using the `legendre` function. In order to get meaningful computing time estimates, it is best to increase the number of computing points to 500 points evenly spaced on the interval $[-1, 1]$ and to increase simultaneously the degree of the linear combination to 50. The ratio between the computing times is then higher than 100, which is unquestionably in favor of the script *SPE_LegLinComb.m*. Using the function `legendre` in this context implies a great number of redundant or useless computations.

Solution of Exercise 5.2

The computation of Gauss abscissas and integration weights is done by the function `SPE_xwGauss`. The abscissas are the eigenvalues of the matrix M defined by (5.10); the function therefore starts by building the matrix and using the MATLAB built-in function `eig` to compute its spectrum.

Once the abscissas and weights are computed and stored in two column vectors `x` and `w`, the quadrature formula (5.8) is encoded with a single MATLAB command. It consists in computing the scalar product of the vector `w` with the vector holding the values of the function at the integration abscissas `x`: `I=w'*f(x);`

The script *SPE_TestIntGauss.m* tests the quadrature formula on a smooth function, here the function e^x, and also compares this integration method with the method proposed by MATLAB, which is programmed in the built-in function `quad`.

The calling syntax is: `q = quad(@fun,a,b)`. This command returns the value of the integral of the function defined in *fun.m* between the bounds `a` and `b` to a default precision of 10^{-6}. The algorithm used in `quad` is the adaptive version of Simpson's rule (see (4.5) in Chap. 4), and one can specify the required precision by adding a fourth input argument `q = quad(@fun,a,b,preci)`. It is also possible to get in the output the number of calls to the integrand that were performed: `[q,nb ] = quad(@fun,a,b,preci)`.

In order to compare the computing time performances of the function `quad` with the Gauss method, we use for the latter a number of points large enough to obtain the value of the integral with six significant digits. Four points are sufficient in the case of the function e^x, for instance. The respective computing times are estimated using functions `tic` and `toc` as in the previous exercise. Simpson's method being less accurate than the Gauss quadrature on four points, it requires more evaluations of the integrand and is therefore slower. Hence in the context of our project, where a great number of integrals must be performed, using Gauss quadrature is more suitable.

Solution of Exercise 5.3
The comparison of the function with its truncated Legendre expansion is performed in the script *SPE_AppLegExp.m*. It produces Fig. 5.2, where the function $f(x) = \sin(6x)\exp(-x)$ is displayed along with $\mathcal{L}_6(f)$ and $\mathcal{L}_9(f)$. Slight modification produces Fig. 5.5 (a), where the function $f(x) = |x|$ is compared with its truncated series $\mathcal{L}_p f$ to order $p = 30$, and Fig. 5.5 (b), for $f(x) = \text{sign}(x)$.

This script calls the function `SPE_CalcLegExp`, which receives in its input arguments:

- `s`: the degree of the Gauss quadrature to be used to compute the coefficients of the expansion (5.14),
- `P`: the degree of the truncated expansion,
- `npt`: the number of points in the interval $[-1, 1]$ where the expansion is computed,
- `test`: the name of the function whose expansion is computed, which should be defined either by an `inline` function or in a file.

The function returns the output arguments:

- `x`: the `npt` abscissas,
- `y`: the values of the expansion at abscissas `x`,
- `err`: the error in the supremum norm between the function and its expansion, estimated on the values at abscissas `x`.

This function is also used in the script *SPE_LegExpLoop.m* to answer question 5 of the exercise, illustrated in Figs. 5.3 and 5.4. The Legendre expansion of a test function and the error with the function itself is computed for different degrees, varying here between 2 and 30 with an increment of 2. The error in the norm L^∞ is then displayed as a function of the degree of the truncated expansion. For a smooth function we expect exponential behavior for the error, which is actually what we obtain numerically for the function $f(x) = \sin(6x)\exp(-x)$. For less-smooth functions, for instance $f(x) = \text{abs}(x)$, the error decreases proportionally with $1/P$. Eventually, for a discontinuous function, such as $f(x) = \text{sign}(x)$, the error does not go to 0 when the degree of the expansion increases, due to the Gibbs phenomenon (see Fig. 5.5).

Solution of Exercise 5.4
We select here as a test case the function $u(x) = \sin(\pi x)\cos(10x)$, which satisfies the homogeneous Dirichlet boundary conditions $u(-1) = u(1) = 0$, and we program it in *SPE_special.m*. By setting the right-hand side to

$$f(x) = (\pi^2 + 130)\sin(\pi x)\cos(10x) + 20\pi\cos(\pi x)\sin(10x)$$

and the constant $c = 30$, the function u is a solution of problem (5.1). The right-hand side is programmed in the file *SPE_fbe.m*, using the second derivative of the solution function, which is programmed in *SPE_specsec.m*. The

following script *SPE_SpecMeth.m* computes the numerical solution using the spectral Galerkin method. It then compares it with the solution computed using the finite difference solution:

```
m=16;   % degree of  Legendre approximation
s=m+1;  % degree of Gauss quadrature for the right-hand side.
global c
c=30.;
% Construction of the matrix
A=zeros(m,m);
for i=1:m
 A(i,i)=(i*(i+1))^2*(1./(0.5+i)+...
                          4.*c/((2.*i+1.)*(2*i-1)*(2*i+3))) ;
end
for i=1:m-2
 A(i,i+2)=-2*c*i*(i+1)*(i+2)*(i+3)/((2*i+1)*(2*i+3)*(2*i+5));
end
for i=3:m
 A(i,i-2)=-2*c*i*(i+1)*(i-2)*(i-1)/((2*i-1)*(2*i-3)*(2*i+1));
end
% Construction of the right-hand-side vector
[absc,weights]=SPE_xwGauss(s);
t=SPE_fbe(absc); u=t.*weights;
LX0=ones(s,1);
LX1=absc;
C=zeros(m+2,1);
C(1)=t'*weights/2; C(2)=3*u'*LX1/2;
for k=2:m+1
  % computes $f_k$ in c(k+1)
  % computes values of  $L_k$ at integration abscissa
  % kL_k=(2k-1)xL_k-1 -(k-1)L_k-2
    LX2=((2*k-1)*absc.*LX1-(k-1)*LX0)/k;
    C(k+1)=(2*k+1)*u'*LX2/2;
    LX0=LX1;
    LX1=LX2;
end
B=zeros(m,1);
for i=1:m
  B(i)=2*i*(i+1)*(C(i)/(2*i-1)-C(i+2)/(2*i+3))/(2*i+1);
end
% Solves the linear system
U=linsolve(A,B);
%
% Change of basis
```

```
% (1-x^2)L_i'=(i(i+1)/(2i+1)).(L_i-1 - L_i+1
UN=zeros(1,m+2);
for k=1:m
  CC=(k+1)*k*U(k)/(2*k+1);
  UN(k)=UN(k)+CC;
  UN(k+2)=UN(k+2)-CC;
end
%
% Computes approximate solution and error
%
n=100;
xa=linspace(-1,1,n);
y=SPE_LegLinComb(xa,UN);
es=norm(y-SPE_special(xa),inf);
%
% Computes finite difference solution
mdf=50; h=2/mdf;
xdf=linspace(-1+h,1-h,mdf-1)';
A=toeplitz([2,-1,zeros(1,mdf-3)])/h^2+c*eye(mdf-1,mdf-1);
B=SPE_fbe(xdf); ydf=linsolve(A,B);
%
% Graphical display
%
plot (xa,SPE_special(xa),xa,y,'--',xdf,ydf,'x')
legend('exact','spectral','Finite diff.')
fprintf('erreur spectral= %e finite diff.= %e ',...
                    es,norm(ydf-SPE_special(xdf),inf));
```

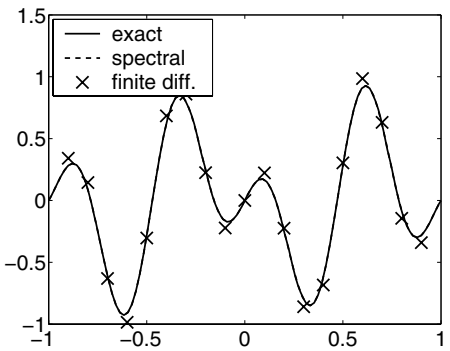

Fig. 5.6. Comparison of the exact, spectral, and finite difference solutions.

Figure 5.6 is obtained with the script *SPE_SpecMeth.m*. It displays the exact solution, the spectral solution in $\mathbb{P}_{21}^0$, and the finite difference solution on 20 points (set `m=21` and `mdf=20` in the script).

It is clear that in this example, the spectral method is much more accurate than the finite difference one, since the approximate solution in $\mathbb{P}_{21}^0$ cannot be distinguished from the exact one. The error in the supremum norm is 5.10^{-5} when it is equal to 6.10^{-2} for the finite difference solution. Furthermore, a finite difference computation using about 800 points would be necessary to obtain the same order of error as with the spectral method.

On the other hand, as soon as the solution of the continuous problem is not regular enough, the performance of the spectral method in terms of accuracy drops and becomes comparable, and even in some cases worse than, the performance of the finite difference method. The reader can easily verify this fact by building another test case, where the right-hand side f of equation (5.1) corresponds to a solution whose second derivative is a step function.

Chapter References

C. Bernardi, M. Dauge, and Y. Maday, *Spectral methods for axisymmetric domains. Numerical algorithms and tests due to Mejdi Azaiez*, Series in Applied Mathematics, 3. Gauthier-Villars, North-Holland, Amsterdam, 1999.

C. Bernardi and Y. Maday, *Spectral Methods* in Handbook of numerical analysis, Vol. V, North-Holland, Amsterdam, 1997.

C. Bernardi, Y. Maday, and F. Rapetti, *Discrétisations variationnelles de problèmes aux limites elliptiques*, Mathématiques & Applications, Vol. 45, Springer-Verlag, Mai 2004.

P. J. Davis, *Interpolation and Approximation*, Dover Publications, Inc., New York, 1975.

A. R. Krommer and C. W. Ueberhuber, *Numerical Integration on Advanced Computer Systems*, Lecture Notes in Computer Science, 848, Springer-Verlag, Berlin, 1994.

G. Szegő, *Orthogonal Polynomials*, fourth edition, American Mathematical Society, Colloquium Publications, Vol. XXIII, Providence, R.I., 1975.

B. I. Wohlmuth, *Discretization Methods and Iterative Solvers Based on Domain Decomposition*, Lecture Notes in Computational Science and Engineering, 17, Springer-Verlag, Berlin, 2001.

6

Signal Processing: Multiresolution Analysis

Project Summary

Level of difficulty:	1
Keywords:	Approximation, multiresolution analysis, wavelets
Application fields:	Signal processing, image processing

6.1 Introduction

This chapter is devoted to a short introduction to multiresolution analysis (MRA). This is a very promising field in mathematics, with numerous theoretical and practical developments in engineering applications. Over the past two decades, wavelet functions have proven to be a very efficient tool for dealing with problems arising from data compression, and signal and image processing. Famous examples of applications are the FBI fingerprint database, and the new image coding standard MPEG3.

6.2 Approximation of a Function: Theoretical Aspect

6.2.1 Piecewise Constant Functions

In this section we introduce the basic ideas of multiresolution analysis. Let Ω be the interval $[0, 1[$, and consider a function $f \in L^1(\Omega)$. For any arbitary fixed integer $j \geq 0$ we define the intervals $\Omega_j^k = [2^{-j}k, 2^{-j}(k+1)[$ for $k = 0, 1, \ldots, 2^j - 1$. We then approximate the function f by its projection $P_j f$ onto the family of functions constant on intervals Ω_j^k (see Fig. 6.2). The value of $P_j f$ on Ω_j^k is computed as

$$P_j^k f = 2^j \int_{\Omega_j^k} f(t)\, dt, \quad \text{for } k = 0, 1, \ldots, 2^j - 1.$$

We also introduce $\phi = \chi_{[0,1[}$, the characteristic function[1] of Ω, and note first that ϕ satisfies the following property, known as *the two-scale relation*:

$$\forall x \in \Omega, \quad \phi(x) = \phi(2x) + \phi(2x - 1). \tag{6.1}$$

This relation is "plotted" in Fig. 6.1.

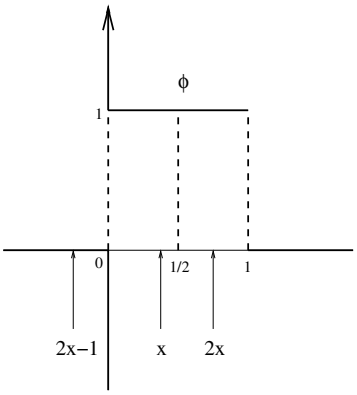

Fig. 6.1. The two-scale relation (Haar basis).

We remark that $x \mapsto \phi(2^j x - k)$ is the characteristic function of the interval $\Omega_j^k = \left[2^{-j}k, 2^{-j}(k+1)\right[$, and we redefine $P_j f$ as

$$\forall x \in \Omega, \quad P_j f(x) = \sum_{k=0}^{2^j - 1} P_j^k f \phi(2^j x - k).$$

Since Ω is a bounded domain, $f \in L^1(\Omega)$ whenever $f \in L^2(\Omega)$, and $P_j f$ is then an element of the vector space

$$V_j = \left\{ f \in L^2(\Omega),\ f_{|\Omega_j^k} \text{ is constant, for } k = 0, 1, \ldots, 2^j - 1 \right\}.$$

The space V_j has finite dimension $\dim V_j = 2^j$. For $k = 0, 1, \ldots, 2^j - 1$, we define the functions ϕ_j^k as

$$\forall x \in \Omega, \quad \phi_j^k(x) = 2^{j/2} \phi(2^j x - k). \tag{6.2}$$

[1] In the following, $\chi_{[a,b[}$ is the characteristic function of the interval $[a, b[$.

The 2^j functions ϕ_j^k span V_j, and are orthonormal relative to the L^2 scalar product: $\langle f, g\rangle = \int_\Omega f(t)g(t)\,dt$. Using this orthonormal basis, we can write

$$\forall x \in \Omega, \quad P_j f(x) = \sum_{k=0}^{2^j-1} \langle f, \phi_j^k\rangle \phi_j^k(x) = \sum_{k=0}^{2^j-1} c_j^k \phi_j^k(x),$$

where the coefficients c_j^k are the components of $P_j f$ in the $\{\phi_j^k\}_{k,j}$ basis; they are computed according to

$$c_j^k = \langle f, \phi_j^k\rangle = \int f(t)\phi_j^k(t)\,dt = 2^{j/2}\int_{\Omega_j^k} f(t)\,dt. \tag{6.3}$$

The application P_j is then the orthogonal projection onto V_j relative to the $L^2(\Omega)$ scalar product. Consider now two arbitrary integers $j' > j \geq 0$, and define as previously two spaces $V_{j'}$ and V_j. The basis functions $\{\phi_{j'}^{k'}\}_{k',j'}$ of the space $V_{j'}$ are constant on intervals $\Omega_{j'}^{k'}$ of length $2^{-j'}$, while the V_j basis functions $\{\phi_j^k\}_{k,j}$ are constant on intervals Ω_j^k of length $2^{-j} > 2^{-j'}$. Because $V_{j'} \subset V_j$, the function $P_{j'}f$ is a more accurate approximation of f than $P_j f$, in the sense that $\|P_{j'}f - f\|_2 < \|P_j f - f\|_2$. It can be proven that this approximation $P_j f$ converges to f in $L^2(\Omega)$ as j goes to infinity (see Fig. 6.2). Furthermore, when $f \in C^0(\Omega)$, the approximation $P_j f$ converges to f according to the uniform norm: $\lim_{j\to+\infty} \|f - P_j f\|_\infty = 0$.

For an arbitrary fixed integer $j \geq 0$, we consider now the two spaces V_j and V_{j+1}. From (6.1) we may write, for any $f \in L^2(\Omega)$ and for $k = 0, 1, \ldots, 2^j - 1$,

$$\sqrt{2}\int f(t)\phi_j^k(t)\,dt = \int f(t)\phi_{j+1}^{2k}(t)\,dt + \int f(t)\phi_{j+1}^{2k+1}(t)\,dt.$$

This leads to a first relation connecting the coefficients c_j^k and $c_{j+1}^{k'}$:

$$c_j^k = (c_{j+1}^{2k} + c_{j+1}^{2k+1})/\sqrt{2}, \text{ for } k = 0, 1, \ldots, 2^j - 1. \tag{6.4}$$

Remark 6.1. In the case of an unbounded domain ($\Omega = \mathbb{R}$ for example), we may change the definition of the space V_j to

$$V_j = \left\{ f \in L^2(\mathbb{R}),\ f_{|\Omega_j^k} \text{ is constant},\ k \in \mathbb{Z} \right\}.$$

6.2.2 Decomposition of the Space V_J

Consider now an arbitrary fixed integer $J \geq 0$. Then for any integer j satisfying $J > j \geq 0$, we define successive functional spaces $V_j, V_{j+1}, \ldots, V_J$, that satisfy $V_j \subset V_{j+1} \subset \cdots \subset V_J$. For any given function $f \in L^2(\Omega)$, a standard way to write the orthogonal projection of f on the subspace V_{j+1} is to consider $P_{j+1}f$ as the orthogonal projection of f onto V_j along with a correction term:

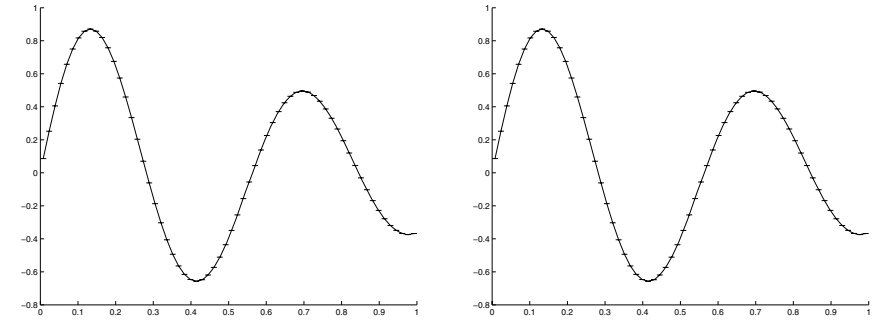

(a) (b)

Fig. 6.2. Approximating a function using mean values: (a) $j = 6$; (b) $j = 8$.

$$P_{j+1}f = P_j f + (P_{j+1}f - P_j f) = P_j f + Q_j f. \tag{6.5}$$

This relation introduces the new operator $Q_j = P_{j+1} - P_j$, which is actually the orthogonal projection operator onto W_j, the orthogonal complement of V_j in V_{j+1}: $V_{j+1} = V_j \oplus W_j$. It is easy to check that the function $\psi = \chi_{[0,1/2[} - \chi_{[1/2,1[}$ satisfies

$$\psi(x) = \phi(2x) - \phi(2x - 1). \tag{6.6}$$

Now we consider the functions ψ_j^k defined by

$$\forall x \in \Omega, \quad \psi_j^k(x) = 2^{j/2}\psi(2^j x - k), \text{ for } k = 0, 1, \ldots, 2^j - 1. \tag{6.7}$$

The 2^j functions ψ_j^k span W_j and are orthonormal relative to the L^2 scalar product. Then for an arbitrary function $f \in L^2(\Omega)$, we compute the coefficients d_j^k according to

$$\begin{aligned} d_j^k &= \langle f, \psi_j^k \rangle = \int f(t)\psi_j^k(t)\, dt \\ &= 2^{j/2} \int_{\Omega_{j+1}^{2k}} f(t)\, dt - 2^{j/2} \int_{\Omega_j^{2k+1}} f(t)\, dt. \end{aligned} \tag{6.8}$$

The coefficient d_j^k is the *fluctuation* of f on the interval Ω_j^k. Using (6.3), we write first

$$d_j^k = (c_{j+1}^{2k} - c_{j+1}^{2k+1})/\sqrt{2} \tag{6.9}$$

and then, by adding (6.9) to (6.4), we get

$$\sqrt{2}\, c_{j+1}^{2k} = c_j^k + d_j^k, \text{ for } k = 0, 1, \ldots, 2^j - 1, \tag{6.10}$$

while subtracting (6.9) from (6.4) leads to

$$\sqrt{2}\, c_{j+1}^{2k+1} = c_j^k - d_j^k, \text{ for } k = 0, 1, \ldots, 2^j - 1. \tag{6.11}$$

These relations are connected to the space decomposition $V_{j+1} = V_j \oplus W_j$. We gather these results in the useful relations (6.12) and (6.13), basic elements of the decomposition and reconstruction algorithms:

$$\begin{cases} c_j^k = (c_{j+1}^{2k} + c_{j+1}^{2k+1})/\sqrt{2}, \\ d_j^k = (c_{j+1}^{2k} - c_{j+1}^{2k+1})/\sqrt{2}, \text{ for } k = 0, 1, \ldots, 2^j - 1; \end{cases} \tag{6.12}$$

$$\begin{cases} c_{j+1}^{2k} = (c_j^k + d_j^k)/\sqrt{2}, \\ c_{j+1}^{2k+1} = (c_j^k - d_j^k)/\sqrt{2}, \text{ for } k = 0, 1, \ldots, 2^j - 1. \end{cases} \tag{6.13}$$

Before going any further, we remark that it is possible to iterate the space decomposition process according to

$$\begin{aligned} V_J &= V_{J-1} \oplus W_{J-1} = V_{J-2} \oplus W_{J-2} \oplus W_{J-1} = \cdots \\ &= V_0 \oplus W_0 \oplus \cdots \oplus W_{J-2} \oplus W_{J-1}. \end{aligned} \tag{6.14}$$

Since the functions ϕ_j^k (respectively ψ_j^k) span an orthonormal basis of V_j (respectively W_j), we are now able to define many orthonormal bases of V_J. Among all possibilities, the emphasis is put on two particular bases: the *canonical basis*, generated by functions ϕ_J^k,

$$P_J f = \sum_{k=0}^{2^J-1} c_J^k \phi_J^k, \tag{6.15}$$

and the so-called *Haar basis*, spanned by ϕ_0^0 and all functions ψ_j^k, for $j = 0, 1, 2, \ldots, J-1$ and $k = 0, 1, \ldots, 2^j - 1$:

$$P_J f = c_0^0 \phi_0^0 + \sum_{j=0}^{J-1} \sum_{k=0}^{2^j-1} d_j^k \psi_j^k. \tag{6.16}$$

Remark 6.2. Since $\phi_0^0 = \phi = \chi_{[0,1[}$ is the characteristic function of the whole domain Ω, the coefficient c_0^0 is simply the mean value of f on Ω: $c_0^0 = \int_\Omega f(t)\, dt$.

Remark 6.3. It is worth noting that the family of functions $\{\phi_J^k\}_{k=0}^{2^J-1}$, which form an orthonormal basis of the finite-dimensional space V_J, converges to an orthonormal basis of the infinite-dimensional space $L^2(\Omega)$ as J goes to infinity. So the coefficients c_J^k are also the components of f in the corresponding basis of $L^2(\Omega)$. Note also that the family of functions $\{\phi\} \cup \{\psi_j^k\}_{k=0,j=0}^{k=2^j-1,j=J-1}$, an orthonormal basis of the finite-dimensional space V_J, converges to an orthonormal basis of the infinite-dimensional space $L^2(\Omega)$ as J goes to infinity. The coefficients c_0^0 and d_j^k are the components of f in the corresponding basis of $L^2(\Omega)$.

6.2.3 Decomposition and Reconstruction Algorithms

In this section, we look at the standard operations required to switch from the expression of a function in the canonical basis of V_J to its expression in the Haar basis, and conversely.

A. Let f be a function in $L^2(\Omega)$ and J an arbitrary fixed integer. We compute the 2^J coefficients c_J^k, either exactly if we have an expression for f, or approximately using a sampling of the 2^J values of f on intervals Ω_k^J. Starting from these 2^J coefficients c_j^k, we successively compute the coefficients c_j^k and d_j^k according to the following algorithm:

$$\begin{array}{l}\textbf{for } j = J-1, \ldots, 1, 0 \textbf{ compute}\\ \quad \textbf{for } k = 0, 1, \ldots, 2^j - 1 \textbf{ compute}\\ \qquad c_j^k = (c_{j+1}^{2k} + c_{j+1}^{2k+1})/\sqrt{2}\\ \qquad d_j^k = (c_{j+1}^{2k} - c_{j+1}^{2k+1})/\sqrt{2}\\ \quad \textbf{end}\\ \textbf{end}\end{array} \tag{6.17}$$

Decomposition algorithm.

This calculation is referred to as the *analysis* or *decomposition algorithm* of f. We may represent step j of this algorithm by the symbolic scheme

$$\begin{array}{ccc} & c_j^k & \\ & (0 \le k < 2^j) & \\ \swarrow & & \searrow \\ c_{j-1}^k & & d_{j-1}^k \\ (0 \le k < 2^{j-1}) & & (0 \le k < 2^{j-1}) \end{array}$$

Once computed, the 2^j coefficients d_j^k are not used in the next steps of the decomposition algorithm; only the 2^j values of the coefficients $\{c_j^k\}_k$ are required in order to compute the coefficients $\{c_{j-1}^k\}_k$ and $\{d_{j-1}^k\}_k$. The computational cost of step j in algorithm (6.17) is that of computing $2 \times 2^{j-1}$ coefficients, that is, exactly 2^{j+1} operations. The computational cost of the decomposition algorithm, required to obtain the values of the 2^J coefficients, is then

$$2^{J+1} + \cdots + 2^j + \cdots + 2^2 + 1 = 2^{J+2} = 4 \times 2^J \text{ operations.}$$

This may be considered as an optimal value, since we are computing 2^J outputs from 2^J inputs for a cost of $O(2^J)$ operations.

B. Conversely, assume that we know c_0^0, the mean value of f on Ω, and all other coefficients d_j^k for $j = 0, \ldots, J-1$. Then we retrieve all the coefficients c_j^k using the following algorithm:

$$
\begin{array}{l}
\textbf{for } j = 0, \ldots, J-1 \textbf{ compute} \\
\quad \textbf{for } k = 0, 1, \ldots, 2^j - 1 \textbf{ compute} \\
\qquad c_{j+1}^{2k} = (c_j^k + d_j^k)/\sqrt{2} \\
\qquad c_{j+1}^{2k+1} = (c_j^k - d_j^k)/\sqrt{2} \\
\quad \textbf{end} \\
\textbf{end}
\end{array}
\tag{6.18}
$$

Reconstruction algorithm.

This calculation is referred to as the *synthesis* or the *reconstruction algorithm* of f. We represent step j of this algorithm by the symbolic scheme

$$
\begin{array}{ccc}
c_{j-1}^k & & d_{j-1}^k \\
(0 \le k < 2^{j-1}) & & (0 \le k < 2^{j-1}) \\
& \searrow \quad \swarrow & \\
& c_j^k & \\
& (0 \le k < 2^j) &
\end{array}
$$

We remark again that the computational cost of step j of this algorithm is that of computing $2 \times 2^{j-1}$ coefficients, that is, 2^{j+1} operations. The total computational cost of the reconstruction algorithm is also $O(2^J)$ operations.

Both algorithms (6.17) and (6.18) are efficient tools for obtaining the components of a function in the *Haar basis* from its components in the *canonical basis*, and conversely. There exist many other orthonormal bases of the space V_J and as many corresponding algorithms; we shall see two further examples of such algorithms, which have strong similarity to (6.17) and (6.18). This calculation is referred as a *multiscale analysis* or *multiresolution analysis*.

6.2.4 Importance of Multiresolution Analysis

We now look more closely at the *data compression* aspect included in the multiresolution analysis formulation. We assume first that the function f is constant ($f = C \neq 0$) on Ω, and compare two expressions for $P_J f$. The first is the representation of f in the canonical basis. According to (6.3), all the 2^J coefficients c_J^k are equal to C, and are thus different from zero. To represent $P_J f$ in this basis, an array of 2^J components is required. From another point of view, the expression for $P_J f$ in the Haar basis needs to compute coefficients $c_{J-1}^{k'}$ and $d_{J-1}^{k'}$ from the c_J^k's according to (6.17). We obtain immediately $c_{J-1}^{k'} = C$ and $d_{J-1}^{k'} = 0$ for $k' = 0, \ldots, 2^{J-1} - 1$. Going further in the computation, we see that $c_j^k = C$ and $d_j^k = 0$ for $j = J-1, \ldots, 0$. Finally, there is only one nonzero coefficient in the Haar basis: $c_0^0 = C$.

In information processing, attention is focused on the most condensed expression of a signal, in order to compute information, store it in memory, or send it through a network. Many algorithms are dedicated to the compression or decompression of data without any loss. We understand with the previous example how useful multiresolution may be in that case. In a more general case, when a function f is no longer constant, the coefficient c_j^k stands for the mean value of f on Ω_j^k, while the coefficient d_j^k represents the variation of f at the scale j. For any slowly varying function f, many coefficients d_j^k have a small value and may be neglected. Then the number of significant coefficients in the Haar basis representation is far smaller than the number of coefficients c_J^k present in the canonical basis. Conversely, a large coefficient d_j^k is associated with a fast variation of the function f within Ω_j^k. This property is of great interest when one wants to look automatically for the singularities of a function. As an illustration we just mention that special events in the sky are automatically detected by computers analyzing thousands of photographs of stars captured daily by telescopes.

Remark 6.4. Fourier analysis is known to be useful for dealing with oscillating signals. It is a very accurate way to capture the frequencies hidden in a signal, but its important drawback is the lack of spatial localization of these oscillations, due to the use of cosine or sine functions oscillating on the whole domain. This drawback is not present in multiresolution analysis, where the basis functions have supports limited to the Ω_k^j. Unfortunately, the frequency localization is then less accurate than with the Fourier basis.

6.3 Multiresolution Analysis: Practical Aspect

In this section we deal with a very simple example in order to understand the practical efficiency of the multiresolution analysis theory. But before doing this, it remains to clarify the way we shall store the different coefficients arising from the previous algorithms. Let $\Omega \subset \mathbb{R}$ be a bounded interval, f a function defined on Ω, and $J > 0$ an arbitrary fixed integer. Using the formulas of algorithm (6.17), we compute for $j = J-1, \ldots, 0$ coefficients c_j^k and d_j^k, for $k = 0, 1, \ldots, 2^j - 1$. These coefficients are stored in the following way: We first compute coefficients c_J^k according to (6.3) and store them in an array $[c_J]$ of 2^J components. Then we compute c_0^0 and $\{\{d_j^k\}_k\}_j$ using (6.17), and store them in an array $[d_J]$ of 2^J components. We begin at step J of algorithm (6.17) by imposing $[d_J] = [c_J]$. Then at step $J-1$ the 2^{J-1} coefficients $c_{J-1}^{k'}$ are stored in the first half of array $[d_J]$ (components 1 up to 2^{J-1}), while the 2^{J-1} coefficients $d_{J-1}^{k'}$ are stored in the second half of array $[d_J]$ (components $2^{J-1}+1$ up to 2^J). At step $J-2$ the 2^{J-2} coefficients $c_{J-2}^{k''}$ are stored in the first quarter of the array (components 1 up to 2^{J-2}), thus erasing the now useless values of coefficients $c_{J-1}^{k'}$ for $k' = 1, 2, \ldots, 2^{J-2}$. Then the 2^{J-2} coefficients $d_{J-2}^{k''}$ are stored in the second quarter of the array (components

$2^{J-2}+1$ up to 2^{J-1}), thus erasing the remaining useless values of coefficients $c_{J-1}^{k'}$ for $k' = 2^{J-2}+1, 2, \ldots, 2^{J-1}$. Note that during this operation the $[d_J]$ components from $2^{J-1}+1$ up to 2^J, which correspond to coefficients $d_{J-1}^{k'}$, are not modified. Proceeding in this way until step $j = 0$, we finally get the following array $[d_J]$:

$$[d_J] = [c_0^0, d_0^0, d_1^0, d_1^1, \ldots, d_j^0, d_j^1, \ldots, d_j^{2^j-1}, \ldots, d_{J-1}^0, \ldots, d_{J-1}^{2^{J-1}-1}]. \quad (6.19)$$

This storage is related to the decomposition of the space V_J according to the scheme

$$V_J \to \begin{cases} W_{J-1} \\ V_{J-1} \to \begin{cases} W_{J-2} \\ V_{J-2} \to \begin{cases} \cdots \\ \cdots \to \begin{cases} W_0 \\ V_0 \end{cases} \end{cases} \end{cases} \end{cases}$$

6.4 Multiresolution Analysis: Implementation

Let f be the function defined on $\Omega = [0,1]$ by $f(x) = \exp(-x)\sin 4\pi x$. We choose $J = 10$ and compute the arrays $[c_J]$ and $[d_J]$ associated with $P_J f$.

Exercise 6.1. 1. Write a program that computes all coefficients c_J^k according to (6.17). Store these coefficients in an array $[c_J]$ with 2^J components.
2. Using the decomposition algorithm (6.17), compute for $j = J-1, \ldots, 0$ all coefficients c_j^k and d_j^k, for $k = 0, 1, \ldots, 2^j - 1$. Store these coefficients in an array $[d_J]$ with 2^J components, as detailed in the previous section.
3. Write a program that computes all coefficients c_J^k from the $[d_J]$ components, according to the reconstruction algorithm (6.18). Check the results.

A solution of this exercise is proposed in Sect. 6.7 at page 148. Using these direct and inverse transformation programs, one can perform some numerical experiments. We shall deal now with an example of a compression algorithm.

Exercise 6.2. 1. Calculate the number of coefficients in an array $[d_J]$ whose absolute values are greater than $\varepsilon = 2^{-J/2} \times 10^{-3}$.
2. Copy array $[d_J]$ into a new array $[d_J^\varepsilon]$ and set to zero every component of $[d_J^\varepsilon]$ whose absolute value is less than ε ($d_j^{\varepsilon,k} = 0$ when $|d_j^k| < \varepsilon$).
3. Compute the array $[c_J^\varepsilon]$ from $[d_J^\varepsilon]$ using the reconstruction algorithm (6.18).
4. Visualize the resulting signal and compare both curves representing $P_J f$ and $P_J^\varepsilon f$.

5. Study the variations of $\|P_J^\varepsilon f - P_J f\|_2$ and the number of nonzero coefficients in $[d_J^\varepsilon]$ as ε varies.

A solution of this exercise is proposed in Sect. 6.7 at page 148. Table 6.1 displays results of this experiment (with $f(x) = \exp(-x)\sin 4\pi x$ and $J = 10$). The number of nonzero coefficients is reported in front of the threshold value, with the corresponding relative error $\|P_J^\varepsilon f - P_J f\|_2 / \|P_J f\|_2$. Fig. 6.3 plots two signals reconstructed after thresholding. We emphasize here the compression capability of the method: using only 352 coefficients instead of the 1024 sample values, we obtain 0.8% relative error.

Threshold	Coefficients	Relative error
0.1000	78	0.0402
0.0500	121	0.0258
0.0100	352	0.0080
0.0050	563	0.0042
0.0010	947	0.0003
0.0005	987	0.0001
0.0001	1015	0.00001

Table 6.1. Thresholding (Haar wavelet).

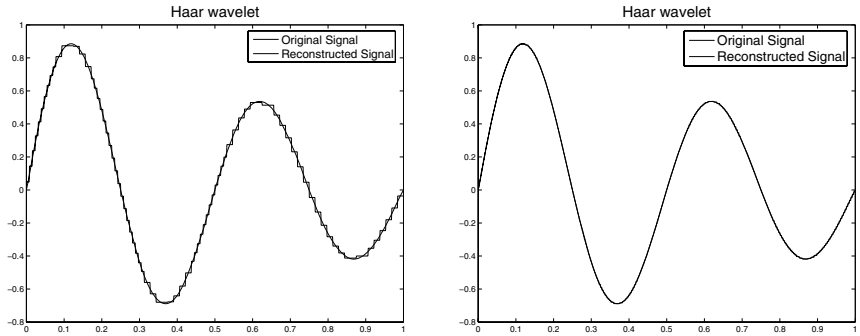

(a) (b)

Fig. 6.3. Reconstruction after thresholding: $J = 10$. (a) $\varepsilon = 0.10$; (b) $\varepsilon = 0.01$.

6.5 Introduction to Wavelet Theory

6.5.1 Scaling Functions and Wavelets

If you have correctly performed the previous numerical experiments, you deserve our warmest congratulations for your first steps in the fabulous world of wavelets! When Haar proposed (in 1910!) the construction of an orthonormal basis of the space $L^2(\Omega)$ like the one discussed previously, he was in fact far from imagining the practical importance of his discovery. Wavelet theory was founded in the sixties, arising from an idea of a petroleum engineer named Morlet, who was looking for algorithms well suited to seismic signal processing, and more accurate than Fourier analysis (see Meyer, 1990).

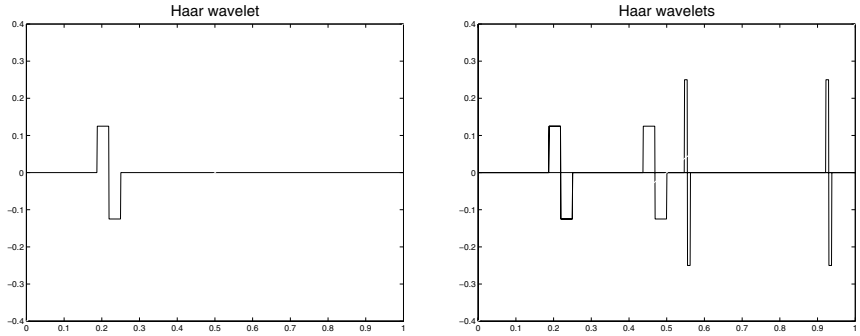

Fig. 6.4. Haar wavelets ($J = 10$). (a) Single wavelet; (b) shifted wavelets.

The Haar basis construction is the foundation of multiresolution analysis. In the associated terminology, functions ϕ_j^k are the called *scaling functions*, while functions ψ_j^k are *wavelet functions*, or *wavelets*, for short. What is the appearance of a wavelet? Have a look at the previous numerical experiments: for $J = 10$ we begin by setting to zero all components of the $[d_J]$ and give the value 1 to only one of the coefficients d_j^k; [2] then using the reconstruction algorithm (6.18), we obtain the associated wavelet ψ_j^k, as plotted in Fig. 6.4(a). Note that the integers k and j have to satisfy the following conditions: $0 < j < J$ and $0 \leq k < 2^j$. Choose now another integer $k' \neq k$ such that $0 \leq k < 2^j$ and repeat the experiment. This leads to a wavelet $\psi_j^{k'}$, which appears (see Fig. 6.4(b)) to be shifted from wavelet ψ_j^k by an offset of $2^{-j}(k' - k)$. Both wavelets belong to the subspace W_j and are hence called level-j wavelets. All level-j wavelets (they are altogether 2^j in level j) are obtained from any one of them by a $p\, 2^{-j}$ shift (p an integer).

[2] The level j coefficient d_j^k is stored in the $(2^j + k + 1)$th component of $[d_J]$ (see (6.19)).

Now, if we choose two integers j' and k'' such that $0 < j' \neq j < J$ and $0 \leq k'' < 2^{j'}$, the corresponding wavelet $\psi_{j'}^{k''}$ has features similar to the previous wavelets: same global shape but different size (amplitude has been multiplied by $2^{j'-j}$, while the length has been divided by the same factor (see Fig. 6.4(b)).

The whole space $V_J \subset L^2(\Omega)$ is then generated by direct summation of the subspace V_0 and all orthogonal subspaces W_j, each of which is spanned by 2^j wavelet functions. When J goes to infinity, we retrieve the structure introduced by Haar (see Remark 6.2): $L^2(\Omega)$ is a direct summation of finite-dimensional orthogonal subspaces. Moreover, for any $f \in L^2(\Omega)$, the multiresolution analysis can be summarized in

$$
\begin{aligned}
P_J f &= \langle f, \phi_0^0 \rangle \phi_0^0 + \sum_{j=0}^{j=J-1} \sum_{k=0}^{2^j-1} \langle f, \psi_j^k \rangle \psi_j^k, \\
f &= \langle f, \phi_0^0 \rangle \phi_0^0 + \sum_{j \geq 0} \sum_{k=0}^{2^j-1} \langle f, \psi_j^k \rangle \psi_j^k, \\
f &= P_J f + \sum_{j \geq J} \sum_{k=0}^{2^j-1} \langle f, \psi_j^k \rangle \psi_j^k.
\end{aligned}
\tag{6.20}
$$

Hence the coefficients c_0^0 and d_j^k are the components of f in the corresponding basis of $L^2(\Omega)$. From that point of view, the wavelet theory appears to be a powerful tool for approximating functions. Since the relation $V_{j+1} = V_j \oplus W_j$ holds at any level $j < J$, we may consider the subspace W_j as a set of *detail functions*, that is, the functions we have to add to the functions of V_j, in order to retrieve all V_{j+1} functions.

By fixing an integer $J < +\infty$, we restrain the space description to the scale 2^{-J}, and consequently we are unable to capture the variation $|f(x) - f(x')|$ when $|x - x'| < 2^{-J}$. On the other hand, we may write $\|P_J f - f\|_2 < C\ 2^{-J}$ for any function f in $L^2(\Omega)$ with bounded variation. This means we know exactly the accuracy of an approximation $P_J f$ of a given f; moreover, we also know the price to pay to improve this result: we have to compute at least 2^J new coefficients.

In the previous example, all *scaling functions* are derived from the same function ϕ by the relation $\phi_j^k(x) = \phi(2^j x - k)$. Likewise, the relation $\psi_j^k(x) = \psi(2^j x - k)$ shows that all *wavelet functions* are derived from the same function ψ, sometimes called the *mother wavelet* function. In this first study, both ϕ and ψ are discontinuous functions; it follows that the approximating function $P_J f$ is also discontinuous, even when f is continuous. How is one to get a more regular approximation? Much work has been done to answer the question; there exist abstract necessary conditions on the pair (ϕ, ψ) in order to generate a general framework for multiresolution analysis. In short, it is

possible to build continuous wavelet approximations for a given continuous function; however, these aspects of wavelet theory are beyond our scope. We refer to Cohen and Ryan (1995), Cohen (2000, 2003), Daubechies (1992), and Mallat (1997) for further details. In the following sections, we introduce two examples of continuous wavelets: the Schauder and the Daubechies wavelets.

For the sake of simplicity we shall limit our study to periodic continuous functions on Ω. Although wavelet theory is able to address the general case, it needs some technical modifications that we want to skip here.

6.5.2 The Schauder Wavelet

We follow here the outline of the previous section and introduce a new V_J space definition:

$$V_j = \left\{ f \in C^0(\Omega),\ f_{|\Omega_j^k} \text{ is affine, for } k = 0, 1, \ldots, 2^j - 1 \right\} \subset L^2(\Omega).$$

We are now dealing with piecewise linear functions continuous on Ω. We consider first the function ϕ defined by

$$\phi(x) = \max(0, 1 - |x|). \tag{6.21}$$

The function ϕ satisfies the two-scale relation (see Fig. 6.5)

$$\phi(x) = \frac{1}{2}\phi(2x - 1) + \phi(2x) + \frac{1}{2}\phi(2x + 1). \tag{6.22}$$

Then we define the functions ϕ_j^k by scaling and shift:

$$\phi_j^k(x) = 2^{j/2}\phi(2^j x - k), \text{ for } k = 0, 1, \ldots, 2^j - 1. \tag{6.23}$$

The functions ϕ_j^k are known as *hat functions* in the finite element method; though they do not span an orthogonal basis of V_j, we shall admit that they provide the Schauder wavelets by the definition $\psi_j^k = \phi_{2j-1}^k$, for $k = 0, 1, \ldots, 2^j - 1$. It is not the only eligible choice in that case, but this is the simplest one (for more details see Mallat (1997)). Fig. 6.6 displays a set of Schauder wavelets when $J = 3$. For any function f we consider again the two representations

$$P_J f = \sum_{k=0}^{2^J-1} c_J^k \phi_J^k \quad \text{and} \quad P_J f = c_0^0 \phi_0^0 + \sum_{j=0}^{J-1} \sum_{k=0}^{2^j-1} d_j^k \psi_j^k. \tag{6.24}$$

This definition leads to the decomposition formulas

$$\begin{cases} c_j^k = \sqrt{2}\, c_{j+1}^{2k}, \\ d_j^k = \sqrt{2}\, \left[c_{j+1}^{2k+1} - \dfrac{1}{2}(c_{j+1}^{2k} + c_{j+1}^{2k+2}) \right], \text{ for } k = 0, 1, \ldots, 2^j - 1, \end{cases} \tag{6.25}$$

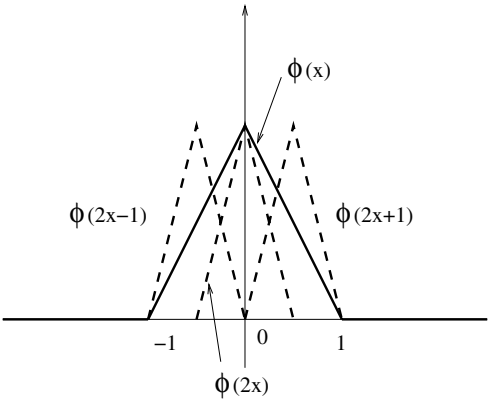

Fig. 6.5. The two-scale relation (Schauder basis).

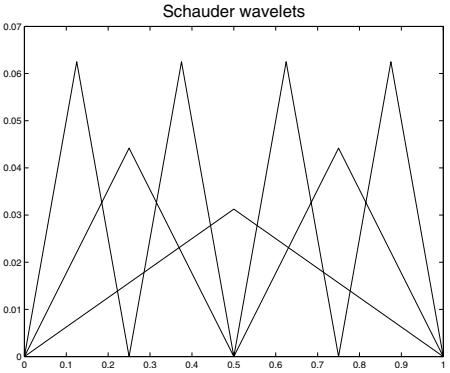

Fig. 6.6. Some Schauder wavelets ($J = 3$).

as well as the reconstruction formulas

$$\begin{cases} c_{j+1}^{2k} = \dfrac{\sqrt{2}}{2}\, c_j^k, \\ c_{j+1}^{2k+1} = \dfrac{\sqrt{2}}{2}\, \left[d_j^k + \dfrac{1}{2}(c_j^k + c_j^{k+1}) \right], \text{ for } k = 0, 1, \ldots, 2^j - 1. \end{cases} \tag{6.26}$$

Any coefficient c_j^k stands here for the (normalized) *value* of f at the point $x_j^k = 2^j x - k$, and a usual interpretation of (6.25) is that the decomposition algorithm proceeds by elimination, keeping only point values of even indices when going from level $j+1$ to level j. Similarly, the coefficient d_j^k appears to be the difference between the (normalized) odd-index point value c_{j+1}^{2k+1} and the linear interpolation of the adjacent (normalized) even-index point values c_{j+1}^{2k} and c_{j+1}^{2k+2}; it is known as the *detail*, that is, the value to be added to the

current level-j values c_j^k and c_j^{k+1}, in order to obtain the level-$(j+1)$ value c_{j+1}^{2k+1}, as can be seen in the reconstruction algorithm (6.26). This process is similar to the multiresolution idea introduced in (6.5) and (6.20). Fig. 6.7 shows a graphical interpretation of this computation.

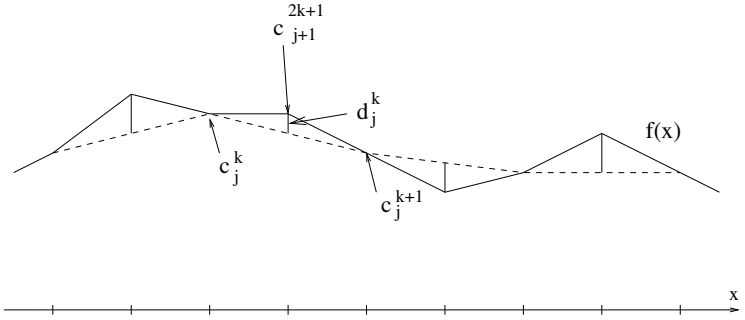

Fig. 6.7. Values and details.

A computer implementation of the relations (6.25–6.26) is easily obtained from the previous algorithms (6.17–6.18). This is a very attractive property of wavelet theory. All decomposition and reconstruction algorithms are similar to (6.17) and (6.18); switching from a particular wavelet basis to another one results from a slight change in the formulas. Moreover, this change arises only from the corresponding two-scale relations. Consequently, both $[c_J]$ and $[d_J]$ share the same structure of 2^J-component arrays. The general computation, common to all decomposition and reconstruction algorithms, is known as the *Mallat transform* (see Mallat, 1997).

6.5.3 Implementation of the Schauder Wavelet

Let f be the function defined on $\Omega = [0,1]$ by $f(x) = \exp(-x)\sin 4\pi x$. We choose $J = 10$ and compute the arrays $[c_J]$ and $[d_J]$ associated with $P_J f$.

Exercise 6.3. 1. Write a program that computes all coefficients c_J^k according to (6.25). Store these coefficients in an array $[c_J]$ with 2^J components.

2. Using the decomposition algorithm (6.25), compute for $j = J-1, \ldots, 0$ all coefficients c_j^k and d_j^k, for $k = 0, 1, \ldots, 2^j - 1$. Store these coefficients in an array $[d_J]$ with 2^J components, as detailed in the previous section.
3. Write a program that computes all coefficients c_J^k from the $[d_J]$ components, according to the reconstruction algorithm (6.26). Check the results.

Remark 6.5. The use of periodic functions requires a particular treatment at both edges of the domain. More precisely, formulas (6.25) and (6.26) use the relation $c_{j+1}^{2j} = c_{j+1}^0$ for $j = 1, 2, \ldots, J-1$.

A solution of this exercise is proposed in Sect. 6.7 at page 148. We deal again with an example of the compression algorithm.

Exercise 6.4. 1. Calculate the number of coefficients in the array $[d_J]$ whose absolute values are greater than $\varepsilon = 2^{-J/2} \times 10^{-3}$.
2. Copy array $[d_J]$ in a new array $[d_J^\varepsilon]$ and set to zero each component of $[d_J^\varepsilon]$ whose absolute value is less than ε ($d_j^\varepsilon = 0$ when $|d_j| < \varepsilon$).
3. Compute the array $[c_J^\varepsilon]$ from $[d_J^\varepsilon]$ using the reconstruction algorithm (6.26).
4. Visualize the resulting signal and compare both curves representing $P_J f$ and $P_J^\varepsilon f$.
5. Study the variations of $\|P_J^\varepsilon f - P_J f\|_2$ and the number of nonzero coefficients in $[d_J^\varepsilon]$ as ε varies.

A solution of this exercise is proposed in Sect. 6.7 at page 149. Table 6.2 displays results of this experiment (with $f(x) = \exp(-x)\sin 4\pi x$ and $J = 10$). The number of nonzero coefficients is reported in front of the threshold value, with the corresponding relative error $\|P_J^\varepsilon f - P_J f\|_2 / \|P_J f\|_2$. Fig. 6.8 plots two signals reconstructed after thresholding. We emphasize the spectacular compression capacity of the method: using only 77 coefficients arising from 1024 values, we obtain a 0.2% relative error. We see that for a smaller number of significant components in array $[d_J]$, we get a better approximation with the Schauder wavelet than with the Haar wavelet. This is not a big surprise because $P_J f$ is now a continuous approximation of the same continuous function f. Note that there is a small increase of the computational cost, due to the use of more coefficients in formulas (6.25) and (6.26).

6.5.4 The Daubechies Wavelet

Is it possible to improve these results? Cohen (2003) has proven that a multiresolution analysis is available as soon as there exists a generalized two-scale relation such as

$$\phi(x) = \sum_{k \in \mathbb{Z}} h_k \phi(2x - k). \tag{6.27}$$

In signal-processing theory, the h_k's are the components of an array h, called a *filter*. Knowledge of a filter is a necessary and sufficient condition to

Threshold	Coefficients	Relative error
0.1000	25	0.0155
0.0500	41	0.0072
0.0100	77	0.0020
0.0050	102	0.0010
0.0010	205	0.0003
0.0005	246	0.0002
0.0001	459	0.00005

Table 6.2. Thresholding (Schauder wavelet).

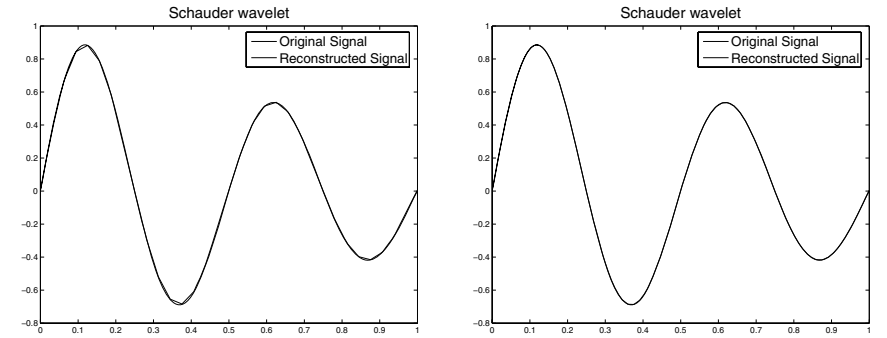

(a) (b)

Fig. 6.8. Reconstruction after thresholding: $J = 10$. (a) $\varepsilon = 0.10$; (b) $\varepsilon = 0.01$.

build a multiresolution analysis. From (6.27) one may write the complementary relation

$$\psi(x) = \sum_{k \in \mathbb{Z}} \tilde{h}_k \psi(2x - k). \tag{6.28}$$

Both relations are related to decomposition and reconstruction algorithms, as previously established in (6.17–6.18) for the Haar wavelet, or (6.25–6.26) for the Schauder wavelet. Daubechies (1992) has proven that the mother wavelet regularity depends on the *filter length*, that is, the number of nonzero coefficients h_k used in relation (6.27). A general method for defining compact-support wavelets with arbitrary regularity has been proposed, introducing the *Daubechies wavelets* family. To put it in a nutshell, the more nonzero coefficients appear in the two-scale relation (6.27), the more accurate is the wavelet approximation. To end with this study, we shall deal now with the Daubechies wavelet D4, which is defined by the following formulas:

Decomposition:

$$\begin{cases} c_j^k = C_0\, c_{j+1}^{2k-1} + C_1\, c_{j+1}^{2k} + C_2\, c_{j+1}^{2k+1} + C_3\, c_{j+1}^{2k+2}, \\ d_j^k = C_3\, c_{j+1}^{2k-1} - C_2\, c_{j+1}^{2k} + C_1\, c_{j+1}^{2k+1} - C_0\, c_{j+1}^{2k+2}. \end{cases} \tag{6.29}$$

Reconstruction:

$$\begin{cases} c_{j+1}^{2k} = C_3\, c_j^{k-1} - C_0\, d_j^{k-1} + C_1\, c_j^k - C_2\, d_j^k, \\ c_{j+1}^{2k+1} = C_2\, c_j^k + C_1\, d_j^k + C_0\, c_j^{k+1} + C_3\, d_j^{k+1}. \end{cases} \tag{6.30}$$

According to Daubechies (1992), the values of C_k are respectively

$$\begin{cases} C_0 = \dfrac{1+\sqrt{3}}{4\sqrt{2}}, \qquad C_1 = \dfrac{3+\sqrt{3}}{4\sqrt{2}}, \\ C_2 = \dfrac{3-\sqrt{3}}{4\sqrt{2}}, \qquad C_3 = \dfrac{1-\sqrt{3}}{4\sqrt{2}}. \end{cases} \tag{6.31}$$

6.5.5 Implementation of the Daubechies Wavelet D4

Let f be the function defined on $\Omega = [0,1]$ by $f(x) = \exp(-x)\sin 4\pi x$. We choose $J = 10$ and compute the arrays $[c_J]$ and $[d_J]$ associated with $P_J f$.

Exercise 6.5. 1. Write a program that computes all coefficients c_J^k according to (6.29). Store these coefficients in an array $[c_J]$ with 2^J components.
2. Using the decomposition algorithm (6.25), compute for $j = J-1, \ldots, 0$ all coefficients c_j^k and d_j^k, for $k = 0, 1, \ldots, 2^j - 1$. Store these coefficients in an array $[d_J]$ with 2^J components, as detailed in the previous sections.
3. Write a program that computes all coefficients c_J^k from the $[d_J]$ components, according to the reconstruction algorithm (6.30). Check the results.
4. Visualize a Daubechies wavelet (see Fig. 6.9; what a surprise!).

Remark 6.6. As previously noticed, we consider here periodic functions, and special formulas are required to treat the domain edges.

A solution of this exercise is proposed in Sect. 6.7 at page 149. We deal again with an example of a compression algorithm.

Exercise 6.6. 1. Calculate the number of coefficients in array $[d_J]$ whose absolute values are greater than $\varepsilon = 2^{-J/2} \times 10^{-3}$.
2. Copy array $[d_J]$ in a new array $[d_J^\varepsilon]$ and set to zero each component of $[d_J^\varepsilon]$ whose absolute value is less than ε ($d_j^\varepsilon = 0$ when $|d_j| < \varepsilon$).
3. Compute the array $[c_J^\varepsilon]$ from $[d_J^\varepsilon]$ using the reconstruction algorithm (6.26).
4. Visualize the resulting signal and compare both curves representing $P_J f$ and $P_J^\varepsilon f$.

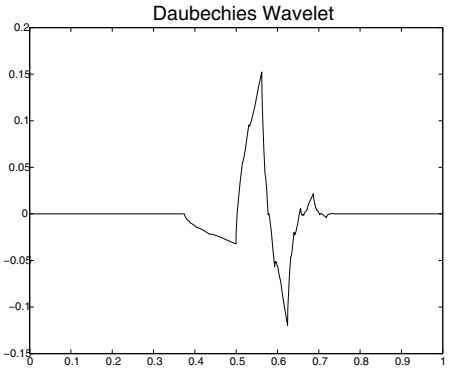

Fig. 6.9. The Daubechies wavelet D4.

5. Study the variations of $\|P_J^\varepsilon f - P_J f\|_2$ and the number of nonzero coefficients in $[d_J^\varepsilon]$ as ε varies.

A solution of this exercise is proposed in Sect. 6.7 at page 149. Table 6.3 displays results of this experiment (with $f(x) = \exp(-x)\sin 4\pi x$ and $J = 10$). The number of nonzero coefficients is reported in front of the threshold value, with the corresponding relative error $\|P_J^\varepsilon f - P_J f\|_2 / \|P_J f\|_2$. Fig. 6.10 plots two signals reconstructed after thresholding. We emphasize again the spectacular compression capacity of the method: by using only 78 coefficients arising from 1024 values, we obtain a 0.3% relative error.

Threshold	Coefficients	Relative error
0.1000	30	0.0200
0.0500	43	0.0108
0.0100	78	0.0031
0.0050	108	0.0015
0.0010	207	0.0003
0.0005	233	0.0002
0.0001	454	0.00007

Table 6.3. Thresholding (Daubechies wavelet D4).

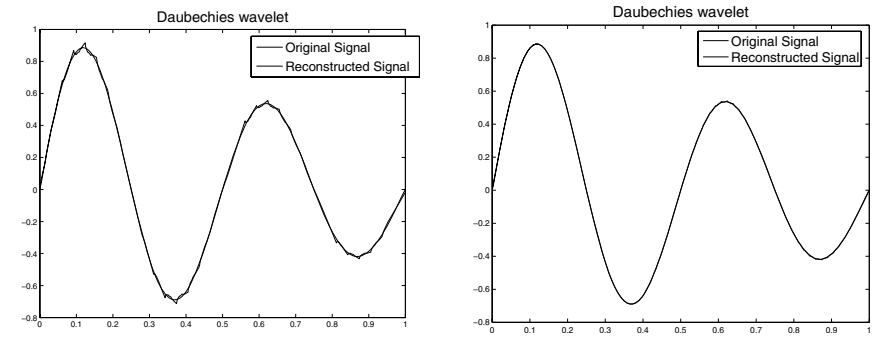

(a) (b)

Fig. 6.10. Reconstruction after thresholding: $J = 10$. (a) $\varepsilon = 0.10$; (b) $\varepsilon = 0.01$.

6.6 Generalization: Image Processing

Generalization of the previous results to image processing is straightforward. We might define a wavelet function of two variables $\psi_2(x, y)$; meanwhile, the tensor product is easier to deal with. We then consider a mother wavelet of the form $\psi_2(x, y) = \psi(x)\psi(y)$. This choice introduces a two-dimensional Mallat transform, where the image to treat is a matrix $[c_J]$: we begin to proceed to a row-by-row decomposition. The resulting transformed rows are stored in a matrix $[\tilde{c}_J]$; we proceed then to a decomposition of the $[\tilde{c}_J]$ columns, and the final results are stored (column by column) in a matrix $[d_J]$. This matrix contains all the components of the image in the wavelet basis. It is then possible to compress this object using a thresholding algorithm, and the compressed data are stored in a matrix $[d_J^\varepsilon]$. The use of a column-by-column reconstruction algorithm followed by a row-by-row reconstruction algorithm provides a new image $[c_J^\varepsilon]$ from $[d_J^\varepsilon]$. From a practical point of view, some operations may be performed using the $[d_J]$ representation directly rather than the $[c_J]$ initial one:

- Two distinct images may be compared in the (compressed) wavelet format; this is very helpful for saving computing time. As an example of such utilization, we cite the research of suspected fingerprints in a criminal fingerprints database. As the information is more condensed into wavelet storage, comparisons go very fast.
- Storage in $[d_J]$ format is also useful to detect singularities because they are associated with large values of coefficients $[d_J]_{k,l}$. So the presence (or absence) of such coefficients may reveal special features of the original image $[c_J]$ very quickly.

6.6.1 Image Processing: Implementation

We assume here that F is an image defined as a two-dimensional pixel array $[c_J]$.

Exercise 6.7. 1. Write a procedure performing decomposition and reconstruction of a given image $[c_J]$ for all three wavelet functions described in the previous sections.
2. Check the thresholding compression algorithm.
3. Compare and visualize all results.

A solution of this exercise is proposed in Sect. 6.7 at page 149. Fig. 6.11 and Fig. 6.12 display original and reconstructed images. For a threshold value $\varepsilon = 10^{-3} \times (2^J)^2$, the numbers of nonzero components in $[d_J^\varepsilon]$ are respectively $nbc_H^\varepsilon = 2298$ using the Haar wavelet, $nbc_S^\varepsilon = 11295$ using the Schauder wavelet, and $nbc_D^\varepsilon = 1887$ using the D4 Daubechies wavelet. The original document is a 256×256 pixel image, corresponding to a 65536 coefficient matrix $[c_J]$.

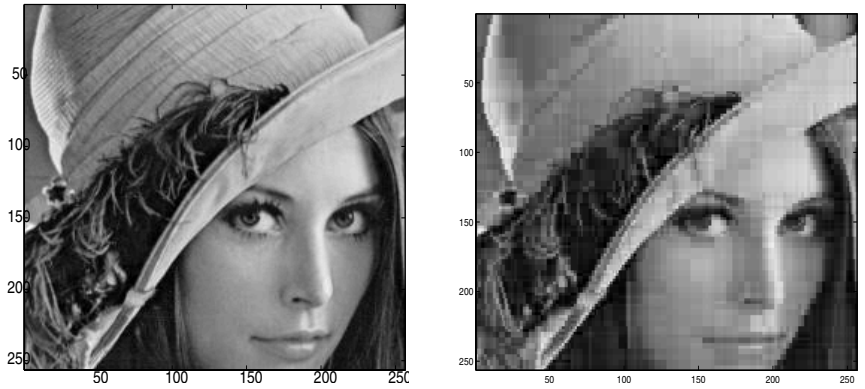

(a) (b)

Fig. 6.11. Images. (a) Original; (b) reconstructed (Haar wavelet).

Multiresolution analysis is rich in theoretical and practical developments. Numerous projects are progressing all around the world, making it one of the most active areas of research in the mathematical sciences. Readers will find a large literature on this subject. Among many papers of interest, we cite Cohen (2000, 2003), Daubechies (1992), Mallat (1997), and Meyer (1990).

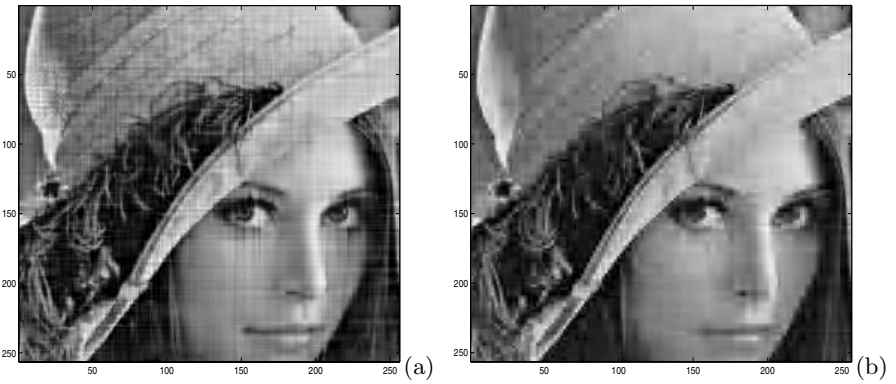

Fig. 6.12. Reconstructed images. (a) Schauder wavelet; (b) Daubechies wavelet.

6.7 Solutions and Programs

Solution of Exercise 6.1

The file *MRA_haar.m* provides the procedure related to decomposition and reconstruction algorithm (6.17) and (6.18). A flag parameter allows one to switch from decomposition ($[c_J] \longrightarrow [d_J]$) to reconstruction ($[d_J] \longrightarrow [c_J]$) formulas.
The file *MRA_haar_ex1.m* provides the procedure that generates a sampling of a function on the interval $[0, 1]$ (for this particular example, the function contained in the file *MRA_function.m* is defined by $f(x) = \exp(-x)\sin 4\pi x$). This sampling is then used to define a piecewise constant function with the help of the procedure `MRA_pwcte`. Decomposition and reconstruction computations are then performed by the procedure `MRA_haar`.

Solution of Exercise 6.2

The file *MRA_haar_ex2.m* provides the procedure for performing the same computations as `MRA_haar_ex1`, with the difference that all coefficients whose absolute values are smaller than the threshold are set to zero. This procedure is used for the compression tests of Table 6.1 and Fig. 6.3.

Solution of Exercise 6.3

The file *MRA_schauder.m* provides the procedure related to decomposition and reconstruction algorithm (6.25) and (6.26). A flag parameter allows one to switch from decomposition ($[c_J] \longrightarrow [d_J]$) to reconstruction ($[d_J] \longrightarrow [c_J]$) formulas.

The file *MRA_schauder_ex1.m* provides the procedure that generates a sampling of a function on the interval $[0, 1]$ (for this particular example, the function contained in the file *MRA_function.m* is defined by $f(x) = \exp(-x)\sin 4\pi x$). This sampling is then used to define a piecewise constant function with the help of the procedure `MRA_pwcte`. Decomposition and reconstruction computations are then performed by the procedure `MRA_schauder`.

Solution of Exercise 6.4

The file *MRA_schauder_ex2.m* provides the procedure for performing the same computations as `MRA_schauder_ex1`, with the difference that all coefficients whose absolute values are smaller than the threshold are set to zero. This procedure is used for the compression tests of Table 6.2 and Fig. 6.8.

Solution of Exercise 6.5

The file *MRA_daube4.m* provides the procedure related to decomposition and reconstruction algorithm (6.29) and (6.30). A flag parameter allows one to switch from decomposition ($[c_J] \longrightarrow [d_J]$) to reconstruction ($[d_J] \longrightarrow [c_J]$) formulas.
The file *MRA_daube4_ex1.m* provides the procedure that generates a sampling of a function on the interval $[0, 1]$ (for this particular example, the function contained in file *MRA_function.m* is defined by $f(x) = \exp(-x)\sin 4\pi x$). This sampling is then used to define a piecewise constant function with the help of the procedure `MRA_pwcte`. Decomposition and reconstruction computations are then performed by the procedure `MRA_daube4`.

Solution of Exercise 6.6

The file *MRA_daube4_ex2.m* provides the procedure for performing the same computations as `MRA_daube4_ex1`, with the difference that all coefficients whose absolute values are smaller than the threshold are set to zero. This procedure is used for the compression tests of Table 6.3 and Fig. 6.10.

Solution of Exercise 6.7

The files *MRA_haar_ex3.m*, *MRA_schauder_ex3.m*, and *MRA_daube4_ex3.m* provide procedures that read an image in the file `lenna.jpg` and then perform decomposition, compression, and reconstruction steps with the Haar wavelet (respectively Schauder and Daubechies wavelets). Figs. 6.11 and 6.12 were obtained in this way. Note that in these procedures, decomposition and reconstruction are performed by successive uses of one-dimensional decomposition and the reconstruction algorithm.

Chapter References

A. Cohen, *Wavelet Methods in Numerical Analysis*, Handbook of Numerical Analysis, vol. VII, P.G. Ciarlet and J.L. Lions eds., North-Holland, Amsterdam, 2000.

A. Cohen, *Numerical Analysis of Wavelet Methods*, Studies in Mathematics and its Applications, North-Holland, Amsterdam, 2003.

A. Cohen and R. Ryan, *Wavelets and Multiscale Signal Processing*, Chapman and Hall, London, 1995.

I. Daubechies, *Ten Lectures on Wavelets*, Society for Industrial and Applied Mathematics, Philadelphia, Pennsylvania, 1992.

S.G. Mallat, *A Wavelet Tour of Signal Processing*, Academic Press, New York, 1997.

Y. Meyer, *Ondelettes et Opérateurs. Tomes I à III*, Hermann, Paris, 1990.

7

Elasticity: Elastic Deformation of a Thin Plate

Project Summary

Level of difficulty:	2
Keywords:	Finite difference method, Laplacian, bilaplacian
Application fields:	Linear elasticity: deformation of a membrane or plate

7.1 Introduction

We study in this chapter the deformation of a thin plate. In our example, the plate is part of a condenser microphone, such as one may find inside a telephone (or a cellular phone). When the user speaks, the plate (which is in fact a metalized plastic diaphragm) moves in response to changes in the acoustic pressure induced by sound waves. Since the plate is also the side of an electric capacitor, its dynamic deformations infer variations of the electric potential, which is amplified to generate a measurable signal. For the sake of simplicity, we shall consider here a thin rectangular plate in the device displayed in Fig. 7.1.

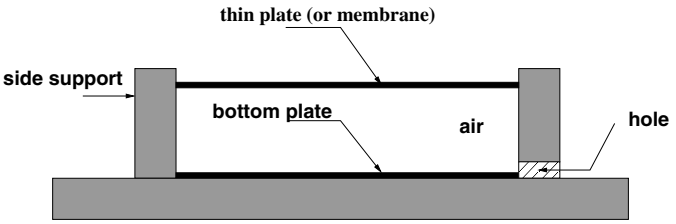

Fig. 7.1. Sketch of the pressure sensor (side view).

7.2 Modeling Elastic Deformations (Linear Problem)

As a first stage of approximation, we shall neglect electrostatic forces in the device and consider that the plate bends exclusively because of the difference between the inside and outside values of the acoustic pressure (see Fig. 7.2). The pressure is assumed constant inside the device, and we take into account only variations of the outside acoustic pressure. There are two physical models relating the deformation f_a to the pressure value P_a:

- for a high-strained plate,

$$-c_1 \Delta f_a = P_a, \tag{7.1}$$

- and for a low-strained plate (the term "membrane" is then more appropriate than "plate"),

$$c_2 \Delta^2 f_a = P_a. \tag{7.2}$$

The coefficients c_1 and c_2 are physical constants depending on the material and defined as

$$c_1 = T \quad \text{and} \quad c_2 = \frac{Ee^3}{12(1-\nu)},$$

where e is the thickness of the plate, T the mechanical stress, E the Young modulus, and ν the Poisson coefficient.

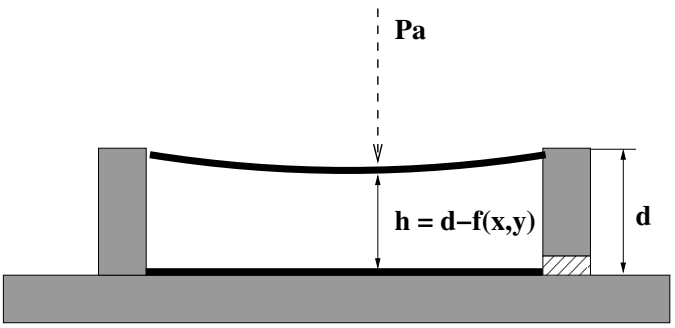

Fig. 7.2. Deformation of the plate.

In previous equations the symbol Δ denotes the Laplacian, a differential operator defined in two dimensions as

$$\Delta f_a = \frac{\partial^2 f_a}{\partial x^2} + \frac{\partial^2 f_a}{\partial y^2}.$$

The bilaplacian (or biharmonic operator) Δ^2 is defined accordingly as $\Delta^2 f_a = \Delta(\Delta f_a)$.

In order to have a general formulation of the problem we shall consider in the following the "mixed" equation

$$c_2 \Delta^2 f_a - c_1 \Delta f_a = P_a. \tag{7.3}$$

This is a partial differential equation (PDE) of fourth order. For any physically acceptable value of P_a, there exists a solution f_a to equation (7.3) (for mathematical details see Ciarlet (1978, 2000)). In fact, the solution is not unique, since for any harmonic function f_h (i.e., a function such that $\Delta f_h = 0$), $f_a + f_h$ is also a solution. This is a direct consequence of the linearity of the Laplacian and bilaplacian. [1]

To ensure uniqueness (which is a crucial feature for the success of a numerical computation) we shall prescribe appropriate boundary conditions. We want the solution satisfying a realistic condition: the plate is assumed to be fastened along the four sides of the rectangle. This means that the deformation f_a is null all along the rim:

$$f_a|_{\partial\Omega} = 0, \tag{7.4}$$

where $\partial\Omega$ denotes the boundary of the domain Ω covered by the plate. This is called a *Dirichlet homogeneous boundary condition* and is a sufficient condition to obtain the uniqueness of the solution of equation (7.1), because the Laplacian is a second-order differential operator (for the proof, see, for example, Ciarlet (2000)). When considering equation (7.2) or (7.3), a supplementary boundary condition is required, since the bilaplacian is a fourth-order differential operator. Denoting by $\mathbf{n}$ the outward normal vector[2] to $\partial\Omega$, this supplementary condition simulates the elastic "clamping" of the plate along all the boundary:

$$\left.\frac{\partial f_a}{\partial n}\right|_{\partial\Omega} = 0. \tag{7.5}$$

The boundary condition (7.5) is referred to mathematically as a *Neumann condition*.

7.3 Modeling Electrostatic Forces (Nonlinear Problem)

Relax the pressure for a while, and have a new look at Fig. 7.1. The plate and the bottom of the cavity are both made of metallic material and form the two parts of a capacitor whose dielectric is the air within the cavity. A dielectric material is a substance that is poor conductor of electricity, but

[1] $\Delta(f_a + f_h) = \Delta f_a + \Delta f_h$ and consequently $\Delta^2(f_a + f_h) = \Delta^2 f_a + \Delta^2 f_h$.

[2] The normal vector, often simply called the "normal", to a surface is a vector perpendicular to it.

an efficient support of electrostatic fields. So, when both parts of the capacitor have different electric potential values, there exists a force bringing them closer.

We start with basic relationships expressing the electrostatic energy W and force F:

$$W = \frac{1}{2}CU^2 = \frac{\varepsilon S U^2}{2h}, \qquad F = -\frac{dW}{dh} = \frac{\varepsilon S U^2}{2h^2},$$

as functions of the capacitance C, the potential difference U, the air permittivity ε, the surface S of the plate, and the capacitor thickness h (i.e., the distance between the top and bottom plates; see Fig. 7.2). The electrostatic pressure acting on the plate is then obtained as

$$P_e = \frac{F}{S} = \frac{\varepsilon U^2}{2h^2}.$$

As with the acoustic pressure, the effect of the electrostatic pressure is to bend the plate. Consequently, the resulting deformation f_e is the solution of an equation similar to (7.3), with modified right-hand side P_e. The difference between the two cases is that the electrostatic pressure P_e is no longer a constant, like P_a, but depends on the position (x, y) since (see Fig. 7.2) $h = d - f_e(x, y)$.

In conclusion, the mathematical model taking into account the electrostatic forces consists of the following nonlinear PDE:

$$c_2 \Delta^2 f_e - c_1 \Delta f_e = P_e(f_e) = \frac{\varepsilon U^2}{2(d - f_e(x, y))^2}, \tag{7.6}$$

with Dirichlet and Neumann boundary conditions (which make the solution unique)

$$f_e = 0 \quad \text{and} \quad \frac{\partial f_e}{\partial \mathbf{n}} = 0 \quad \text{on} \quad \partial\Omega. \tag{7.7}$$

7.4 Numerical Discretization of the Problem

In this section we shall not worry about the right-hand side of the model equation (7.3) or (7.6) and discuss only the discretization of the differential operators (Laplacian and bilaplacian). We consider, for example, the equation (7.3) with boundary conditions (7.7).

Since it is not generally possible to obtain an exact (analytical) form of the solution f_a, we shall compute an approximate solution on a regular mesh representing the rectangular plate $\Omega = [0, L_x] \times [0, L_y]$ (see Fig. 7.3). We use the notation $M_{i,j}$ for the grid point of coordinates (x_i, y_j), with

$$x_i = i \cdot h_x, \quad i = 0, \ldots, mx + 1, \quad h_x = L_x/(mx + 1), \tag{7.8}$$

$$y_j = j \cdot h_y, \quad j = 0, \ldots, my + 1, \quad h_y = L_y/(my + 1). \tag{7.9}$$

Note that we have to compute only $mx \cdot my$ discrete values $f_{i,j}$ ($i = 1, \ldots, mx$, $j = 1, \ldots, my$), approximating the values $f_a(M_{i,j}) = f_a(x_i, y_j)$ of the exact solution, because the values on the boundaries are known (i.e., $f_{0,j} = f_{mx+1,j} = f_{i,0} = f_{i,my+1} = 0$). These values are obtained by approximating the differential operators in (7.3) using the *finite difference* method (see Chap. 1, or for more details Strikwerda (1989)).

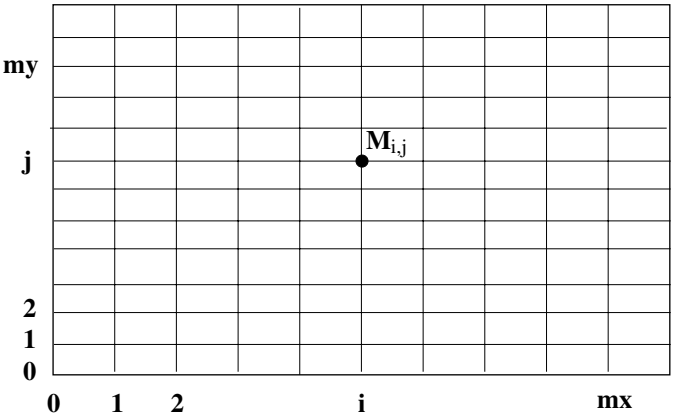

Fig. 7.3. A regular mesh (or grid).

To begin with, we address the case of the Laplacian. The easiest way to approximate second derivatives in this differential operator is to use centered differences, leading to the well-known 5-point (difference) scheme:

$$\begin{aligned} -(\Delta_5 f)_{i,j} = &\frac{1}{h_x^2}(-f_{i+1,j} + 2f_{i,j} - f_{i-1,j}) \\ &+ \frac{1}{h_y^2}(-f_{i,j+1} + 2f_{i,j} - f_{i,j-1}). \end{aligned} \tag{7.10}$$

This scheme is second-order accurate at any point of the grid, that is,

$$-(\Delta_5 f)_{i,j} = -(\Delta f)_{i,j} + O(h_m^2), \quad \text{with} \quad h_m = \max(h_x, h_y).$$

We proceed in the same manner to discretize the bilaplacian Δ^2. We first substitute in equation (7.10) all $f_{i,j}$ by $-(\Delta_5 f)_{i,j}$:

$$\begin{aligned} (\Delta_{13}^2 f)_{i,j} = &\frac{1}{h_x^2}(-(\Delta_5 f)_{i+1,j} + 2(\Delta_5 f)_{i,j} - (\Delta_5 f)_{i-1,j}) \\ &+ \frac{1}{h_y^2}(-(\Delta_5 f)_{i,j+1} + 2(\Delta_5 f)_{i,j} - (\Delta_5 f)_{i,j-1}). \end{aligned}$$

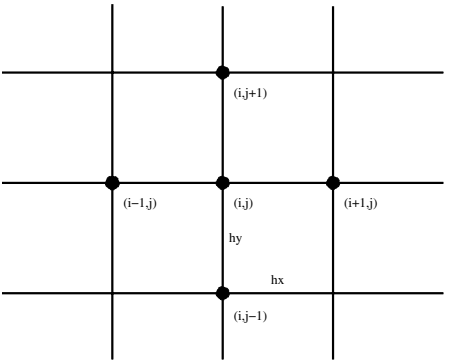

Fig. 7.4. Discretization of the two-dimensional Laplacian with a 5-point scheme.

Then, by inserting the expression of $-(\Delta_5 f)_{i,j}$ according to (7.10), we obtain the so-called 13-point scheme (see Fig. 7.5), which is also an approximation of second order:

$$\begin{aligned}(\Delta_{13}^2 f)_{i,j} = {} & \frac{1}{h_y^4} f_{i,j-2} \\ & + \frac{2}{h_x^2 h_y^2} f_{i-1,j-1} - \left(\frac{4}{h_x^2 h_y^2} + \frac{4}{h_y^4}\right) f_{i,j-1} + \frac{2}{h_x^2 h_y^2} f_{i+1,j-1} \\ & + \frac{1}{h_x^4} f_{i-2,j} - \left(\frac{4}{h_x^2 h_y^2} + \frac{4}{h_x^4}\right) f_{i-1,j} \\ & + \left(\frac{8}{h_x^2 h_y^2} + \frac{6}{h_x^4} + \frac{6}{h_y^4}\right) f_{i,j} \\ & - \left(\frac{4}{h_x^2 h_y^2} + \frac{4}{h_x^4}\right) f_{i+1,j} + \frac{1}{h_x^4} f_{i+2,j} \\ & + \frac{2}{h_x^2 h_y^2} f_{i-1,j+1} - \left(\frac{4}{h_x^2 h_y^2} + \frac{4}{h_y^4}\right) f_{i,j+1} + \frac{2}{h_x^2 h_y^2} f_{i+1,j+1} \\ & + \frac{1}{h_y^4} f_{i,j+2}.\end{aligned} \tag{7.11}$$

Finally, the discrete form of our PDE reads

$$c_2(\Delta_{13}^2 f)_{i,j} - c_1(\Delta_5 f)_{i,j} = P(M_{i,j}) = P_{i,j}, \tag{7.12}$$

where P stands for either acoustic or electrostatic pressure. These equations, written for any grid point $M_{i,j}$, with $i = 1, 2, \ldots, mx$ and $j = 1, 2, \ldots, my$, form a linear system whose unknowns are the $mx \cdot my$ values $f_{i,j}$. It is not difficult to observe that the discretization (7.11) is not well posed for grid

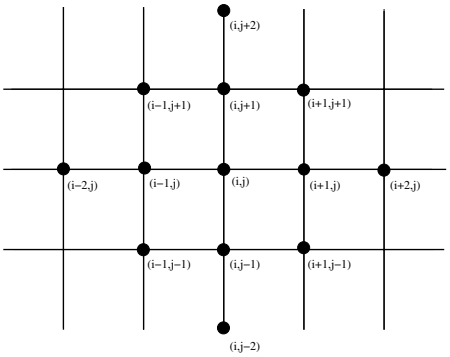

Fig. 7.5. Discretization of the two-dimensional bilaplacian with a 13-point scheme.

points near the boundaries, since it involves "ghost" points that do not exist (for example, the equation for $i = 1$ and any j requires the value of $f_{-1,j}$, which is not defined). We are fortunately rescued from this critical situation by the (Neumann) boundary condition on the normal derivative (7.5), which allows us to define such ghost points. Indeed, the derivative $\partial f/\partial n$ can be discretized by the first-order backward finite differences

$$(f_{i,j} - f_{i-1,j})/h_x = 0 \quad \text{and} \quad (f_{i,j} - f_{i,j-1})/h_y = 0,$$

for any point $M_{i,j}$ located on the boundary (i.e., $i = 0$ or $mx + 1$ and $j = 0$ or $my + 1$). Keeping in mind that $f_{i,j} = 0$ in any point $M_{i,j}$, following the (Dirichlet) boundary condition (7.5), we deduce that $f_{i,j} = 0$ for any ghost point.

Remark 7.1. We can use a simple programming trick when computing the $(mx \cdot my)^2$ matrix of the linear system (7.12). For the rows corresponding to $i = 1$ or $j = 1$ (and similarly, for $i = mx$ or $j = my$), we simply set the nonexistent (ghost) values to zero (i.e., if $i < 1$ or $j < 1$ and similarly for $i > mx$ or $j > my$). The right-hand side of the system is thus not affected.

Remark 7.2. Since one should expect from the discussion on the uniqueness of the solution of the continuous PDE (7.3), implementing discrete boundary conditions results in rendering the matrix of the linear system (7.12) invertible.

7.5 Programming Tips

7.5.1 Modular Programming

In the previous section, different logical steps have been pointed out when implementing the finite difference method:

1. definition of the coordinates (x_i, y_j) of any mesh point,

2. construction of the linear system (7.12),
3. introduction of the boundary conditions,
4. solving the linear system,
5. visualization of the results.

Any scientific package has to deal separately with each item of this list by associating a specialized computing procedure. These procedures are called *modules*. Results (outputs) of a given step module are data (inputs) for the next step module. Several modules may exist for the same logical step; in this case they all have to share similar formatted input and provide similar formatted output.

For the present study, we shall also proceed step by step, by setting up progressively the numerical operators. First, we neglect the effect of the electrostatic pressure in order to check the programs required to solve the linear problem (7.12). Then we shall deal with the nonlinear problem by iterating on successive linear problems.

7.5.2 Program Validation

Some questions can be asked when one uses a numerical approximation to solve a problem such as (7.3). Are we sure the good solution is computed with an effective procedure? How many points are required in order to get an accurate numerical solution? There is a simple way to answer these questions: it consists in solving a problem for which an exact solution is known, and then comparing the computed result to the exact one.

Let us consider, for example, the Laplace equation (7.1). We may choose a more or less complicated solution of the PDE, as for example

$$\tilde{f}_a(x,y) = 100\sin(3.7\pi x)\sin(5.4\pi y) + (3.7x - 5.4y), \tag{7.13}$$

and calculate the corresponding right-hand side (considering $c_1 = 1$):

$$\tilde{P}_a(x,y) = -\Delta\tilde{f}_a(x,y) = 100(3.7^2 + 5.4^2)\pi^2\sin(3.7\pi x)\sin(5.4\pi y). \tag{7.14}$$

A program solving the PDE $-\Delta f_a = P_a$, with boundary conditions $f_{a|\partial\Omega} = g(x,y)$, needs two inputs: $P_a(x,y)$ and $g(x,y)$. Inserting in the program (as discrete input data) the expression (7.14) for $P_a(x,y)$ and (7.13) for $g(x,y)$, we should obtain numerical values $f_{i,j}$ close to the exact values $\tilde{f}_a(x_i,y_j)$ at the same grid points (x_i,y_j). We are now able to compare the two solutions (exact and numerical) qualitatively by plotting the results in the same graphical window and quantitatively by computing, for example, the following relative approximation error:

$$\text{Error} = \frac{\sum_{i,j}|\tilde{f}_a(x_i,y_j) - f_{i,j}|^{1/2}}{\sum_{i,j}|\tilde{f}_a(x_i,y_j)|^{1/2}}. \tag{7.15}$$

This error has to be "reasonably" small and to diminish when the number of grid points is increased. If this is not the case, the program must be checked.

The same validation procedure can be used for the PDEs (7.2) and (7.3).

7.6 Solving the Linear Problem

In order to solve the linear problem (7.12) we note that

1. $n = mx \cdot my$, is the total number of grid points,
2. Ah_5 is the matrix associated with the 5-point scheme (including boundary conditions),
3. Ah_{13} is the matrix associated with the 13-point scheme (including boundary conditions),
4. b_5, b_{13} are the corresponding right-hand sides.

Exercise 7.1. 1. Write a program generating all the coordinates (x_i, y_j) of the grid points $M_{i,j}$, for $i = 1, 2, \ldots, mx$ and $j = 1, 2, \ldots, my$.
2. Write a program computing the matrix Ah_5 and the corresponding right-hand side b_5, in order to solve equation (7.1).
3. Write a program computing the matrix Ah_{13} and the corresponding right-hand side b_{13}, in order to solve equation (7.2).
4. Write a program computing the matrix Ah and the corresponding right-hand side b, in order to solve the complete problem (7.3), including the boundary conditions. Solve this problem for a given value of the pressure.
5. Visualize the results.

N.B. All the programs must be checked using the validation procedure described above.

A solution of this exercise and related procedures are described in Sect. 7.8 at page 162. We show here (see Fig. 7.6) a plot of the numerical solution obtained from validating the program solving the linear problem (7.3). The right-hand side of the PDE was calculated such that (7.13) becomes the exact solution. Even though a coarse mesh was used ($nx = 20$ and $ny = 30$), the numerical solution is very close to the exact one. The relative error (7.15) for this numerical experiment has the value Error = 0.0375. This error diminishes as the number of grid points increases (Error = 0.0095 for $nx = 40$ and $ny = 60$), but the computing time is considerably larger for this last run!

7.7 Solving the Nonlinear Problem

We now address the nonlinear problem, corresponding to a more realistic case when the plate is part of a microphone and subject to both acoustic and electrostatic pressures.

7.7.1 A Fixed-Point Algorithm

The resulting nonlinear problem is

$$c_2 \Delta^2 f - c_1 \Delta f = P_a + P_e(f), \tag{7.16}$$

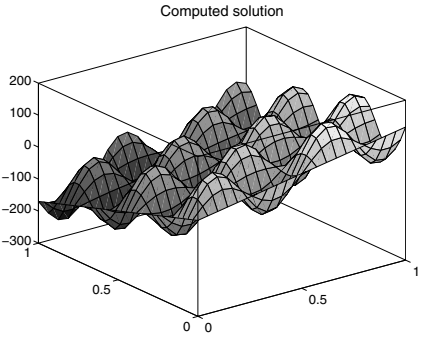

Fig. 7.6. Numerical solution obtained in validating the program solving the linear problem (7.3) by "imposing" the exact solution (7.13).

with Dirichlet and Neumann boundary conditions

$$f = 0 \quad \text{and} \quad \frac{\partial f}{\partial n} = 0 \quad \text{on} \quad \partial\Omega. \tag{7.17}$$

To solve this problem we use a fixed-point algorithm. We start by solving the linear problem (7.3) corresponding to $P_e = 0$; we denote by f_0 this solution. We define then the sequence $\{f_k\}_{k \in N}$ of solutions of successive linear problems:

$$c_2 \Delta^2 f_{k+1} - c_1 \Delta f_{k+1} = P_a + P_e(f_k). \tag{7.18}$$

Since the fixed-point algorithm is an iterative method, we have to choose a stopping criterion to decide whether a solution f_k is accurate enough to be a good approximation of the exact solution. A classical criterion is based on the relative variation of the approximate solution f_k:

$$\max_{x,y} |f_{k+1}(x,y) - f_k(x,y)| < \varepsilon \max_{x,y} |f_k(x,y)|, \tag{7.19}$$

where ε is the convergence threshold.

7.7.2 Numerical Solution

Once again, we shall first consider a test problem before solving (7.16) in order to validate the procedures. We choose the same test solution f as previously (7.13) and compute the corresponding right-hand side. For this case, we also have to impose the expression of the nonlinear term $P_e(f)$, depending on the solution. For example, we can use the function defined by

$$P_e(f) = \frac{100}{(200 - f)^2}.$$

For this choice and for the same grid ($nx = 20$ and $ny = 30$), the solution converges after only two iterations of the fixed-point algorithm (the convergence threshold is fixed to $\varepsilon = 0.001$). We check that the plot of the solution is similar to that displayed in Fig. 7.6. More details on the solution procedures can be found in Sect. 7.8 at page 162.

We consider now a more realistic choice of the values of the physical parameters[3] appearing in problem (7.16). The atmospheric pressure value is set to 10^5 [Pa] or [N/m^2], the acoustic pressure P_a then goes from 10^{-3} [Pa] to 10 [Pa]. It is established that the human ear can perceive pressure variations from 2×10^{-5} [Pa] up to 2 [Pa]. We may choose, without any damage to one's hearing or numerical procedures, the value of 1 [Pa] for the acoustic pressure variation.

We assume that the plate is made of silicon; for such a material the Young modulus is $E = 1.3 \cdot 10^{11}$ [Pa] and the Poisson coefficient is $\nu = 0.25$. The device displayed in Fig. 7.1 has the following characteristic dimensions: length 1 [mm], width 1 [mm], and thickness $e = 1$ [μm]. The mechanical stress of the plate is $T = 100$ [N/m]. Concerning the capacitor, the thickness (without pressure variations) is $d = 5$ [μm]. The dry-air permittivity is $\varepsilon = 8.85 \cdot 10^{-12}$ [F/m], and the polarization potential is $V = 25$ [V]. The mesh of the plate, as displayed in Fig. 7.3, has $nx = 20$ and $ny = 30$ grid points, resulting in a total number of 600 discretization points, and the same number of unknowns.

Exercise 7.2. 1. Modify the procedure used to solve Exercise 7.1 in order to use the above realistic data for the linear problem (7.3).
2. Write a program implementing the fixed-point algorithm.
3. Solve the nonlinear problem (7.16).
4. Visualize the results.

A solution of this exercise is proposed in Sect. 7.8 at page 162.

Hint: We first solve the acoustic problem (7.3) with boundary conditions (7.7) and obtain a deformation as plotted in Fig. 7.7. The maximum deformation value is located at the center of the plate ($\max f_a = 0.080$ [μm]).

In the next step, we consider the complete problem (7.16) including boundary conditions (7.17). The fixed-point algorithm will converge within three iterations when we use the stopping criterion (7.19) with $\varepsilon = 0.001$. The maximum deformation of the plate (see Fig. 7.7) is reached again at the center of the plate ($\max f_e = 0.077$ [μm]).

Remark 7.3. It is important to note that relative values of the acoustic pressure P_a and the polarization potential V were chosen in order to respect the constraint $\max f_a < d$ (see Fig. 7.2).

[3] As physical units, we use [Pa] = Pascal, [N] = Newton, [m] = meter, [mm] = millimeter, [μm] = micrometer [F] = Faraday, [V] = Volt.

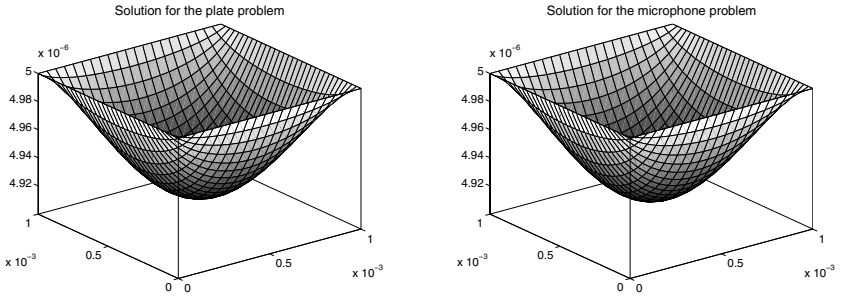

(a) (b)

Fig. 7.7. Numerical solution of the realistic problem. (a) linear; (b) nonlinear.

7.8 Solutions and Programs

Solution of Exercise 7.1

The file *ELAS_plate_ex.m* contains the procedure that solves the problem (7.3) and computes the test solution defined in *ELAS_solution.m*. This procedure calls the functions written in the files *ELAS_lap_matrix.m* and *ELAS_lap_rhs.m*, which compute the linear system obtained from the discretization of the equation (7.1). Similarly, procedures in the files *ELAS_bilap_matrix.m* and *ELAS_bilap_rhs.m* compute the linear system corresponding to equation (7.2). The computed test solution is plotted in Fig. 7.6.

Solution of Exercise 7.2

The main program solving the nonlinear problem (7.6) with realistic coefficients is written in the file *ELAS_microphone_ex.m*. It also contains the fixed-point algorithm. Functions in the files *ELAS_lap_matrix.m* and *ELAS_lap_rhs.m* (for the Laplacian part of the PDE) and in the files *ELAS_bilap_matrix.m* and *ELAS_bilap_rhs.m* (for the bilaplacian part of the PDE) are used as previously.

The new procedure `ELAS_pressure` defines the nonlinear term. The obtained numerical solutions are displayed in Fig. 7.7.

7.8.1 Further Comments

In this section we address the important point of the construction of the matrices arising from the approximation of the operators. The use of the rectangular mesh (displayed in Fig. 7.3), with a lexical ordering of the nodes, [4] added to the 5-point scheme approximation of the Laplacian (see Fig. 7.4),

[4] We order the nodes starting from the bottom line, from left to right $1, 2, \ldots, mx$; then we continue with the line just above, from left to right $mx + 1, mx + 2, \ldots, 2mx$, and so on.

lead altogether to a very particular pattern of the matrix Ah_5, displayed in Fig. 7.8. Such a matrix is called *banded*, of bandwidth $2mx + 1$, because its coefficients satisfy the relationship $(Ah_5)_{i\,j} = 0$ if $|i - j| > mx$. Note that this matrix is *sparse* because it contains only $5mx \cdot my$ nonzero coefficients. For the same reasons, the matrix associated with the bilaplacian (see Fig. 7.9) is banded of bandwidth $4mx+1$, and sparse with $13mx \cdot my$ nonzero coefficients. These properties are useful for reducing storage, because increasing the number of unknowns leads to huge use of memory. Scientific programs have to deal carefully with these properties; thankfully MATLAB is a user-friendly environment and provides very simple ways to build such matrices. For example, the following procedure (`ELAS_lap_matrix`) computes the matrix Ah_5:

```
n=nx*ny;
h2x=hx*hx;h2y=hy*hy;
Ah5=sparse(n,n);
Dx=toeplitz( [2.d0 -1.d0 zeros(1,nx-2) ] ) ;
Dx = Dx / h2x ;
Dy=eye(nx,nx) ;
Dy = - Dy / h2y ;
Dx = Dx - 2.d0 * Dy ;
for k=1:(ny-1)
    i=(k-1)*nx ; j=k*nx ;
    Ah5( (i+1) : (i+nx) , (i+1) : (i+nx) ) = Dx ;
    Ah5( (j+1) : (j+nx) , (i+1) : (i+nx) ) = Dy ;
    Ah5( (i+1) : (i+nx) , (j+1) : (j+nx) ) = Dy ;
end ;
i=(ny-1)*nx ;
Ah5( (i+1) : (i+nx) , (i+1) : (i+nx) ) = Dx ;
```

This program calls MATLAB built-in functions:

1. `sparse` is used to declare a low-storage sparse matrix;
2. `toeplitz` is used to define a Toeplitz matrix; here Dx is an $nx \times nx$ symmetric tridiagonal matrix whose entries are $(Dx)_{i\,i} = 2$ and $(Dx)_{i\,i-1} = -1$;
3. `eye` is used to define the $nx \times nx$ identity matrix;
4. then, the nonzero coefficients of Ah_5 are defined "block by block", using Dx to set diagonal blocks, respectively Dy for off-diagonal blocks.

Unfortunately, such a structure occurs in a very particular case, strongly depending on the geometry: for a nonrectangular mesh or with a random ordering of the nodes, the resulting matrix has a less-regular pattern (see for instance Chap. 11). Nevertheless, it remains sparse because this property is related only to the approximation scheme.

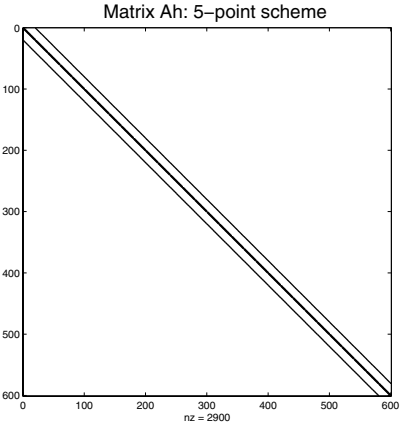

Fig. 7.8. Matrix Ah_5.

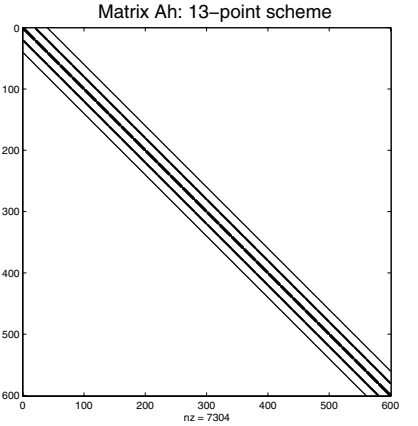

Fig. 7.9. Matrix Ah_{13}.

Chapter References

P. G. Ciarlet, *The Finite Element Method for Elliptic Problems*, North Holland, Amsterdam, 1978.

P. G. Ciarlet, *Mathematical Elasticity, Volumes I, II, III*, North Holland, Amsterdam, 2000.

J. C. Strikwerda, *Finite Difference Schemes and Partial Differential Equations*, Wadsworth and Brooks/Cole, 1989.

8

Domain Decomposition Using a Schwarz Method

Project Summary

Level of difficulty:	2
Keywords:	Domain decomposition, Schwarz method with overlapping, Laplacian discretization, 1D and 2D finite difference
Application fields:	Thermal analysis, steady heat equation

8.1 Principle and Application Field of Domain Decomposition

Realistic modeling of physical problems often involves systems of partial differential equations (PDE), usually nonlinear, and defined on domains that can have both large size and complex shape. In most cases, the selected numerical method requires that one discretize the domain, and the number of degrees of freedom can easily be more than what the available computer will handle. Modeling of the air flow around an aircraft with 3D finite elements requires, for instance, the discretization of the surrounding domain with a few million points, with several unknowns to determine at each point. The numerical scheme can furthermore be implicit and hence involve a linear-systems solution with this impressive number of unknowns. If we do not have a supercomputer at hand, which only very specialized research centers do, the matrix of such a system cannot even fit within the memory of the computer.

A simple answer to this technological lock is to subdivide the problem into smaller ones, that is, to compute the solution piecewise, as the solution of problems defined on subdomains of the initial one. Eventually, the global solution is the patch of all the solutions of partial problems.

This method can also simplify the solution of problems set originally on complexly shaped domains, by selecting a decomposition in which each subdomain has a simpler, elementary shape, making the local solution simpler to compute. Another possible extension is the coupling of equations in order to treat interactions between two different physical phenomena defined on neighboring domains, fluid structure interaction, for instance.

The main difficulty arising in adopting this method is the definition of boundary conditions on each subdomain. Actually, the internal boundaries, in contrast to boundaries of the global domain, are fictitious, and the physics of the problem doesn't provide boundary conditions. Two strategies, both iterative, can be adopted: The first one consists in doing a domain decomposition with partial overlapping of the subdomains, and using the previous iteration solution on neighboring subdomains to define the boundary conditions on the current subdomain. The second strategy consists in partitioning the global domain into nonoverlapping subdomains and imposing continuity conditions at the interfaces.

Once the decomposition strategy is selected, the solution method on each subdomain is the same as on the global domain, with now a reasonably small number of unknowns. To fix the ideas, consider the simple example of a scalar equation solved by finite differences on a structured mesh that can be decomposed into P subdomains of the same size N. The numerical treatment will require solving P linear systems costing $O(N^2)$ on each subdomain, that is, a total cost of $O(PN^2)$ per iteration, instead of $O(P^2N^2)$ for the global problem. The added cost of the new method comes from the iterative nature of the algorithm, and therefore the size and the number of the subdomains must be carefully selected in order to ensure the competitiveness of the algorithm.

In any case, even if the computing time increases compared to the initial global scheme, we always gain the crucial advantage of being able to fit the problem in the computer's memory.

Last but not least, even though this advantage cannot be illustrated within the scope of a MATLAB project, domain decomposition methods have really found their full worthiness with the development of parallel computing (see for instance Smith, Bjørstad, and Gropp (1996)). The solution of problems set on the subdomains can be distributed to different processors, with a serious hope of computing-time speedup as well as memory savings.

To illustrate the principles of the method, this project proposes an implementation of the Schwarz method with overlapping on model problems of the 1D and 2D Laplacian

$$\begin{cases} -\Delta u(x) + c(x)u(x) = f(x), & \text{for} \quad x \in \Omega \subset \mathbb{R}^n, \\ u = g, & \text{on} \quad \partial\Omega. \end{cases} \tag{8.1}$$

8.2 One-Dimensional Finite Difference Solution

In one dimension, the above problem becomes

$$\begin{cases} -u''(x) + c(x)u(x) = f(x), \quad \text{for} \quad x \in (a,b), \\ u(a) = u_a, \\ u(b) = u_b. \end{cases} \tag{8.2}$$

This problem models, for instance, the bending of a beam of length $b-a$, of constant section and of stiffness coefficient $c(x)$, pulled across its longitudinal axis and submitted to a transverse charge $f(x)dx$. The finite difference method for second-order boundary value problems such as the one above is described in detail in Lucquin and Pironneau (1996), and we just summarize the main features here. We discretize the interval $[a,b]$ on $n+2$ points $x_i = a + ih$ for $i = 0, \ldots, n+1$ with a uniform step $h = \frac{b-a}{n+1}$. We denote by U the vector formed by the approximation of the solution $u(x)$ at points x_i. We set $U_0 = u_a$ and $U_{n+1} = u_b$ to ensure that the numerical solution satisfies the boundary conditions. The finite difference discretization of the second derivative (as described, for instance, in Chap. 1) leads to the linear system

$$(S) \qquad A_h U = B_h,$$

where A_h is the $n \times n$ tridiagonal matrix

$$A_h = \frac{1}{h^2} \begin{pmatrix} 2+h^2c_1 & -1 & 0 & \ldots & \ldots & 0 \\ -1 & 2+h^2c_2 & \ddots & \ddots & \ddots & \vdots \\ 0 & \ddots & 2+h^2c_3 & \ddots & \ddots & \vdots \\ \vdots & \ddots & \ddots & \ddots & \ddots & 0 \\ \vdots & \ddots & \ddots & \ddots & 2+h^2c_{n-1} & -1 \\ 0 & \ldots & \ldots & 0 & -1 & 2+h^2c_n \end{pmatrix},$$

where $c_i = c(x_i)$ and B_h is the following vector in $\mathbb{R}^n$:

$$B_h = \begin{pmatrix} f(a+h) + \dfrac{u_a}{h^2} \\ f(a+2h) \\ . \\ . \\ f(b-h) + \dfrac{u_b}{h^2} \end{pmatrix}.$$

8.3 Schwarz Method in One Dimension

For simplicity, we first decompose the computational domain $[a,b]$ into two subdomains with overlapping: we choose an odd value n and two integer values i_l and i_r symmetric with respect to $\frac{n+1}{2}$ such that $i_l < \frac{n+1}{2} < i_r$. We set $x_l = i_l h$ and $x_r = i_r h$, thus defining two intervals $]a, x_r[$ and $]x_l, b[$ with a nonempty overlap $[a,x_r] \cap [x_l,b] = [x_l,x_r] \neq \emptyset$. We now plan to compute the solution u of the problem (8.2) by solving two problems set on the subintervals $[a,x_r]$ and $[x_l,b]$:

$$(P_1)\begin{cases} -u_1''(x) + c(x)u_1(x) = f(x), & \text{for} \quad x \in \ ]a, x_r[, \\ u_1(a) = u_a, \\ u_1(x_r) = \alpha; \end{cases}$$

and

$$(P_2)\begin{cases} -u_2''(x) + c(x)u_2(x) = f(x), & \text{for} \quad x \in \ ]x_l, b[, \\ u_2(x_l) = \beta, \\ u_2(b) = u_b. \end{cases}$$

The solution u_1 (respectively u_2) is expected to be the restriction on the interval $[a, x_r]$ (respectively $[x_l, b]$) of the solution u of the problem set on the full interval $[a, b]$. The two solutions u_1 and u_2 must therefore be identical within the overlapping region $[x_l, x_r]$, which allows us to define the boundary conditions in x_l and x_r:

$$u_1(x_r) = \alpha = u_2(x_r) \quad \text{and} \quad u_2(x_l) = \beta = u_1(x_l).$$

Since we do not know a priori the values of α and β, we solve the two problems iteratively: α is fixed arbitrarily, at first, for instance, by linear interpolation of the global boundary conditions

$$\alpha = \frac{1}{b-a}(u_a(b - x_r) + u_b(x_r - a)).$$

Then we set $u_2^0(x_r) = \alpha$ and we compute for $k = 1, 2, \ldots$ the solutions u_1^k and u_2^k of the following problems:

$$(P_1)\begin{cases} -u_1''(x) + c(x)u_1(x) = f(x), & \text{for} \quad x \in (a, x_r), \\ u_1(a) = u_a, \\ u_1(x_r) = u_2^{k-1}(x_r); \end{cases}$$

then

$$(P_2)\begin{cases} -u_2''(x) + c(x)u_2(x) = f(x), & \text{for} \quad x \in (x_l, b), \\ u_2(x_l) = u_1^k(x_l), \\ u_2(b) = u_b. \end{cases}$$

We claim that when the overlap region is nonempty, this algorithm converges to the solution u of the global problem (8.2) as $k \longrightarrow \infty$. This result was first proved using fixed point theorem by Schwarz (1870), in the case $c(x) = 0$. It was rediscovered one century later using a variational formulation approach by Lions (1988). More efficient methods from the algorithmic point of view have been developped since then, which do not require overlap but impose additionnal transfer conditions between subdomains. The following paragraphs will illustrate numerically the convergence, after discretization of $(P1)$ and $(P2)$ by finite difference.

8.3.1 Discretization

The problems P_1 and P_2 are solved using finite differences, in the same manner as used for the global problem (8.2) in the previous section. The bounds x_l and

x_r have been set so that the two subdomains are of the same size. Denoting by V^k (respectively W^k) the vector of the approximate discrete solution on the subdomain $[a, x_r]$ (respectively $[x_l, b]$) the algorithm for the kth iteration is as follows:

$$\left\| \begin{array}{l} \text{initialization :} \quad W_{i_r}^0 = \alpha \\ \text{for} \quad k = 1, 2, \ldots, \quad \text{do} \\ \qquad A_{h,l} V^k = B_{h,l} + \dfrac{1}{h^2}[u_a, 0, \ldots, 0, W_{i_r}^{k-1}]^T, \\ \qquad A_{h,r} W^k = B_{h,r} + \dfrac{1}{h^2}[V_{i_l}^k, 0, \ldots, 0, u_b]^T, \\ \text{end} \end{array} \right. \tag{8.3}$$

where $A_{h,l}$ (respectively $A_{h,r}$) is the discretization matrix for the operator $-\Delta + c\mathrm{I}$ on $]a, x_r[$ (respectively $]x_l, b[$) in $\mathbb{R}^{i_r - 1} \times \mathbb{R}^{i_r - 1}$:

$$A_{h,l} = \frac{1}{h^2} \begin{pmatrix} 2 + h^2 c_1 & -1 & 0 & \ldots & \ldots & 0 \\ -1 & 2 + h^2 c_2 & -1 & 0 & \ddots & \vdots \\ 0 & \ddots & \ddots & \ddots & \ddots & \vdots \\ \vdots & \ddots & \ddots & \ddots & \ddots & 0 \\ \vdots & \ddots & 0 & -1 & 2 + h^2 c_{i_r - 2} & -1 \\ 0 & \ldots & \ldots & 0 & -1 & 2 + h^2 c_{i_r - 1} \end{pmatrix}$$

and

$$A_{h,r} = \frac{1}{h^2} \begin{pmatrix} 2 + h^2 c_{i_l + 1} & -1 & 0 & \ldots & \ldots & 0 \\ -1 & 2 + h^2 c_{i_l + 2} & -1 & 0 & \ddots & \vdots \\ 0 & \ddots & \ddots & \ddots & \ddots & \vdots \\ \vdots & \ddots & \ddots & \ddots & \ddots & 0 \\ \vdots & \ddots & 0 & -1 & 2 + h^2 c_{n-1} & -1 \\ 0 & \ldots & \ldots & 0 & -1 & 2 + h^2 c_n \end{pmatrix}.$$

The vectors B_l and B_r contain the values of the right-hand-side term f evaluated at the discretization points

$$\begin{aligned} (B_{h,l})_i &= f(x_i), \quad \text{for} \quad i = 1, \ldots, i_r - 1, \\ (B_{h,r})_i &= f(x_{i+i_l}), \quad \text{for} \quad i = 1, \ldots, n - i_l. \end{aligned}$$

The stopping criterion in the iteration loop is obtained by measuring the gap between the two solutions within the overlap region $[x_l, x_r]$, where they should coincide in the limit:

$$\|e^k\| \leq \varepsilon, \quad \text{with} \quad e_{i-i_l}^k = V_i^k - W_{i-i_l}^k, \quad \text{for} \quad i = i_l + 1, \ldots, i_r - 1.$$

In order to test the performance of the method, we can also compare the results with the solution U obtained in Sect. 8.2 using the classical method on the whole domain.

We accordingly compute two vectors e_l^k and e_r^k of components

$$(e_l^k)_i = U_i - V_i^k, \quad \text{for} \quad i = 1, \ldots, i_r - 1,$$
$$(e_r^k)_{i-i_l} = U_i - W_{i-i_l}^k, \quad \text{for} \quad i = i_l + 1, \ldots, n,$$

and we observe the decay of their norm with iteration along with the e_k norm decay.

Exercise 8.1. Write a program to implement Algorithm 8.3. Display in the same graphics window but with different colors the solutions V^k, W^k, and U, refreshing the graphics at each iteration k. One should obtain a sequence of graphs as in Fig. 8.2. Represent the evolution of the three errors $\|e^k\|$, $\|e_l^k\|$, and $\|e_r^k\|$ as functions of k in another graphics window as in Fig. 8.1.
A solution of this exercise is proposed in Sect. 8.5 at page 181.

Exercise 8.2. Modify the program of Exercise 8.1 and turn it into a function receiving as input argument the number of points $n_o = i_r - i_l - 1$ in the overlap region. This function computes and returns as output arguments the number of iterations necessary to reach the tolerance error and the computing time. Write a program that calls this function for varying values of n_o and analyze the influence of the size of the overlap region on the algorithm's convergence.
A solution of this exercise is proposed in Sect. 8.5 at page 182.

Figures 8.1 and 8.2 illustrate the results for a beam of length 1 meter, with a constant stiffness coefficient $c = 10$. The left end of the beam is fixed equal to 10 cm higher than the right end. The beam is subject to its own weight of 1 N/m as well as to an overload of 9 N/m on a 40 cm portion, starting 20 cm from its left end.

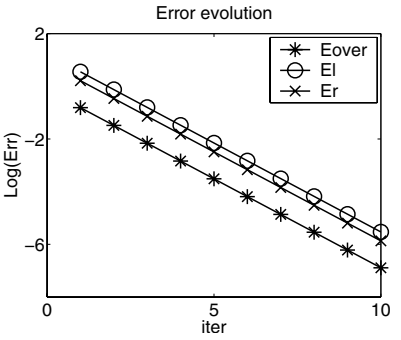

Fig. 8.1. Logarithm of the L^2 norm of the error versus the number of iterations.

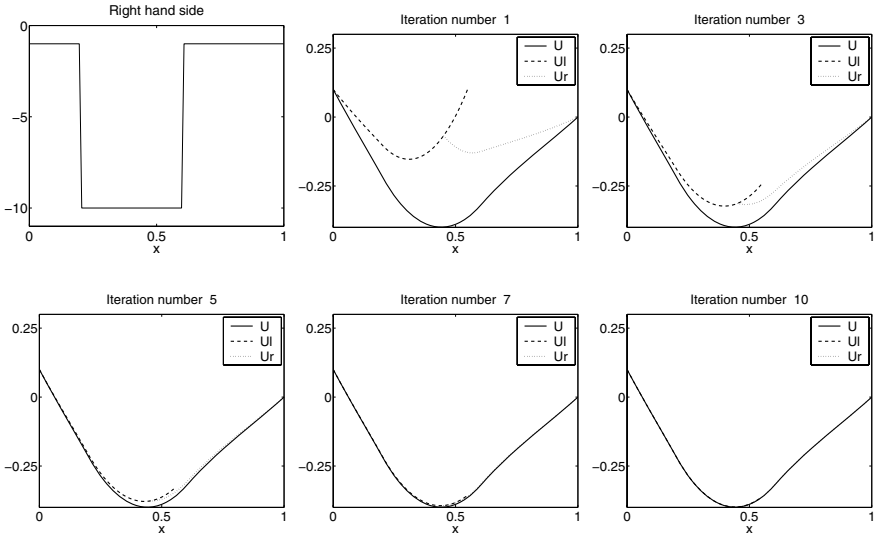

Fig. 8.2. Right-hand side $f(x)$, global, and local solutions for varying numbers of iterations.

8.4 Extension to the Two-Dimensional Case

We now focus on the 2D problem (8.1) set on a rectangle. We restrict ourselves to the case $c = 0$, thus modeling a steady heat conduction 3D problem in a metallic piece where one dimension is much larger than the two others (see Fig. 8.3). Variations in the temperature will be neglected in this direction. In the first case, we impose on the boundary inhomogeneous Dirichlet conditions:

$$\begin{cases} -\Delta u(x_1, x_2) = F(x_1, x_2), & \text{for} \quad (x_1, x_2) \in \ ]a_1, b_1[\times]a_2, b_2[, \\ u(a_1, x_2) = f_2(x_2), & \text{for} \quad x_2 \in \ ]a_2, b_2[, \\ u(b_1, x_2) = g_2(x_2), & \text{for} \quad x_2 \in \ ]a_2, b_2[, \\ u(x_1, a_2) = f_1(x_1), & \text{for} \quad x_1 \in \ ]a_1, b_1[, \\ u(x_1, b_2) = g_1(x_1), & \text{for} \quad x_1 \in \ ]a_1, b_1[. \end{cases} \tag{8.4}$$

From a practical point of view this computation models, for instance, a **thermal shock** test on a metallic beam. An experimental setup can consist, for instance, of a null temperature on faces $x_1 = a_1$ and $x_1 = b_1$, that is, $f_2(x_2) = g_2(x_2) = 0$, a temperature of 50°C on the face $x_2 = a_2$, that is, $f_1(x_1) = 50$, and a temperature of 100°C on the face $x_2 = b_2$, that is, $g_1(x_1) = 100$. Furthermore, since no internal heat sources are present, the right-hand side is null: $F(x_1, x_2) = 0$.

8.4.1 Finite Difference Solution

We restrict ourselves to the case in which the domain dimensions are such that it is possible to use the same discretization step in both directions x_1 and x_2.

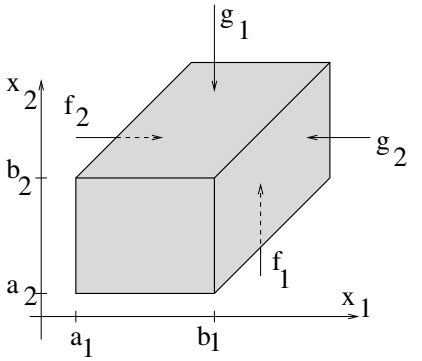

Fig. 8.3. Sketch of the metallic piece subject to a thermal shock.

We therefore define $h = \frac{b_1 - a_1}{n_1} = \frac{b_2 - a_2}{n_2}$. On this regular grid (see Fig. 8.4), we denote by $u_{i,j} = u(a_1 + ih, a_2 + jh)$ (respectively $f_{i,j}$) the discretized value of the solution $u(x_1, x_2)$ (respectively $F(x_1, x_2)$) at the discretization points. In that case, using Taylor expansions in x_1 and in x_2 in order to approximate

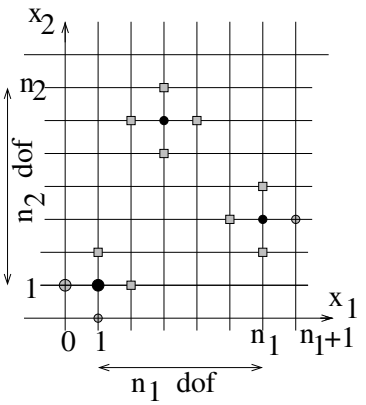

Fig. 8.4. Discretization of the domain interior Ω using $n_1 \times n_2$ points.

partial derivatives in both directions, we obtain the Laplacian discretization with a five-point scheme,

$$\Delta u_{i,j} \approx \frac{4u_{i,j} - u_{i-1,j} - u_{i+1,j} - u_{i,j-1} - u_{i,j+1}}{h^2},$$

which is an $O(h^2)$ approximation if u is smooth enough (i.e., $u \in C^4$). The finite difference solution W is hence a solution of the following linear system:

$$\frac{4u_{i,j} - u_{i-1,j} - u_{i+1,j} - u_{i,j-1} - u_{i,j+1}}{h^2} = f_{i,j}, \tag{8.5}$$

where the unknowns are the $u_{i,j}$ for $i = 1, \ldots, n_1$ and $j = 1, \ldots, n_2$. In fact, the values of the solution on the boundaries, corresponding to indices $i = 0$ or $i = n_1 + 1$ and $j = 0$ or $j = n_2 + 1$, are set by the boundary conditions

$$\begin{aligned} u_{0,j} &= f_2(a_2 + jh), \quad u_{n+1,j} = g_2(a_2 + jh), \\ u_{i,0} &= f_1(a_1 + ih), \quad u_{i,n+1} = g_1(a_1 + ih). \end{aligned}$$

Each row of the linear system (8.5) has at most five nonzero terms: the diagonal term coefficient is $\frac{4}{h^2}$, and for the off-diagonal terms, corresponding to the neighbors with indices

$$(i+1, j), \quad (i-1, j), \quad (i, j-1), \quad \text{and} \quad (i, j+1),$$

which do not belong to the boundary, the coefficients are equal to $\frac{-1}{h^2}$. These nodes are represented by squares in Fig. 8.4.
We can build the matrix using block matrix symbolism: the degrees of freedom (i, j), $(i+1, j)$, and $(i-1, j)$ are neighbors in the grid and also consecutive in the global numbering of the degrees of freedom. The coefficients of the linear system that link nodes belonging to a given row j, for $j = 1, \ldots, n_2$, can therefore be rewritten as a tridiagonal matrix

$$T = \frac{1}{h^2} \begin{pmatrix} 4 & -1 & 0 & \ldots & \ldots & 0 \\ -1 & 4 & -1 & \ddots & \ddots & \vdots \\ 0 & \ddots & 4 & \ddots & \ddots & \vdots \\ \vdots & \ddots & \ddots & \ddots & \ddots & 0 \\ \vdots & \ddots & \ddots & \ddots & 4 & -1 \\ 0 & \ldots & \ldots & 0 & -1 & 4 \end{pmatrix} \tag{8.6}$$

The two other neighbors of the node (i, j) in the grid are the nodes $(i, j-1), (i, j+1)$, which are n_1 nodes away on each side of the central node in the global numbering, and their connection is ensured through a diagonal matrix $D = \frac{-1}{h^2} I_{n_1 \times n_1}$ on each side of the matrix T. The matrix of the global linear system $AU = B$ is hence a tridiagonal block matrix of size $n_2 \times n_2$, each block being of size $n_1 \times n_1$:

$$A = \begin{pmatrix} T & D & 0 & \ldots & 0 \\ D & T & D & \ddots & \vdots \\ 0 & \ddots & \ddots & \ddots & 0 \\ \vdots & \ddots & D & T & D \\ 0 & \ldots & 0 & D & T \end{pmatrix}. \tag{8.7}$$

The right-hand side B of the linear system is a vector of size $n_1 \cdot n_2$, which can be built as a matrix to benefit from the numbering of the degrees of freedom associated with the grid. We start by initializing the right-hand-side vector using the right-hand-side function $F(x_1, x_2)$ at the grid nodes:

$$B_{i,j} = f_{i,j}, \quad \text{for} \quad 1 \le i \le n_1, \quad 1 \le j \le n_2. \tag{8.8}$$

If the node (i, j) has a neighbor on the grid boundary (represented by a gray circle in Fig. 8.4), the contribution $\frac{u_{i',j'}}{h^2}$ of this neighbor (i', j') in the Laplacian discretization at point (i, j) must be added to the (i, j) right-hand side coefficient, the value of $u_{i',j'}$ being set by the boundary condition. The boundary condition contributions are therefore added to all terms $B_{1,i}$, $B_{n_1,i}$ for $i = 1, \ldots, n_2$ and $B_{i,1}$, B_{i,n_2} for $i = 1, \ldots, n_1$. Beware of the special case occuring at the four corners!

$$\begin{cases} B_{1,i} = B_{1,i} + \dfrac{f_2(a_2 + ih)}{h^2}, \\ B_{n_1,i} = B_{n_1,i} + \dfrac{g_2(a_2 + ih)}{h^2}, \end{cases} \quad \text{for} \quad 1 \le i \le n_1,$$

$$\begin{cases} B_{i,1} = B_{i,1} + \dfrac{f_1(a_1 + ih)}{h^2}, \\ B_{i,n_2} = B_{i,n_2} + \dfrac{g_1(a_1 + ih)}{h^2}, \end{cases} \quad \text{for} \quad 1 \le j \le n_2. \tag{8.9}$$

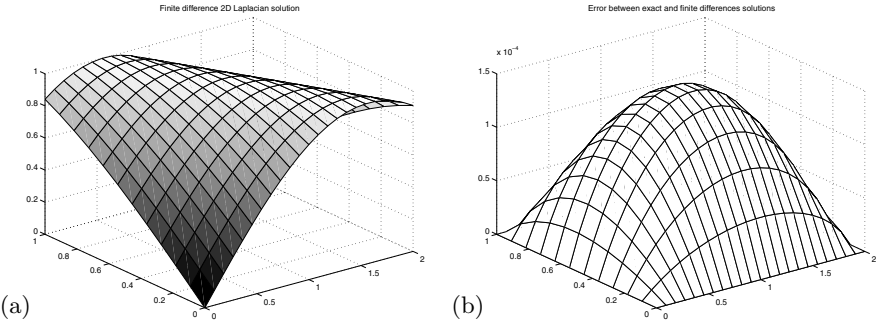

Fig. 8.5. (a) Global solution and (b) error between exact solution and finite difference approximation.

Exercise 8.3. 1. Write a function `DDM_LaplaceDirichlet` to compute the matrix A of size $n_1 n_2 \times n_1 n_2$ of the global linear system. The function computes and returns the matrix A. It receives in its input arguments the lower bounds of the domain, a_1 and a_2; the number of points in each direction, n_1 and n_2; and the discretization step h. The matrix A will be built by blocks using a tridiagonal matrix T and the identity matrix, both of size $n_1 \times n_1$.

2. Write a function `DDM_RightHandSide2d` to compute the right-hand-side vector of the linear system. The function returns the vector B. It receives in its input arguments the lower bounds of the domain, a_1 and a_2; the number of points in each direction, n_1 and n_2; and the discretization step

h. It calls the function `rhs2d(x1,x2)`, which computes the value of the right-hand-side function $F(x_1, x_2)$.

3. Write a function `DDM_FinDif2d` to compute the finite difference solution. The calling sequence should be

```
function [n2,b2,Solm]=DDM_FinDif2d(n1,a1,a2,b1,b2, rhs2d,...
                        f1,g1,f2,g2,RightHandSide2d,Laplace),
```

   where `f1,g1,f2,g2` are the names of the functions defining the boundary conditions.

4. We select a function $u(x_1, x_2) = \sin(x_1 + x_2)$ that is the exact solution of the problem $-\Delta u = f$ with the right-hand-side function $F(x_1, x_2) = 2\sin(x_1 + x_2)$ and with boundary conditions equal to the restrictions of the exact solution on the boundaries:

$$f_1(x_1) = \sin(x_1 + a_2), \quad g_1(x_1) = \sin(x_1 + b_2),$$
$$f_2(x_2) = \sin(a_1 + x_2), \quad g_2(x_2) = \sin(b_2 + x_2).$$

   Program the functions `DDM_rhs2dExact(x1,x2)`, `DDM_f1Exact(x1)`, `DDM_g1Exact(x1)`, `DDM_f2Exact(x2)`, `DDM_g2Exact(x2)` corresponding to this test case, along with the function `DDM_u2dExact(x1,x2)`, which will be used to compute the exact solution at the grid discretization points.

5. Write a program `DDM_TestFinDif2d` to test the previously defined functions: the size of the domain must be carefully chosen to ensure that the discretization step is the same in both directions. The solution computed with the parameters $a_1 = a_2 = 0$, $b_1 = 1$, $b_2 = 2$, $n_1 = 20$, is represented in Fig. 8.5(a). Check the computation by displaying the error, that is, the difference between the exact solution $u(x_1, x_2) = \sin(x_1 + x_2)$ and the finite difference solution, as in Fig. 8.5(b).

6. Modify the previous program and adapt it to the thermal shock case (8.4) defined in Sect. 8.4, to obtain the solution displayed in Fig. 8.6. Use first a square domain of size $b_1 - a_1 = b_2 - a_2 = 6$, then a rectangular one of dimensions $b_1 - a_1 = 6$ and $b_2 - a_2 = 20$.

   A solution of this exercise is proposed in Sect. 8.5 at page 182.

8.4.2 Domain Decomposition in the Two-Dimensional Case

We will now apply the technique described in Sect. 8.3 in the 2D case. The global domain is decomposed into n_s subdomains with an overlap in the direction x_2. Here again, in order to simplify the implementation, we assume that the domain can be discretized with the same step h in both directions. Furthermore, we also impose that all subdomains have the same size $(n_2+1)h$ and that all overlap regions have the same number of grid cells n_o. Figure 8.7 shows an example of a decomposition satisfying these constraints. Note that they are very restrictive and might not be satisfied for an arbitrary domain

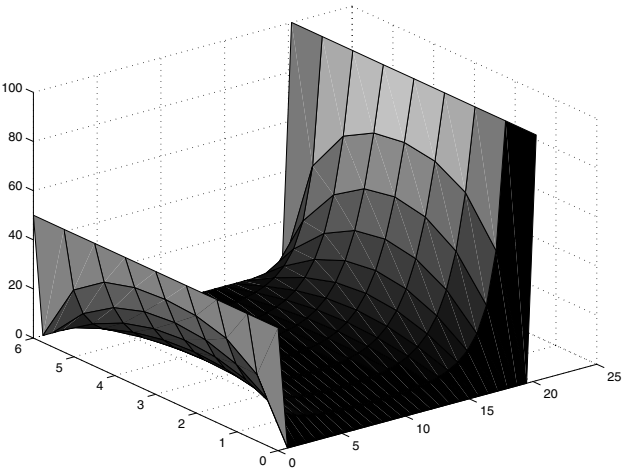

Fig. 8.6. Solution of the thermal shock problem.

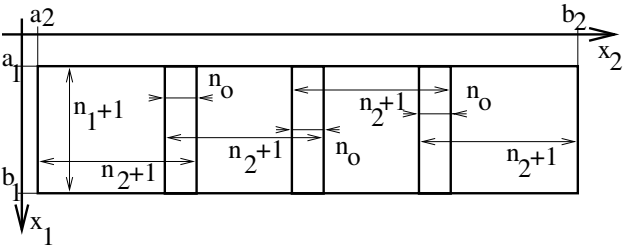

Fig. 8.7. Decomposition into four identical subdomains with constant overlap.

$[a_1, b_1] \times [a_2, b_2]$. It might be necessary to adjust the total length $b_2 - a_2$. We denote by $u^{s,k}$ the solution on the sth subdomain $[a_1, b_1] \times [a_2^s, b_2^s]$, for $s = 1, \ldots, n_s$, at iteration number k, for $k = 0, 1, \ldots$. The bounds of the subdomain, a_2^s and b_2^s, are equal to $a_2^1 = a_2$ and $a_2^s = a_2^{s-1} + (n_2 + 1 - n_o)h$ for $k > 1$ and $b_2^s = a_2^s + (n_2 + 1)h$.

With this notation, $u^{s,k}$ is solution of the problem

$$
\begin{cases}
-\Delta u^{s,k}(x_1, x_2) = F(x_1, x_2), \quad \text{for } (x_1, x_2) \in (a_1, b_1) \times (a_2^s, b_2^s), \\
u^{k,s}(a_1, x_2) = f_2(x_2), \quad \text{for } x_2 \in (a_2^s, b_2^s), \\
u^{s,k}(b_1, x_2) = g_2(x_2), \quad \text{for } x_2 \in (a_2^s, b_2^s), \\
u^{s,k}(x_1, a_2^s) = \begin{cases} f_1(x_1), \quad \text{for} \quad s = 1, \\ u^{s-1,k}(x_1, a_2^s), \quad \text{for} \quad s = 2, \ldots, n_s, \end{cases} \quad \text{for} \quad x_1 \in (a_1, b_1), \\
u^{s,k}(x_1, b_2^s) = \begin{cases} g_1(x_1), \quad \text{for} \quad s = n_s, \\ u^{s+1,k-1}(x_1, b_2^s), \quad \text{for} \quad s = 1, \ldots, n_s - 1, \end{cases} \quad \text{for } x_1 \in (a_1, b_1).
\end{cases}
$$

At the first iteration, the boundary condition on the right end of the subdomain is not defined, except for the last one, where it is the global boundary condition. For all others it must therefore be arbitrarily fixed, for instance by

linear interpolation of the global boundary conditions f_1 and g_1:

$$u^{s+1,0}(x_1, b_2^s) = ((b_2 - b_2^s) f_1(x_1) + (b_2^s - a_2) g_1(x_1))/(b_2 - a_2).$$

The iterations stop whenever the sum (or the maximum) of the error norm on each overlap region is below a given tolerance.

We denote by X_1 the vector of the abscissa $a_1 + jh$, for $j = 1, \ldots, n_1$, and by X_2^s the vector of the ordinates in the sth subdomain $a_2 + jh + (s-1)(n_2+1-n_o)$, for $j = 1, \ldots, n_2$. The Schwarz algorithm in two dimensions can be written as

$$\begin{array}{l}
\text{Initialization:} \\
\quad U_{a_2 l} = f_1(X_1), \quad U_{b_2 r} = g_1(X_1), \\
\quad U^{s,0}_{.,n_o} = ((b_2 - b_2^s) U_{b_2 r} + (b_2^s - a_2) U_{a_2 l})/(b_2 - a_2)), \quad \text{for } s = 2, \ldots, n_s, \\
\quad U^s_{a_1} = f_1(X_2^s), \quad U^s_{b_1} = g_1(X_2^s), \quad B^s_{.,.} = F(X_1, X_2^s), \\
\quad B^s_{1,.} = B^s_{1,.} + U^s_{a_1}/h^2, \quad B^s_{n_1,.} = B^s_{n_1,.} + U^s_{b_1}/h^2, \\
\text{for} \quad k = 1, 2, \ldots \quad \text{do} \\
\quad \text{for} \quad s = 1, \ldots, n_s \quad \text{do} \\
\qquad \text{if } s = 1, \quad U^s_{a_2} = U_{a_2 l} \quad \text{else} \quad U^s_{a_2} = U^{s-1,k}_{.,n_2+1-n_o} \\
\qquad \text{if } s = n_s, \quad U^s_{b_2} = U_{b_2 r} \quad \text{else} \quad U^s_{b_2} = U^{s+1,k-1}_{.,n_o} \\
\qquad B^{s,k} = B^s, \quad B^{s,k}_{.,1} = B^{s,k}_{.,1} + U^s_{a_2}/h^2 \quad B^{s,k}_{.,n_2} = B^{s,k}_{.,n_2} + U^s_{b_2}/h^2 \\
\qquad \text{solve } A U^{s,k} = B^{s,k} \\
\qquad \text{if } s > 1, \quad R^s_{.,j} = U^{s,k}_{.,j} - U^{s-1,k}_{.,n_2-n_o+1+j}, \quad \text{for } j = 1, \ldots, n_o - 1 \\
\quad \text{end} \\
\quad E^k = \sup_{s=2,\ldots,n_s} \|R^s\| \\
\text{if } E^k < \varepsilon \quad \text{end}
\end{array} \tag{8.10}$$

In this algorithm, A is the matrix resulting from the discretization of the operator $-\Delta$, defined by (8.7). It is here the same matrix for all subdomains.

Exercise 8.4. 1. Write a function `DDM_Schwarz2d` to implement the above algorithm. The calling syntax should be

```
function [conviter,cpu,mem,n2,b2]=DDM_Schwarz2d(n1,ns,no,...
  a1,a2,b1,b2,rhs2d,f1,g1,f2,g2,RightHandSide2d,Laplace,n11),
```

where the input parameters are

- `n1`, the number of cells in direction x_1,
- `n11`, the number of degrees of freedom in direction x_1,
- `ns`, the number of subdomains,
- `no`, the number of cells in the overlap regions in direction x_2,
- `Laplace`, the name of the function to compute the Laplacian discretization matrix,
- `RightHandSide2d`, the name of the function to compute the right-hand side,
- `rhs2d`, the name of the function $F(x_1, x_2)$,
- `f1`, the name of the function $f1(x_1)$ defining the boundary condition on the edge $x_2 = a_2$,

- `g1`, the name of the function $g1(x_1)$ defining the boundary condition on the edge $x_2 = b_2$,
- `f2`, the name of the function $f2(x_2)$ defining the boundary condition on the edge $x_1 = a_1$,
- `g2`, the name of the function $g2(x_2)$ defining the boundary condition on the edge $x_1 = b_1$.

The function returns as output arguments

- `conviter`, the number of iterations necessary to have a maximum error in the overlap regions below the specified tolerance `tol`,
- `cpu`, the computing time,
- `mem`, the necessary memory.

2. Write a program `DDM_TestSchwarz2d` to test the algorithm with the same function f as in the global case for the following parameter values: $a_1 = a_2 = 0$, $b_1 = 1$, $n_1 = 9$, $b_2 = 30$, $n_o = 10$, $n_s = 20$.
   A solution of this exercise is proposed in Sect. 8.5 at page 184.

Study of the method's performance: we now study the influence of the subdomain size on the convergence speed. We therefore need to estimate, for a given subdomain decomposition, the computing time necessary to achieve the specified accuracy. Computing time is measured within MATLAB using the commands `tic` and `toc` at the beginning and end of the script, or part of the script, that is to be monitored. Since it is the elapsed time that is actually measured, this is best done on a single-user computer. Furthermore, in order to be able to compare several configurations, only one parameter should vary. We keep constant the dimensions of the global domain, which imposes constraints on the number of subdomains, their size, and the size of the overlap region.

Exercise 8.5. Fix the parameters $b_1 = 1$, $b_2 = 50$, $n_1 = 9$, and the overlap size $n_o = 4$. We assume that realistic values for the number s of subdomains will run from 5 to 60. For each value of n_s within this range, check whether the decomposition is possible, and if it is, compute the solution using the function `DDM_Schwarz2`. Display the performance in computing time, memory, number of iterations, as a function of parameters n_o and n_s. Analyze the influence of the overlap size on the algorithm's convergence.
A solution of this exercise is proposed in Sect. 8.5 at page 187.

8.4.3 Implementation of Realistic Boundary Conditions

More realistic heat conduction test cases require the implementation of additional boundary conditions besides the Dirichlet one that we have used so far. Let us consider, for instance, the temperature field within a bus bar like the one sketched in Fig. 8.8. The electric field produces heat at the uniform rate $F(x_1, x_2) = q = 10^6$ W/m^3. The following temperatures are imposed on the electrodes: 40°C on the left end and 10°C on the right end, thanks to

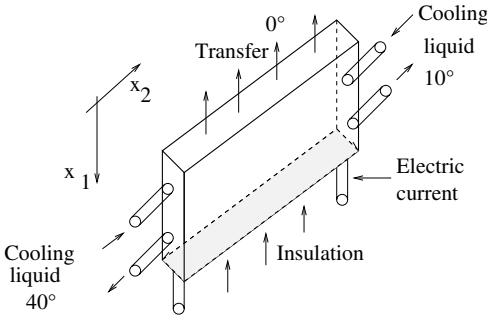

Fig. 8.8. Bus bar sketch.

a cooling liquid circulation device. The two lateral faces of the bar as well as the bottom face are insulated, meaning that a Neumann boundary condition has to be imposed. On the upper face, we impose a Fourier, or Robin, boundary condition in order to model the natural convection-driven cooling phenomenon. The thermal transfer coefficient is equal to $c_{\text{th}} = 75$ W/m^2 and the outside temperature is 0°C. The thermal diffusivity coefficient of the alloy is equal to $k = 20$ W/m K. Solving for $\tilde{u} = u - u_{\text{ext}}$, problem (8.1) becomes in this particular case

$$\begin{cases} -k\Delta u(x_1, x_2) = q, \quad \text{for} \quad x \in \Omega, \\ u = 40, \quad \text{on} \quad x_2 = a_2, \\ u = 10, \quad \text{on} \quad x_2 = b_2, \\ \dfrac{\partial u}{\partial n} = 0, \quad \text{on} \quad x_1 = b_1, \\ \dfrac{\partial u}{\partial n} + c_{\text{th}} u = 0, \quad \text{on} \quad x_1 = a_1. \end{cases} \tag{8.11}$$

Here $\frac{\partial}{\partial n}$ denotes the derivative with respect to the normal vector to the surface. In order to discretize these Neumann and Fourier boundary conditions we introduce in the system the degrees of freedom corresponding to these nodes on the faces $x_1 = a_1$ and $x_1 = b_1$. There are now $n_1 + 2$ nodes in the x_1 direction instead of the n_1 in the Dirichlet case. For the nodes where the Neumann condition applies, we write

$$u_{n_1+1,j} = u_{n_1+2,j},$$

which eliminates the outside node reference $u_{n_1+2,j}$ in the Laplacian discretization at nodes of indices $(n_1 + 1, j)$, giving eventually

$$\frac{3u_{n_1+1,j} - u_{n_1,j} - u_{n_1+1,j-1} - u_{n_1+1,j+1}}{h^2} = f_{n_1+1,j} = \frac{q}{k},$$

On the other hand, the Fourier condition is discretized as

$$u_{0,j} - u_{-1,j} + hc_{\text{th}} u_{0,j} = 0,$$

which eliminates the reference to nodes $(-1, j)$ in the Laplacian discretization at nodes of indices $(0, j)$, leading eventually to

$$\frac{3u_{0,j} - hc_{\text{th}}u_{0,j} - u_{1,j} - u_{0,j-1} - u_{0,j+1}}{h^2} = f_{0,j}.$$

Exercise 8.6. 1. Modify Algorithm (8.10) to take into account the Fourier and Neumann boundary conditions.
2. Implement a function `DDM_LaplaceFourier` that builds the linear system tridiagonal block matrix.
3. Implement functions `DDM_RightHandSide2dFourier`, `DDM_f1BB`, `DDM_g1BB`, and `DDM_rhs2dBB` for the bus bar problem.
4. Modify function `DDM_FinDif2d` and script `DDM_TestFinDif2d` in order to treat this problem with the global finite difference algorithm.
5. Modify function `DDM_Schwarz2d` and script `DDM_TestSchwarz2d` in order to treat this problem with the Schwarz algorithm.

Solutions of this exercise are proposed in Sect. 8.5 at page 183 for the global solution and at page 188 for the domain decomposition solution.

The global treatment provides the solution displayed in Fig. 8.9. The influence of the Fourier condition is clearly seen on the boundary at $x_1 = 0$, where the solution decreases toward the outside temperature value.

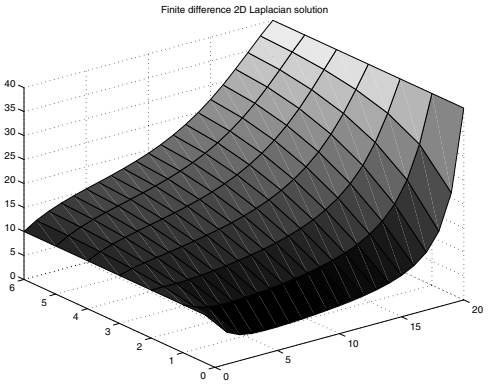

Fig. 8.9. Temperature in the bus bar.

8.4.4 Possible Extensions

The first extension from the point of view of the domain decomposition is of course to adapt the implementation to a decomposition on subdomains of different sizes. The degrees of freedom bookkeeping is then more complicated, and each subdomain requires the computation of a specific matrix. Should

these matrices be computed once and for all and stored in memory, or computed again at each iteration? What is the influence of this strategic issue on the computing time?

Another extension of the project can be the domain decomposition in both directions, which will enable the treatment of problems set on domains with complex geometry. The storage of the solution and the connection of the degrees of freedom in the overlapping regions requires a rigorous implementation.

8.5 Solutions and Programs

Solution of Exercises 8.1 and 8.2
The function `DDM_FunSchwarz1d` implements the Schwarz algorithm in the case of two subdomains of the same size. This constraint greatly simplifies the implementation, since the matrices of the local linear systems have the same dimensions for both subdomains. In the case that the coefficient $c(x)$ is constant, the matrix is exactly the same in both subdomains. The enforcement of the constraint requires a careful translation of the mathematical indices into MATLAB (once again, keep in mind that the indices of an array in MATLAB start from 1). One method consists in setting the number of space steps in the global domain to an even number, and therefore the number of discretization points, including the edges at $x = a$ and b, to an odd number n_x. The space step is denoted by $h = (b-a)/(n_x-1)$. Then the (even) number of space steps within the overlap is fixed to $2n_o$, with the parameter n_o sent as input to the function. From these data the position x_l of the left side of the right-hand-side subdomain is computed:

$$x_l = 0.5(a+b) - n_o h,$$

along with the position x_r of the right edge of the left-hand-side subdomain:

$$x_r = 0.5(a+b) + n_o h.$$

Eventually, the number of space steps in each subdomain is equal to

$$i_l = i_r = (n_x+1)/2 + n_o - 1.$$

Once these parameters are set, the finite difference matrix for the subdomains, of size $i_g - 1 \times i_g - 1$, can be computed. Two right-hand-side vectors are also defined. The influence of the boundary conditions at points x_r and x_l is not included at this stage since they vary at each iteration.

The function `DDM_FunSchwarz1d` uses the function `DDM_rhs1d` to compute the right-hand side.

The output parameters of the function are the number of iterations required to reach the convergence tolerance, and the computing time, estimated using the `tic` and `toc` MATLAB commands.

To answer Exercise 8.1, the function is called once with $n_o = 10$ from the script `DDM_CallSchwarz1d`. The parameter `detail` is set to 1 so that the solution is displayed at each iteration, and the evolution of the error as a function of the iterations is also displayed once convergence has been reached.

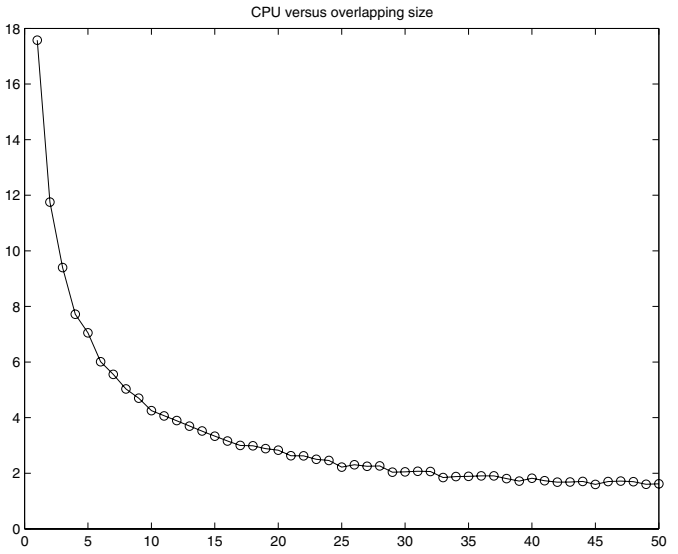

Fig. 8.10. Computing time performance of the decomposition versus the size of the overlapping region.

The script *DDM_PerfSchwarz1d* does the performance study required in Exercise 8.2. It calls the function `DDM_FunSchwarz1d` for all values n_o between 1 and $n_x/10$, and stores the corresponding number of iterations and computing time in arrays. A graph of the computing time as a function of the overlap size is displayed in Fig. 8.10. The method converges faster as the overlap increases, and the computing time for each iteration does not vary that much; therefore the overall computing time decreases as the size of the overlap region increases.

Solution of Exercise 8.3

To implement the 2D problem, it is interesting to preserve the double numbering of the discretization nodes associated with the Cartesian grid for the graphical representation of the solution, the boundary conditions, and the right-hand-side implementation. The global numbering of the degrees of freedom in a column vector can be used only to solve the linear systems. MATLAB can easily convert an $n_1 \times n_2$ array containing the unknowns $u_{i,j}$ into an array u_k with $k = 1, \ldots, n_1 \times n_2$, and conversely, as in the following script:

```
% If size(tab)=[n1,n2]
```

```
col=tab(:); % size(col)=[n1*n2,1] and col((j-1)*n1+i)=tab(i,j)
% inversely if  size(col)=[n1*n2,1]
tab=zeros(n1,n2);
tab(:)=col;
```

We first give MATLAB programming solutions for the functions: the finite difference matrix for the 2D Laplacian operator in the case of Dirichlet boundary conditions is built by the function `DDM_LaplaceDirichlet`.

In the test case proposed in question 5, the boundary conditions compatible with the exact solution

$$u(x_1, x_2) = \sin(x_1 + x_2)$$

are programmed in files *DDM_f1Exact.m*, *DDM_g1Exact.m*, *DDM_f2Exact.m*, *DDM_g2Exact.m*. The right-hand-side function

$$f(x_1, x_2) = -\nabla u(x_1, x_2) = 2\sin(x_1 + x_2)$$

is programmed in the function *DDM_rhs2dExact.m*. The right-hand side of the linear system in the case of Dirichlet boundary conditions is assembled by the function `DDM_RightHandSide2dDirichlet`. It uses the right-hand-side function as specified in (8.8) and the boundary conditions as specified in (8.9). The computation of the finite difference solution is performed by the function `DDM_FinDif2dDirichlet`. It receives in its input arguments the functions `DDM_f1Exact`, `DDM_g1Exact`, `DDM_f2Exact`, `DDM_g2Exact`, and `DDM_rhs2dExact`, whose local names are respectively `f1`, `g1`, `f2`, `g2`, `rhs2d`. It is able to treat other test cases and other boundary conditions. In the present case of inhomogeneous Dirichlet boundary conditions on all the boundaries, the number of degrees of freedom in the x_1 (respectively x_2) direction is equal to n_1 (respectively n_2), that is, the number of inside nodes in this direction.

The test case proposed in question 5 of Exercise 8.3 is treated in the first part of the calling script *DDM_TestFinDif2d*. The finite difference solution is compared with the exact solution by displaying their difference. The solution of the thermal shock described in Fig. 8.3, for which the exact solution is not known, is treated by calling the function `DDM_FinDif2dDirichlet` with the functions `DDM_rhs2dCT`, `DDM_f1CT`, `DDM_g1CT`, and `DDM_f2CT` as input arguments in order to compute the right-hand side. Eventually, the last computation performed in the script *DDM_TestFinDif2d.m* corresponds to the bus bar problem of Exercise 8.6. It is actually done by the function `DDM_FinDif2dFourier`. The Laplacian matrix is computed by `DDM_Laplace-Fourier`, where Neumann boundary conditions on the edge $x_1 = a_1$ and Fourier boundary conditions on the edge $x_1 = b_1$ are handled. Different functions `DDM_RightHandSideFourier` and `DDM_rhs2dBB` are used to compute the right-hand side. The inhomogeneous Dirichlet conditions, defined on edges parallel to x_1, are taken into account using functions `DDM_f1BB` and `DDM_g1BB`.

Solution of Exercise 8.4
Algorithm (8.10) corresponding to the Schwarz method in the case of Dirichlet boundary conditions on all four edges is programmed in the function DDM_Schwarz2dDirichlet below and is tested in the script DDM_TestSchwarz2d for the two examples treated in the previous exercise:

```
function [conviter,cpu,mem,n2,b2]=DDM_Schwarz2dDirichlet(n1,...
                    ns,no,a1, a2,b1,b2,f,f1,g1,f2,g2,detailed)
%%%%%%%%%%%%%%%%%%%%%%%%%%%%%%%%%%%%%%%%%%%%%%%%%%%%%%%%%%%%%%%%%%%%%%%%
%% function [conviter,cpu,mem,n2,b2]=DDM_Schwarz2dDirichlet(n1,...
%%          ns,no,a1, a2,b1,b2,f1,f1,g1,f2,g2,detailed)
%% Exercise 8.4
%% Schwarz  method of domain decomposition with overlap
%% for the finite difference solution of the boundary conditions
%% problem
%%  -nabla u=f  on [a1,b1]x[a2,b2]
%%  + Dirichlet b. c.
%%  u(a1,x2)=f2(x2)          u(x1,a2)=f1(x1)
%%  u(b1,x2)=g2(x2)          u(x1,b2)=g1(x1)
%%
%% Input parameters:
%%    n1 : number of cells  on [a1,b1]
%%    ns  : number of subdomains in the x2 direction
%%    no   : number of cells in overlapping region
%%    a1, a2, b1, b2: minimal and maximal abscissa and
%%           ordinates of the rectangular domain
%%    f : right-hand-side function of the problem
%%    f1, g1,f2,g2 : functions defining the inhomogeneous
%%     Dirichlet boundary condition on the four edges of the domain
%%    detailed: nonzero to have intermediate graphical displays.
%%
%% Output parameters:
%%    conviter: number of iterations
%%    cpu     : computing time
%%    mem     : memory   needed to store the solution and the matrix
%%    n2      : number of points per subdomain in the x2 direction
%%    b2      : total size of domain in the x2 direction
%%%%%%%%%%%%%%%%%%%%%%%%%%%%%%%%%%%%%%%%%%%%%%%%%%%%%%%%%%%%%%%%%%%%%%%%
tic  % computing time counter start
h=(b1-a1)/(n1+1);
n2tot=round(b2/h);        % there are n2tot cells in total domain,
n2=round((n2tot-no*(1-ns))/ns)-1; % and n2+1 cells in each subdomain
n2tot= ns*(n2+1)+no*(1-ns);
b2=a2+h*n2tot;          % final global size
% memory   needed to store the solution and the matrix
```

```
mem=(n1*n2)^2+ns*n1*n2;
%
% the size of each subdomain is  n1 x n2
%
a11=a1-h;  % Dirichlet condition on the edge // to X2
%
% Boundary conditions independent of iterations are set in arrays
Ua2l=feval(f1,a1+h*[1:n1])' ; % boundary condition on edge x2=a2
Ub2r=feval(g1,a1+h*[1:n1])';  % boundary condition on edge  x2=b2
% The right-hand side on each subdomain is an array to which the
% contribution of internal edges will be added at each iteration
RHS=zeros(n1*n2,ns);
starts=0; % starting index of subdomain s
Rhsm=zeros(n1,n2);
Solm=zeros(n1,n2);
for s=1:ns
  RHS(:,s)=DDM_RightHandSide2dDirichlet(f,h,n1,n2,a1,a2+starts*h);
  % Dirichlet boundary condition on edge x1=a1
  Ua1(s,:)=feval(f2,a2+starts*h+[1:n2]*h);
  % Dirichlet boundary condition on edge  x1=b1
  Ub1(s,:)=feval(g2,a2+starts*h+[1:n2]*h);
  Rhsm(1,:)=Ua1(s,:)/h^2;
  Rhsm(n1,:)=Ub1(s,:)/h^2;
  RHS(:,s)=  RHS(:,s)+Rhsm(:);
  Solm(:,no)=(i*Ub2r+(ns-s)*Ua2l)/ns;
  Solcol(:,s)=Solm(:);
  starts=starts+n2+1-no;
end
Rhsm=zeros(n1,n2);
Lapl=-DDM_LaplaceDirichlet(h,n1,n2);
maxiter=100; conviter=1; err=1; epsilon=0.001;
Solcol=zeros(n1*n2,ns);
ERR=[];
while err>epsilon & conviter<maxiter
  starts=0;
  err=0;
  Ua2=Ua2l; %left edge in x2 contains n1+2 row
  for s=1:ns
    if s<ns
      % The boundary condition on the right edge is obtained
      % from the solution at previous iteration on the right-hand-side
      % neighboring subdomain
      Solmr=zeros(n1,n2);Solmr(:)=Solcol(:,s+1);
      Ub2=Solmr(:,no);
    else
```

```
      Ub2=Ub2r; % the exact boundary condition is used on the right edge.
    end
    %
    Rhsm(:,1)=  Ua2/h^2;
    Rhsm(:,n2)= Ub2/h^2;
    Rhscol=RHS(:,s)+Rhsm(:);
    Solcol(:,s)=Lapl Rhscol;
    Solm=zeros(n1,n2);Solm(:)=Solcol(:,s);
  % The boundary condition on the left edge is obtained for the
  % next subdomain on the right
    Ua2=Solm(:,n2-no+1);
    if s>1 % the overlapping region is extracted
      OVER=Solml(:,n2-no+2:n2)-Solm(:,1:no-1);
      err=max(err,norm(OVER(:),inf));
    end
    Solml=Solm;
    if detailed,
      surf(a2+h*starts+h*[1:n2],a11+h*[1:n1],Solm);
      title(strcat('iteration ',int2str(conviter)))
      if s==1
        hold on
      end
    end
    starts=starts+n2+1-no;
  end
  ERR=[ERR,err];
  conviter=conviter+1;
end
cpu=toc; % computing time counter starts here
if detailed, % Visualization after convergence
  Ua2l=[feval(f1,a1); Ua2l;feval(f1,b1)] ;
  Ub2r=[feval(g1,a1); Ub2r;feval(g1,b1)] ;
  figure;  hold on ;
  Solmr=zeros(n1,n2);Solmr(:)=Solcol(:,1);
  % In the case of  Dirichlet bc on edges // to x2 two rows
  % corresponding to the boundary conditions on x1=a1 and x1=b1
  %  are added to the solution on each subdomain
  starts=0;
  Solmr= [Ua1(1,:);Solmr;Ub1(1,:)]; % Dirichlet bc
  Solmr=[Ua2l,Solmr]; % exact boundary condition on left edge
  surf(a2+h*starts+h*[0:n2],a1+h*[0:n1+1],Solmr);
  starts   =starts+n2+1-no;
  for s=2:ns-1
    Solmr=zeros(n1,n2);Solmr(:)=Solcol(:,s);
    Solmr= [Ua1(s,:);Solmr;Ub1(s,:)];
```

```
    surf(a2+h*starts+h*[1:n2],a1+h*[0:n1+1],Solmr);
    starts=starts+n2+1-no;
  end
  Solmr=zeros(n1,n2);Solmr(:)=Solcol(:,ns);
  Solmr= [Ua1(ns,:);Solmr;Ub1(ns,:)];
  Solmr=[Solmr,Ub2r];  %exact boundary condition on right edge
  surf(a2+h*starts+h*[1:n2+1],a1+h*[0:n1+1],Solmr);
  title('Final solution')
end
```

An interesting programming feature is the array `RHS` indexed by the subdomain, which contains the right-hand side of the linear system for the corresponding subdomain. This array is initialized with the contribution of the right-hand-side function $f(x_1, x_2)$ as well as the Dirichlet boundary conditions on the global domain edges. The array is used in the subsequent iterations, in the loop on subdomains, to initialize the right-hand-side vector `Rhsm` of the local linear system. The contribution of the Dirichlet boundary condition on internal edges, which depends on the solution on neighboring subdomains, is then added before the linear system is solved.
The matrix `Lapl` of the linear system is the same for all subdomains and does not depend on the solution; it is therefore computed once and for all outside the loop on iterations.

Figure 8.11 displays the solutions after 1 and 4 iterations for the first test case, where the exact solution is known.

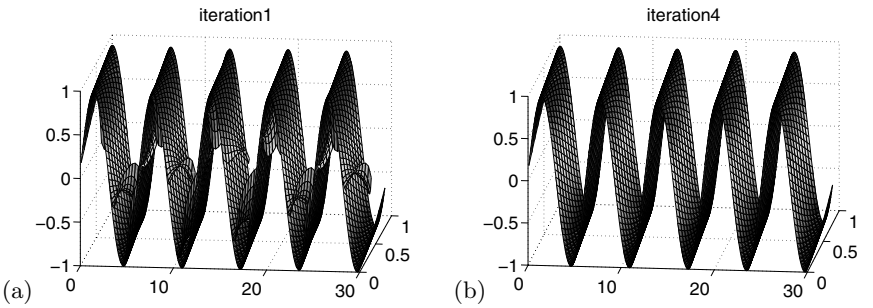

Fig. 8.11. Solutions computed on 20 subdomains, after (a) 1 and (b) 4 iterations.

Solution of Exercise 8.5
To analyze the convergence, we propose the script *DDM_Perf.m*, which also calls the function `DDM_Schwarz2dDirichlet`. The first test case is considered, with this time a larger domain in the x_2 direction: $b_2 - a_2 = 50$. The width of the domain remains equal to 1 and is discretized with 11 cells, leading to $n_1 = 10$ degrees of freedom in the x_1 direction. The size of the overlap region is

fixed to 10 cells in the x_2 direction. All "reasonable" values for the number of subdomains are tried in a loop, from $n_s = 5$ subdomains (which corresponds to 117 degrees of freedom per subdomain in the x_2 direction) to $n_s = 60$ subdomains (which corresponds to 18 degrees of freedom per subdomain). Since the discretization step must be the same in both directions x_1 and x_2, some configurations are impossible: the step h is fixed by the number of points in the x_1 direction, $n_1 = 10$, that is, $h = (b_1 - a_1)/(n_1 + 1)$. Therefore the number of internal points in the x_2 direction is also fixed to $n_2^{\text{total}} = (b_2 - a_2)/h$, with the constraint that n_2 must be an integer. Furthermore, the number of points in the x_2 direction in one subdomain, n_2, taking into account the overlap region, must satisfy $n_s(n_2 + 1) = n_2^{\text{total}} - n_o(1 - n_s)$, while being also an integer. Only the decomposition configurations leading to a total length of 50 with a 0.2% tolerance are considered.

For these allowable configurations, the function `DDM_Schwarz2dDirichlet` is called, with this time the input argument `detailed` set equal to 0 to inhibit some of the intermediate graphical outputs. On the other hand, output parameters return the number of iterations, the computing time, the memory size, and the number of points per subdomain n_2. Figure 8.12 shows the results obtained for two different sizes of the overlap regions: $n_o = 4$ and $n_o = 10$ cells in the x_2 direction. A comparison of the computing time curve with the number of iterations curve is particularly interesting. One would expect that the number of iterations should increase with the number of subdomains, but since the computing time necessary for each subdomain decreases along with their size, the evolution of the global computing time is less predictable. The simulations indicate that the optimal number of subdomains might depend on the size of the overlap.

For comparison, the direct computation of the global solution on 9×499 degrees of freedom would require 35 seconds of computing time, which is more than the decomposition method requirement in the worst configuration case. The memory necessary to store the matrix of a global linear system on the order of 2.10^7 is also prohibitive.

Solution of Exercise 8.6

We now denote by X_1 the vector containing the $n_1 + 2$ abscissa $a_1 + jh$, $j = 0, \ldots, n_1 + 1$, including a_1 and b_1. The vectors X_2^i of Algorithm (8.10) are unchanged. The Laplacian matrix is modified in order to take into account the Neumann and Fourier boundary conditions, using the block representation (8.7). The T and D matrices are now of dimension $(n_1 + 2) \times (n_1 + 2)$, and the matrix T is different from the previous one (8.6) in the first and last rows

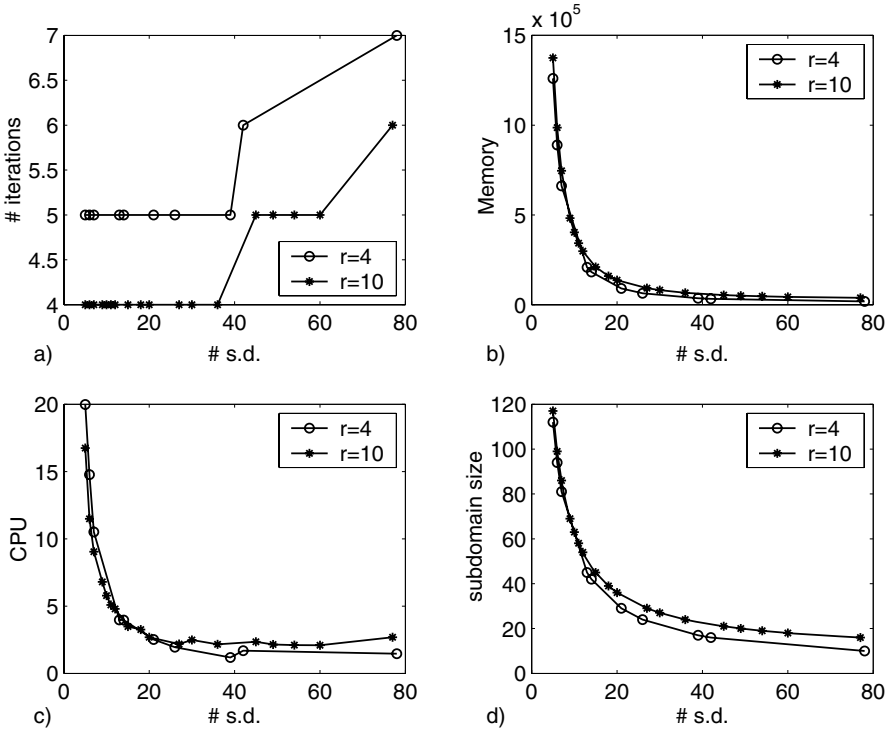

Fig. 8.12. Performances of the decomposition versus the number of subdomains for two different sizes of the overlap.

$$T = \frac{1}{h^2} \begin{pmatrix} 3 - hc_{\text{th}} & -1 & 0 & \dots & \dots & 0 \\ -1 & 4 & -1 & \ddots & \ddots & \vdots \\ 0 & \ddots & 4 & \ddots & \ddots & \vdots \\ \vdots & \ddots & \ddots & \ddots & \ddots & \vdots \\ \vdots & \ddots & \ddots & \ddots & 4 & -1 \\ 0 & \dots & \dots & 0 & -1 & 3 \end{pmatrix}.$$

Since the outside temperature is equal to 0°C, there is no contribution of the Fourier boundary condition on the right-hand side. The Schwarz algorithm is now as follows:

$$
\begin{array}{l}
\text{initialization :} \\
\quad U_{a_2 l} = f_2(X_1), \quad U_{b_2 r} = g_2(X_1) \\
\quad U^{i,0}_{.,n_o} = (iU_{b_2 r} + (n_s - s)U_{a_2 l})/n_s, \quad \text{for} \quad s = 2, \ldots, n_s \\
\quad B^s_{.,.} = F(X_1, X_2^s), \quad \text{for} \quad s = 1, \ldots, n_s \\
\text{for} \quad k = 1, 2, \ldots, \quad \text{do} \\
\quad \text{for} \quad s = 1, \ldots, n_s \quad \text{do} \\
\qquad \text{if } s = 1, \quad U^s_{a_2} = U_{a_2 l} \quad \text{else} \quad U^s_{a_2} = U^{s-1,k}_{.,n_2+1-n_o} \\
\qquad \text{if} s = n_s, \quad U^s_{b_2} = U_{b_2 r} \quad \text{else} \quad U^s_{b_2} = U^{s+1,k-1}_{.,n_o} \\
\qquad B^{s,k} = B^s, \quad B^{s,k}_{.,1} = B^{s,k}_{.,1} + U^s_{a_2}/h^2 \quad B^{s,k}_{.,n_2} = B^{s,k}_{.,n_2} + U^s_{b_2}/h^2 \\
\qquad \text{solve } AU^{s,k} = B^{s,k} \\
\qquad \text{if } s > 1, \quad R^s_{.,j} = U^{s,k}_{.,j} - U^{s-1,k}_{.,n_2-n_o+1+j}, \quad \text{for } j = 1, \ldots, n_o - 1 \\
\quad \text{end of} \quad s \\
\quad E^k = \sup_{s=2,\ldots,n_s} \|R^s\| \\
\text{if } E^k < \varepsilon \quad \text{end of} \quad k
\end{array}
\tag{8.12}
$$

This algorithm is programmed in the function `DDM_Schwarz2dFourier` and tested in the third example of the script *DDM_TestSchwarz2d.m*.

Chapter References

This project has provided the general idea of domain decomposition, which is to decompose a global problem into suitable subproblems of smaller complexity. In practice, however, domain decomposition methods are mostly implemented for complex shapes discretized with finite element schemes. Nonoverlapping algorithms as in Quarteroni and Valli (1999) are then preferable, and a large number of such techniques makes use of the so-called *mortar* formulation (see Wohlmuth (2001)).

P. L. Lions, *On the alternating Schwarz method I* . In R. Gowinski, G. H. Golub, G. A. Meurant and J. Périaux, editors. First International Symposium on Domain Decomposition Methods for Partial Differential Equations, pp. 1–42, SIAM, Philadelphia, 1988.

B. Lucquin and O. Pironneau, *Introduction to Scientific Computing*, Willey, Chichester, 1998.

A. Quarteroni and A. Valli, *Domain Decomposition Methods for Partial Differential Equations*, Numerical Mathematics and Scientific Computation, The Clarendon Press Oxford University Press, New York, 1999.

H. A. Schwarz, *Gesammelte Mathematische Abhandlungen.* Volume 2. Springer, Berlin, 1890. First published in Vierteljahrsschrift Naturforsch. Ges. Zurich, 1870.

B. F. Smith, P. E. Bjørstad, and W. D. Gropp, *Domain Decomposition, Parallel Multilevel Methods for Elliptic Partial Differential Equations*, Cambridge University Press, Cambridge, 1996.

B. I. Wohlmuth, *Discretization Methods and Iterative Solvers Based on Domain Decomposition*, Lecture Notes in Computational Science and Engineering, 17, Springer-Verlag, Berlin, 2001.

9

Geometrical Design: Bézier Curves and Surfaces

Project Summary

Level of difficulty:	2
Keywords:	Bézier curves, Bézier surfaces
Application fields:	Computer-aided geometric design, geometric modeling, computational graphics

9.1 Introduction

Many fields in the computational science area need descriptions of complex objects: virtual reality, computational graphics, geometric modeling, computer-aided geometric design (CAGD). These descriptions are commonly obtained using basic elements: points, curves, surfaces, and volumes. Elementary tools used to handle these elements are mathematical functions such as polynomials and rational functions, which allow easy graphical representation in many situations: union of objects, intersection, complement.

The very first studies in geometrical design go back to the sixties and were related to industrial projects. For example, J. Ferguson (Boeing) and S. Coons (Ford) in the United States, P. de Casteljau (Citroën) and P. Bézier (Renault) in France, were pioneers in the discipline. This chapter gives an introduction to geometrical design by studying some properties of the so-called Bézier curves and surfaces.

9.2 Bézier Curves

Let $n \geq 2$ be an integer and $t \in [0, 1]$ a parameter; consider $m + 1$ points in $\mathbb{R}^n$: P_0, P_1, $\ldots$, P_m (distinct or not) and define the point $P(t)$ by

$$P(t) = \sum_{k=0}^{m} C_m^k t^k (1-t)^{m-k} P_k, \tag{9.1}$$

where $C_m^k = \frac{m!}{k!(m-k)!}$ is the binomial coefficient. The *Bézier curve* $\mathcal{B}_m$ with *control points* P_0, P_1, $\ldots$, P_m is the trajectory described by $P(t)$ as t goes from 0 to 1. The polynomials $B_m^k(t) = C_m^k t^k (1-t)^{m-k}$ are the *Bernstein polynomials* of degree m, with the following properties:

$$\begin{cases} \forall t \in [0,1],\ 0 < B_m^k(t) < 1,\ \displaystyle\sum_{k=0}^{m} B_m^k(t) = 1, \\ B_m^k(0) = 0, \text{ for } 0 < k \leq m,\ B_m^0(0) = 1, \\ B_m^k(1) = 0, \text{ for } 0 \leq k < m,\ B_m^m(1) = 1. \end{cases} \tag{9.2}$$

It follows from (9.1) and (9.2) that $P(0) = P_0$ and $P(1) = P_m$. Generally, P_0 and P_m are the only control points on the curve $\mathcal{B}_m$. Definition (9.1) allows one to represent, exactly and in a condensed form, a great diversity of curves in $\mathbb{R}^n$. Fig. 9.1(a) displays an example of a Bézier curve defined in $\mathbb{R}^2$ with five control points. Note that the order in which the control points are considered in (9.1) will dictate the shape of the curve: for example, in Figs. 9.1(a) and (b) the same control points are used, but P_0 and P_4 have been interchanged. More generally, attempting to change any control point will result in the entire curve being modified.

Since Bernstein polynomials are linearly independent functions, two Bézier curves coincide for the same value of m when they share the same control points. Nevertheless, it is important to note that the same Bézier curve admits different representations of type (9.1), corresponding to different values of m. For example, consider two points P_0 and P_1 and define Q_1 to be the midpoint of P_0P_1; the line segment P_0P_1 is defined by either

$$P(t) = \sum_{k=0}^{1} C_1^k t^k (1-t)^{1-k} P_k \qquad (m = 1)$$

or

$$Q(t) = \sum_{k=0}^{2} C_2^k t^k (1-t)^{2-k} Q_k \qquad (m = 2)$$

with $t \in [0,1]$, $Q_0 = P_0$, and $Q_2 = P_1$. If we introduce the new control points $R_0 = P_0$, $R_1 = (2P_0 + P_1)/3$, $R_2 = (P_0 + 2P_1)/3$, and $R_3 = P_1$, the Bézier curve corresponding to the definition

$$R(t) = \sum_{k=0}^{3} C_3^k t^k (1-t)^{3-k} R_k \qquad (m = 3)$$

with $t \in [0,1]$ is still the line segment P_0P_1 ! (check that $P(t) = Q(t) = R(t)$).

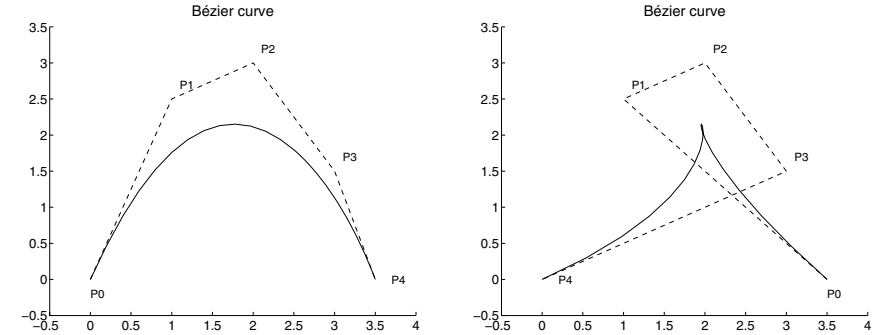

a) b)

Fig. 9.1. Two Bézier curves.

Remark 9.1. The control point P_k, for any $1 < k < m$, does not generally belong to the Bézier curve; it is, however, possible to introduce another type of Bézier curve, called a *Bézier interpolation curve*; which contains all its control points. Both kinds of curves belong to the family of *spline curves*. Spline curves are generated using the general definition (9.3), in which functions f_k are polynomials of degree m:

$$P(t) = \sum_{k=0}^{m} f_k(t) P_k. \tag{9.3}$$

Many other curves (B-splines, NURBS) are defined by way of such a formula (Coons (1974), Hoschek and Lasser (1997), or Piegl and Tiller (1995)). In (9.3) the blending functions f_k may be polynomials (of degree $p \neq m$), rational functions, etc. All the corresponding curves are entirely defined by setting the control points and choosing the associated functions. Note that a curve may be also defined "piecewise", as the union of distinct curves sharing the same endpoints. In this chapter we shall limit our study to Bézier defined by formula (9.1).

9.3 Basic Properties of Bézier Curves

In this section we study some properties of Bézier curves, which are relevant for practical applications.

9.3.1 Convex Hull of the Control Points

According to (9.1), the point $P(t)$ is defined as the barycenter of the $m + 1$ control points P_k, with corresponding weights $B_m^k(t)$. If follows from the first relationship in (9.2) that $P(t)$ belongs to the convex hull of the control points.

We may see in Fig. 9.2(a) that a Bézier curve lies entirely within the convex hull of the control points. Note that this convex hull contains the polygon $P_0P_1 \ldots P_mP_0$, which is commonly referred as the *control polygon*. From a more general point of view, it is worth noting that in many situations the control polygon is not convex (as can be seen from Fig. 9.2(b)).

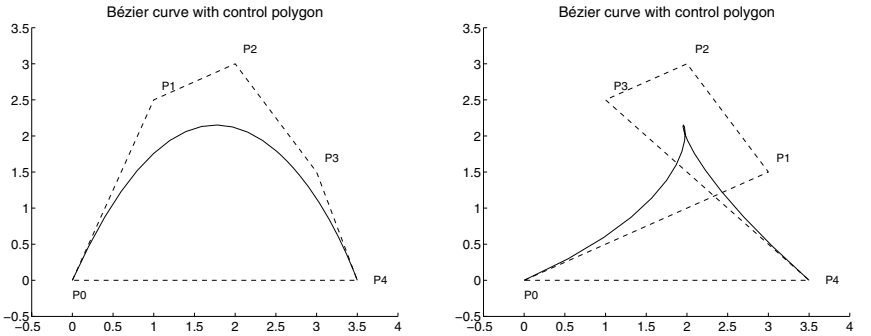

(a) (b)

Fig. 9.2. Control polygon. (a) convex; (b) nonconvex.

9.3.2 Multiple Control Points

When defining a Bézier curve, it is not necessary to use distinct control points. This allows us to create more or less complicated shapes, closed or open curves, as displayed in Figs. 9.3 and 9.4.

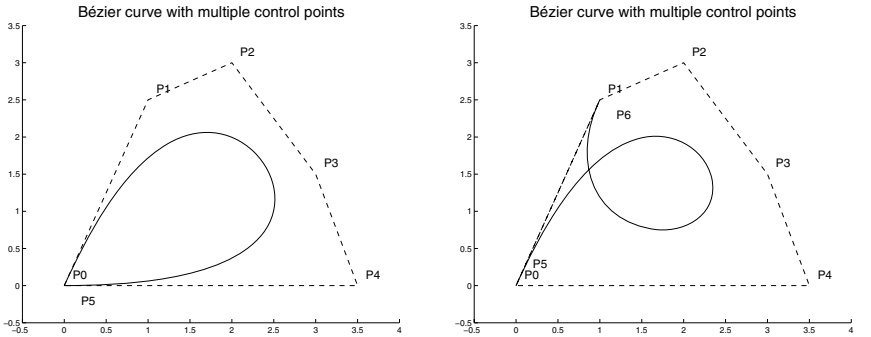

Fig. 9.3. Multiple control points (1).

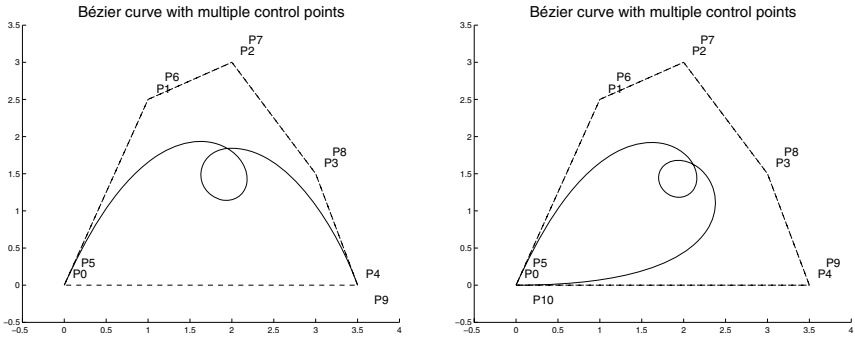

Fig. 9.4. Multiple control points (2).

9.3.3 Tangent Vector to a Bézier Curve

Let $P(t)$ be the point of the Bézier curve $\mathcal{B}_m$ corresponding to the value t of the parameter. The tangent vector to $\mathcal{B}_m$ at $P(t)$ is defined by

$$\boldsymbol{\tau}(t) = \frac{d}{dt}P(t) = \sum_{k=0}^{m} \frac{d}{dt}B_m^k(t)P_k. \tag{9.4}$$

It follows from definition (9.3) that

$$\frac{d}{dt}B_m^k(t) = \begin{cases} -m(1-t)^{m-1}, \text{ if } k=0, \\ m(1-mt)(1-t)^{m-2}, \text{ if } k=1, \\ C_m^k(k-mt)t^{k-1}(1-t)^{m-k-1}, \text{ if } 1<k<m-1, \\ mt^{m-2}(m-1-mt), \text{ if } k=m-1, \\ mt^{m-1}, \text{ if } k=m. \end{cases}$$

Consequently, when $P_0 \neq P_1$, the tangent vector at P_0 is $\boldsymbol{\tau}(0) = mP_0P_1$. The Bézier curve $\mathcal{B}_m$ is tangent at P_0 to the edge P_0P_1 of the control polygon. Similarly, if $P_{m-1} \neq P_m$, then $\boldsymbol{\tau}(1) = mP_{m-1}P_m$ and the curve is tangent at P_m to the edge $P_{m-1}P_m$. This property is illustrated in the previous figures.

Remark 9.2. More generally, it can be proved that

$$\frac{d}{dt}B_m^k(t) = m(B_{m-1}^{k-1}(t) - B_{m-1}^k(t)).$$

This formula may be useful to compute the tangent vector $\boldsymbol{\tau}(t)$.

9.3.4 Junction of Bézier Curves

We address now the problem of linking two Bézier curves. Consider the Bézier curve defined with $m+1$ control points $P_0, P_1, \ldots, P_m$ and another curve defined with $m'+1$ control points $P'_0, P'_1, \ldots, P'_{m'}$. We are interested in studying

how these two curves connect, and more particularly how this junction looks on a display. This is an important problem in CAGD, where maximum quality in the rendering of pictures is expected.

In order to get a $\mathcal{C}^0$ connection (that is, a continuous junction of the two curves) we have to lay down a basic condition: $P_m = P'_0$. Then, since the first curve $\mathcal{B}_m$ is tangent to the line segment $P_{m-1}P_m$ at P_m and the second curve $\mathcal{B}'_{m'}$ is tangent to $P'_0P'_1$ at P'_0, a tangential connection of the curves is obtained if and only if the three points P_{m-1}, P_m (or P'_0), and P'_1 lie on a straight line. This condition, which is called the $\mathcal{G}^1$ continuity condition, is generally sufficient to get a satisfactory layout. Nevertheless, for a better rendering, it is natural to ask for more, namely a $\mathcal{C}^1$ continuity condition. This will be satisfied if the tangent vector $\boldsymbol{\tau}$ passes continuously from the first curve to the second one. We know that the tangent vector to $\mathcal{B}_m$ at P_m is $m\overrightarrow{P_{m-1}P_m}$, while for $\mathcal{B}'_m$ the tangent vector at P'_0 is $m\overrightarrow{P'_0P'_1}$. The $\mathcal{C}^1$ continuity condition is then satisfied when $\overrightarrow{P_{m-1}P_m} = \overrightarrow{P'_0P'_1}$. This is equivalent to saying that $P_m = P'_0$ is the midpoint of the line segment $P_{m-1}P'_1$.

Figure 9.5 shows an example of a $\mathcal{G}^1$ junction (left), together with an example of a $\mathcal{C}^1$ junction (right). The actual difference is not visible here; but it is clear from Fig. 9.5(b) that P_4 (point $P_4 \equiv P'_0$) is the midpoint of the line segment $P_3P'_1$, while this is not true in Fig. 9.5(a). Distinguishing between these two kinds of junction is important when one has to handle evenly spaced points on the curve $\mathcal{B} = \mathcal{B}_m \cup \mathcal{B}'_m$.

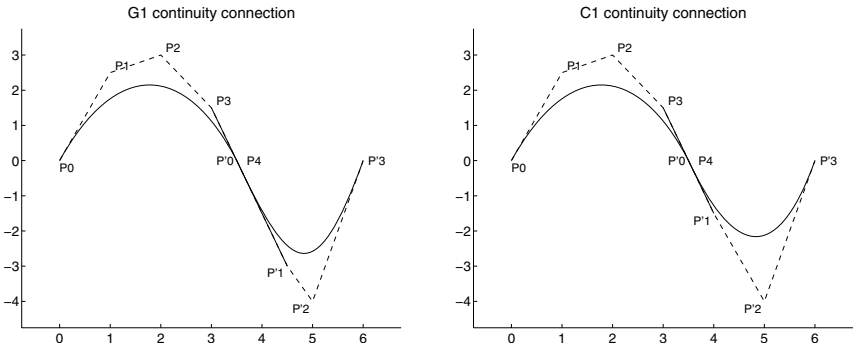

Fig. 9.5. Junction of curves. (a) $\mathcal{G}^1$ continuity; (b) $\mathcal{C}^1$ continuity.

9.3.5 Generation of the Point $P(t)$

Although the point $P(t)$ is exactly defined from (9.1), the effective construction of $P(t)$ for a given value of the parameter $t \in [0, 1]$ in this way is time-consuming. Furthermore, since the calculation of high degree polynomials val-

ues is not an accurate process, the point resulting from (9.1) will be generally different from the actual $P(t)$. Fortunately, there is another way, cheap and accurate, to obtain $P(t)$ using the recurrence between Bernstein polynomials:

$$B_{m+1}^k(t) = tB_m^{k-1}(t) + (1-t)B_m^k(t). \tag{9.5}$$

This result is proved by writing

$$\begin{aligned} t\, B_m^{k-1}(t) + (1-t)B_m^k(t) &= t\, C_m^{k-1}t^{k-1}(1-t)^{m-k+1} + (1-t)C_m^k t^k(1-t)^{m-k} \\ &= (C_m^{k-1} + C_m^k)t^k(1-t)^{m-k+1} \\ &= C_{m+1}^k t^k(1-t)^{m+1-k} = B_{m+1}^k(t). \end{aligned}$$

This property is useful for displaying Bézier curves: for a chosen value of $t \in [0,1]$, the points P_q^p, for $p = 0, 1, \ldots, m$ and $q = p, p+1, \ldots, m$, are successively defined by

$$\begin{array}{l} \text{initialization: for } p = 0, \text{ do} \\ \quad \text{for } q = 0, 1, \ldots, m, \text{ do} \\ \quad\quad P_q^0 = P_q \\ \quad \text{end do} \\ \text{end do} \\ \text{construction: for } p = 1, 2, \ldots, m, \text{ do} \\ \quad \text{for } q = p, p+1, \ldots, m, \text{ do} \\ \quad\quad P_q^p = tP_{q-1}^{p-1} + (1-t)P_q^{p-1}. \\ \quad \text{end do} \\ \text{end do} \end{array} \tag{9.6}$$

We shall prove now that $P_m^m = P(t)$. We first note that in (9.6), at step p, any of the $m-p$ points P_q^p is defined as the barycenter of P_{q-1}^{p-1} and P_q^{p-1}, which are the two points obtained in the previous step. Using mathematical induction on p, we prove that P_q^p satisfies, for $p = 0, 1, \ldots, m$ and $q = p, p+1, \ldots, m$, the relationship

$$P_q^p = \sum_{j=0}^{m} B_p^j P_j.$$

This is trivial when $p = 0$ because of the definition of the points P_q^0 $(q = 0, 1, \ldots, m)$. We then assume the property to be satisfied to rank $p-1$ (included) and prove it for rank p. For $q = p, p+1, \ldots, m$, we write

$$P_q^p = tP_{q-1}^{p-1} + (1-t)P_q^{p-1} = \sum_{j=0}^{m}(tB_{q-1}^j + (1-t)B_q^j)P_j = \sum_{j=0}^{m} B_q^j P_j.$$

The relation is also satisfied for rank p, and then for any value of $p \leq m$. When $p = m$, this relation leads to

$$P_m^m = \sum_{j=0}^{m} B_m^j P_j = P(t).$$

It follows that any point $P(t)$ of the Bézier curve $\mathcal{B}_m$ with control points $P_0, P_1, \ldots, P_m$ can be built by means of algorithm (9.6), which is called *de Casteljau's algorithm*. The computational cost to generate $P(t)$ in this way is equivalent to performing $m + \cdots + 1 = m(m+1)/2$ linear combinations; this is much cheaper (and more accurate) than the use of formula (9.1). The construction process is displayed in Fig. 9.6.

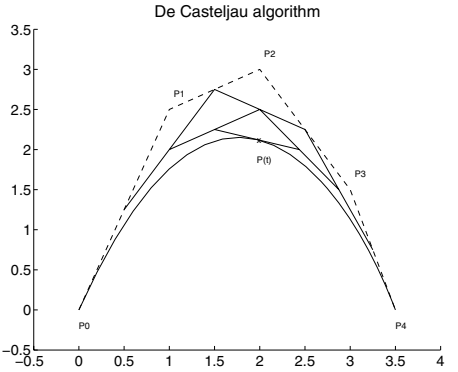

Fig. 9.6. De Casteljau's algorithm.

9.4 Generation of Bézier Curves

It is now time to deal with a few examples. We shall see how easy it is to construct Bézier curves using de Casteljau's algorithm.

Exercise 9.1. 1. Choose $m + 1$ points P_0, P_1, $\ldots$, P_m in $\mathbb{R}^2$.
2. Write a general procedure generating a point $P(t)$ of the Bézier curve with control points P_0, P_1, $\ldots$, P_m, using de Casteljau's algorithm (9.6), for any value $t \in [0, 1]$.
3. Compute and display the corresponding Bézier curve.
4. Repeat the experiment for different values of m and different sets of control points.
5. Check the different continuity conditions.

A solution of this exercise is proposed in Sect. 9.10 at page 210.

Remark 9.3. One may want to construct the curve displayed in Fig. 9.1(a). In this particular case, $m = 4$ and the control points are $P_0 = (0, 0)$, $P_1 = (1, 2.5)$, $P_2 = (2, 3)$, $P_3 = (3, 1.5)$, $P_4 = (3.5, 0)$.

9.5 Splitting Bézier Curves

Let $\mathcal{B}_m$ be the Bézier curve defined by $m+1$ control points $P_0, P_1, \ldots, P_m$. Let θ be a given value in $[0, 1]$. The point $P(\theta)$ of $\mathcal{B}_m$ is associated with θ by the algorithm (9.6). We successively construct the points P_q^p, for $p = 0, 1, \ldots, m$ and $q = p, p+1, \ldots, m$, and finally set $P(\theta) = P_m^m$. Consider now the Bézier curve $\tilde{\mathcal{B}}_m$ defined by the $m+1$ control points $P_0^0, P_1^1, \ldots, P_m^m$. The point $\tilde{P}(\tilde{t})$ on this curve is defined by

$$\tilde{P}(\tilde{t}) = \sum_{k=0}^{m} C_m^k \tilde{t}^k (1-\tilde{t})^{m-k} P_k^k, \tag{9.7}$$

where the parameter $\tilde{t}$ belongs to the interval $[0, 1]$. Note that $\tilde{P}(0) = P_0$ and $P(\theta) = P_m^m$. We are going to prove now that the Bézier curve $\tilde{\mathcal{B}}_m$, with ending points P_0 and $P(\theta)$, is the part of the curve $\mathcal{B}_m$ obtained when the parameter t covers the interval $[0, \theta]$. We first check that the points P_q^p generated by the algorithm (9.6) satisfy, for $1 \le p \le m$ and $p \le q \le m$,

$$P_q^p = \sum_{k=0}^{p} C_p^k \theta^k (1-\theta)^{p-k} P_{q-k}. \tag{9.8}$$

This result is obtained by mathematical induction on p. Using definition (9.6) we obtain, when $p = 1$ and $1 \le q \le m$,

$$P_q^1 = \theta P_{q-1}^0 + (1-\theta) P_q^0 = \sum_{k=0}^{1} C_1^k \theta^k (1-\theta)^{1-k} P_{q-k}.$$

We assume that the property is true up to the value $p-1$. Then we write, for $p \le q \le m$,

$$\begin{aligned}
P_q^p =& \theta P_{q-1}^{p-1} + (1-\theta) P_q^{p-1} \\
=& \sum_{k=0}^{p-1} C_{p-1}^k \theta^{k+1} (1-\theta)^{p-1-k} P_{q-1-k} + \sum_{k=0}^{p-1} C_{p-1}^k \theta^k (1-\theta)^{p-k} P_{q-k} \\
=& \sum_{k=0}^{p-2} C_{p-1}^{p-1-k} \theta^{k+1} (1-\theta)^{p-1-k} P_{q-1-k} + \theta^p P_{q-p} \\
&+ (1-\theta)^p P_q + \sum_{k=1}^{p-1} C_{p-1}^k \theta^k (1-\theta)^{p-k} P_{q-k}.
\end{aligned}$$

We obtain

$$\begin{aligned} P_q^p &= \sum_{k=1}^{p-1} C_{p-1}^{p-k} \theta^k (1-\theta)^{p-k} P_{q-k} + \theta^p P_{q-p} \\ &\quad + (1-\theta)^p P_q + \sum_{k=1}^{p-1} C_{p-1}^{k} \theta^k (1-\theta)^{p-k} P_{q-k} \\ &= \theta^p P_{q-p} + \sum_{k=1}^{p-1} (C_{p-1}^{p-1-(k-1)} + C_{p-1}^{k}) \theta^k (1-\theta)^{p-k} P_{q-k} + (1-\theta)^p P_q. \end{aligned}$$

Finally,

$$P_q^p = \sum_{k=0}^{p} C_p^k \theta^k (1-\theta)^{p-k} P_{q-k}.$$

The point $\tilde{P}(\tilde{t})$ of $\tilde{\mathcal{B}}_m$, defined by the $m+1$ control points $P_0^0, P_1^1, \ldots, P_m^m$, satisfies

$$\begin{aligned} \tilde{P}(\tilde{t}) &= \sum_{k=0}^{m} C_m^k \tilde{t}^k (1-\tilde{t})^{m-k} P_k^k \\ &= \sum_{k=0}^{m} C_m^k \tilde{t}^k (1-\tilde{t})^{m-k} \sum_{l=0}^{k} C_k^l \theta^l (1-\theta)^{k-l} P_{k-l}. \end{aligned} \tag{9.9}$$

Let p an integer ($0 \le p \le m$). By gathering in this sum all the terms related to P_p, we obtain

$$\tilde{P}(\tilde{t}) = \sum_{p=0}^{m} \sum_{l=0}^{m-p} C_m^{p+l} C_{p+l}^p \theta^{p+l} (1-\theta)^{m-p-l} \tilde{t}^p (1-\tilde{t})^l P_p.$$

Then we recall that $C_m^{p+l} C_{p+l}^p = C_m^p C_{m-p}^l$, and note that

$$\theta^{p+l} (1-\theta)^{m-p-l} \tilde{t}^p (1-\tilde{t})^l = (\theta\tilde{t})^p (\theta - \theta\tilde{t})^l (1-\theta)^{m-p-l}.$$

The formula (9.9) is then written as

$$\begin{aligned} \tilde{P}(\tilde{t}) &= \sum_{p=0}^{m} C_m^p (\theta\tilde{t})^p \sum_{l=0}^{m-p} C_{m-p}^l (\theta - \theta\tilde{t})^l (1-\theta)^{m-p-l} P_p \\ &= \sum_{p=0}^{m} C_m^p (\theta\tilde{t})^p (1-\theta\tilde{t})^{m-p} P_p. \end{aligned} \tag{9.10}$$

For any given value of θ in $[0,1]$, the product $\theta\tilde{t}$ lies in $[0,\theta]$ when the parameter $\tilde{t}$ covers $[0,1]$. When $\tilde{t} \in [0,1]$ the point $\tilde{P}(\tilde{t})$ defined by (9.9) or (9.10) covers the Bézier curve with ending points P_0 and $P(\theta)$.

How do we get the complementary part of the curve? By a reverse ordering of the control points and by changing θ into $1-\theta$. Actually, the point $P(\theta)$ of the Bézier curve with control points $P_0, P_1 \ldots, P_m$ is defined according to

$$P(\theta) = \sum_{k=0}^{m} C_m^k \theta^k (1-\theta)^{m-k} P_k = \sum_{k=0}^{m} C_m^k (1-\theta)^k \theta^{m-k} P_{m-k}.$$

Then $P(\theta)$ is the same point as the point $Q(1-\theta)$ of the Bézier curve with control points $P_m, P_{m-1}, \ldots, P_0$. In order to obtain the part of the curve with ending points $P(\theta)$ and P_m, we first generate the points $Q_0^0, Q_1^1, \ldots, Q_m^m$ associated with the Bézier curve with control points $P_m, P_{m-1}, \ldots, P_0$. Then we set

$$\tilde{Q}(t) = \sum_{k=0}^{m} C_m^k t^k (1-t)^{m-k} Q_k^k.$$

Remark 9.4. This result may be generalized to B-spline curves for which more properties can be established in relation to basic operations such as moving, removing and inserting a control point.

9.6 Intersection of Bézier Curves

We address now the problem of finding the intersection of two Bézier curves $\mathcal{B}_m$ and $\mathcal{B}'_{m'}$ defined in $\mathbb{R}^2$ by their control points. We describe the two curves by their generic points

$$\begin{aligned} P(t) &= \sum_{k=0}^{m} C_m^k t^k (1-t)^{m-k} P_k, \\ P'(t') &= \sum_{k'=0}^{m'} C_{m'}^{k'} (t')^{k'} (1-t')^{m'-k'} P'_{k'}. \end{aligned} \tag{9.11}$$

Now, is it possible to find two values t and t' such that $P(t) = P'(t')$? How do we compute them when they exist? According to the theory of algebraic geometry, one can deduce implicit representations $f(x,y)$ and $f'(x,y)$ of both curves $\mathcal{B}_m$ and $\mathcal{B}'_{m'}$. But within the corresponding formulation, searching for a possible common point is equivalent to finding the roots of a polynomial of degree $m+m'$. This is a too complicated and time-consuming way to get the solution. We propose here a method based on particular properties of Bézier curves. We proceed as follows: Since any Bézier curve $\mathcal{B}_m$ is entirely contained in the convex hull $\mathcal{E}_m$ of its control points, we know that the intersection set $\mathcal{B}_m \cap \mathcal{B}'_{m'}$ is empty when the convex hulls $\mathcal{E}_m$ and $\mathcal{E}'_{m'}$ do not intersect. Conversely, both curves $\mathcal{B}_m$ and $\mathcal{B}'_{m'}$ may intersect when the convex hulls intersect; in order to obtain a more accurate view of the problem in this case,

we can split both curves into two parts and check the intersection of the corresponding convex hulls. Splitting a Bézier curve $\mathcal{B}_m$ into two subcurves $\mathcal{B}_m^1$ and $\mathcal{B}_m^2$ with their associated control points sends us back to the previous section. We denote by $\mathcal{B}_m^1$ the curve corresponding to the part of the curve $\mathcal{B}_m$ obtained for $t \in [0, 0.5]$, while $\mathcal{B}_m^2$ corresponds to the part of the curve $\mathcal{B}_m$ obtained for $t \in [0.5, 1]$. The control points of both curves $\mathcal{B}_m^1$ and $\mathcal{B}_m^2$ are defined by (9.8). We proceed then by successive iterations as long as there exist two intersecting convex hulls. The corresponding algorithm is the following:

$$
\begin{array}{l}
\text{initialization :} \\
\quad \mathcal{E}_1 = \mathcal{E}_m,\ \mathcal{E}'_1 = \mathcal{E}'_{m'} \\
\text{iterations: while } \mathcal{E}_k \cap \mathcal{E}'_k \neq \emptyset \text{ , do} \\
\quad \text{split: } \mathcal{B}_k = \mathcal{B}_{k_1} \cup \mathcal{B}_{k_2} \\
\quad \text{associate: } \mathcal{E}_{k_1},\ \mathcal{E}_{k_2} \\
\quad \text{split: } \mathcal{B}'_{k'} = \mathcal{B}'_{k'_1} \cup \mathcal{B}'_{k'_2} \\
\quad \text{associate: } \mathcal{E}'_{k'_1},\ \mathcal{E}'_{k'_2} \\
\quad \text{check: } \mathcal{E}_{k_i} \cap \mathcal{E}'_{k'_j} \qquad (*) \\
\text{end do}
\end{array}
\tag{9.12}
$$

The intersection of two bounded convex sets is a bounded convex set, so $\mathcal{E}_{k_i} \cap \mathcal{E}'_{k'_j}$ is convex and contained in both $\mathcal{E}_{k_i}$ and $\mathcal{E}'_{k'_j}$; thus its "size" is decreasing as the algorithm (9.12) evolves. This algorithm converges in the following way: Either all intersections are empty and then curves $\mathcal{B}_m$ and $\mathcal{B}'_{m'}$ do not intersect, or there exists at least one intersection whose size is vanishing as (9.12) proceeds; then the convex intersection is shrinking to a point common to both curves. Note that algorithm (9.12) is able to cope with multiple intersections.

In order to check automatically whether sets $\mathcal{E}_k$ and $\mathcal{E}'_k$ intersect, we need to compute the convex hull of $m+1$ given points in $\mathbb{R}^2$. Since $\mathcal{E}_k$ is bounded by a convex polygon $\mathcal{P}_k$, its computer representation is a *mesh* of $\mathcal{P}_k$. This mesh $\mathcal{M}_k$ may be any set of triangles whose union is equal to $\mathcal{P}_k$. Their vertices are the control points and they satisfy the classical rule that the intersection of two distinct triangles is either empty or reduced to a common vertex or a common edge. We can then check whether $\mathcal{E}_k$ and $\mathcal{E}'_k$ intersect by testing the intersection of all pairs of triangles $(T_{k,i}, T'_{k,j}) \in \mathcal{M}_k \times \mathcal{M}'_k$.

Although this method is correct, it is too tedious for our purpose. For the sake of simplicity, we proceed as follows: Each convex hull $\mathcal{E}_k$ is embedded in a rectangle $R_k = [x_m^k, x_M^k] \times [y_m^k, y_M^k]$ defined by the extreme values of the coordinates of the control points. Then we replace in (9.12) the line quoted by $(*)$ by *check* $R_{k_i} \cap R_{k'_j}$. Since $\mathcal{E}_k \subset R_k$, this may slow down the convergence of (9.12), but the modified algorithm is very simple to implement (the

intersection of two rectangles, when it exists, is a rectangle that is easy to compute).

Stopping criterion: it is necessary to stop the iterations in algorithm (9.12). An efficient way to check the accuracy of the result is to set an acceptable smallest size σ of the rectangle $R = R_k \cap R_{k'}$. When the length (or the width) of R is smaller than σ, we define the common point $S = \mathcal{B}_m \cap \mathcal{B}'_{m'}$ as the intersection of both diagonals of R. Finally, once S has been spotted, it remains to set it on the Bézier curve $\mathcal{B}_m$; in other words, we have to compute the corresponding value of the parameter t such that

$$S = S(t) = \sum_{k=0}^{m} C_m^k t^k (1-t)^{m-k} P_k.$$

This value is obtained by a linear approximation:

$$t \approx t(M_2)\frac{x(S) - x(M_1)}{x(M_2) - x(M_1)} + t(M_1)\frac{x(M_2) - x(S)}{x(M_2) - x(M_1)}. \tag{9.13}$$

We proceed in the same way to compute the value of t':

$$\begin{aligned} S = S'(t') &= \sum_{k'=0}^{m'} C_{m'}^{k'} (t')^{k'} (1-t')^{m'-k'} P'_{k'}, \\ t' &\approx t'(M'_2)\frac{x(S) - x(M'_1)}{x(M'_2) - x(M'_1)} + t'(M'_1)\frac{x(M'_2) - x(S)}{x(M'_2) - x(M'_1)}. \end{aligned} \tag{9.14}$$

Remark 9.5. We use ordinates $y(M_1)$ and $y(M_2)$ in (9.13) when $x(M_1) = x(M_2)$.

Remark 9.6. The stopping criterion may be modified by computing the distance between the curve and the straight line M_1M_2, instead of the size of the rectangle R. This is obtained via an approximation of the curvature. For example, if (x_k, y_k) are the coordinates of sampling points of $\mathcal{B}_m$, we may use a value of h, defined by

$$h = \max_k(|x_{k-1} - 2x_k + x_{k+1}|, |y_{k-1} - 2y_k + y_{k+1}|).$$

9.6.1 Implementation

Exercise 9.2. 1. Compute and display two Bézier curves $\mathcal{B}_m$ and $\mathcal{B}'_{m'}$ defined in $\mathbb{R}^2$.
2. Implement the algorithm (9.12) in its simplified formulation. Check the intersection of the curves.
3. Compute the values of t and t' according to (9.13) and (9.14). Display the corresponding points $S(t)$ and $S'(t')$. Compare to the values obtained by (9.12).

A solution of this exercise is proposed in Sect. 9.10 at page 211.

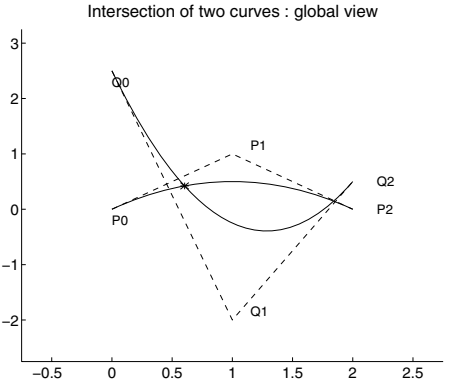

Fig. 9.7. Intersection of Bézier curves.

9.7 Bézier Surfaces

Similar to Bézier curves, a pleasant and easy-to-handle representation of surfaces is obtained using two parameters t_1 and t_2. Let m_1 and m_2 be two positive integers, and consider $(m_1+1)\times(m_2+1)$ control points $P_{k_1,k_2}\in\mathbb{R}^3$. For all $(t_1,t_2)\in[0,1]\times[0,1]$, we define the point $P(t_1,t_2)$ by the relation

$$P(t_1,t_2)=\sum_{k_1=0}^{m_1}\sum_{k_2=0}^{m_2}C_{m_1}^{k_1}C_{m_2}^{k_2}t_1^{k_1}(1-t_1)^{m_1-k_1}t_2^{k_2}(1-t_2)^{m_2-k_2}P_{k_1,k_2}. \quad (9.15)$$

As (t_1,t_2) ranges in $[0,1]\times[0,1]$, the corresponding point $P(t_1,t_2)$ covers a surface, referred to as a *Bézier patch* by CAGD specialists (see Fig. 9.8). A Bézier surface is then the union of the Bézier patches (see Fig. 9.9).

Remark 9.7. There is no assumption made on the layout of the points P_{k_1,k_2} in using definition (9.15). Nevertheless, this layout has a significant influence on the final rendering of the generated surface. In order to modify the surface by moving some control points, it is easier to use points P_{k_1,k_2} situated on a rectangular grid. The resulting surface is called a *rectangular* patch, opposed to a *triangular* patch, whose control points are situated on a triangular grid and the generating point is defined by

$$P(t_1,t_2,t_3)=\sum_{k_1+k_2+k_3=m}\frac{m!}{k_1!k_2!k_3!}t_1^{k_1}t_2^{k_2}t_3^{k_3}P_{k_1,k_2,k_3}. \quad (9.16)$$

9.8 Basic properties of Bézier Surfaces

9.8.1 Convex Hull

The point $P(t)$ is the barycenter of the $(m_1+1)\times(m_2+1)$ control points P_{k_1,k_2} with the corresponding weights $B_{m_1}^{k_1}(t_1)B_{m_2}^{k_2}(t_2)$. It follows from (9.2)

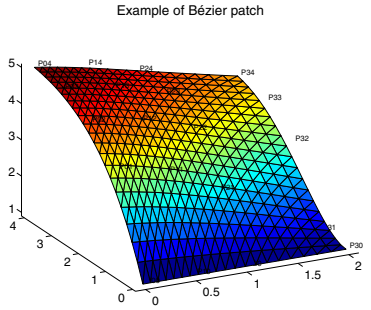

Fig. 9.8. Bézier patch.

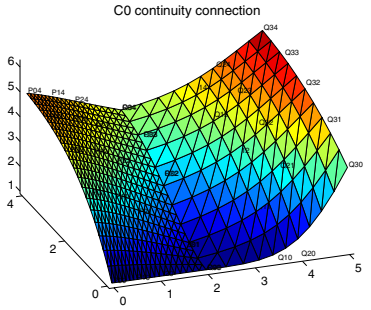

Fig. 9.9. $\mathcal{C}^0$ continuity.

that $P(t)$ lies in the convex hull of the points P_{k_1,k_2}, which is a volume with polygonal faces.

9.8.2 Tangent Vector

The tangent plane to the Bézier surface at the point $P(t_1, t_2)$ is defined by the two tangent vectors $\boldsymbol{\tau}_1(t_1, t_2) = \frac{d}{dt_1} P(t_1, t_2)$ and $\boldsymbol{\tau}_2(t_1, t_2) = \frac{d}{dt_2} P(t_1, t_2)$. Consequently, when $P_{0,0} \neq P_{1,0}$ and $P_{0,0} \neq P_{0,1}$, the Bézier surface is tangent to the triangle $P_{1,0}P_{0,0}P_{0,1}$ at point $P_{0,0}$. The same property holds for vertices $P_{m_1,0}$, P_{0,m_2} and P_{m_1,m_2}.

9.8.3 Junction of Bézier Patches

Let $\mathcal{S}_{m_1,m_2}$ be the Bézier patch defined by the $(m_1 + 1) \times (m_2 + 1)$ control points P_{k_1,k_2} $(1 \leq k_1 \leq m_1,\ 1 \leq k_2 \leq m_2)$, and $\mathcal{S}'_{m_1,m_2}$ the Bézier patch defined by the $(m'_1 + 1) \times (m'_2 + 1)$ control points $P'_{k'_1,k'_2}$ $(1 \leq k'_1 \leq m'_1,\ 1 \leq k'_2 \leq m'_2)$. We address now the problem of connecting these two patches.

The simplest junction corresponds to so-called $\mathcal{C}^0$ continuity, supposing that there exists a common curve located on the rim of the surfaces. Such a curve corresponds to an extreme value of t_1 or t_2 (namely 0 or 1). According to definition (9.15) and properties (9.2), such a curve is a Bézier curve. The $\mathcal{C}^0$ continuity is then satisfied when the corresponding Bézier curves fit; this is true, for example, when the control points are identical on both curves.

Now we look further for a better rendering of the junction, and suppose that $P_{m_1,k_2} = P_{0,k_2}$ for $k_2 = 0, 1, \ldots, m_2$. A $\mathcal{G}^1$ connection is obtained when vectors $\boldsymbol{\tau}_1(1, t_2) = \frac{d}{dt_1} P(1, t_2)$ and $\boldsymbol{\tau}'_1(0, t'_2) = \frac{d}{dt'_1} P'(0, t'_2)$ are collinear at any common point. This condition is equivalent to saying that $P_{m_1,k_2} = P'_{0,k_2}$ is the midpoint of $P_{m_1-1,k_2} P'_{1,k_2}$ for $k_2 = 0, 1, \ldots, m_2$. Furthermore, when the tangent vectors $\boldsymbol{\tau}_2(1, t_2) = \frac{d}{dt_2} P(1, t_2)$ and $\boldsymbol{\tau}'_2(0, t'_2) = \frac{d}{dt'_2} P'(0, t'_2)$ are identical at any common point, a $\mathcal{C}^1$ connection is realized. Examples illustrating the different connections are displayed in Figs. 9.9 and 9.10.

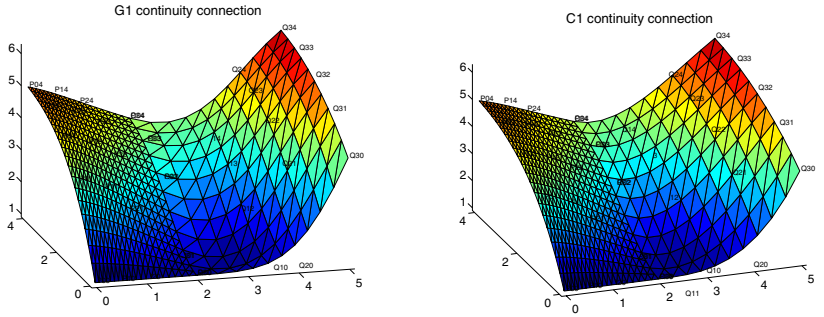

(a) (b)

Fig. 9.10. Junction of patches. (a) $\mathcal{G}^1$ continuity; (b) $\mathcal{C}^1$ continuity.

9.8.4 Construction of the Point $P(t)$

According to definition (9.15), any point $P(t_1, t_2)$ may be computed by an algorithm similar to (9.6). We write

$$P(t_1, t_2) = \sum_{k_1=0}^{m_1} C_{m_1}^{k_1} t_1^{k_1} (1 - t_1)^{m_1 - k_1} P_{k_1}, \tag{9.17}$$

with

$$P_{k_1} = \sum_{k_2=0}^{m_2} C_{m_2}^{k_2} t_2^{k_2} (1 - t_2)^{m_2 - k_2} P_{k_1, k_2}. \tag{9.18}$$

Let k_1 be a given integer. According to (9.17-9.18) the point P_{k_1} appears to be the point $P_{k_1}(t_2)$ of the Bézier curve defined by the $m_2 + 1$ control points $P_{k_1,0}, P_{k_1,1}, \ldots, P_{k_1,m_2}$. It is then possible to calculate its coordinates by means of de Casteljau's algorithm (9.6). Once the $m_1 + 1$ points P_{k_1} are computed, a new application of (9.6) generates the point $P(t_1, t_2)$ on the Bézier patch. The whole patch is then defined as the union of all rectangular faces generated by vertices $P(t_1, t_2)$, $P(t_1 + \Delta t_1, t_2)$, $P(t_1 + \Delta t_1, t_2 + \Delta t_2)$, and $P(t_1, t_2 + \Delta t_2)$ (here Δt_1 and Δt_2 are the sampling step sizes for t_1 and t_2). The corresponding construction algorithm (9.19) is called the *de Boor–Coox algorithm*:

for $p_1 = 0$, initialization:

for $q_1 = 0, 1, \ldots, m_1$, do

construction of point P_{q_1} by (9.6)

for $p_2 = 0$, initialization:

for $q_2 = 0, 1, \ldots, m_2$, do

$$P^0_{q_1,q_2} = P_{q_1,q_2}$$

end do

end do

for $p_2 = 1, 2, \ldots, m_2$, do

for $q_2 = p_2, p_2 + 1, \ldots, m_2$, do

$$P^{p_2}_{q_1,q_2} = t_2 P^{p_2-1}_{q_1,q_2-1} + (1 - t_2) P^{p_2-1}_{q_1,q_2}. \tag{9.19}$$

end do

end do: set $P_{q_1} = P_{q_1,m_2}$

end of computation of P_{q_1}, set: $P^0_{q_1} = P_{q_1}$

end do

for $p_1 = 1, 2, \ldots, m_1$, do

for $q_1 = p_1, p_1 + 1, \ldots, m_1$, do

$$P^{p_1}_{q_1} = t_1 P^{p_1-1}_{q_1-1} + (1 - t_1) P^{p_1-1}_{q_1}.$$

end do

end do: set $P(t_1, t_2) = P^{m_1}_{m_1}$

9.9 Construction of Bézier Surfaces

Exercise 9.3. 1. Choose $(m_1 + 1) \times (m_2 + 1)$ points $P_{0,0}, P_{1,0}, \ldots, P_{m_1,m_2}$ in $\mathbb{R}^3$.

2. Write a general procedure generating the point $P(t_1, t_2)$ of the Bézier patch with control points $P_{0,0}, P_{1,0}, \ldots, P_{m_1,m_2}$, using the de Boor–Coox algorithm for any value $(t_1, t_2) \in [0, 1] \times [0, 1]$.
3. Compute and display the corresponding Bézier patch.
4. Repeat the computation for different values of (m_1, m_2) and different sets of control points.

5. Check the different continuity conditions.

A solution of this exercise is proposed in Sect. 9.10 at page 211.

Exercise 9.4. (for the brave) Extend the method for computing the intersection of two curves to compute the intersection of Bézier surfaces. Write and check the corresponding procedure.

9.10 Solutions and Programs

Solution of Exercise 9.1

The file *CAGD_ex1.m* contains the procedure `CAGD_ex1`, which defines a set of control points, and builds and displays the resulting Bézier curve, as shown in Fig. 9.1(a). This procedure calls the function `CAGD_cbezier`, which computes a set of sampling points, and the function `CAGD_casteljau`, which builds a point according to the de Casteljau's algorithm (9.6).

Listing 9.1 *(CAGD_casteljau.m)*

```
function [x,y]=CAGD_casteljau(t,XP,YP)
%%
%%   Construction of a point of a Bezier curve
%%   according to de Casteljau's algorithm
%%
m=size(XP,2)-1;
xx=XP;yy=YP;
for kk=1:m
xxx=xx; yyy=yy;
for k=kk:m
xx(k+1)=(1-t)*xxx(k)+t*xxx(k+1);
yy(k+1)=(1-t)*yyy(k)+t*yyy(k+1);
end
end
x=xx(m+1);y=yy(m+1);
```

The procedure `CAGD_ex1` then calls the function `CAGD_tbezier`, which displays the Bézier curve and its control points. The control polygon, as shown in Fig. 9.2, is available for calling procedures `CAGD_ex1b` and `CAGD_pbezier`. Exchanging the points P_1 and P_3 will have as result the generation of a different curve, with a nonconvex control polygon (see procedure `CAGD_ex1c`).

Procedures `CAGD_connectCC0`, `CAGD_connectCG1`, and `CAGD_connectCC1` plot examples of $\mathcal{C}^0$, $\mathcal{G}^1$, and $\mathcal{C}^1$ continuity.

Solution of Exercise 9.2

The procedure `CAGD_ex2` defines two sets of control points, and builds and displays both corresponding Bézier curves. Each curve is then located within a rectangle by the function `CAGD_drectan`. A possible intersection of these rectangles is then tested by the procedure `CAGD_rbezier`. When this is successful, the function `CAGD_dbezier` is used; this procedure is an implementation of algorithm (9.12), seeking iteratively the intersection of both curves. When the rectangular intersection is small enough, the coordinates of the intersection point are computed; then an approximation of the corresponding value of the parameter t is obtained from (9.13) and (9.14).

Finally, the procedure calls the function `CAGD_cbezier`, which computes a sampling of points of a Bézier curve, using the functions `CAGD_casteljau` and `CAGD_tbezier`. The resulting curve and control points are then displayed.

Solution of Exercise 9.3

The procedure `CAGD_ex3` defines a set of control points, and builds and displays the corresponding Bézier patch, as represented in Fig. 9.8 (you can use the "Rotate 3D" button to obtain a global view of the surface). This procedure calls the functions `CAGD_sbezier`, which gives a sampling of points of a Bézier surface; `CAGD_coox`; and `CAGD_ubezier`, which finally displays both the surface and its control points. The procedure `CAGD_coox` builds one point of a Bézier surface according to the de Boor–Coox algorithm (9.19).

Listing 9.2 *(CAGD_coox.m)*

```
function [x,y,z]=CAGD_coox(t1,t2,XP,YP,ZP)
%%
%%   Construction of a point on a Bzier surface
%%   according to the de Boor--Coox algorithm
%%
np1=size(XP,1);np2=size(XP,2);
xx1=zeros(np1,1);yy1=zeros(np1,1);zz1=zeros(np1,1);
for k1=1:np1
xx2=zeros(np2,1);yy2=zeros(np2,1);zz2=zeros(np2,1);
for k2=1:np2
xx2(k2)=XP(k1,k2);yy2(k2)=YP(k1,k2);zz2(k2)=ZP(k1,k2);
end
[x,y,z]=CAGD\_cast3d(t2,xx2,yy2,zz2);
xx1(k1)=x;yy1(k1)=y;zz1(k1)=z;
end
[x,y,z]=CAGD\_cast3d(t1,xx1,yy1,zz1);
```

The procedures `CAGD_connectSC0`, `CAGD_connectSG1`, and `CAGD_connectSC1` display examples of $\mathcal{C}^0$ (respectively $\mathcal{G}^1$ and $\mathcal{C}^1$) and to 9.10. The obtained results correspond to Figs. 9.9 and 9.10.

Chapter References

P. Bézier, *Courbes et Surfaces*, Mathématiques et CAO, vol 4, Hermes, Paris, 1986.

P. de Casteljau, *Formes à Pôles*, Mathématiques et CAO, vol 2, Hermes, Paris, 1985.

S.A. Coons, *Surface Patches and B-splines Curves*, CAGD, 1974.

G. Farin and D. Hansford, *The Essentials of CAGD*, AK Peters, 2000.

G. Farin, *Curves and Surfaces for CAGD: A Practical Guide*, Academic Press 4th ed. New York, 1996.

J. Ferguson, *Multivariable Curve Interpolation*, Journal of the Association for Computing Machinery, 1964.

J. Hoschek and D. Lasser, *Fundamentals of Computer Aided Geometric Design*, Peters, Massachusetts, 1997.

L. Piegl and W. Tiller, *The NURBS Book*, Springer, Berlin, 1995.

10

Gas Dynamics: The Riemann Problem and Discontinuous Solutions: Application to the Shock Tube Problem

Project Summary

Level of difficulty:	3
Keywords:	Nonlinear hyperbolic systems, Euler equations for gas dynamics, centered schemes: Lax–Wendroff, MacCormack; upwind schemes: Godunov, Roe
Application fields:	Shock tube, supersonic flows

The interest in studying the shock tube problem is threefold. From a fundamental point of view, it offers an interesting framework to introduce some basic notions about nonlinear hyperbolic systems of partial differential equations (PDEs). From a numerical point of view, this problem constitutes, since the exact solution is known, an inevitable and difficult test case for any numerical method dealing with discontinuous solutions. Finally, there is a practical interest, since this model is used to describe real shock tube experimental devices.[1]

10.1 Physical Description of the Shock Tube Problem

The fundamental idea of the shock tube is the following: consider a long one-dimensional (1D) tube, closed at its ends and divided into two equal regions by a thin diaphragm (see Fig. 10.1). Each region is filled with the same gas, but with different thermodynamic parameters (pressure, density, and temperature). The region with the highest pressure is called the *driven*

[1] The first shock tube facility was built in 1899 by Paul Vieille to study the deflagration of explosive charges. Nowadays, shock tubes are currently used as low-cost high-speed wind tunnels, in which a wide variety of aerodynamic or aeroballistic topics are studied: supersonic aircraft flight, gun performance, asteroid impacts, shuttle atmospheric entry, etc.

section of the tube, while the low-pressure part is the *working section*. The gas being initially at rest, the sudden breakdown of the diaphragm generates a high-speed flow, which propagates in the working section (this is the place where the model of a free-flying object, such as a supersonic aircraft, will be placed).

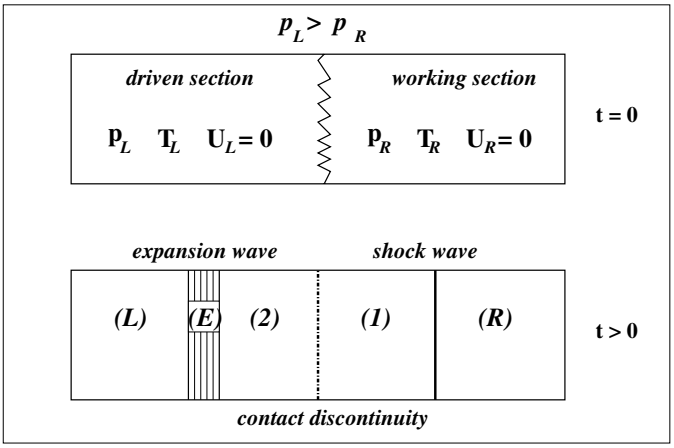

Fig. 10.1. Sketch of the initial configuration of the shock tube ($t = 0$) and waves propagating in the tube after the diaphragm breakdown ($t > 0$).

Let us get into a more detailed analysis of the problem. Consider (Fig. 10.1) that the left part of the tube is the driven section, defined by the pressure p_L, the density ρ_L, the temperature T_L, and the initial velocity $U_L = 0$. Similarly, the parameters of the (right part) working section are $p_R < p_L$, ρ_R, T_R, and $U_R = 0$.

At time $t = 0$ the diaphragm breaks, generating a process that naturally tends to equalize the pressure in the tube. The gas at high pressure expands through an *expansion (or rarefaction) wave* and flows into the working section, pushing the gas of this part. The rarefaction is a continuous process and takes place inside a well-defined region (the expansion fan) that propagates to the left (region (E) in Fig. 10.1); the width of the expansion fan grows in time.

The compression of the low-pressure gas generates a *shock wave* propagating to the right. The expanded gas is separated from the compressed gas by a *contact discontinuity*, which can be regarded as a fictitious membrane traveling to the right at constant speed. At this point of our simplified description, we just note that some of the physical functions defining the flow in the tube ($p(x), \rho(x), T(x)$, and $U(x)$) are discontinuous across the shock wave and the contact discontinuity. These discontinuities, which cause the difficulty of the problem, will be described in greater detail in the following sections.

10.2 Euler Equations of Gas Dynamics

To simplify the mathematical description of the shock tube problem we consider an infinitely long tube (to avoid reflections at the tube ends) and neglect viscous effects in the flow. We also suppose that the diaphragm is completely removed from the flow at $t = 0$. Under these simplifying hypotheses, the compressible flow in the shock tube is described by the one-dimensional (1D) Euler system of PDEs (see, for instance, Hirsch, 1988; LeVeque, 1992)

$$\frac{\partial}{\partial t}\underbrace{\begin{pmatrix}\rho\\ \rho U\\ E\end{pmatrix}}_{W(x,t)}+\frac{\partial}{\partial x}\underbrace{\begin{pmatrix}\rho U\\ \rho U^2+p\\ (E+p)U\end{pmatrix}}_{F(W)}=0, \tag{10.1}$$

where ρ is the density of the gas and E the total energy:

$$E=\frac{p}{\gamma-1}+\frac{\rho}{2}U^2. \tag{10.2}$$

To close this system of equations, we need to write the constitutive law of the gas (or equation of state). Considering the perfect gas model, the equation of state is

$$p=\rho\mathcal{R}T. \tag{10.3}$$

The constants $\mathcal{R}$ and γ characterize the thermodynamic properties of the gas ($\mathcal{R}$ is the universal gas constant divided by the molecular mass and γ is the ratio of specific heat coefficients). It is also useful to define the local speed of sound a, the Mach number M, and the total enthalpy H:

$$a=\sqrt{\gamma\mathcal{R}T}=\sqrt{\gamma\frac{p}{\rho}},\quad M=\frac{U}{a},\quad H=\frac{E+p}{\rho}=\frac{a^2}{\gamma-1}+\frac{1}{2}U^2. \tag{10.4}$$

Considering the column vector of unknowns $W=(\rho,\rho U,E)^t$, the Euler system of equations (10.1) can be written in the following *conservative* form:

$$\frac{\partial W}{\partial t}+\frac{\partial}{\partial x}F(W)=0, \tag{10.5}$$

with the initial condition (we denote by x_0 the abscissa of the diaphragm):

$$W(x,0)=\begin{cases}(\rho_L,\rho_L U_L,E_L),\ x\le x_0,\\ (\rho_R,\rho_R U_R,E_R),\ x>x_0.\end{cases} \tag{10.6}$$

The vector W contains the conserved variables and $F(W)$ the conserved fluxes. Note that with this choice of the vector of unknowns W, the pressure is not an unknown, since it can be derived from (10.2) using the components of W.

The mathematical analysis of the Euler system of PDEs usually considers its *quasilinear* form:[2]

$$\frac{\partial W}{\partial t} + A\frac{\partial W}{\partial x} = 0, \tag{10.7}$$

with the Jacobian matrix

$$A = \frac{\partial F}{\partial W} = \begin{pmatrix} 0 & 1 & 0 \\ \frac{1}{2}(\gamma-3)U^2 & (3-\gamma)U & \gamma-1 \\ \frac{1}{2}(\gamma-1)U^3 - UH & H-(\gamma-1)U^2 & \gamma U \end{pmatrix}. \tag{10.8}$$

It is interesting to note that the matrix A satisfies the following remarkable relationship:

$$AW = F(W). \tag{10.9}$$

Furthermore, we can easily calculate its eigenvalues

$$\lambda^0 = U, \quad \lambda^+ = U + a, \quad \lambda^- = U - a, \tag{10.10}$$

and the corresponding eigenvectors

$$v^0 = \begin{pmatrix} 1 \\ U \\ \frac{1}{2}U^2 \end{pmatrix}, \quad v^+ = \begin{pmatrix} 1 \\ U+a \\ H+aU \end{pmatrix}, \quad v^- = \begin{pmatrix} 1 \\ U-a \\ H-aU \end{pmatrix}. \tag{10.11}$$

We conclude that the Jacobian matrix A is diagonalizable, i.e., it can be decomposed as $A = P\Lambda P^{-1}$, where

$$\Lambda = \begin{pmatrix} U-a & 0 & 0 \\ 0 & U & 0 \\ 0 & 0 & U+a \end{pmatrix}, \quad P = \begin{pmatrix} 1 & 1 & 1 \\ U-a & U & U+a \\ H-aU & \frac{1}{2}U^2 & H+aU \end{pmatrix}. \tag{10.12}$$

We can easily verify that

$$P^{-1} = \begin{pmatrix} \frac{1}{2}\left(\alpha_1 + \frac{U}{a}\right) & -\frac{1}{2}\left(\alpha_2 U + \frac{1}{a}\right) & \frac{\alpha_2}{2} \\ 1-\alpha_1 & \alpha_2 U & -\alpha_2 \\ \frac{1}{2}\left(\alpha_1 - \frac{U}{a}\right) & -\frac{1}{2}\left(\alpha_2 U - \frac{1}{a}\right) & \frac{\alpha_2}{2} \end{pmatrix}, \tag{10.13}$$

where $\alpha_1 = (\gamma-1)U^2/(2a^2)$ and $\alpha_2 = (\gamma-1)/a^2$.

Definition 10.1. *The system (10.7) with the matrix A diagonalizable with real eigenvalues is called hyperbolic.*

The hyperbolic character of the system (10.7) has important consequences on the propagation of the information in the flow field. Certain quantities,

[2] The reader who has already explored Chap. 1 of this book may notice that this form is similar to that of the convection equation. The underlying idea is here to generalize the analysis of characteristics in the case of a system of PDEs.

called *invariants*,[3] are transported along particular curves in the plane (x,t), called *characteristics*. From a numerical point of view, this suggests a simple way to calculate the solution in any point $P(x,t)$ by gathering all the information transported through the characteristics starting from P and going back to regions where the solution is already known (imposed by the initial condition, for example).

The general form of the equation defining a characteristic is $dx/dt = \lambda$, where λ is an eigenvalue of the Jacobian matrix A. Since the corresponding invariant r is constant along the characteristic, it satisfies

$$\frac{dr}{dt} = \frac{\partial r}{\partial t} + \frac{\partial r}{\partial x}\frac{dx}{dt} = 0, \quad \text{or} \quad \frac{\partial r}{\partial t} + \lambda \frac{\partial r}{\partial x} = 0. \tag{10.14}$$

In the simplest case of the convection equation $\partial u/\partial t + c\,\partial u/\partial x = 0$, with constant transport velocity c, there exists a single characteristic curve, which is the line $x = c\,t$, and the corresponding invariant is the solution itself, $r = u$ (see also Chap. 1). From (10.10) we infer that the system (10.7) has three distinct characteristics:

$$C^0 : \frac{dx}{dt} = U, \quad C^+ : \frac{dx}{dt} = U + a, \quad C^- : \frac{dx}{dt} = U - a. \tag{10.15}$$

The invariants can be generally expressed as differential relations (see, for instance, Hirsch (1988); Godlewski and Raviart (1996) for details)

$$dr^0 = dp - a^2\, d\rho = 0, \quad dr^+ = dp + \rho a\, dU = 0, \quad dr^- = dp - \rho a\, dU = 0,$$

which have to be integrated along the corresponding characteristic curves. In the case of an isentropic flow[4] we obtain

$$r^0 = p/\rho^\gamma, \quad r^+ = U + \frac{2a}{\gamma - 1}, \quad r^- = U - \frac{2a}{\gamma - 1}. \tag{10.16}$$

The above relations will be used in the following to derive the exact solution of the shock tube problem.

Definition 10.2. *The nonlinear hyperbolic system of PDEs (10.5) and piecewise constant initial condition (10.6) define the Riemann problem.*

---

[3] For a rigorous analysis of hyperbolic systems of PDEs and related definitions (in particular the definition of Riemann invariants), the reader can refer to Hirsch (1988); LeVeque (1992); Godlewski and Raviart (1996).

[4] The entropy variation of a perfect gas during its evolution starting from a reference state A is $s - s_A = C_v \ln\left(\frac{p/p_A}{(\rho/\rho_A)^\gamma}\right)$, where $C_v = \mathcal{R}/(\gamma - 1)$ is the heat coefficient under constant volume. For an isentropic flow, since the entropy remains unchanged ($s = s_A$), we deduce that the ratio p/ρ^γ is constant.

10.2.1 Dimensionless Equations

When building numerical applications we usually prefer to remove physical units from equations and work with dimensionless variables. This simplifies the problem formulation and may reduce computational round-off errors. Physical variables in previous equations are nondimensionalized (or scaled) using a reference state defined by the parameters of the working section:

$$\begin{aligned} \rho^* = \rho/\rho_R,\ U^* = U/a_R,\ a^* = a/a_R,\ T^* = T/(\gamma T_R), \\ p^* = p/(\rho_R a_R^2) = p/(\gamma p_R),\ E^* = E/(\rho_R a_R^2),\ H^* = H/a_R^2. \end{aligned} \quad (10.17)$$

We also nondimensionalize space and time variables as $x^* = x/L$, $t^* = t/(L/a_R)$, where L is the length of the tube.

The Euler equations for the dimensionless variables (denoted by the star superscript) keep the same differential form as previously:

$$\frac{\partial}{\partial t^*} \underbrace{\begin{pmatrix} \rho^* \\ \rho^* U^* \\ E^* \end{pmatrix}}_{W^*(x^*,t^*)} + \frac{\partial}{\partial x^*} \underbrace{\begin{pmatrix} \rho^* U^* \\ \rho^* U^{*2} + p^* \\ (E^* + p^*) U^* \end{pmatrix}}_{F^*(W^*)} = 0. \quad (10.18)$$

Dimensionless total energy E^* and total enthalpy H^* become

$$E^* = \frac{p^*}{\gamma - 1} + \frac{\rho^*}{2} U^{*2}, \quad H^* = \frac{(a^*)^2}{\gamma - 1} + \frac{1}{2} U^{*2}. \quad (10.19)$$

Differences with respect to previous physical equations appear in the equation of state

$$p^* = \rho^* T^*, \quad (10.20)$$

and in the definition of the speed of sound

$$a^* = \sqrt{\gamma \frac{p^*}{\rho^*}} = \sqrt{\gamma T^*}. \quad (10.21)$$

In the interests of simplicity, we drop the star superscript in subsequent equations; only dimensionless variables will be considered in the following sections.

10.2.2 Exact Solution

The exact solution of the shock tube problem follows the physical and mathematical descriptions given in previous sections. The tube is separated (see Fig. 10.1) into four uniform regions, i.e., with constant parameters (pressure, density, temperature, and velocity): the left (L) and right (R) regions (which keep the parameters imposed by the initial condition) and two intermediate regions, denoted by subscripts 1 and 2.

It is important to identify these regions in the (x,t) plane (see Fig. 10.2). All the waves are centered at the initial position of the diaphragm ($t=0, x=x_0$). Since the shock and the contact discontinuity propagate in uniform zones, they have constant velocities and hence are displayed as lines in the (x,t) diagram. The expansion wave extends through the new zone (E), the expansion fan, in which the flow parameters vary continuously (see below). We remember that the shock wave and the contact discontinuity propagate to the right, while the expansion fan moves to the left.

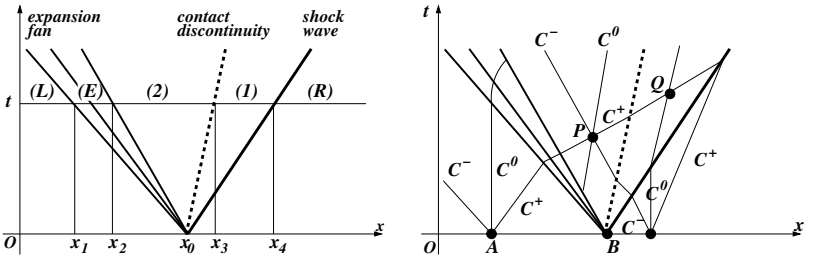

Fig. 10.2. Diagram in the (x,t) plane of the exact solution of the shock tube problem (left). Characteristics used to calculate the exact solution (right).

We start the calculation of the exact solution by writing the dimensionless parameters of the (L) and (R) regions (which are in fact the input parameters for a computer program):

$$\text{Region (R):} \quad \rho_R = 1,\ p_R = 1/\gamma,\ T_R = 1/\gamma,\ a_R = 1,\ U_R = 0, \tag{10.22}$$

$$\text{Region (L):} \quad \rho_L,\ p_L,\ T_L,\ a_L,\ U_L = 0 \text{ (given quantities).} \tag{10.23}$$

We then use the jump relations across the discontinuities and take into account the propagation of the information along the characteristics, as follows:

1. The shock wave implies the discontinuity of all the parameters of the flow. The jump between regions (1) and (R) is described by the Rankine–Hugoniot relations (see, for example, Hirsch (1988)):

$$\frac{p_1}{p_R} = \frac{2\gamma}{\gamma+1} M_s^2 - \frac{\gamma-1}{\gamma+1}, \tag{10.24}$$

$$\frac{\rho_R}{\rho_1} = \frac{2}{\gamma+1}\frac{1}{M_s^2} + \frac{\gamma-1}{\gamma+1}, \tag{10.25}$$

$$U_1 = \frac{2}{\gamma+1}\left(M_s - \frac{1}{M_s}\right), \tag{10.26}$$

where M_s is the Mach number of the shock, defined in physical units as $M_s = U_s^{phys}/a_R^{phys}$. We note that using our scaling, $M_s = U_s$, where U_s is the dimensionless propagation speed of the shock. We remember that U_s is constant.

2. The contact discontinuity is in fact a discontinuity of the density function, the pressure and the velocity being continuous. Hence

$$U_2 = U_1, \quad p_2 = p_1. \tag{10.27}$$

3. We now link the parameters of region (2) to those of region (L). For this purpose, we consider a point P inside the region (2) and draw the characteristics passing through this point (see Fig. 10.2). We notice that only C^0 and C^+ characteristics will cross the expansion fan to search the information in region (L). Using the expressions (10.15) for the invariants r^0 and r^+ and taking into account that $U_L = 0$, we obtain

$$\frac{\rho_2}{\rho_L} = \left(\frac{p_2}{p_L}\right)^{1/\gamma}, \quad U_2 = \frac{2}{\gamma - 1}(a_L - a_2). \tag{10.28}$$

4. Finally, we combine the previous relations to obtain an implicit equation for the unknown M_s. The detailed calculation follows:

$$M_s - \frac{1}{M_s} \overset{(10.26)}{=} \frac{\gamma+1}{2}U_1 \overset{(10.27)}{=} \frac{\gamma+1}{2}U_2 \overset{(10.28)}{=} a_L\frac{\gamma+1}{\gamma-1}\left(1 - \frac{a_2}{a_L}\right).$$

Since

$$\frac{a_2}{a_L} \overset{(10.21)}{=} \left(\frac{p_2}{p_L}\frac{\rho_L}{\rho_2}\right)^{1/2} \overset{(10.28)}{=} \left(\frac{p_2}{p_L}\right)^{\frac{\gamma-1}{2\gamma}} \overset{(10.27)}{=} \left(\frac{p_1}{p_L}\right)^{\frac{\gamma-1}{2\gamma}},$$

we replace p_1/p_L from (10.24) and finally get the following *compatibility equation*:

$$M_s - \frac{1}{M_s} = a_L\frac{\gamma+1}{\gamma-1}\left\{1 - \left[\frac{p_R}{p_L}\left(\frac{2\gamma}{\gamma+1}M_s^2 - \frac{\gamma-1}{\gamma+1}\right)\right]^{\frac{\gamma-1}{2\gamma}}\right\}. \tag{10.29}$$

Once this implicit nonlinear equation is solved (using an iterative Newton method, for example), the value of M_s will be used in previous relations to determine all the parameters of uniform regions (1) and (2).

To complete the exact solution, we need to determine the extent of each region (i.e., calculate the values of the abscissas x_1, x_2, x_3, x_4 in Fig. 10.2) for a given time value t. We proceed as follows:

- The expansion fan (E) is left-bounded by the C^- characteristic starting from the point B, considered to belong to region (L), i.e., the line of slope $dx/dt = -a_L$. The right bound of the expansion fan is the C^- characteristic starting from the same point B, but considered this time to belong to region (2), i.e., the line of slope $dx/dt = U_2 - a_2$. The values of x_1 and x_2 are consequently

$$x_1 = x_0 - a_L t, \quad x_2 = x_0 + (U_2 - a_2)t. \tag{10.30}$$

Consider now a point (x,t) inside the region (E), i.e., $x_1 \leq x \leq x_2$. Since this point belongs to a C^- characteristic starting from B, necessarily $(x - x_0)/t = U - a$. Using the C^+ characteristic coming from region (L), we also get that $a + (\gamma - 1)U/2 = a_L$. Combining these two relations and remembering that the flow is isentropic, we can conclude that the exact solution inside the expansion fan is

$$U = \frac{2}{\gamma+1}\left(a_L + \frac{x - x_0}{t}\right),\ a = a_L - (\gamma-1)\frac{U}{2},\ p = p_L\left(\frac{a}{a_L}\right)^{\frac{2\gamma}{\gamma-1}}. \tag{10.31}$$

- The contact discontinuity is transported at constant velocity $U_2 = U_1$, so

$$x_3 = x_0 + U_2 t. \tag{10.32}$$

- Since the shock wave also propagates at constant dimensionless velocity $U_s = M_s$, we finally obtain

$$x_4 = x_0 + M_s t. \tag{10.33}$$

Remark 10.1. The exact solution $W(x,t)$ of the shock tube problem depends only on the ratio x/t, as one would have expected from the characteristics analysis of the Euler system of PDEs.

Exercise 10.1. Write a MATLAB function to compute the exact solution of the shock tube problem. The definition header of the function will be as follows:

```
function uex=HYP_shock_exact(x,x0,t)
% Input arguments:
% x   vector of abscissas of dimension M
%      x0  the initial position of the diaphragm
%      t   time at which the solution is calculated
% Output arguments:
% uex  vector of dimensions (3,n) containing the solution as
% uex(1,1:M) the density
% uex(2,1:M) the velocity
% uex(3,1:M) the pressure
```

Plot the dimensionless exact solution ($\rho(x)$, $U(x)$ and $p(x)$) at time $t = 0.2$. Consider $x \in [0,1]$, $x_0 = 0.5$, and a regular (equidistant) grid with $M = 81$ computational points. The physical parameters correspond to those used by Sod (see also Hirsch, 1988): $\gamma = 1.4$, $\rho_L = 8$, $p_L = 10/\gamma$.
Hint: define all the physical parameters as global variables; use the MATLAB built-in function `fzero` to solve the compatibility equation (10.29).

The expected result is displayed in Fig. 10.3. This solution was obtained using the MATLAB program presented in Sect. 10.4 at page 232.

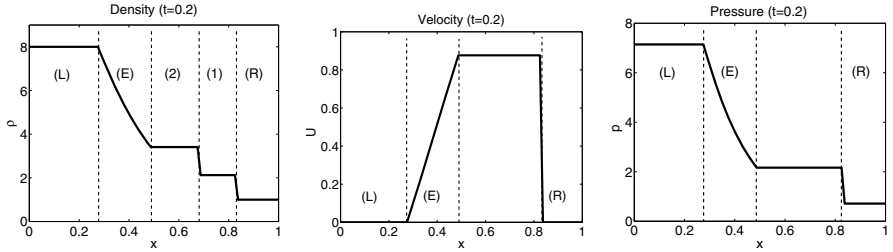

Fig. 10.3. Exact solution of the shock tube problem (Sod's data) at time $t = 0.2$.

10.3 Numerical Solution

The first idea one would have in mind when attempting to numerically solve the Euler system of PDEs (10.18) is to use *elementary* discretization methods discussed in Chap. 1 for scalar PDEs, for example, an Euler or a Runge–Kutta method for the time integration and centered finite differences for the space discretization. We shall see, however, that such methods are not appropriate to compute discontinuous solutions, since they generate nonphysical oscillations. This drawback of the space-centered schemes for computing the shock tube problem will be illustrated using the more sophisticated Lax–Wendroff and MacCormack schemes. We shall also give a quick description of upwind schemes that take into account the hyperbolic character of the system and allow a better numerical solution. Results using Roe's upwind scheme will be discussed at the end.

10.3.1 Lax–Wendroff and MacCormack Centered Schemes

The space-centered schemes were historically the first to be derived to solve hyperbolic systems. The two most popular schemes, the Lax and Wendroff scheme and the MacCormack scheme, are still used in some industrial numerical codes. We shall apply these schemes to solve the Euler system (10.18) written in the conservative form

$$\frac{\partial W}{\partial t} + \frac{\partial}{\partial x} F(W) = 0. \tag{10.34}$$

We use a regular (or equidistant) discretization of the domain of definition of the problem $(x, t) \in [0, 1] \times [0, T]$:

- in space

$$x_j = (j-1)\delta x, \quad \delta x = \frac{1}{M-1}, \quad j = 1, 2, \ldots, M, \tag{10.35}$$

- and in time

$$t^n = (n-1)\delta t, \quad \delta t = \frac{T}{N-1}, \quad n = 1, 2, \ldots, N. \tag{10.36}$$

For both schemes, the numerical solution W_j^{n+1} (at time t_{n+1} and space position x_j) is computed in two steps (a predictor and a corrector step) following the formulas displayed in Fig. 10.4.

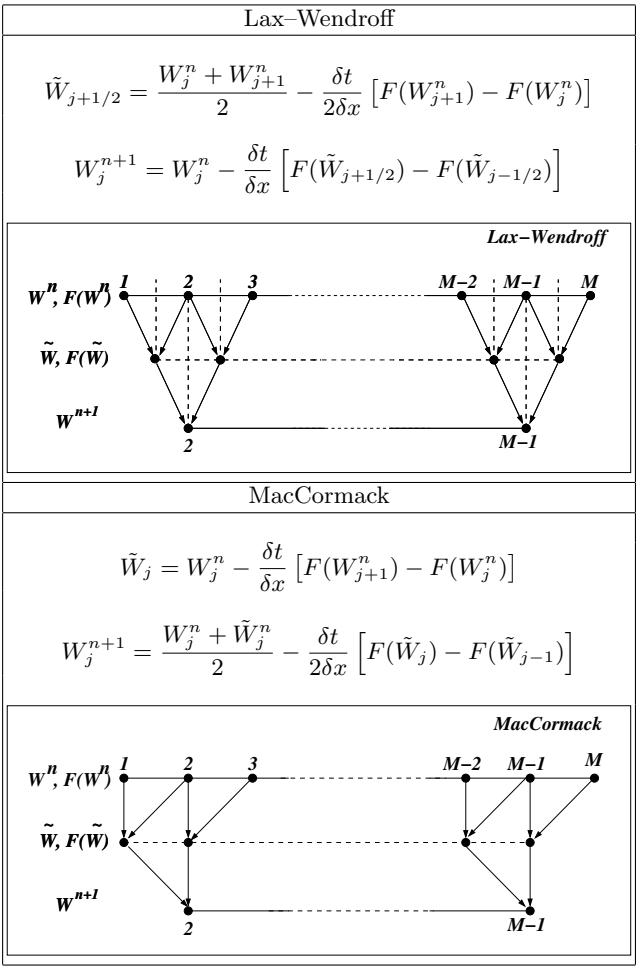

Fig. 10.4. Formulas of Lax–Wendroff and MacCormack space-centered schemes. Schematic representation of their predictor and corrector steps.

We discuss in the following some remarkable features of these schemes.

1. (*Boundary values.*) From the schematic representation of the predictor and corrector steps in Fig. 10.4, we notice that only the components $j = 2, \ldots, (M-1)$ of the solution are calculated. The remaining components for $j = 1$ and $j = M$ need to be prescribed by appropriate boundary conditions.

Since the tube is assumed infinite, we impose $W_1^n = W_L$ and $W_M^n = W_R$ at any time level t_n. Practically, this is equivalent to leaving unchanged the first and last components of the solution vector. Meanwhile, it is obvious that the computation must stop before one of the waves (expansion or shock) hits the boundary.

2. (*Propagation of information.*) The predictor step of the Lax–Wendroff scheme computes an intermediate solution at interfaces $\left(j+\frac{1}{2}\right)$ and $\left(j-\frac{1}{2}\right)$ using forward finite differences. These intermediate values are then used in the centered finite difference scheme of the corrector step.

The MacCormack scheme combines backward differences for the predictor step with forward differences for the corrector step. We can show in fact that the idea behind this scheme is the following Taylor expansion:

$$W_j^{n+1} = W_j^n + \left(\frac{\overline{\partial W}}{\partial t}\right)_j \delta t, \tag{10.37}$$

where

$$\left(\frac{\overline{\partial W}}{\partial t}\right)_j = \frac{1}{2}\left[\left(\frac{\partial W}{\partial t}\right)_j^n + \left(\frac{\partial \tilde{W}}{\partial t}\right)_j\right] = \frac{1}{2}\left[\frac{\tilde{W}_j - W_j^n}{\delta t} - \frac{F(\tilde{W}_j) - F(\tilde{W}_{j-1})}{\delta x}\right]$$

is an approximation of the first derivative in time.

In conclusion, the information is searched on both sides of the computed point j. The information propagation along characteristics is not taken into account, since no distinction is made between upstream and downstream influences. We shall see that this lack of physics in the numerical schemes will generate unwanted (nonphysical) oscillations of the solution.

3. (*Accuracy.*) Both schemes use a three-point stencil $(j-1, j, j+1)$ to reach second-order accuracy in time and space.

4. (*Stability.*) Both schemes are explicit and consequently subject to stability conditions. Similar to the (scalar) convection equation (see Chap. 1), we can write the stability (or CFL[5]) condition in the general form

$$\max_i\{|\lambda_i|\}\cdot\frac{\delta t}{\delta x} \leq 1,$$

where λ_i, $i = 1, 2, 3$, are the eigenvalues of the Jacobian matrix $\partial F/\partial W$, regarded here as propagation speeds of the corresponding characteristic waves ($dx/dt = \lambda$). Using (10.15), we obtain the stability condition

$$(|U| + a)\,\frac{\delta t}{\delta x} \leq 1. \tag{10.38}$$

For numerical applications, this condition is used to compute the time step

$$\delta t = \text{cfl}\cdot\frac{\delta x}{|U| + a}, \quad \text{with} \quad \text{cfl} < 1. \tag{10.39}$$

[5] Courant–Friedrichs–Lewy

Exercise 10.2. For the same physical and numerical parameters as in the previous exercise, compute the numerical solution of the shock tube problem at $t = 0.2$ using Lax–Wendroff and MacCormack centered schemes. Compare to the exact solution and comment on the results. Hints:
• set an array `w(1:3,1:M)` to store the discrete values of the vector $W = (\rho, \rho U, E)^t$ of conservative variables;
• using (10.39) with cfl $= 0.95$, compute the time step in a separate function `function dt = HYP_calc_dt(w,dx,cfl)`;
• write a function to compute $F(W)$;
• use vectorial programming to translate the formulas in Fig. 10.4 into MATLAB program lines (avoid loops!); for example, the predictor step of the Lax–Wendroff scheme will be coded in a single line:

```
wtilde=0.5*(w(:,1:M-1)+w(:,2:M))-0.5*dt/dx*(F(:,2:M)-F(:,1:M-1));
```

• for each scheme, superimpose numerical and exact solutions for (ρ, U, p) as in Fig. 10.5.
A solution of this exercise is proposed in Sect. 10.4 at page 232.

The numerical results of both schemes, displayed in Fig. 10.5, show good accuracy in smooth regions, whereas unwanted oscillations appear at the interfaces between different regions of the solution. The contact discontinuity is also poorly captured. The MacCormack scheme seems to capture the shock discontinuity better, but introduces higher-amplitude oscillations at the end of the expansion wave where the flow is strongly accelerated.

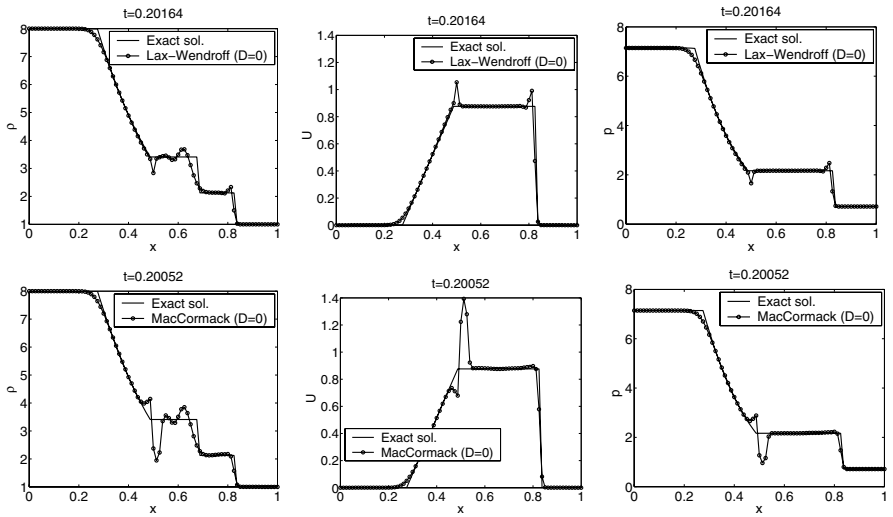

Fig. 10.5. Numerical results for the shock tube problem (Sod's parameters) using centered schemes. Lax–Wendroff scheme (up) and MacCormack scheme (down).

Artificial Dissipation

The oscillations generated by the centered schemes around discontinuities can be damped by adding a supplementary term to the initial equation (10.34):

$$\frac{\partial W}{\partial t} + \frac{\partial}{\partial x} F(W) - \delta x^2 \frac{\partial}{\partial x} \left(D(x) \frac{\partial W}{\partial x} \right) = 0. \tag{10.40}$$

The mathematical form of this term is inspired by the heat equation (discussed in Chap. 1). The idea is to simulate the effects of a physical dissipation (or diffusion) process which is well known to have a smoothing effect[6] on the solution. Since the dissipation term is proportional to the gradient $\partial W/\partial x$ of the solution, the smoothing will be important in regions with sharp gradients (as the shock discontinuity) where numerical oscillations are expected to disappear.

The coefficient $D(x)$, also called *artificial viscosity* by analogy with Navier–Stokes equations (see Chap. 12), has to be positive to ensure a stabilizing effect[7] on the numerical solution. Moreover, its value has to be chosen such that the influence of the artificial term is negligible (i.e., of an order greater than or equal to the truncation error) in the smooth regions of the solution.

Several methods have been proposed to prescribe the artificial viscosity $D(x)$ and to modify classical centered schemes accordingly (see, for instance, Hirsch (1988), Fletcher (1991)). We illustrate the simplest technique, which considers a constant coefficient $D(x) = D$ and writes (10.40) in the conservative form (10.34) with a modified flux $F^*(W)$:

$$\frac{\partial W}{\partial t} + \frac{\partial}{\partial x} F^*(W) = 0, \quad \text{where} \quad F^*(W) = F(W) - D\delta x^2 \frac{\partial W}{\partial x}. \tag{10.41}$$

In order to use the same three-points stencil to define the schemes, the new vector $F^*(W)$ will be discretized

- using backward differences in the predictor step

$$F^*(W_j) = F(W_j) - (D\delta x)(W_j - W_{j-1}), \tag{10.42}$$

- and forward differences in the corrector step

$$F^*(\tilde{W}_j) = F(\tilde{W}_j) - (D\delta x)(\tilde{W}_{j+1} - \tilde{W}_j). \tag{10.43}$$

Exercise 10.3. Modify the previous program by adding an artificial dissipation term to both Lax–Wendroff and MacCormack schemes. Use (10.42)–(10.43) to modify the flux $F(W)$. Discuss the effect of the value of the artificial viscosity D (take $0 \leq D \leq 10$). What is the influence of D on the value of the time step?

[6] This smoothing effect is nicely illustrated for the heat equation in Chap. 1, Exercise 1.10.

[7] The heat equation with negative diffusivity has physically unstable solutions!

The results obtained with an artificial dissipation term are displayed in Fig. 10.6. Numerical oscillations are reduced near the shock and expansion waves, but large dissipation is also introduced in other regions of the solution. In particular, the contact discontinuity (see the graph for $\rho(x)$) is considerably smeared. Increasing the value of D allows one to completely remove the oscillations, but the overall accuracy is not satisfactory. More sophisticated methods have been proposed (see the references at the end of the chapter) to render the dissipation more selective with respect to the nature of discontinuities, but the general tradeoff between damping the oscillations and overall accuracy suggests that the artificial dissipation does not bring a real solution to the problem. A different approach, including more physics in the numerical approximation, is presented in the next section.

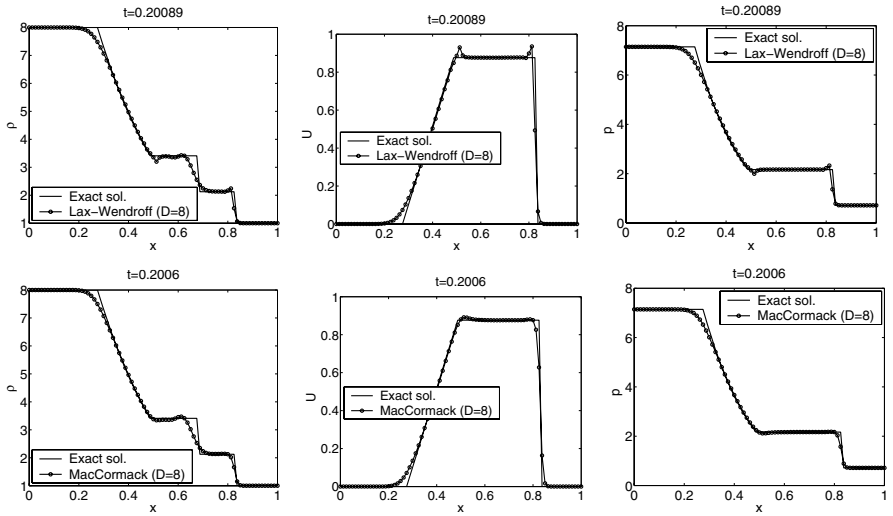

Fig. 10.6. Numerical results for the shock tube problem (Sod's parameters) using centered schemes with artificial dissipation. Lax–Wendroff scheme (up) and MacCormack scheme (down).

10.3.2 Upwind Schemes (Roe's Approximate Solver)

The origin of the numerical oscillations generated by the centered schemes discussed in the previous section comes from complete ignorance of the hyperbolic character of the Euler system of PDEs, in particular the propagation of the information along characteristics. These important (physical) features will be considered in deriving upwind schemes.

Physical information can be introduced at different levels of the numerical approximation. We distinguish between:

1. *flux splitting upwind schemes*, which use different directional discretization of the flux $F(W)$, depending on the sign of the eigenvalues λ of the Jacobian matrix (10.8); since λ corresponds to the propagation speed of the associated characteristic, these schemes include only the information on the direction of propagation of waves (up- or downstream);
2. *Godunov-type schemes*, which introduce a higher level of physical approximation by considering a discretization based on the exact solution of the Riemann problem at each interface between computational points; when the local Riemann problem is solved approximatively, we talk about Riemann solvers.

The following sections present the basic principle of Godunov schemes and the Riemann approximate solver of Roe.

Godunov-Type Schemes

The basic principle of a Godunov-type scheme is the following: the solution W^n is considered to be piecewise constant over each grid cell defined as the interval $]x_{j-1/2}, x_{j+1/2}[$; this allows us to define locally a Riemann problem at each interface between the cells; each local Riemann problem is solved **exactly** to calculate the solution W^{n+1} at the next time level.

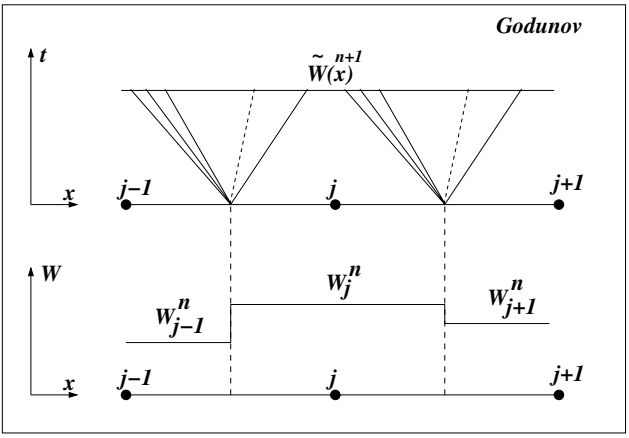

Fig. 10.7. Principle of a Godunov-type scheme.

More precisely, the numerical solution is advanced from time level $t_n = n\delta t$ to $t_{n+1} = t_n + \delta t$ in three steps (see Fig. 10.7):

Step 1. Using the known values W_j^n, define the piecewise constant function

$$W^n(x) = W_j^n, \quad x \in](j-1/2)\delta x, (j+1/2)\delta x[\,. \tag{10.44}$$

Step 2. Calculate the solution function $\tilde{W}^{n+1}(x)$, $x \in](j-1/2)\delta x, (j+1/2)\delta x[$ by gathering the exact solutions of the two Riemann problems defined at interfaces $\left(j-\frac{1}{2}\right)$ and $\left(j+\frac{1}{2}\right)$. This step requires that the waves issued from the two neighboring Riemann problems not intersect. This implies that the time step should be limited such that

$$\max_j \left(|U|+a\right)_{j+1/2}^n \frac{\delta t}{\delta x} \leq \frac{1}{2}. \tag{10.45}$$

Step 3. Obtain the solution $W^{n+1}(x)$, which is also a piecewise constant function, by averaging $\tilde{W}^{n+1}(x)$ over each cell:

$$W_j^{n+1} = \frac{1}{\delta x} \int_{(j-1/2)\delta x}^{(j+1/2)\delta x} \tilde{W}^{n+1}(x) dx. \tag{10.46}$$

We can show that the Godunov scheme can be written in the following *conservative* form:

$$\frac{W_j^{n+1} - W_j^n}{\delta t} + \frac{\Phi(W_j^n, W_{j+1}^n) - \Phi(W_j^n, W_{j-1}^n)}{\delta x} = 0, \tag{10.47}$$

where the flux vector is generally defined as

$$\Phi(W_j^n, W_{j+1}^n) = F(\tilde{W}_{j+1/2}^{n+1}). \tag{10.48}$$

The advantage of the conservative form is that it is valid over the entire domain of definition of the problem, even though the solution is discontinuous. This form is also used to derive approximate Riemann solvers. The exact form of the flux vector will be presented in the next section for the Roe solver.

Roe's Approximate Solver

The approximate solver of Roe is based on a simple and ingenious idea: the Riemann problem (10.7) at interface $\left(j+\frac{1}{2}\right)$ is replaced by the *linear* Riemann problem

$$\frac{\partial \tilde{W}}{\partial t} + A_{j+1/2} \frac{\partial \tilde{W}}{\partial x} = 0, \quad \tilde{W}(x, n\delta t) = \begin{cases} W_j^n, & x \leq \left(j+\frac{1}{2}\right)\delta x \\ W_{j+1}^n, & x > \left(j+\frac{1}{2}\right)\delta x \end{cases} \tag{10.49}$$

The first question raised by this approach is how to properly define the matrix $A_{j+1/2}$, which depends on W_j^n and W_{j+1}^n. This matrix is a priori chosen such that:

1. The hyperbolic character of the initial equation is conserved by the linear problem; hence $A_{j+1/2}$ admits a decomposition similar to (10.12):

$$A_{j+1/2} = P_{j+1/2}\, \Lambda_{j+1/2}\, P_{j+1/2}^{-1}. \tag{10.50}$$

In order to take into account the sign of the propagation speed of characteristic waves, it is useful to define the matrices following:

- $\text{sign}(A_{j+1/2}) = P_{j+1/2}\,(\text{sign}(\Lambda))\,P^{-1}_{j+1/2}$, where $\text{sign}(\Lambda)$ is the diagonal matrix defined by the signs of the eigenvalues λ_l: $\text{sign}(\Lambda) = \text{diag}(\text{sign}\lambda_l)$.
- $|A_{j+1/2}| = P_{j+1/2}|\Lambda|P^{-1}_{j+1/2}$, where $|\Lambda| = \text{diag}(|\lambda_l|)$.

2. The linear Riemann problem is consistent with the initial problem, i.e., for all variables u,
$$A_{j+1/2}(u,u) = A(u,u). \tag{10.51}$$
3. The numerical scheme is conservative, i.e., for all variables u and v,
$$F(u) - F(v) = A_{j+1/2}(u,v)(u-v). \tag{10.52}$$

For the practical calculation of the matrix $A_{j+1/2}$, the original idea of Roe was to express the conservative variables W and conservative fluxes $F(W)$ in (10.18) as quadratic forms of the components of the column vector $Z = \sqrt{\rho}(1,U,H)^t = (z_1,z_2,z_3)^t$:

$$W = \begin{pmatrix} z_1^2 \\ z_1 z_2 \\ \frac{1}{\gamma} z_1 z_3 + \frac{\gamma-1}{2\gamma} z_2^2 \end{pmatrix}, \quad F(W) = \begin{pmatrix} z_1 z_2 \\ \frac{\gamma-1}{\gamma} z_1 z_3 + \frac{\gamma-1}{2\gamma} z_2^2 \\ z_2 z_3 \end{pmatrix}. \tag{10.53}$$

Using the following identity, valid for arbitrary quadratic functions f, g,

$$(fg)_{j+1} - (fg)_j = \bar{f}(g_{j+1} - g_j) + \bar{g}(f_{j+1} - f_j), \quad \text{where} \quad \bar{f} = \frac{f_{j+1} + f_j}{2},$$

we can find two matrices $\bar{B}$ and $\bar{C}$ such that

$$\begin{cases} W_{j+1} - W_j = \bar{B}(Z_{j+1} - Z_j), \\ F(W_{j+1}) - F(W_j) = \bar{C}(Z_{j+1} - Z_j). \end{cases} \tag{10.54}$$

This implies that

$$F(W_{j+1}) - F(W_j) = (\bar{C}\ \bar{B}^{-1})(W_{j+1} - W_j), \tag{10.55}$$

which corresponds exactly to (10.52). Consequently, a natural choice for the matrix $A_{j+1/2}$ will be

$$A_{j+1/2} = \bar{C}\ \bar{B}^{-1}. \tag{10.56}$$

A remarkable property of this matrix (the reader is invited to derive it as an exercise!) is that it can be calculated from (10.8) by replacing the variables (ρ, U, H) with the corresponding *Roe's averages*

$$\bar{\rho}_{j+1/2} = R_{j+1/2}\rho_j,\ \bar{U}_{j+1/2} = \frac{R_{j+1/2}U_{j+1} + U_j}{1 + R_{j+1/2}},\ \bar{H}_{j+1/2} = \frac{R_{j+1/2}H_{j+1} + H_j}{1 + R_{j+1/2}},$$

$$\bar{a}^2_{j+1/2} = (\gamma - 1)\left(\bar{H}_{j+1/2} - \frac{\bar{U}^2_{j+1/2}}{2}\right), \text{ where } R_{j+1/2} = \sqrt{\frac{\rho_{j+1}}{\rho_j}}. \tag{10.57}$$

It is also remarkable that eigenvalue and eigenvector formulas (10.10) and (10.11) still apply to $A_{j+1/2}$ if one uses the corresponding Roe's averaged variables. This considerably simplifies the calculation of matrices $\text{sign}(A_{j+1/2})$ and $|A_{j+1/2}|$, which accounts for the popularity of Roe's approximate solver.

Once the matrix $A_{j+1/2}$ is defined, the upwinding in Roe's scheme follows the general principle of first-order upwind schemes applied to *linear* systems (see, for instance, Hirsch (1988) for more details). The flux in the general conservative form (10.47) becomes for Roe's solver

$$\Phi(W_j^n, W_{j+1}^n) = \frac{1}{2}\left\{F(W_j^n) + F(W_{j+1}^n) - \text{sign}(A_{j+1/2})[F(W_{j+1}^n) - F(W_j^n)]\right\}, \tag{10.58}$$

or, if we use (10.52),

$$\Phi(W_j^n, W_{j+1}^n) = \frac{1}{2}\left\{F(W_j^n) + F(W_{j+1}^n) - |A|_{j+1/2}[W_{j+1}^n - W_j^n]\right\}. \tag{10.59}$$

To summarize, Roe's scheme will be used in the form

$$W_j^{n+1} = W_j^n - \frac{\delta t}{\delta x}\left[\Phi(W_j^n, W_{j+1}^n) - \Phi(W_j^n, W_{j-1}^n)\right], \tag{10.60}$$

with the flux Φ given by (10.59); the matrix $|A_{j+1/2}| = P_{j+1/2}|\Lambda|P_{j+1/2}^{-1}$ will be calculated using Roe's averages (10.57) in (10.12) and (10.13).

Remark 10.2. Roe's scheme is first-order accurate in time and space.

Exercise 10.4. Use Roe's scheme (10.60) to solve numerically the shock tube problem (Sod's parameters). Compare to the numerical results previously obtained using centered schemes.

The results obtained using Roe's scheme are displayed in Fig. 10.8. Compared to centered schemes, the numerical solution is smooth, without oscillations. The shock wave is accurately and sharply captured, but the scheme proves too dissipative around the contact discontinuity, which is strongly smeared.

More accurate Riemann solvers can be derived in the framework of Godunov-type schemes by increasing the space accuracy. For example, we can use piecewise linear functions in steps 1 and 3 of the Godunov scheme to obtain solvers of second order in space. Several other approaches have been proposed in the literature to include more physics in the numerical discretization, leading to other classes of numerical methods, including TVD (total variation diminishing) and ENO (essentially nonoscillatory) schemes, which are now currently used to solve hyperbolic systems of PDEs. The reader who wishes to pursue the study of upwind schemes beyond this introductory presentation is referred to more specialized texts such as Fletcher (1991); Hirsch (1988); LeVeque (1992); Saad (1998).

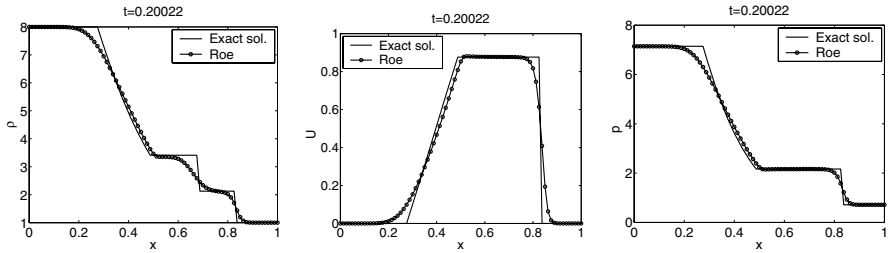

Fig. 10.8. Numerical computation of the shock tube problem (Sod's parameters) using Roe's approximate solver.

10.4 Solutions and Programs

The exact solution of the shock tube problem for a given time value t is computed in the script *HYP_shock_tube_exact.m*. The compatibility relation (10.29) is implemented as an implicit function (i.e., $f(x) = 0$) in the script *HYP_mach_compat.m*; this function is used as the first argument of the MATLAB built-in function `fzero` to compute the root corresponding to the value of M_s. The final solution, containing the discrete values for (ρ, U, p), is computed according to relations in Sect. 10.2.2. Note the use of the MATLAB built-in function `find` to compute the abscissas x separating the different regions of the solution.

The main program resulting from successively solving all the exercises of this project is *HYP_shock_tube.m*. After defining the input data (which are the parameters of regions (L) and (R)) as global variables, the space discretization is built and the solution is initialized using Sod's parameters. Three main arrays are used for the computation:

`usol(1:3,1:M)` to store the nonconservative variables $(\rho, U, p)^t$,
`w(1:3,1:M)` for the conservative vector $W = (\rho, \rho U, E)^t$,
and `F(1:3,1:M)` for the conservative fluxes $F(W)$.

The program allows one to choose among three numerical schemes: Lax–Wendroff, MacCormack, and Roe. When a centered scheme is selected, the value of the artificial dissipation is requested. The numerical solution is superimposed on the exact solution using the function `HYP_plot_graph` implemented in the script *HYP_plot_graph.m*. The most important functions called from the main program are:

- `HYP_trans_usol_w`: computes $W = (\rho, \rho U, E)^t$ from $usol = (\rho, U, p)^t$;
- `HYP_trans_w_usol`: computes $usol = (\rho, U, p)^t$ from $W = (\rho, \rho U, E)^t$;
- `HYP_trans_w_f`: computes $F = (\rho U, \rho U^2 + p, (E + p)U)^t$ from $W = (\rho, \rho U, E)^t$;
- `HYP_calc_dt`: computes $\delta t = \text{cfl} \cdot \delta x / (|U| + a)$ from $W = (\rho, \rho U, E)^t$.

All these functions are written with a concern for transparency with respect to the mathematical formulas. For this purpose, the vectorial programming

capabilities of MATLAB were used. Let us explain in detail this technique for the predictor step of the Lax–Wendroff scheme (see Fig. 10.4):
• the flux $F(W)$ is computed from W values for all $j = 1, \ldots, M$ components

```
F = HYP_trans_w_f(w);
```

• the artificial dissipation vector is added following (10.42); we use the MATLAB built-in function `diff` to compute differences $W_j - W_{j-1}$; these differences are computed along the rows of the array `w` and only for $j \geq 2$; according to the left-boundary conditions, the artificial dissipation vector will be completed by zeros for $j = 1$:

```
F = F-Ddx*[zeros(3,1) diff(w,1,2)];
```

• the intermediate solution $\tilde{W}$ is computed only for the components $j = 1, \ldots, M-1$:

```
wtilde=0.5*(w(:,1:M-1)+w(:,2:M))-0.5*dt/dx*(F(:,2:M)-F(:,1:M-1));
```

A similar MATLAB code will be written for the corrector step, having in mind that for this step, right-boundary conditions apply, and consequently, only the components $j = 2, \ldots M-1$ of W^{n+1} are computed:

```
Ftilde = HYP_trans_w_f(wtilde);
Ftilde=Ftilde-Ddx*[diff(wtilde,1,2) zeros(3,1)];
w(:,2:M-1)=w(:,2:M-1)-dt/dx*(Ftilde(:,2:M-1)-Ftilde(:,1:M-2));
```

Particular attention was devoted to the implementation of Roe's scheme, which requires a separate function `HYP_flux_roe` to compute the conservative flux Φ. In order to reduce memory storage, the flux at the interface $\left(j + \frac{1}{2}\right)$ is computed using this once (and once is not habit!) a `for` loop and several local variables that can be easily identified from mathematical relations. Note also that the analytical form (10.13) for $P^{-1}_{j+1/2}$ was used instead of the (time-consuming) MATLAB built-in function `inv`, which calculates the inverse of a matrix.

Chapter References

C. A. J. Fletcher, *Computational Techniques for Fluid Dynamics*, Springer-Verlag, 1991.
E. Godlewski and P.-A. Raviart, *Numerical Approximation of Hyperbolic Systems of Conservation Laws*, Springer-Verlag, 1996.
C. Hirsch, *Numerical Computation of Internal and External Flows*, John Wiley & Sons, 1988.
R. LeVeque, *Numerical Methods for Conservation Laws*, Birkhäuser, 1992.
M. Saad, *Compressible Fluid Flow*, Pearson Education, 1998.

11

Thermal Engineering: Optimization of an Industrial Furnace

Project Summary

Level of difficulty:	2
Keywords:	Finite element method, Laplace differential operator, direct problem, inverse problem
Application fields:	Thermal engineering, optimization

11.1 Introduction

In this chapter we deal with a simple but realistic optimization problem. We have to find the optimal temperature of an industrial furnace in which are made resin pieces, such as car bumpers. The heating system is based on electric resistances, and the first part of this study is to compute the temperature field inside the oven when the values of the resistances are known. This work is called the *direct* problem: the resistances' values are known and the temperature field is unknown. It is important here to emphasize that the mechanical properties of the bumper depend on the temperature during the cooking; so the second part of the study is devoted to computing the resistances' values in order to maintain the bumper temperature at the "*good*" value. This optimization problem is called an *inverse* problem: the temperature is an input and the resistances values are outputs.

The computation of the temperature field is performed with the finite element method. Only the main features of this method are recalled here; for further details we refer to Ciarlet (1978), Norrie and de Vries (1973), and Zienkiewicz (1971).

11.2 Formulation of the Problem

For the sake of simplicity we limit the geometry of the problem to elementary shapes: the bumper is a rectangle placed in a rectangular domain Ω representing the oven; the edges are referred to as the boundary $\partial\Omega$ (see Fig. 11.1). This boundary is the union of three nonempty parts: $\partial\Omega_D$, $\partial\Omega_N$, and $\partial\Omega_F$, satisfying the following conditions:

$$\partial\Omega = \partial\Omega_D \cup \partial\Omega_N \cup \partial\Omega_F \text{ and } \partial\Omega_D \cap \partial\Omega_N = \partial\Omega_D \cap \partial\Omega_F = \partial\Omega_F \cap \partial\Omega_N = \emptyset.$$

The partial differential equation arising from the heat diffusion phenomenon in the oven can be written as

$$\begin{cases} \text{Find } T \in V \text{ such that} \\ \text{div } \left[-\mathbb{K}\, \overrightarrow{\text{grad}}\, T\right] = F \text{ in } \Omega. \end{cases} \tag{11.1}$$

For physical and mathematical reasons, the temperature field has to satisfy some conditions on the wall of the oven. First we impose $T = T_D$ on $\partial\Omega_D$; this is commonly referred to as a *Dirichlet boundary condition*. Another condition rules the thermal flux across $\partial\Omega_N$. This is referred to as a *Neumann boundary condition*. A last condition is devoted to the temperature balance between the inside and the outside of the oven. This *Fourier boundary condition* states that the heat transfer through $\partial\Omega_F$ is proportional to $T - T_F$, the difference between internal and external temperatures.

All these arguments are translated into mathematical terms, and we add them to the formulation of problem (11.1). They are summarized in

$$\begin{cases} T = T_D \text{ on } \partial\Omega_D, \\ \sum_{i,j} \mathbb{K}_{i,j} \dfrac{\partial T}{\partial x_j} \nu_i = f \text{ on } \partial\Omega_N, \\ \sum_{i,j} \mathbb{K}_{i,j} \dfrac{\partial T}{\partial x_j} \nu_i = g(T - T_F) \text{ on } \partial\Omega_F. \end{cases} \tag{11.2}$$

We have employed here the following notations:

1. T is the temperature in the domain Ω.
2. V is the set of all feasible temperatures.
3. $\mathbb{K} \in \mathbb{R}^{2\times 2}$ is the thermal conductivity tensor. In a homogeneous isotropic medium, we have $\mathbb{K} = cI_2$, where c is the heat conductivity coefficient, and I_2 is the identity matrix.
4. The volume and surface heat sources are denoted by F and f.
5. The ambient temperature (inside the oven) is set to the value T_D on $\partial\Omega_D$.
6. The outside temperature is set to the value T_F on $\partial\Omega_F$.
7. g is the heat transfer coefficient on $\partial\Omega_F$.
8. $\boldsymbol{\nu} = (\nu_1, \nu_2)^t$ is the outward normal vector on $\partial\Omega$.

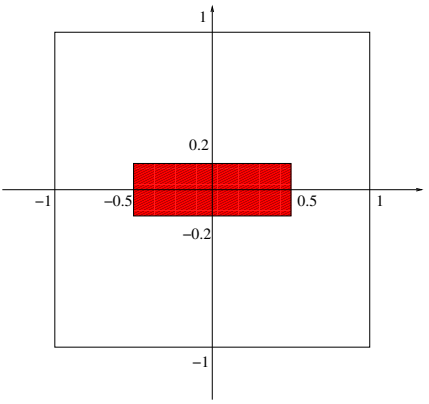

Fig. 11.1. Object and oven.

For the sake of simplicity we assume here perfect thermal insulation, that is, $f = 0$ and $g = 0$. All data necessary to deal with the problem are now determined, and we use a *Green formula*,

$$\forall T, T' \in V, \quad \int_\Omega \text{div}\left[-\mathbb{K}\,\overrightarrow{\text{grad}}\,T\right]\,T' dx$$
$$= \sum_{i,j} \int_\Omega \mathbb{K}_{i,j} \frac{\partial T}{\partial x_j}\frac{\partial T'}{\partial x_i}\,dx - \sum_{i,j}\int_{\partial\Omega} \mathbb{K}_{i,j}\frac{\partial T}{\partial x_j} T'\,\nu_i\,ds.$$

Let us introduce now the subspace $V^0 \subset V$ by $V^0 = \{T' \in V, T' \mid_{\partial\Omega_D} = 0\}$, and write the *variational formulation* of problem (11.1):

$$\begin{cases} \text{Find } T \in V^0 + T_D \text{ such that} \\ \forall T' \in V^0 \quad \displaystyle\sum_{K\in\mathcal{T}_h} \int_K (\overrightarrow{\text{grad}}\,T')^t\,\mathbb{K}\,\overrightarrow{\text{grad}}\,T\,dx = \sum_{K\in\mathcal{T}_h}\int_K T'\,F\,dx. \end{cases} \tag{11.3}$$

It has been proved that problem (11.3) is equivalent to problem (11.1)+(11.2) and has a unique solution T (see Ciarlet, 1978).

11.3 Finite Element Discretization

In a real case, the physical data of problem (11.3) are provided by experimental measures; they are not trivial and neither is the geometry of the domain Ω. Consequently, it is not possible to write an explicit solution $T(x, y)$ of problem (11.1)+(11.2). This solution is estimated by the way of an approximation method such as the finite element method. This method uses piecewise polynomial functions defined on triangles or rectangles in 2D formulation

(tetrahedra, hexahedra in 3D). In this study we first split the domain Ω into triangular elements, gathered in a triangulation. In the finite element theory a *triangulation* $\mathcal{T}_h$ (or *mesh*) of the domain Ω is a set of triangles satisfying the following properties:

$$\overline{\Omega} = \bigcup_{K \in \mathcal{T}_h} K,$$

$$\forall K, K' \in \mathcal{T}_h \quad K \cap K' = \begin{cases} \emptyset, \\ \text{or a vertex common to } K \text{ and } K', \\ \text{or an edge common to } K \text{ and } K'. \end{cases}$$

Then a finite-dimensional vector subspace $V_h \subset V$ is introduced. A simple example of such a subspace is provided by the so-called "Lagrange finite element" of degree 1. For an arbitrary triangle K in $\mathcal{T}_h$, with vertices A_1, A_2, and A_3, an element T'_h of V_h is defined by

$$T'_h(M) = T'_h(A_1)\lambda_1 + T'_h(A_2)\ \lambda_2 + T'_h(A_3)\lambda_3, \tag{11.4}$$

where $T'_h(A_i)$ is the temperature value at A_i, one of the three vertices of triangle K, while λ_1, λ_2, and λ_3 are the barycentric coordinates of the point M in triangle K.

Remark 11.1. Let K be an arbitrary triangle with vertices A_1, A_2, and A_3. The barycentric coordinates of point M are three real numbers λ_1, λ_2, and λ_3 such that $\lambda_1 + \lambda_2 + \lambda_3 = 1$ and

$$\overrightarrow{OM} = \lambda_1 \overrightarrow{OA}_1 + \lambda_2 \overrightarrow{OA}_2 + \lambda_3 \overrightarrow{OA}_3.$$

If x, y are the Cartesian coordinates of M, then the barycentric coordinates λ_1, λ_2 are a solution of the linear system

$$\begin{cases} x = x(A_3) + [x(A_1) - x(A_3)]\lambda_1 + [x(A_2) - x(A_3)]\lambda_2, \\ y = y(A_3) + [y(A_1) - y(A_3)]\lambda_1 + [y(A_2) - y(A_3)]\lambda_2, \end{cases} \tag{11.5}$$

where $(x(A_i), y(A_i))$ are the Cartesian coordinates of vertex A_i. The uniqueness of these values is guaranteed if and only if A_1, A_2, and A_3 are not on a straight line.

The definition (11.4) of the approximate temperature T'_h leads to the new relation

$$T'_h(M) = T'_h(A_3) + [T'_h(A_1) - T'_h(A_3)]\lambda_1 + [T'_h(A_2) - T'_h(A_3)]\lambda_2.$$

We introduce then the subspace $V_h^0 \subset V_h$ by

$$V_h^0 = \{T' \in V_h, T' \mid_{\partial\Omega_D} = 0\}.$$

Let T_D be the element of V_h whose components are all zero, except for $T_D(A_i)$, with point A_i located on the boundary $\partial\Omega_D$, whose values come from (11.2). The discrete variational formulation of problem (11.3) is then

$$\left\{\begin{array}{l} \text{Find } T_h \in T_D + V_h^0 \text{ such that} \\ \forall T_h' \in V_h^0 \quad \displaystyle\sum_{K\in\mathcal{T}_h} \int_K (\overrightarrow{\text{grad}}\ T_h')^t\ \mathbb{K}\ \overrightarrow{\text{grad}}\ T_h\ dx = \sum_{K\in\mathcal{T}_h} \int_K T_h'\ F\ dx. \end{array}\right. \quad (11.6)$$

11.4 Implementation

Formulation (11.6) uses integral calculation on triangles of $\mathcal{T}_h$. Before going further into the details, we examine these terms when K is an arbitrary triangle. One has to compute the value of

$$\int_K (\overrightarrow{\text{grad}}\ T_h')^t\ \mathbb{K}\ \overrightarrow{\text{grad}}\ T_h\ dx \quad \text{and} \quad \int_K T_h'\ F\ dx.$$

Matrix Computation

The vector $\overrightarrow{\text{grad}}\ T_h'$ has to be calculated for each T_h' in V_h and each K in $\mathcal{T}_h$. We first write

$$\frac{\partial T_h'}{\partial \lambda_i} = \frac{\partial T_h'}{\partial x} \times \frac{\partial x}{\partial \lambda_i} + \frac{\partial T_h'}{\partial y} \times \frac{\partial y}{\partial \lambda_i} \quad \text{for } i = 1, 2. \quad (11.7)$$

Then, using (11.4) and (11.5), we get

$$\left|\begin{array}{l} \dfrac{\partial T_h'}{\partial \lambda_1} = T_h'(A_1) - T_h'(A_3), \\ \dfrac{\partial T_h'}{\partial \lambda_2} = T_h'(A_2) - T_h'(A_3), \end{array}\right. \left|\begin{array}{l} \dfrac{\partial x}{\partial \lambda_1} = x(A_1) - x(A_3), \\ \dfrac{\partial x}{\partial \lambda_2} = x(A_2) - x(A_3), \end{array}\right. \left|\begin{array}{l} \dfrac{\partial y}{\partial \lambda_1} = y(A_1) - y(A_3), \\ \dfrac{\partial y}{\partial \lambda_2} = y(A_2) - y(A_3). \end{array}\right. \quad (11.8)$$

So a new formulation of (11.7) is

$$\begin{bmatrix} T_h'(A_1) - T_h'(A_3) \\ \\ T_h'(A_2) - T_h'(A_3) \end{bmatrix} = \begin{bmatrix} x(A_1) - x(A_3) & y(A_1) - y(A_3) \\ x(A_2) - x(A_3) & y(A_2) - y(A_3) \end{bmatrix} \begin{bmatrix} \dfrac{\partial T_h'}{\partial x} \\ \\ \dfrac{\partial T_h'}{\partial y} \end{bmatrix}. \quad (11.9)$$

The matrix determinant in (11.9) is

$$\Delta_K = (x(A_1) - x(A_3))\,(y(A_2) - y(A_3)) - (x(A_2) - x(A_3))\,(y(A_1) - y(A_3))\,.$$

Since $|\Delta_K|$ is twice the area of triangle K, matrix (11.9) is invertible when K is not a *flat* triangle (i.e., the three vertices are not on a straight line). We introduce then an array $[dl\ T_h']_K$ and a matrix B_K by

$$[dl\ T_h']_K = \begin{bmatrix} T_h'(A_1) \\ T_h'(A_2) \\ T_h'(A_3) \end{bmatrix}$$

and

$$B_K = \frac{1}{\Delta_K} \begin{bmatrix} y(A_2) - y(A_3) & y(A_3) - y(A_1) & y(A_1) - y(A_2) \\ x(A_3) - x(A_2) & x(A_1) - x(A_3) & x(A_2) - x(A_1) \end{bmatrix}$$

and write

$$\int_K (\overrightarrow{\text{grad}}\ T'_h)^t\ \mathbb{K}\ \overrightarrow{\text{grad}}\ T_h\ dx = [dl\ T'_h]^t_K [A_K][dl\ T_h]_K.$$

Matrix $[A_K]$ is the *element matrix*, and is computed by

$$[A_K] = \frac{1}{2} c_K \Delta_K B_K^t B_K.$$

Remark 11.2. The value of c_K, the thermal conductivity coefficient, is different in the air and in the resin, and so depends on K.

Right-Hand Side Computation

We assume in the following that the heat source function F_r associated with an electrical resistance located at point $P_r(x_r, y_r)$ has the form

$$F_r(x, y) = \frac{F_0}{2} \exp\left[-d^2(x, y)\right], \text{ with } d^2(x, y) = \frac{1}{2R_r^2} \left((x - x_r)^2 + (y - y_r)^2\right),$$

so using the previous notation we may write

$$\pi R_r^2 \int_\Omega F_r\ dx = F_0 \text{ and } \int_K T'_h F_r\ dx = [dl\ T'_h]^t_K [b_K],$$

where the array $[b_K]$ is the *element right-hand side*, computed by means of the numerical integration formula

$$[b_K] = \frac{\Delta_K}{24} \begin{bmatrix} 2 & 1 & 1 \\ 1 & 2 & 1 \\ 1 & 1 & 2 \end{bmatrix} \begin{bmatrix} F_r(A_1) \\ F_r(A_2) \\ F_r(A_3) \end{bmatrix}.$$

The Linear System

Gathering all these results, we rewrite problem (11.6) in the new form

$$\begin{cases} \text{Find } T_h \in T_D + V_h^0 \text{ such that} \\ \forall T'_h \in V_h^0 \quad \displaystyle\sum_{K \in \mathcal{T}_h} [dl\ T'_h]^t_K [A_K][dl\ T_h]_K = \sum_{K \in \mathcal{T}_h} [dl\ T'_h]^t_K [b_K]. \end{cases} \tag{11.10}$$

In this formulation, the array $[dl\ T'_h]_K$ represents the temperature values of an arbitrary function T'_h in V_h. It is an array whose three components are the temperature values at the vertices of K, an arbitrary triangle of $\mathcal{T}_h$. When

we compute the summation in (11.10), element K replaces all triangles of $\mathcal{T}_h$, so all functions T'_h in V_h are taken into account. We then rewrite (11.10) as

$$\begin{cases} \text{Find } T_h \in T_D + V_h^0 \text{ such that} \\ \forall T'_h \in V_h^0 \qquad [dl\ T'_h]^t\ [A]\ [dl\ T_h] = [dl\ T'_h]^t\ [b]. \end{cases} \tag{11.11}$$

Let nv be the number of vertices in triangulation $\mathcal{T}_h$; then $[A]$ is a square matrix of $\mathbb{R}^{nv \times nv}$ and $[b]$ is an array of R^{nv}. Note that

$$[dl\ T'_h]^t = [T'_h(A_1), T'_h(A_2), \ldots, T'_h(A_{nv})]^t$$

and

$$[dl\ T_h]^t = [T_h(A_1), T_h(A_2), \ldots, T_h(A_{nv})]^t$$

are arrays whose nv components are the temperature values at the vertices of $\mathcal{T}_h$. To end, we remark that (11.6) is a linear system with nv equations and nv unknowns:

$$[A]\ [dl\ T_h] = [b]. \tag{11.12}$$

11.5 Boundary Conditions

It is time now to take the boundary conditions into account. The condition $T'_h = 0$ on Ω_D, specified in the definition of the space V_h^0, involves important modifications of the linear system (11.12). For the sake of simplicity, we shall assume in the following lines that the vertices located on Ω_D have the largest numbers when the points of triangulation $\mathcal{T}_h$ are ordered. More precisely, the numbers of these nv_D vertices are supposed to be $nv - nv_D + 1, nv - nv_D + 2, \ldots, nv$. Any element of the finite-dimensional space V_h is then an array of nv real components, and any element of the subspace V_h^0 is an array whose nv_D last components are null. So the linear system (11.12) arising from (11.11) seems to have only $(nv - nv_D)$ rows but nv unknowns! Fortunately, since the solution T_h of problem (11.11) belongs to the space $T_D + V_h^0$, its nv_D last components are well known and determined by the data T_D associated with the Dirichlet boundary condition $T_h\ |_{\partial\Omega_D} = T_D$. Finally, the linear system (11.12) has $(nv - nv_D)$ unknowns for the same number of equations! Nevertheless, this treatment has heavy consequences for the computer formulation of (11.12). We write first

$$\begin{bmatrix} A_1 & A_2 \\ A_2^t & A_3 \end{bmatrix} \times \begin{bmatrix} T_h \\ T_{hD} \end{bmatrix} = \begin{bmatrix} b \\ c \end{bmatrix}.$$

The square matrix A_1 is of order $(nv - nv_D)$, A_2 has $(nv - nv_D)$ rows and nv_D columns, and A_3 is a square matrix of order nv_D. When we take the condition $T'_h\ |_{\partial\Omega_D} = 0$ into account, we see that the nv_D last rows of the

linear system vanish. These rows are replaced by the nv_D relations $T_h\,|_{\partial\Omega_D} = T_{hD} = T_D$, so the linear system is now

$$\begin{bmatrix} A_1 & A_2 \\ 0 & I \end{bmatrix} \times \begin{bmatrix} T_h \\ T_{hD} \end{bmatrix} = \begin{bmatrix} b \\ T_D \end{bmatrix},$$

where I is the identity matrix of order nv_D. For matrix storage reasons it is important to preserve the symmetry of the initial problem. A final modification is then necessary: the matrix A_2 is eliminated in order to obtain

$$\begin{bmatrix} A_1 & 0 \\ 0 & I \end{bmatrix} \times \begin{bmatrix} T_h \\ T_{hD} \end{bmatrix} = \begin{bmatrix} b - A_2 T_D \\ T_D \end{bmatrix},$$

which is the symmetric linear system solved by the computer.

11.5.1 Modular Implementation

When implementing the finite element method, different logical steps have to be taken into account:

1. definition of the triangulation $\mathcal{T}_h$,
2. construction of the linear system (11.12),
3. introduction of the boundary conditions,
4. solution of the modified linear system,
5. visualization of the results.

Any scientific package has to deal with all elements of this list: there exists a distinct procedure corresponding to each step encountered during the implementation. These procedures are called *modules*. Results (output) of the kth-step module are data (input) for $(k+1)$th-step module. Several modules may exist for the same logical step, in which case they have to share similar formatted input and provide similar formatted output.

11.5.2 Numerical Solution of the Problem

In solving problem (11.11), the very first step is the mesh construction. Numerous packages are devoted to this work, and 2D meshes are easily created. See, for example the mesh displayed in Fig. 11.2(a) obtained with the INRIA code *emc2*. [1] There are altogether 304 triangles and 173 vertices. Another mesh, displayed in Fig. 11.2(b), was computed by the MATLAB "toolbox" PDE-tool, with 1392 triangles and 732 vertices.

The mesh description, as provided by the code *emc2*, is summarized in the following list

1. Nbpt, Nbtri (two integers): number of vertices (points), number of triangles

[1] http://www-rocq1.inria.fr/gamma/cdrom/www/emc2/eng.htm.

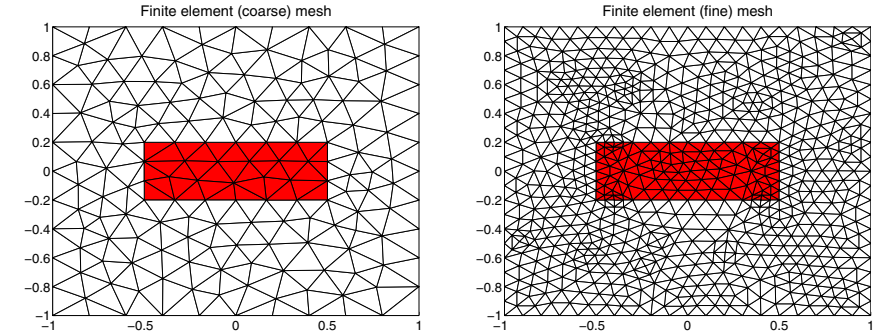

Fig. 11.2. Mesh of the domain. (a) coarse; (b) fine.

2. List of all vertices: for Ns=1,Nbpt
   - Ns, Coorpt[Ns,1], Coorpt[Ns,2] ,Refpt[Ns] (one integer, two reals, one integer): vertex number, coordinates, and boundary reference;
3. List of all triangles: for Nt=1,Nbtri,
   - Nt, Numtri[Nt,1:3], Reftri[N] (five integers): triangle number, three vertex numbers, and medium reference (air or resin).

Exercise 11.1. 1. Create a mesh (or read one of the data files provided with the procedures). Check contents of arrays `Coorpt` and `Numtri`.
2. Compute element matrix and right-hand side for each triangle.
3. Write a procedure that assembles the linear system from element data.
4. Modify the linear system in order to take the boundary conditions into account. [2]
5. Solve the resulting linear system.
6. Visualize the results, plot the isotherm curves.

Hint: Use the following algorithm to assemble A and b:

```
for K=1:Nbtri
   (a) read data for triangle K
      XY  = coordinates of triangle K vertices
      NUM = triangle K vertices numbers
   (b) Compute element matrix AK(3,3) and right-hand side bK(3)
   (c) Build global matrix A(Nbpt,Nbpt)
      for i=1:3
      for j=1:3
         A(Num(i),Num(j))=A(Num(i),Num(j))+AK(i,j)
```

[2] For this experiment $\partial\Omega_D$ is the union of the lines $y = -1$ and $y = 1$, $\partial\Omega_N$ is is the union of the lines $x = -1$ and $x = 1$, and $\partial\Omega_F = \emptyset$.

```
        end
        end
    (d) Build global right-hand side  b(Nbpt)
        for i=1:3
            b(Num(i))=b(Num(i))+bK(i)
        end
end
```

A solution of this exercise is proposed in Sect. 11.8 at page 248. A computed temperature field is displayed in Fig. 11.3(a), representing the variations of temperature within the domain Ω. It corresponds to the following data: $T_D = 50°$ Celsius on the upper part of the oven ($y = 1$), $T_D = 100°$ on the lower part ($y = -1$), and no heating sources ($F = 0$, $f = 0$). Another temperature field is displayed in Fig. 11.3(b): plotting the temperature variations according to the previous boundary conditions but with four heating resistances (common value is 25 000). It is obvious in Fig. 11.3 that the temperature value in the bumper is far from 250°, which is supposed to be the ideal one in our study. To fix this problem we have to increase the resistance values. Yes, but by how much? In the previous computation we have used the resistance values as data and obtained the temperature field inside the oven as result; this is referred to as the *direct* formulation of the problem. But what we are interested in is the resistance values that produce the optimal temperature inside the bumper; this is called the *inverse* problem. We shall address the inverse problem in the following section.

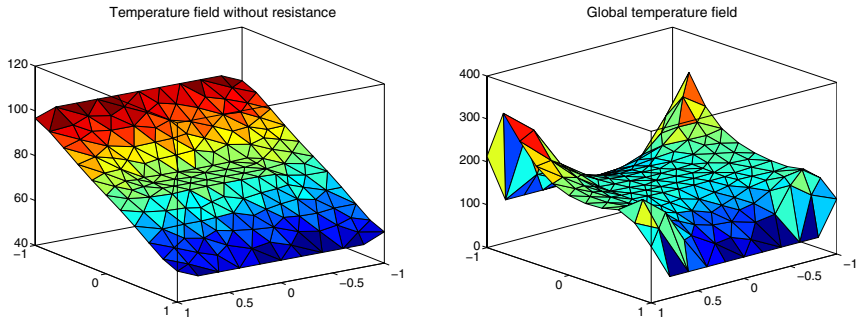

(a) (b)

Fig. 11.3. Temperature fields. (a) without resistance; (b) with four resistances.

11.6 Inverse Problem Formulation

We emphasize now an important property of (11.1)–(11.2): the problem is *linear*. This means that if T' is the unique solution of problem (11.1)–(11.2)

corresponding to data $\{F', T'_D, f'\}$, and T'' is the unique solution corresponding to data $\{F'', T''_D, f''\}$, then $\alpha T' + \beta T''$ is the unique solution corresponding to data $\{\alpha F' + \beta F'', \alpha T'_D + \beta T''_D, \alpha f' + \beta f''\}$ for any real numbers α and β. In order to determine the values of the resistances that lead to a correct heating of the object, this propriety is of great interest. Assume that there are nwr heating resistances and that the boundary conditions are temperature value T_D imposed on $\partial\Omega_D$ and heat flux f imposed on $\partial\Omega_N$. Then the corresponding temperature field T is written as

$$T = T_0 + \sum_{k=1}^{nwr} \alpha_k T_k,$$

where α_k is the k^{th} resistance value and T_k represents the temperature field when resistance k is the unique resistance heating the oven. These coefficients α_k are the unknowns of the inverse problem, and we are going to compute the values corresponding the desired temperature T_{opt} by minimizing the quantity

$$J(\alpha) = \int_S \left[T_{opt}(x) - T_0(x) - \sum_{k=1}^{nwr} \alpha_k \; T_k(x) \right]^2 dx.$$

Here $\alpha = (\alpha_1, \ldots, \alpha_{nwr})^t$ and S stands for the bumper. The quadratic functional J is a strictly convex function of the variable α, and its unique minimum is reached when $\nabla J(\alpha) = 0$. For $k = 1, 2, \ldots, nwr$, the gradient kth component is

$$\frac{\partial J}{\partial \alpha_k} = 2 \int_S \left(T_{opt}(x) - T_0(x) - \sum_{k'=1}^{nwr} \alpha_{k'} \; T_{k'}(x) \right) \; T_k(x) dx,$$

and the minimum is reached when

$$\sum_{k'=1}^{nwr} \alpha_{k'} \int_S \; T_{k'}(x) \; T_k(x) dx = \int_S \left(T_{opt}(x) - T_0(x) \right) \; T_k(x) dx,$$

for $k = 1, 2, \ldots, nwr$. We introduce now the matrix $\tilde{A} \in \mathbb{R}^{nwr \times nwr}$ and the array $\tilde{b} \in \mathbb{R}^{nwr}$ by

$$\tilde{A}_{k,k'} = \int_S T_k(x) \; T_{k'}(x) dx \text{ and } \tilde{b}_k = \int_S \left(T_{opt}(x) - T_0(x) \right) \; T_k(x) dx.$$

The optimal $\tilde{\alpha} = (\tilde{\alpha}_1, \ldots, \tilde{\alpha}_{nwr})^t$ is the unique solution of the linear system

$$\tilde{A}\tilde{\alpha} = \tilde{b}. \tag{11.13}$$

11.7 Implementation of the Inverse Problem

Exercise 11.2. 1. Compute and solve the linear system (11.13) arising from the optimization problem.

2. Compute and plot the temperature field corresponding to the optimal value. Comment on the results.

A solution of this exercise is proposed in Sect. 11.8 at page 249. We have first to solve the $nwr+1$ direct problems in order to compute the temperature fields $T_0, T_1, \ldots, T_{nwr}$. They are obtained by the use of $nwr+1$ calls of the program written to solve the direct problem. Each computation corresponds to a distinct value of the data T_D, f, and F (note that the localization of the resistances in the oven is a geometrical datum of great importance). The corresponding temperature fields are then stored in $nwr+1$ distinct arrays.

Now we solve problem (11.1)–(11.2) without any heating term ($F = 0$), but with a temperature $T_D \neq 0$ and thermal flux $f = 0$ given on the boundary. The solution of this problem is denoted by T_0, and displayed in Fig. 11.3(a). We can see that the boundary conditions are well respected: temperature value is $T = 100$ when $y = -1$ and $T = 50$ when $y = 1$. The heat conductivity coefficient is set to the value $c = 1$ within the air and $c = 10$ within the object (air is a good insulation medium). The vanishing thermal flux on the other parts of the boundary corresponds to isotherm lines parallel to the normal vector when $x = -1$ and $x = 1$.

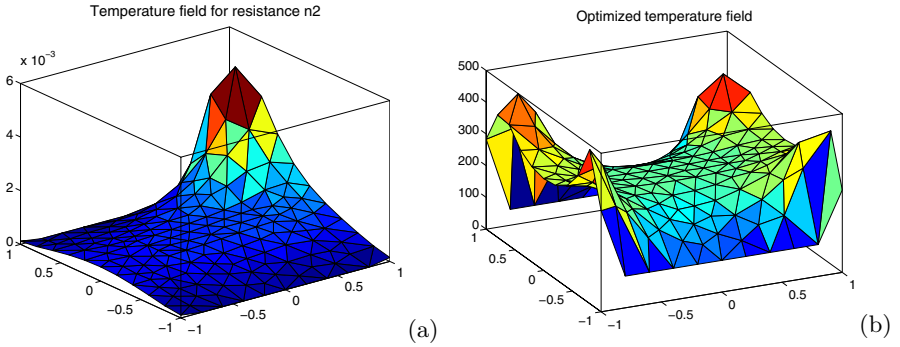

Fig. 11.4. Temperature fields. (a) T_2 field; (b) optimized field.

Then we solve nwr successive problems (11.1)–(11.2) (one problem by resistance). Each case consists in computing the temperature field when only one resistance is heating the oven. The boundary conditions are temperature $T_D = 0$ on $\partial\Omega_D$ and thermal flux $f = 0$ on $\partial\Omega_N$ for all cases. The nv components of array T_k represent the temperature field related to the k^{th} resistance. Figure 11.4(a) displays the temperature field associated with a single heating resistance. Note the tiny values of the temperature.

We notice again that the boundary conditions are well satisfied: the temperature vanishes when $y = -1$ and $y = 1$ (Dirichlet condition), and the Neumann condition (null flux condition) leads to isotherm lines perpendicular to lines $x = -1$ and $x = 1$.

To solve the inverse problem, we have now to construct the linear system (11.13) and then compute the terms

$$\int_S T_k(x)\ T_{k'}(x)dx$$

from the temperature fields T_k and $T_{k'}$ computed in the previous step. This computation is performed in the same way as before: we first write the integral term on the complete object as summation of integral terms on all triangles of the object:

$$\int_S T_k(x)\ T_{k'}(x)dx = \sum_{K \subset S} \int_K T_k(x)\ T_{k'}(x)dx.$$

Then any integral on K is evaluated using the expression for $T_k(x)$ and $T_{k'}(x)$ in triangle K

$$T_k(x) = T_k(A_3) + [T_k(A_1) - T_k(A_3)]\lambda_1 + [T_k(A_2) - T_k(A_3)]\lambda_2.$$

In this formula λ_i is the ith barycentric coordinate of the point $M(x, y)$ in K, and A_i is one of the vertices of triangle K. So we may write

$$\int_K T_k(x)\ T_{k'}(x)dx = [dl\ T_{k,K}]^t\ [M_K]\ [dlT_{k',K}].$$

This leads us to introduce the matrix $[M_K]$, the so-called element mass matrix. The element mass matrix associated with the Lagrange finite triangular element of degree 1 is

$$[M_K] = \frac{\Delta_K}{24} \begin{bmatrix} 2 & 1 & 1 \\ 1 & 2 & 1 \\ 1 & 1 & 2 \end{bmatrix}.$$

So in computing the linear system (11.13), the matrix coefficient $\tilde{A}_{k,k'}$ is obtained by summation over all triangles laying inside the objects of the terms $[dl\ T_{k,K}]^t\ [M_K][dlT_{k',K}]$. The right-hand side $\tilde{b}$ is computed in the same way. An example of calculation, corresponding to the case of four heating resistances, is displayed in Fig. 11.5(a). We may see there the optimized temperature field obtained after computation of coefficients α_k. Figure 11.5(b) displays the solution corresponding to six heating resistances. The value of the temperature within the rectangle $[-0.5, 0.5] \times [-0.2, 0.2]$ is very near to the target value (250°).

It is very important to notice that the optimal value of coefficients α_k depends on the number of resistances but also on the position of these resistances in relation to the object. An interesting development of this study is to try to optimize the layout of the resistances inside the oven. The practical aim of such an additional study should be the optimization of the thermal power dissipated by the resistances. In this particular case, we want to optimize the

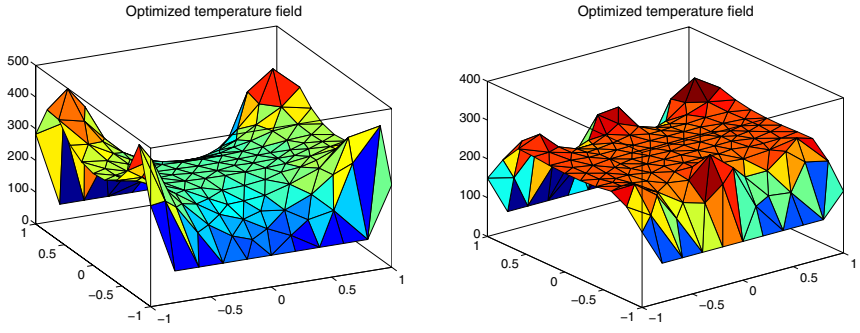

(a) (b)

Fig. 11.5. Optimized temperature fields. (a) four resistances; (b) six resistances.

temperature value in the object and the thermal (or electric) energy used to warm the oven. This is modeled by adding a special term to the functional

$$J(\alpha) = \int_S \left(T_{opt}(x) - T_0(x) - \sum_{k=1}^{nwr} \alpha_k \; T_k(x) \right)^2 dx + C \sum_{k=1}^{nwr} \alpha_k^2.$$

Remark 11.3. You may get very small values (even negative) for the coefficients α_k. This means that the corresponding resistances are located too close to the object and then have to cool it instead of heating it.

It may be seen in Fig. 11.6(a) that a device with six heating resistances produces a larger "well heated" area than with four resistances. Note also that this computing is performed with a rather coarse mesh (173 vertices and 304 triangles). The results are satisfying; they prove the efficiency of the finite element method to solve this problem, and provide a validation of all the procedures, and of the whole process. Nevertheless, in order to get more realistic and more accurate results, it is necessary to solve the problem on a "finer" mesh. We have proceeded to a second computation on a mesh with 732 vertices and 1392 triangles (and still six resistances). The final result is plotted in Fig. 11.6(b), showing a true improvement, especially around the object *and* the resistances. This improvement, predicted by the finite element method (the smaller the element size, the better is the result) leads to an increase of the computational time.

11.8 Solutions and Programs

Solution of Exercise 11.1

The file *THER_oven_ex1.m* contains the procedure `THER_oven_ex1`, which realizes the numerical experiment by defining the physical parameters of the

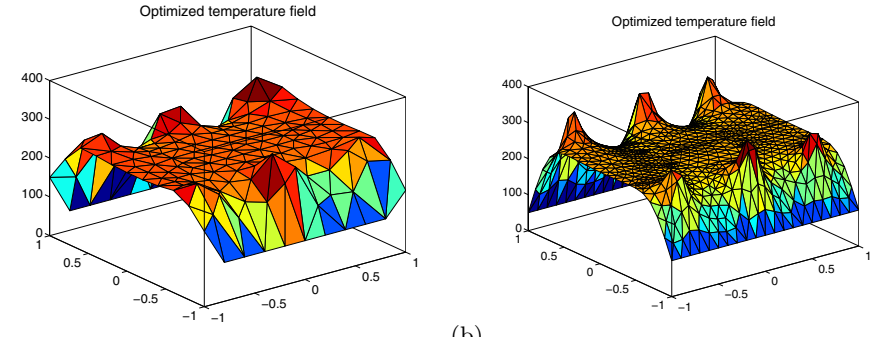

(a) (b)

Fig. 11.6. Optimized temperature fields. (a) coarse mesh; (b) fine mesh.

problem (localization of the resistances, heat conductivity coefficients, boundary temperature values). It calls the procedure of the file *THER_oven.m*, which computes the corresponding temperature field.

The file *THER_matrix_dir.m* contains a procedure that builds the linear system arising from the heat equation problem. We notice that the right-hand side vanishes outside those elements that contain a resistance. The procedure of the file *THER_local.m* builds the right-hand side for given resistances coordinates. The procedure contained in file *THER_elim.m* takes the boundary conditions into account.

Solution of Exercise 11.2

The file *THER_oven_ex2.m* contains the procedure `THER_oven_ex2`, which computes the resistances' values corresponding to the optimal temperature field. It calls the procedure of the file *THER_matrix_inv.m* computing matrix and right-hand side of the optimization problem.

Remark 11.4. We also provide an interactive version of the solution of this project, allowing one to realize numerous numerical experiments by changing data through a graphical user interface. To launch the interface, just run the script *Main* from the subdirectory *interactive*.

11.8.1 Further Comments

In this last section we address the important point of the structure of matrix A. The matrix is sparse because this property is related only to the approximation scheme and the differential operator, which is here similar to the Laplacian operator. [3] The shape of A (see Fig. 11.7(a)) is not as regular as the one

[3] The value of the heat conductivity coefficient c is not relevant for the matrix structure.

displayed in Chap. 7 (compare to Fig. 7.3). This difference results from the use of a finite element mesh with triangles, instead of a rectangular grid. Furthermore, the structure of A is strongly depending on the nodes ordering as can be seen by comparing the matrices obtained on the coarse mesh (Fig. 11.7(a)) and on a finer mesh (Fig. 11.7(b)). The obvious difference is due to a reordering of the nodes for the coarse-mesh calculation.

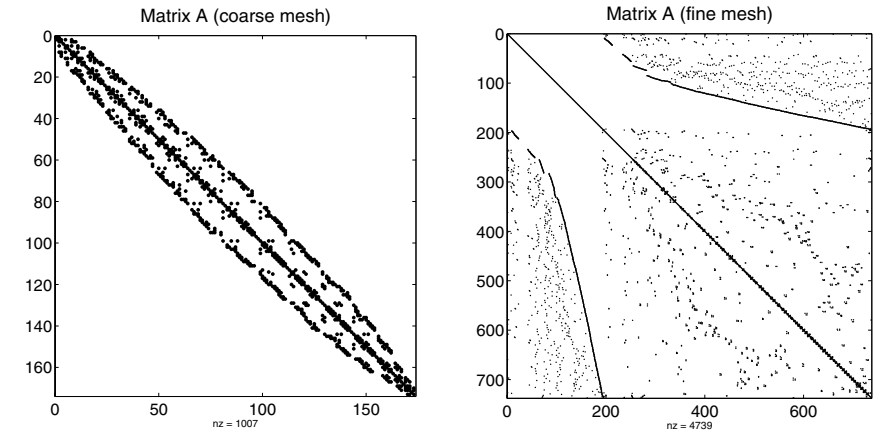

(a) (b)

Fig. 11.7. Associated matrix. (a) coarse mesh; (b) fine mesh.

Chapter References

P. G. Ciarlet, *The Finite Element Method for Elliptic Problems*, North Holland, Amsterdam, 1978.

D. N. Norrie and G. de Vries, *The Finite Element Method*, Academic Press, New York 1973.

J. C. Strikwerda, *Finite Difference Schemes and Partial Differential Equations*, Wadsworth and Brooks/Cole, 1989.

O. C. Zienkiewicz, *The Finite Element Method in Engineering Science*, McGraw-Hill, London 1971.

12

Fluid Dynamics: Solving the Two-Dimensional Navier–Stokes Equations

Project Summary

Level of difficulty:	3
Keywords:	Navier–Stokes equations, Helmholtz equation, Poisson equation, projection method, ADI factorization, FFT Fourier transform
Application fields:	Incompressible flows, jet flow, Kelvin–Helmholtz instability, vortex dipole

12.1 Introduction

The Navier–Stokes system of partial differential equations (PDEs) contains the main conservation laws that universally describe the evolution of a fluid (i.e., liquid or gaseous) flow. Even though these laws have been well established since the nineteenth century, the complete description of their intrinsic properties remains one of the challenging topics of modern physics and mathematics.

In this chapter, we consider some simplifying hypotheses that make the Navier–Stokes equations tractable with relatively simple numerical methods:

- the density of the fluid is assumed constant ($\rho = \rho_0$), i.e., the fluid is *incompressible*;
- the flow parameters depend on only two space variables (x and y), i.e., the flow is *two-dimensional* or 2D;
- all the variables are considered as periodic functions of both x and y, i.e., we impose *periodic boundary conditions*.

This model allows the study of simple, but fascinating, phenomena that turn out to give us an understanding of more complicated flows too. In this project, we shall numerically simulate:

- the Kelvin–Helmholtz instability of a mixing layer, and
- the evolution of a particular vortex structure, the vortex dipole.

From a numerical point of view, this computational project introduces the following algorithms or numerical schemes of more general interest:

- the space discretization using a *staggered grid* and *2D finite difference* schemes;
- the combined *Adams–Bashforth* and *Crank–Nicolson* schemes for the time integration;
- an *alternating direction implicit*, or ADI, method for solving the Helmholtz equation;
- a solver for the periodic *Poisson* equation based on *fast Fourier transforms*, or FFTs;
- the *Thomas algorithm* for solving a tridiagonal linear system.

12.2 The Incompressible Navier–Stokes Equations

The 2D flow-field of an incompressible fluid is completely described by the velocity vector $q = (u(x, y), v(x, y)) \in \mathbb{R}^2$ and the pressure $p(x, y) \in \mathbb{R}$. These functions are a solution of the following conservation laws (see, for instance, Hirsch, 1988):

- mass conservation:
$$\operatorname{div}(q) = 0, \tag{12.1}$$
or, written using the explicit form of the *divergence*[1] operator,
$$\frac{\partial u}{\partial x} + \frac{\partial v}{\partial y} = 0. \tag{12.2}$$

- the momentum conservation equations in the compact form[2]
$$\frac{\partial q}{\partial t} + \operatorname{div}(q \otimes q) = -\mathcal{G}p + \frac{1}{Re}\Delta q, \tag{12.3}$$
or, in explicit form,
$$\begin{cases} \dfrac{\partial u}{\partial t} + \dfrac{\partial u^2}{\partial x} + \dfrac{\partial uv}{\partial y} = -\dfrac{\partial p}{\partial x} + \dfrac{1}{Re}\left(\dfrac{\partial^2 u}{\partial x^2} + \dfrac{\partial^2 u}{\partial y^2}\right), \\ \dfrac{\partial v}{\partial t} + \dfrac{\partial uv}{\partial x} + \dfrac{\partial v^2}{\partial y} = -\dfrac{\partial p}{\partial y} + \dfrac{1}{Re}\left(\dfrac{\partial^2 v}{\partial x^2} + \dfrac{\partial^2 v}{\partial y^2}\right). \end{cases} \tag{12.4}$$

[1] We recall the definitions of the differential operators *divergence, gradient*, and *Laplacian* for a 2D field: if $v = (v_x, v_y) : \mathbb{R}^2 \mapsto \mathbb{R}^2$ and $\varphi : \mathbb{R}^2 \mapsto \mathbb{R}$, then
$$\operatorname{div}(v) = \frac{\partial v_x}{\partial x} + \frac{\partial v_y}{\partial y}, \quad \mathcal{G}\varphi = \left(\frac{\partial \varphi}{\partial x}, \frac{\partial \varphi}{\partial y}\right), \quad \Delta\varphi = \operatorname{div}(\mathcal{G}\varphi) = \frac{\partial^2 \varphi}{\partial x^2} + \frac{\partial^2 \varphi}{\partial y^2},$$
and $\Delta v = (\Delta v_x, \Delta v_y)$.

[2] We denote by $\otimes$ the tensor product.

The previous equations are written in the *dimensionless* form, using the following scaled variables:

$$x = \frac{x^*}{L}, \quad y = \frac{y^*}{L}, \quad u = \frac{u^*}{V_0}, \quad v = \frac{v^*}{V_0}, \quad t = \frac{t^*}{L/V_0}, \quad p = \frac{p^*}{\rho_0 V_0^2}, \tag{12.5}$$

where the superscript $(^*)$ denotes variables measured in physical units. The constants L, V_0 are, respectively, the reference length and velocity that characterize the simulated flow. The dimensionless number Re is called the *Reynolds number* and quantifies the relative importance of inertial (or convective) terms and viscous (or diffusion)[3] terms in the flow:

$$Re = \frac{V_0 L}{\nu}, \tag{12.6}$$

where ν is the kinematic viscosity of the flow.

To summarize, the Navier–Stokes system of PDEs that will be numerically solved in this project is defined by (12.2) and (12.4); the initial condition (at $t = 0$) and the boundary conditions will be discussed in the following sections.

12.3 Numerical Algorithm

We start by presenting the *fractional-step method* (Kim and Moin, 1985; Orlandi, 1999; Ferziger and Perić, 2002) as a general algorithm to solve the Navier–Stokes equations. This algorithm belongs to the class of so-called projection methods and has become rather popular in computational fluid dynamics. An extensive presentation of this method in a more general framework can be found in the recent book by Orlandi (1999).

We use a fractional-step method that consists of two steps:

1. The predictor step: we solve the momentum equations (12.3) written in the compact form

$$\frac{\partial q}{\partial t} = -\mathcal{G}p + \mathcal{H} + \frac{1}{Re}\Delta q, \quad \text{for} \quad q = (u, v) \in \mathbb{R}^2, \tag{12.7}$$

where $\mathcal{H}$ is the vector containing the convective terms

$$-\mathcal{H} = \left(\frac{\partial u^2}{\partial x} + \frac{\partial uv}{\partial y}, \ \frac{\partial uv}{\partial x} + \frac{\partial v^2}{\partial y} \right), \tag{12.8}$$

and $\mathcal{G}p$ the pressure gradient vector. Time discretization of (12.7) combines the explicit Adams–Bashforth scheme (for the convective terms $\mathcal{H}$) with the semi-implicit Crank–Nicolson scheme (for the diffusion terms

[3] The model scalar equations describing the convection and diffusion phenomena are discussed in Chap. 1.

Δq). If δt denotes the calculation time step (supposed constant), the time advancement of the solution from $t_n = n\delta t$ to $t_{n+1} = (n+1)\delta t$ follows the scheme

$$\frac{q^* - q^n}{\delta t} = -\mathcal{G}p^n + \underbrace{\frac{3}{2}\mathcal{H}^n - \frac{1}{2}\mathcal{H}^{n-1}}_{\text{Adams–Bashforth}} + \underbrace{\frac{1}{Re}\Delta\left(\frac{q^* + q^n}{2}\right)}_{\text{Crank–Nicolson}}. \tag{12.9}$$

In the previous equation, the pressure is treated as an explicit term (computed at time t_n). As a consequence, the velocity vector q^* does not satisfy the mass conservation equation (12.1).

2. The corrector (or projection) step: the velocity q^* is corrected such that the velocity field q^{n+1} is divergence-free (or *solenoidal*). We use the following correction equation:[4]

$$q^{n+1} - q^* = -\delta t\, \mathcal{G}\phi. \tag{12.10}$$

The variable ϕ (related to the pressure, but without any physical meaning) is calculated by taking the divergence of (12.10); using that $\mathrm{div}(q^{n+1}) = 0$ and $\mathrm{div}(\mathcal{G}\phi) = \Delta\phi$, we obtain a Poisson equation

$$\Delta\phi = \frac{1}{\delta t}\,\mathrm{div}(q^*). \tag{12.11}$$

To close the algorithm, the pressure for the next time step is updated using[5]

$$p^{n+1} = p^n + \phi - \frac{\delta t}{2Re}\Delta\phi. \tag{12.12}$$

To summarize, the numerical algorithm consists of the following steps, rearranged below in the form that will be used in computer programs:

Algorithm 12.1. *To solve the Navier–Stokes equations (12.2)–(12.4). Given the field* (u^n, v^n, p^n)*, compute:*

[4] The idea behind this equation comes from the observation that q^* and q^{n+1} have the same *curl*. Indeed, the pressure in the Navier–Stokes equation can be eliminated by taking the curl of the momentum equations. We recall that for the vector field $v = (v_x, v_y)$, $\mathrm{curl}(v) = \partial v_y/\partial x - \partial v_x/\partial y$ measures the amount of rotation or the angular momentum of the field.

[5] This equation is obtained as follows: we write (12.9) with an implicit discretization of the pressure term

$$\frac{q^{n+1} - q^n}{\delta t} = -\mathcal{G}p^{n+1} + \frac{3}{2}\mathcal{H}^n - \frac{1}{2}\mathcal{H}^{n-1} + \frac{1}{Re}\Delta\left(\frac{q^{n+1} + q^n}{2}\right)$$

and subtract this equation from (12.9). After replacing q^* from (12.10), we get (12.12), up to an additive constant. Note that this constant is discarded by taking the gradient of the pressure in the momentum equations.

(A) the explicit terms $\mathcal{H}^n$:

$$\mathcal{H}_u^n = -\left(\frac{\partial u^2}{\partial x} + \frac{\partial uv}{\partial y}\right), \tag{12.13}$$

$$\mathcal{H}_v^n = -\left(\frac{\partial uv}{\partial x} + \frac{\partial v^2}{\partial y}\right); \tag{12.14}$$

(B) the nonsolenoidal field $q^* = (u^*, v^*)$ by solving the Helmholtz equations

$$\left(I - \frac{\delta t}{2Re}\,\Delta\right) u^* = u^n + \delta t\left[-\frac{\partial p^n}{\partial x} + \frac{3}{2}\mathcal{H}_u^n - \frac{1}{2}\mathcal{H}_u^{n-1} + \frac{1}{2Re}\Delta u^n\right], \tag{12.15}$$

$$\left(I - \frac{\delta t}{2Re}\,\Delta\right) v^* = v^n + \delta t\left[-\frac{\partial p^n}{\partial y} + \frac{3}{2}\mathcal{H}_v^n - \frac{1}{2}\mathcal{H}_v^{n-1} + \frac{1}{2Re}\Delta v^n\right]; \tag{12.16}$$

(C) the variable ϕ by solving the Poisson equation

$$\Delta\phi = \frac{1}{\delta t}\left(\frac{\partial u^*}{\partial x} + \frac{\partial v^*}{\partial y}\right); \tag{12.17}$$

(D) the solenoidal field $q^{n+1} = (u^{n+1}, v^{n+1})$, with

$$u^{n+1} = u^* - \delta t\,\frac{\partial \phi}{\partial x}, \tag{12.18}$$

$$v^{n+1} = v^* - \delta t\,\frac{\partial \phi}{\partial y}; \tag{12.19}$$

(E) the new pressure:

$$p^{n+1} = p^n + \phi - \frac{\delta t}{2Re}\Delta\phi. \tag{12.20}$$

Steps (A)–(E) are repeated for each time step.

12.4 Computational Domain, Staggered Grids, and Boundary Conditions

Numerically solving the Navier–Stokes equations is considerably simplified by considering a rectangular domain $L_x \times L_y$ (see Fig. 12.1) with periodic boundary conditions everywhere. The periodicity of the velocity $q(x, y)$ and pressure $p(x, y)$ fields is mathematically expressed as

$$q(0, y) = q(L_x, y), \quad p(0, y) = p(L_x, y), \quad \forall y \in [0, L_y], \tag{12.21}$$

$$q(x, 0) = q(x, L_y), \quad p(x, 0) = p(x, L_y), \quad \forall x \in [0, L_x]. \tag{12.22}$$

The points at which the solution will be computed are distributed in the domain following a rectangular and uniform 2D grid. Since not all the variables share the same grid in our approach, we first define a *primary* grid (see

Fig. 12.1) generated by taking n_x computational points along x and, respectively, n_y points along y:

$$x_c(i) = (i-1)\delta x, \quad \delta x = \frac{L_x}{n_x - 1}, \quad i = 1, \ldots, n_x, \tag{12.23}$$

$$y_c(j) = (j-1)\delta y, \quad \delta y = \frac{L_y}{n_y - 1}, \quad j = 1, \ldots, n_y. \tag{12.24}$$

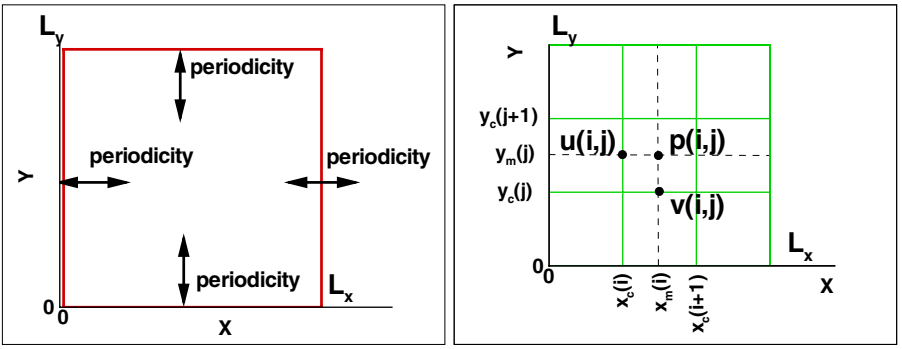

Fig. 12.1. Computational domain, staggered grids, and boundary conditions.

A *secondary* grid is defined by the centers of the primary grid cells:

$$x_m(i) = (i - 1/2)\delta x, \quad i = 1, \ldots, n_{xm}, \tag{12.25}$$

$$y_m(j) = (j - 1/2)\delta y, \quad j = 1, \ldots, n_{ym}, \tag{12.26}$$

where we have used the shorthand notation $n_{xm} = n_x - 1$, $n_{ym} = n_y - 1$. Inside a computational cell defined as the rectangle $[x_c(i), x_c(i+1)] \times [y_c(j), y_c(j+1)]$, the unknown variables u, v, p will be computed as approximations of the solution at different space locations:

- $u(i,j) \approx u(x_c(i), y_m(j))$ (west face of the cell),
- $v(i,j) \approx v(x_m(i), y_c(j))$ (south face of the cell),
- $p(i,j) \approx p(x_m(i), y_m(j))$ (center of the cell).

This *staggered* arrangement of the variables has the advantage of a strong coupling between pressure and velocity. It also helps (see the references at the end of the chapter) to avoid some problems of stability and convergence experienced with *collocated* arrangements (where all the variables are computed at the same grid points).

12.5 Finite Difference Discretization

In this section, Algorithm 12.1 will be written in a discrete form that will be used in the computer programs of this project. We start by noticing that the

periodic boundary conditions take the following discrete form:

$$\begin{array}{l} u(1,j) = u(n_x,j),\ \forall j = 1,\ldots,n_y, \\ u(i,1) = u(i,n_y),\ \forall i = 1,\ldots,n_x, \end{array} \tag{12.27}$$

and similar relations for v and p. As a consequence, the unknowns of the problem are only the $n_{xm} \times n_{ym}$ values

$$u(i,j), \quad v(i,j), \quad p(i,j), \quad \text{for} \quad i = 1,\ldots,n_{xm}, \quad j = 1,\ldots,n_{ym}.$$

A very useful programming trick (see also Chap. 1) in implementing discrete periodic boundary conditions (12.27) consists in defining the supplementary arrays

$$\begin{cases} ip(i) = i+1,\ i = 1,\ldots,(n_{xm}-1), \\ ip(n_{xm}) = 1, \end{cases} \quad \begin{cases} jp(j) = j+1,\ j = 1,\ldots,(n_{ym}-1), \\ jp(n_{ym}) = 1, \end{cases} \tag{12.28}$$

$$\begin{cases} im(i) = i-1,\ i = 2,\ldots,n_{xm}, \\ im(1) = n_{xm}, \end{cases} \quad \begin{cases} jm(j) = j-1,\ j = 2,\ldots,n_{ym}, \\ jm(1) = n_{ym}, \end{cases} \tag{12.29}$$

and using the vectorial capabilities of MATLAB to write the finite difference discretization of the differential operators in a very compact form. For example, to compute $(\partial\psi/\partial x)(i,j)$ for a fixed j and all $i = 1,\ldots,n_{xm}$, the second-order centered finite difference scheme is explicitly written as

$$\frac{\partial\psi}{\partial x}(i,j) \approx \frac{\psi(i+1,j) - \psi(i-1,j)}{2\delta x}, \quad i = 2,\ldots,(n_{xm}-1),$$

with a particular treatment of indices $i = 1$ and $i = n_{xm}$:

$$\frac{\partial\psi}{\partial x}(1,j) \approx \frac{\psi(2,j) - \psi(n_{xm},j)}{2\delta x}, \quad \frac{\partial\psi}{\partial x}(n_{xm},j) \approx \frac{\psi(1,j) - \psi(n_{xm}-1,j)}{2\delta x}.$$

Using the vectors im and ip from (12.28) and (12.29) we can compress the previous relations into a single one:

$$\frac{\partial\psi}{\partial x}(i,j) \approx \frac{\psi(ip(i),j) - \psi(im(i),j)}{2\delta x}, \quad i = 1,\ldots,n_{xm}. \tag{12.30}$$

Remark 12.1. As a general programming rule, in a finite difference scheme with periodic boundary conditions, we shall replace indices $(i+1)$ by $ip(i)$ and $(i-1)$ by $im(i)$ (and similarly for j indices).

We are now equipped to present in detail the full discrete form of each step of Algorithm 12.1.

(A) Computation of Explicit Terms

The two components $\mathcal{H}_u^n$ (12.13) and $\mathcal{H}_v^n$ (12.14) of the explicit term $\mathcal{H}^n$ are computed at the same points of the grid as the corresponding velocities. To follow the logic of the discretization below, the reader is invited to add to Fig. 12.1 the adjacent cells $(i, j \pm 1)$, $(i \pm 1, j)$. Using the centered finite difference scheme (12.30) we easily obtain:
• for the computation of the velocity u (located at $(x_c(i), y_m(j))$):
for $i = 1, \ldots, n_{xm}$, $j = 1, \ldots, n_{ym}$,

$$\begin{aligned}
\frac{\partial u^2}{\partial x}(i,j) &\approx \frac{1}{\delta x}\left[\left(\frac{u(i,j)+u(ip(i),j)}{2}\right)^2 - \left(\frac{u(i,j)+u(im(i),j)}{2}\right)^2\right], \\
\frac{\partial uv}{\partial y}(i,j) &\approx \frac{1}{\delta y}\left[\left(\frac{u(i,j)+u(i,jp(j))}{2}\right)\left(\frac{v(i,jp(j))+v(im(i),jp(j))}{2}\right)\right. \\
&\qquad \left. - \left(\frac{u(i,j)+u(i,jm(j))}{2}\right)\left(\frac{v(i,j)+v(im(i),j)}{2}\right)\right], \\
\mathcal{H}_u^n(i,j) &= -\frac{\partial u^2}{\partial x}(i,j) - \frac{\partial uv}{\partial y}(i,j);
\end{aligned} \tag{12.31}$$

• and similarly for the velocity v (located at $(x_m(i), y_c(j))$):
for $i = 1, \ldots, n_{xm}$, $j = 1, \ldots, n_{ym}$,

$$\begin{aligned}
\frac{\partial v^2}{\partial y}(i,j) &\approx \frac{1}{\delta y}\left[\left(\frac{v(i,j)+v(i,jp(j))}{2}\right)^2 - \left(\frac{v(i,j)+u(i,jm(j))}{2}\right)^2\right], \\
\frac{\partial uv}{\partial x}(i,j) &\approx \frac{1}{\delta x}\left[\left(\frac{u(ip(i),j)+u(ip(i),jm(j))}{2}\right)\left(\frac{v(i,j)+v(ip(i),j)}{2}\right)\right. \\
&\qquad \left. - \left(\frac{u(i,j)+u(i,jm(j))}{2}\right)\left(\frac{v(i,j)+v(im(i),j)}{2}\right)\right], \\
\mathcal{H}_v^n(i,j) &= -\frac{\partial uv}{\partial x}(i,j) - \frac{\partial v^2}{\partial y}(i,j).
\end{aligned} \tag{12.32}$$

(B) Computation of the Nonsolenoidal Velocity Field

We first notice that (12.15) and (12.16) can be written in the compact form of a Helmholtz equation:

$$\underbrace{\left(I - \frac{\delta t}{2Re}\,\Delta\right)}_{\text{Helmholtz operator}}\delta q^* = \underbrace{\delta t\left[-\mathcal{G}p^n + \frac{3}{2}\mathcal{H}^n - \frac{1}{2}\mathcal{H}^{n-1} + \frac{1}{Re}\Delta q^n\right]}_{\text{RHS}^n}, \tag{12.33}$$

where we have introduced the notation $\delta q^* = q^* - q^n$. When periodic boundary conditions are imposed, this equation is usually solved using *fast Fourier*

transforms (or FFT).[6] We present in the following a different method, the *alternating direction implicit* (or ADI) method, which is easier to implement and has the advantage that it easily takes into account other types of boundary conditions. The Helmholtz operator is approximated since the terms $\mathcal{O}(\delta t^2)$ are neglected:

$$\left(I - \frac{\delta t}{2Re}\,\Delta\right)\delta q^* \approx \left(I - \frac{\delta t}{2Re}\,\frac{\partial^2}{\partial x^2}\right)\left(I - \frac{\delta t}{2Re}\,\frac{\partial^2}{\partial y^2}\right)\delta q^*. \tag{12.34}$$

This second-order accurate factorization[7] is use to solve (12.33) in two steps:

$$\left(I - \frac{\delta t}{2Re}\,\frac{\partial^2}{\partial x^2}\right)\overline{\delta q^*} = \mathrm{RHS}^n \quad (+\,\text{periodicity along } x), \tag{12.35}$$

$$\left(I - \frac{\delta t}{2Re}\,\frac{\partial^2}{\partial y^2}\right)\delta q^* = \overline{\delta q^*} \quad (+\,\text{periodicity along } y). \tag{12.36}$$

It is important to note that we also impose periodic boundary conditions for the field $\overline{\delta q^*}$, which is physically meaningless. This choice, which seems to be natural for our periodic problem, becomes more difficult for other types of boundary conditions (Dirichlet type, for example) and needs further analytical development.

For the discretization of second derivatives in (12.35) and (12.36) we use a second-order centered finite difference scheme, written here in the general form (see also Chap. 1)

$$\begin{aligned}\frac{\partial^2\psi}{\partial x^2}(i,j) &\approx \frac{\psi(i+1,j) - 2\psi(i,j) + \psi(i-1,j)}{\delta x^2},\\ \frac{\partial^2\psi}{\partial y^2}(i,j) &\approx \frac{\psi(i,j+1) - 2\psi(i,j) + \psi(i,j-1)}{\delta y^2}.\end{aligned} \tag{12.37}$$

Finally, the algorithm used in the programs of this chapter is the following:

Algorithm 12.2. *(computes u^* using an ADI method):*

- *First step of ADI: for all $j = 1, \ldots, n_{ym}$ solve the linear system*

$$-\beta_x\overline{(\delta u^*)}(i-1,j) + (1+2\beta_x)\overline{(\delta u^*)}(i,j) - \beta_x\overline{(\delta u^*)}(i+1,j) = \mathrm{RHS}_u^n(i,j), \tag{12.38}$$

where $i = 1, \ldots, n_{xm}$ and $\beta_x = \frac{\delta t}{2Re}\frac{1}{\delta x^2}$. In the previous relation, we take into account the periodicity by imposing

$$\overline{(\delta u^*)}(0,j) = \overline{(\delta u^*)}(n_{xm},j), \qquad \overline{(\delta u^*)}(n_{xm}+1,j) = \overline{(\delta u^*)}(1,j).$$

[6] This is the subject of an exercise of this chapter.

[7] The methods based on this idea are also known as *approximate factorization* or *splitting* methods.

More precisely, we have to solve n_{ym} linear systems with the following matrix of size $n_{xm} \times n_{xm}$:

$$M_x = \begin{pmatrix} 1+2\beta_x & -\beta_x & 0 & . & . & 0 & 0 & -\beta_x \\ -\beta_x & 1+2\beta_x & -\beta_x & . & . & 0 & 0 & 0 \\ . & . & . & . & . & . & . & . \\ 0 & 0 & 0 & . & . & -\beta_x & 1+2\beta_x & -\beta_x \\ -\beta_x & 0 & 0 & . & . & 0 & -\beta_x & 1+2\beta_x \end{pmatrix}. \tag{12.39}$$

This particular matrix pattern will be referred to in the following as a tridiagonal periodic matrix.
An efficient method to solve such systems will be derived later, based on the well-known Thomas algorithm (Algorithm 12.5).
At the end of this step we obtain $\overline{(\delta u^*)}(i,j)$.

- *Second step of ADI: for all $i = 1, \ldots, n_{xm}$ solve the linear system*

$$-\beta_y(\delta u^*)(i,j-1) + (1+2\beta_y)(\delta u^*)(i,j) - \beta_y(\delta u^*)(i,j+1) = \overline{(\delta u^*)}(i,j), \tag{12.40}$$

where $j = 1, \ldots, n_{ym}$ and $\beta_y = \frac{\delta t}{2Re}\frac{1}{\delta y^2}$. The periodicity requires that

$$(\delta u^*)(i,0) = -(\delta u^*)(i,n_{xm}), \qquad (\delta u^*)(i,n_{ym}+1) = (\delta u^*)(i,1).$$

We obtain this time n_{xm} linear systems with tridiagonal and periodic matrices of size $n_{ym} \times n_{ym}$:

$$M_y = \begin{pmatrix} 1+2\beta_y & -\beta_y & 0 & . & . & 0 & 0 & -\beta_y \\ -\beta_y & 1+2\beta_y & -\beta_y & . & . & 0 & 0 & 0 \\ . & . & . & . & . & . & . & . \\ 0 & 0 & 0 & . & . & -\beta_y & 1+2\beta_y & -\beta_y \\ -\beta_y & 0 & 0 & . & . & 0 & -\beta_y & 1+2\beta_y \end{pmatrix}. \tag{12.41}$$

At the end of this step we get $(\delta u^*)(i,j)$ and immediately

$$u^*(i,j) = u(i,j) + (\delta u^*)(i,j).$$

The computation procedure is similar for the other component of the velocity. Considering that it could be helpful to correctly program the algorithm, we present here the details of the computation:

Algorithm 12.3. *(computes v^* using an ADI method):*

- *First step of ADI: for all $j = 1, \ldots, n_{ym}$ solve the linear system*

$$M_x\,\overline{(\delta v^*)}(i,j) = \mathrm{RHS}_v^n(i,j), \tag{12.42}$$

where $i = 1, \ldots, n_{xm}$ and the matrix M_x is given by (12.39).
At the end of this step we obtain $\overline{(\delta v^*)}(i,j)$.

- *Second step of ADI: for all $i = 1, \ldots, n_{xm}$, solve the linear system*

$$M_y \, \overline{(\delta v^*)}(i,j) = \overline{(\delta v^*)}(i,j), \tag{12.43}$$

where $j = 1, \ldots, n_{ym}$ and the matrix M_y is given by (12.41). We obtain $(\delta v^*)(i,j)$ and immediately

$$v^*(i,j) = u(i,j) + (\delta v^*)(i,j).$$

(C) Solving the Poisson Equation

The Poisson equation (12.11) is discretized as

$$\Delta\phi(i,j) = \left(\frac{\partial^2\phi}{\partial x^2} + \frac{\partial^2\phi}{\partial y^2}\right)(i,j) = Q(i,j), \tag{12.44}$$

where $i = 1, \ldots, n_{xm}$, $j = 1, \ldots, n_{ym}$, and

$$Q(i,j) = \frac{1}{\delta t}\,\mathrm{div}(q^*)(i,j) = \frac{1}{\delta t}\left(\frac{\partial u^*}{\partial x} + \frac{\partial v^*}{\partial y}\right)(i,j).$$

To solve this equation, we first use the periodicity along the x direction and expand the variable ϕ in a discrete Fourier series:

$$\phi(i,j) = \sum_{l=1}^{n_{xm}} \widehat{\phi}_l(j) e^{\mathrm{i}\frac{2\pi}{n_{xm}}(i-1)(l-1)}, \quad \forall\, i = 1, \ldots, n_{xm}, \tag{12.45}$$

where $\mathrm{i} = \sqrt{-1}$ is the imaginary unit. The advantage of using a Fourier series expansion is to *diagonalize* the Laplace operator and thus reduce the initial 2D problem (12.44) to a 1D problem. Indeed, considering an approximation of $\partial^2\phi/\partial x^2$ by second-order centered differences, we obtain

$$\begin{aligned}
\frac{\partial^2\phi}{\partial x^2}(i,j) &\approx \frac{\phi(i+1,j) - 2\phi(i,j) + \phi(i-1,j)}{\Delta x^2} \\
&= \frac{1}{\Delta x^2}\sum_{l=1}^{n_{xm}} \widehat{\phi}_l(j) e^{\mathrm{i}\frac{2\pi}{n_{xm}}(i-1)(l-1)} \left(e^{\mathrm{i}\frac{2\pi}{n_{xm}}(l-1)} - 2 + e^{-\mathrm{i}\frac{2\pi}{n_{xm}}(l-1)}\right) \\
&= \sum_{l=1}^{n_{xm}} \widehat{\phi}_l(j) e^{\mathrm{i}\frac{2\pi}{n_{xm}}(i-1)(l-1)} \underbrace{\frac{2}{\Delta x^2}\left[\cos\left(\frac{2\pi}{n_{xm}}(l-1)\right) - 1\right]}_{k_l}.
\end{aligned} \tag{12.46}$$

Using a similar Fourier series expansion for the right-hand-side function Q (which is also periodic),

$$Q(i,j) = \sum_{l=1}^{n_{xm}} \widehat{Q}_l(j) e^{\mathrm{i}\frac{2\pi}{n_{xm}}(i-1)(l-1)},$$

we find that solving the initial problem (12.44) is equivalent to solving n_{xm} 1D equations

$$\frac{\partial^2}{\partial y^2}\widehat{\phi}_l(j) + k_l\widehat{\phi}_l(j) = \widehat{Q}_l(j), \tag{12.47}$$

where $l = 1, \ldots, n_{xm}$ is the *wave number* of the Fourier expansion.

At this point of our numerical algorithm, equations (12.47) can be solved using either a similar Fourier expansion along y or a finite difference scheme to discretize the second derivative. Since the first method can be applied only for periodic boundary conditions, we choose the second one, which can be easily adapted to more general cases required by further development of this project (a *wall* boundary condition, for example). With this choice, (12.47) becomes, for $j = 1, \ldots, n_{ym}$,

$$\frac{1}{\delta y^2}\widehat{\phi}_l(j-1) + \left(-\frac{2}{\delta y^2} + k_l\right)\widehat{\phi}_l(j) + \frac{1}{\delta y^2}\widehat{\phi}_l(j+1) = \widehat{Q}_l(j). \tag{12.48}$$

This equation must be supplemented with discrete boundary conditions for $j = 1$ and $j = n_{ym}$. In our case, we naturally use the periodicity of the function $\widehat{\phi}$.

It is important to note that special treatment is required for the wave number $l = 1$ for which $k_l = 0$. For this value, it is easy to see that the matrix of the system (12.48) is singular and our formulation is not well-posed! Indeed, the solution of the Poisson equation with periodic boundary conditions is determined up to an additive constant. This constant is exactly the first term (or the average value) of the discrete Fourier expansion (12.45). Since the absolute value of the pressure is of no significance for an incompressible flow (we saw that only the gradient of the pressure appears in the equations), we shall not worry about this constant, which will be freely fixed! Nevertheless, a reasonable choice would be to impose $\widehat{\phi}_0(j) = 0$, for $j = 1, \ldots, n_{ym}$, which yields zero average solutions $\widehat{\phi}_l$. The final algorithm to solve the Poisson equation is presented in great detail in the following.

Algorithm 12.4. *To compute the pressure correction ϕ at points of coordinates $(x_m(i), y_m(j))$:*

- *Compute the array $Q(i,j)$, for $i = 1, \ldots, n_{xm}$ and $j = 1, \ldots, n_{ym}$, by*

$$Q(i,j) = \frac{1}{\delta t}\left(\frac{u^*(ip(i),j) - u^*(i,j)}{\delta x} + \frac{v^*(i,jp(i)) - v^*(i,j)}{\delta y}\right). \tag{12.49}$$

- *Apply a fast Fourier transform FFT to each column of the array Q:*

$$\widehat{Q}(l,j) = FFT(Q(i,j)), \quad l = 1, \ldots, n_{xm}, \quad j = 1, \ldots, n_{ym}. \tag{12.50}$$

  The reader is of course aware that the values $\widehat{Q}$ are complex!
- *For $l = 1$ impose $\widehat{\phi}_1(j) = 0$, for $j = 1, \ldots, n_{ym}$.*

- *For each* $l = 2, \ldots, n_{xm}$, *solve the linear system* $M_l \widehat{\phi}_l = \widehat{Q}(l,j)^T$ *of a tridiagonal matrix of size* $(n_{ym} \times n_{ym})$*:*

$$M_l = \frac{1}{\delta y^2} \begin{bmatrix} -2+\delta y^2\, k_l & 1 & 0\,..\,0 & 0 & 1 \\ 1 & -2+\delta y^2\, k_l & 1\,..\,0 & 0 & \\ . & . & .\,.\,.\,. & . & . \\ 0 & 0 & 0\,..\,1 & -2+\delta y^2\, k_l & 1 \\ 1 & 0 & 0\,..\,0 & 1 & -2+\delta y^2\, k_l \end{bmatrix}, \tag{12.51}$$

where

$$k_l = \frac{2}{\Delta x^2}\left[\cos\left(\frac{2\pi}{n_{xm}}(l-1)\right) - 1\right].$$

- *Build the array* $\widehat{\Phi}(l,j)$*, whose rows are the already computed vectors* $\widehat{\phi}_l$*.*
- *Apply an inverse Fourier transform (IFFT) to obtain the final solution*

$$\phi(i,j) = IFFT(\widehat{\Phi}(l,j)), \qquad i = 1, \ldots, n_{xm}, \quad j = 1, \ldots, n_{ym}. \tag{12.52}$$

(D) Computation of the Solenoidal Field

After solving the Poisson equation for the pressure correction, it is easy to correct the velocity field:

- for $i = 1, \ldots, n_{xm}, \quad j = 1, \ldots, n_{ym}$,

$$u^{n+1}(i,j) = u^*(i,j) - \delta t\, \frac{\phi(i,j) - \phi(im(i),j)}{\delta x}, \tag{12.53}$$

- for $i = 1, \ldots, n_{xm}, \quad j = 1, \ldots, n_{ym}$,

$$v^{n+1}(i,j) = v^*(i,j) - \delta t\, \frac{\phi(i,j) - \phi(i,jm(j))}{\delta y}. \tag{12.54}$$

(E) Computation of the Pressure Field

Using (12.20), the new pressure field is computed as

- for $i = 1, \ldots, n_{xm}, \quad j = 1, \ldots, n_{ym}$,

$$p^{n+1}(i,j) = p^n(i,j) + \phi(i,j) - \frac{\delta t}{2Re}\left[\frac{\phi(ip(i),j) - 2\phi(i,j) + \phi(im(i),j)}{\delta x^2} + \frac{\phi(i,jp(j)) - 2\phi(i,j) + \phi(i,jm(j))}{\delta y^2}\right]. \tag{12.55}$$

Finally, the pressure gradient is updated for the next time step:

- for $i = 1, \ldots, n_{xm}, \quad j = 1, \ldots, n_{ym}$,

$$\frac{\partial p^{n+1}}{\partial x}(i,j) = \frac{p^{n+1}(i,j) - p^{n+1}(im(i),j)}{\delta x}, \tag{12.56}$$

- for $i = 1, \ldots, n_{xm}, \quad j = 1, \ldots, n_{ym}$,

$$\frac{\partial p^{n+1}}{\partial y}(i,j) = \frac{p^{n+1}(i,j) - p^{n+1}(i,jm(j))}{\delta y}. \tag{12.57}$$

Calculation of the Time Step

The last point to discuss for our numerical algorithm is how to compute the value of the time step δt. Since we use a semi-implicit scheme, the time step value will be bounded through an inequality called the *CFL*[8] *condition*. This condition comes from a stability analysis of the scheme, which is far from a trivial matter when one is dealing with Navier–Stokes equations.[9] For the applications considered in this project, a fair CFL condition would be

$$dt = \frac{\text{cfl}}{\max\left(\left|\frac{u}{\delta x}\right| + \left|\frac{v}{\delta y}\right|\right)}, \tag{12.58}$$

where $\text{cfl} < 1$ is a constant that controls the time step value. In practice, we shall use, when possible, a constant time step, computed from the condition (12.58) applied to the initial flow field.

12.6 Flow Visualization

An important point for numerically solving the Navier–Stokes equations is the postprocessing of the obtained data. Various interesting physical information can be extracted from a numerical field. For the unsteady flows considered in this project, we use visualization techniques offering an intuitive picture (even for a nonspecialist user) of the flow evolution.

A simple way to visualize the simulated flow is to calculate the *vorticity vector field* $\boldsymbol{\omega}$ by taking the *curl* of the velocity. As we shall see, this is an effective visualization mean for flows dominated by large vortices (the reader can find nice illustrations of vortex flows in the remarkable *Album of Fluid Motion* by Van Dyke (1982)). For 2D flows, the vorticity vector has a single nonzero component, perpendicular to the flow evolution plane:

[8] Courant–Friedrichs–Lewy

[9] Exact CFL conditions are derived for scalar convection and wave equations in Chap. 1. The CFL condition is also discussed for the Navier–Stokes equations with zero viscosity (i.e., the Euler equations) in Chap. 10.

$$\omega = \frac{\partial v}{\partial x} - \frac{\partial u}{\partial y}. \tag{12.59}$$

The discrete values of ω are computed at points $(x_c(i), y_c(j))$ by

$$\omega(i,j) = \frac{v(i,j) - v(im(i),j)}{\delta x} - \frac{u(i,j) - u(i,jm(j))}{\delta y}. \tag{12.60}$$

The isocontours of vorticity (i.e., the lines of points at which the variable takes the same given value)[10] allow one to identify vortical structures in the flow.

A second visualization method consists in following the evolution of a *passive tracer (or scalar)* in the flow. This numerical technique is equivalent to experimental visualizations using smoke (for gases) or dye (for liquids). As suggested by its name, the passive scalar does not affect the flow field evolution; it is just transported by the velocity field, following a convection-diffusion equation

$$\frac{\partial \chi}{\partial t} + \frac{\partial \chi u}{\partial x} + \frac{\partial \chi v}{\partial y} = \frac{1}{Pe} \Delta \chi, \tag{12.61}$$

where the dimensionless number Pe (Peclet number) quantifies the diffusion properties of the passive tracer χ. The values $\chi(i,j)$ are computed at the cell centers $(x_m(i), y_m(j))$ following the same numerical scheme as for momentum equations; this calculation is done at the end of each time step, allowing one to use the velocity values of the updated (solenoidal) field.

12.7 Initial Condition

At this point, we are able to advance the numerical solution in time, but we still have to make precise the starting point of the computation, or the initial condition. We shall see that the initial field will be constructed so as to trigger the unsteady flow that we wish to simulate. In principle, the initial condition must be compatible with the Navier–Stokes equations; in practice, we prescribe only the initial velocity field and set the pressure to zero values everywhere. The correct pressure field will be established by the calculation after the first time step.

In this project we shall simulate two classes of relatively simple flows that illustrate basic mechanisms found in more general and complex real flows.

Dynamics of a 2D Jet: The Kelvin–Helmholtz Instability

The Kelvin–Helmholtz instability generally occurs in flows where shear is present. The basic example for this instability is the flow of two parallel

[10] MATLAB built-in functions `contour` or `pcolor` draw isocontours for a given 2D solution field.

streams of different velocities and, eventually, densities. This flow can be obtained in a simple experiment: put in a long rectangular transparent box two immiscible liquids with large density difference and start to slowly incline the box. The denser liquid will start to flow in the lower part of the box, pushing the lightest liquid into the upper part. Very nice patterns, called Kelvin *cat eyes*, form at the interface between the two liquids (see Fig. 12.2 for a sketch and Fig. 12.5 for a numerical simulation).

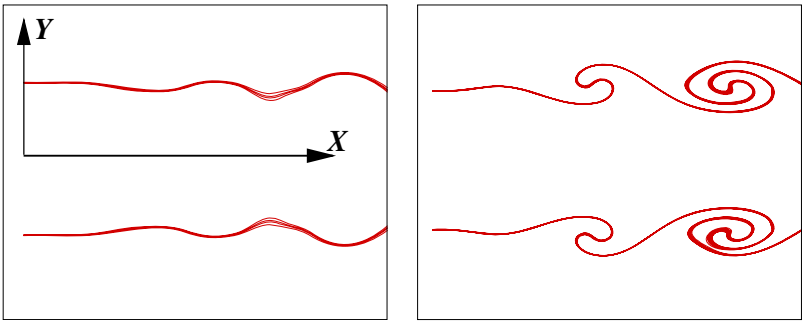

Fig. 12.2. Evolution of the Kelvin–Helmholtz instability in a 2D jet: perturbation of the shear layer forming the contour of the jet (left) and roll-up of Kelvin (*cat eyes*) vortices (right).

This phenomenon also occurs in jet flows that are generated by the injection of fluid into a quiescent environment. The instability develops in the shear layer between the injected fluid and the fluid at rest. Our numerical simulation will start from an initial condition setting the velocity profile corresponding to the shear layers forming the contour of the jet:

$$v(x,y) = 0, \qquad u(x,y) = u_1(y)(1 + u_2(x)), \tag{12.62}$$

where u_1 is the mean velocity profile

$$u_1(y) = \frac{U_0}{2}\left(1 + \tanh\left(\frac{1}{2}P_j\left(1 - \frac{|L_y/2 - y|}{R_j}\right)\right)\right), \tag{12.63}$$

and u_2 the perturbation that triggers the Kelvin–Helmholtz instability

$$u_2(x) = A_x \sin\left(2\pi\,\frac{x}{\lambda_x}\right). \tag{12.64}$$

Note that both velocity profiles respect the periodicity condition at the boundaries. The parameters $U_0, P_j, R_j, A_x, \lambda_x$ will be specified later for numerical applications.

Evolution of a Vortex Dipole

Vortices generated by the Kelvin–Helmholtz instability all rotate in the same sense, i.e., they have vorticities of the same sign. A vortex dipole is a pair of vortices of opposite signs. This configuration is encountered in many areas of practical interest (meteorological and coastal flows, trailing vortices from aircraft, 2D turbulence, swirled injection in stratified charge engines). We consider here symmetric dipoles for which the two vortices have the same vorticity magnitude; this is a stable structure that propagates along its axis of symmetry with a quasiconstant translation velocity generated by a self-induction mechanism. The reader interested in studying vortex motion is referred to Batchelor (1988) and Saffman (1992).

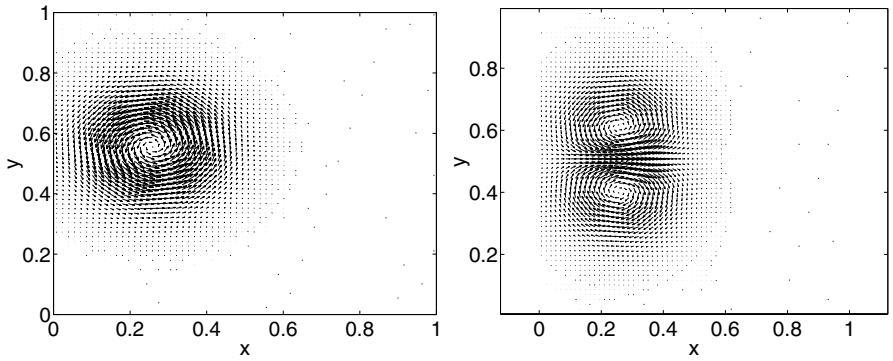

Fig. 12.3. Velocity field of a single vortex (left) and of a vortex dipole (right).

We shall numerically construct a vortex dipole by superimposing the velocity fields of two individual vortices (see Fig. 12.3). Each vortex, defined by its center (x_v, y_v), size l_v, and intensity ψ_0, is analytically described by the following *stream-function*:

$$\psi(x,y) = \psi_0 \, exp\left(-\frac{(x-x_v)^2 + (y-y_v)^2}{l_v^2}\right). \tag{12.65}$$

The stream-function is used to derive the velocity components as

$$\begin{cases} u = \quad \dfrac{\partial \psi}{\partial y} = -\,2\dfrac{(y-y_v)}{l_v^2}\,\psi(x,y), \\ v = -\dfrac{\partial \psi}{\partial x} = \quad 2\dfrac{(x-x_v)}{l_v^2}\,\psi(x,y). \end{cases} \tag{12.66}$$

The dipole is now *assembled* by taking two vortices of the same size l_v but opposite intensities $\pm\psi_0$ and placing them symmetrically about a chosen line, which will be the propagation direction. For example, a dipole propagating to

the right along the x axis will be defined by (see Fig. 12.3)
vortex 1 : $+\psi_0, l_v, x_v, y_v = L_y + a$,
vortex 2 : $-\psi_0, l_v, x_v, y_v = L_y - a$,
where a is the distance separating the vortex centers.

It is important to note that this is not a rigorous method to construct a vortex dipole, since the initial condition is not compatible with the Navier–Stokes equations.[11] However, the velocity and pressure fields will be automatically adjusted to satisfy the equations after the first time step of the numerical simulation.

12.8 Step-by-Step Implementation

The survivors of previous lengthy theoretical developments may now start to implement the numerical algorithm to simulate some physical flows. Since this is a delicate process, we shall proceed step by step to construct our *Navier–Stokes code*. We adopt the programming strategy of building specialized program modules that will be first validated on simpler problems for which an exact solution is known. We start with some preliminary questions.

12.8.1 Solving a Linear System with Tridiagonal, Periodic Matrix

Since there exist different MATLAB built-in functions to solve linear systems, this part is not compulsory for the following numerical developments. Nevertheless, we consider that the reader should be aware of the structure of the involved systems and efficient algorithms to solve them.[12] Moreover, the algorithms in this section can be used in applications using other (less-friendly) programming languages.

We shall use the particular pattern (tridiagonal, periodic) of matrices (12.39), (12.41), (12.51) to build an efficient numerical algorithm to solve the corresponding linear systems. We start by presenting the well-known Thomas algorithm for solving tridiagonal systems.

Algorithm 12.5. *Thomas algorithm for tridiagonal systems.*[13] *The tridiagonal system*

[11] The reader can test more rigorous analytical models for the vortex dipole as, for example, the Lamb–Chaplygin dipole, which corresponds to a steady solution of the 2D Euler equations; see Batchelor (1988); Saffman (1992).

[12] It is always interesting to know what happens behind the *magical* MATLAB command $x = A\backslash b$ that solves the system $Ax = b$.

[13] We can easily show that this algorithm is a particular form of the Gauss elimination method.

$$\begin{pmatrix} b_1 & c_1 & 0 & . & . & 0 & 0 \\ a_2 & b_2 & c_2 & 0 & . & 0 & 0 \\ . & . & . & . & . & . & . \\ . & . & . & . & . & . & . \\ 0 & 0 & 0 & 0 & a_{n-1} & b_{n-1} & c_{n-1} \\ 0 & 0 & 0 & 0 & . & a_n & b_n \end{pmatrix} \begin{pmatrix} X_1 \\ X_2 \\ . \\ . \\ X_{n-1} \\ X_n \end{pmatrix} = \begin{pmatrix} f_1 \\ f_2 \\ . \\ . \\ f_{n-1} \\ f_n \end{pmatrix}$$

is solved by introducing the following recurrence relation:

$$\begin{cases} X_k = \gamma_k - \dfrac{c_k}{\beta_k} X_{k+1}, \quad k = 1, \ldots, (n-1), \\ \\ X_n = \gamma_n. \end{cases} \tag{12.67}$$

Inserting these relations in the initial form of the system, we can calculate the coefficients γ_k *and* β_k*:*

$$\begin{cases} \beta_1 = b_1, \\ \beta_k = b_k - \dfrac{c_{k-1}}{\beta_{k-1}} a_k, \quad k = 2, \ldots, n, \end{cases}$$

$$\begin{cases} \gamma_1 = \dfrac{f_1}{\beta_1} = \dfrac{f_1}{b_1}, \\ \\ \gamma_k = \dfrac{f_k - a_k \gamma_{k-1}}{\beta_k}, \quad k = 2, \ldots, n. \end{cases}$$

After computing the coefficients γ_k *and* β_k*, the unknowns* X_k *are immediately obtained from (12.67) by a backward substitution starting from the known value* $X_n = \gamma_n$*.*

We now note that a periodic tridiagonal matrix has supplementary nonzero coefficients in the upper-right and lower-left corners. The idea of the following algorithm is to eliminate these *intruders* and to work with tridiagonal systems.

Algorithm 12.6. *Thomas algorithm for tridiagonal, periodic systems. The system*

$$\left(\begin{array}{ccccccc} b_1 & c_1 & 0 & . & 0 & 0 & |a_1 \\ a_2 & b_2 & c_2 & . & 0 & 0 & |0 \\ . & . & . & . & . & . & |0 \\ . & . & . & . & . & . & |0 \\ 0 & 0 & 0 & . & a_{n-1} & b_{n-1} & |c_{n-1} \\ -- & -- & -- & -- & -- & -- & -- \\ c_n & 0 & 0 & . & 0 & a_n & |b_n \end{array}\right) \begin{pmatrix} X_1 \\ X_2 \\ . \\ . \\ X_{n-1} \\ -- \\ X_n \end{pmatrix} = \begin{pmatrix} f_1 \\ f_2 \\ . \\ . \\ f_{n-1} \\ -- \\ f_n \end{pmatrix}$$

is reexpressed as[14]

[14] This decomposition is similar to the Shermann–Morrison formula.

$$\left(\begin{array}{ccccccc|c} b_1^* & c_1 & 0 & . & 0 & 0 & 0 & v_1 \\ a_2 & b_2 & c_2 & . & 0 & 0 & 0 & 0 \\ . & . & . & . & . & . & . & 0 \\ . & . & . & . & . & . & . & 0 \\ 0 & 0 & 0 & . & a_{n-1} & b_{n-1} & c_{n-1} & 0 \\ 0 & 0 & 0 & . & 0 & a_n & b_n^* & v_n \\ -- & -- & -- & -- & -- & -- & -- & -- \\ -1 & 0 & 0 & . & 0 & 0 & -1 & 1 \end{array}\right) \left(\begin{array}{c} X_1 \\ X_2 \\ . \\ . \\ X_{n-1} \\ X_n \\ -- \\ X^* \end{array}\right) = \left(\begin{array}{c} f_1 \\ f_2 \\ . \\ . \\ f_{n-1} \\ f_n \\ -- \\ 0 \end{array}\right), \quad (12.68)$$

where

$$\begin{cases} v_1 = a_1, \\ v_n = c_n, \\ b_1^* = b_1 - a_1, \\ b_n^* = b_n - c_n, \end{cases} \qquad \textit{and} \qquad X^* = X_1 + X_n.$$

An equivalent form of (12.68) is

$$\underbrace{\left(\begin{array}{cccccc} b_1^* & c_1 & 0 & . & 0 & 0 \\ a_2 & b_2 & c_2 & 0 & . & 0 \\ . & . & . & . & . & . \\ 0 & 0 & 0 & 0 & . & a_n \end{array}\right.}_{M^*} \left.\begin{array}{c} 0 \\ 0 \\ . \\ b_n^* \end{array}\right) \left(\begin{array}{c} X_1 \\ X_2 \\ . \\ X_n \end{array}\right) + \left(\begin{array}{c} v_1 \\ 0 \\ . \\ v_n \end{array}\right) X^* = \left(\begin{array}{c} f_1 \\ f_2 \\ . \\ f_n \end{array}\right)$$

together with

$$X^* = X_1 + X_n.$$

We now seek a solution of the form

$$X_k = X_k^{(1)} - X_k^{(2)} \cdot X^*, \quad k = 1, \ldots, n, \tag{12.69}$$

with the vectors $X^{(1)}$ and $X^{(2)}$ solutions of two tridiagonal systems of size n:

$$\begin{cases} M^* \cdot X^{(1)} = (f_1\, f_2\, \ldots\, f_{n-1}\, f_n)^T, \\ M^* \cdot X^{(2)} = (v_1\, 0\, \ldots\, 0\, v_n)^T. \end{cases} \tag{12.70}$$

Finally, the supplementary unknown is calculated as

$$X^* = \frac{X_1^{(1)} + X_n^{(1)}}{1 + X_1^{(2)} + X_n^{(2)}}. \tag{12.71}$$

To summarize, the algorithm consists of the following steps:

- *solve the two tridiagonal systems (12.70) using the Thomas algorithm 12.5; note that the program for this step can be optimized since both systems share the same matrix M^*;*
- *compute X^* from (12.71);*
- *compute the final solution using (12.69).*

Exercise 12.1. Write a MATLAB function

```
function fi=NSE_trid_per_c2D(aa,ab,ac,fi)
```

that solves simultaneously m systems with tridiagonal, periodic matrices. Algorithm 12.6 is used to solve each system j (for $1 \leq j \leq m$) defined as follows:

```
for i=1,...,n
  aa(j,i)*X(j,i-1)+ab(j,i)*X(j,i)+ac(j,i)*X(j,i+1)=fi(j,i),
with periodicity condition X(j,1)=X(j,n).
```

Hint: use vectorial programming to apply the relations of the algorithm simultaneously to all m systems; for example, the program lines computing the coefficients b_1^*, b_n^* of the matrix M^* from (12.68) are written as

```
ab(:,1)=ab(:,1)-aa(:,1);
ab(:,n)=ab(:,n)-ac(:,n);
```

which implies that the computation is done for all j (row) indices.

Test this function using as model the MATLAB script *NSE_test_trid.m.*[15]

12.8.2 Solving the Unsteady Heat Equation

Study of the 2D unsteady heat equation provides the ideal framework for testing the procedures that will constitute the core of this project: the Helmholtz and Poisson solvers. We consider the unsteady heat equation (see Chap. 1 for the 1D equation)

$$\frac{\partial u}{\partial t} - \Delta u(t,x,y) = f(x,y), \quad \text{for} \quad (x,y) \in \Omega = [0, L_x] \times [0, L_y], \tag{12.72}$$

with periodic boundary conditions and initial condition $u(0,x,y) = u^0(x,y)$. This equation will be numerically integrated in time until a steady (equilibrium) solution is reached. This solution satisfies

$$-\Delta u_s(x,y) = f(x,y), \quad \text{for} \quad (x,y) \in [0, L_x] \times [0, L_y], \tag{12.73}$$

with the same periodic boundary conditions. The steady solution $u_s(x,y)$ may be interpreted as the limit for $t \to \infty$ of the unsteady solution $u(t,x,y)$.

[15] Although this script is intended to be straightforward, some comments may be helpful: the (diagonal) vectors `aa,ab,ac` are filled with random values; for each j, the matrix A of the system is reconstructed and transformed into a *diagonal dominant* matrix that is known to be invertible; the right-hand side of the system is computed as $f = A * \tilde{X}$, where $\tilde{X}$ is arbitrarily fixed; every system is solved using the MATLAB syntax $X = A \backslash f$; the function `NSE_trid_per_c2D` is validated if the returned solution is exactly $\tilde{X}$. This is a commonly used technique to test programs that solve linear systems.

We adopt in this section the following procedure to test the programs. We set the right-hand-side function

$$f(x,y) = (a^2+b^2)\sin(ax)\cos(by), \quad \text{where} \quad a = \frac{2\pi}{L_x},\ b = \frac{2\pi}{L_y}, \tag{12.74}$$

which satisfies the periodicity along x and y. For this choice, the exact solution of (12.73) is

$$u_{ex}(x,y) = \sin(ax)\cos(by). \tag{12.75}$$

Indeed, it is obvious that f was chosen such that $f(x,y) = -\Delta u_{ex}$. Using $f(x,y)$ as input data in the programs, we get a numerical solution that has to fit the exact (analytical) solution. If this is not the case, debugging is necessary!

Explicit Solver

The simplest method to solve (12.72) is based on the explicit Euler scheme (see Chap. 1)

$$u^{n+1} = u^n + \delta t\,(f + \Delta u^n)\,. \tag{12.76}$$

Assuming that the solution is computed at grid points (x_c, y_m) (see Fig. 12.1), the discrete form of the scheme becomes ($i = 1,\ldots,n_{xm}, j = 1,\ldots,n_{ym}$):

$$u^{n+1}(i,j) = u^n(i,j) + \delta t\left[f(i,j) + \frac{u(ip(i),j) - 2u(i,j) + u(im(i),j)}{\delta x^2} + \frac{u(i,jp(j)) - 2u(i,j) + u(i,jm(j))}{\delta y^2}\right]. \tag{12.77}$$

The time integration starts from the initial condition $u^0 = 0$ and stops when the convergence to a steady solution is reached. We impose the following numerical convergence criterion:

$$\varepsilon = \|u^{n+1} - u^n\|_2 < 10^{-6}, \tag{12.78}$$

where the norm is defined as $\|\varphi\|_2 = \left(\int_\Omega \varphi^2\,dx\,dy\right)^{1/2}$.

The drawback of this scheme in computing steady solutions is that the time step value is limited by a stability (CFL) condition. For the 2D heat equation, the CFL condition is expressed as (see, for instance, Hirsch (1988)):

$$\delta t\left(\frac{1}{\delta x^2} + \frac{1}{\delta y^2}\right) = \frac{\text{cfl}}{2}, \quad \text{cfl} \le 1. \tag{12.79}$$

Exercise 12.2. Compute the solution of the unsteady heat equation (12.72) using the explicit scheme (12.77). Compare the obtained steady solution to the exact solution (12.75). Use the following input parameters: $L_x = 1, L_y = 2$, $n_x = 21, n_y = 51, \text{cfl} = 1$. Hints:

• the grid parameters may be defined as global variables;
• write modular programs with specialized functions that can be reused for subsequent applications; for example, write separate functions to compute f, Δu^n, to plot the solution, etc.;
• use a `while` loop for the time advancement, which allows one to easily implement the convergence criterion;
• avoid `for` loops and use vectorial programming, more compact and easier to compare with mathematical relations; for example, the following function computes the discrete values of the Laplacian Δu^n using directly the array u (of size $n_{xm} \times n_{ym}$) and the vectors ip, jp, im, jm defined by (12.28) and (12.29):

```
function hc=NSE_calc_lap(u)
global dx dy
global im ip jp jm ic jc
hc =...
(u(ip,jc)-2*u+u(im,jc))/(dx*dx)+(u(ic,jp)-2*u+u(ic,jm))/(dy*dy);
```

• plot in the same figure the isocontours of the numerical steady solution and the exact solution (12.75).
A solution of this exercise is proposed in Sect. 12.9 at page 277.

Figure 12.4 displays a typical result for the isocontours of the steady solution. Note that the numerical and exact solutions are difficult to distinguish in the plot (a more quantitative comparison can be made by computing $\|u - u_{ex}\|_2$). The slow convergence to the steady solution is also illustrated in the same figure. We conclude that the explicit solver is easy to implement but requires small time steps and, consequently, large computational times. This suggests that an implicit solver able to take larger time steps is more appropriate for this problem.

Implicit Solver

We use the combined Adams–Bashforth and Crank–Nicolson schemes described previously to discretize (12.72)

$$\frac{u^{n+1}-u^n}{\delta t} = \underbrace{\frac{3}{2}\mathcal{H}^n - \frac{1}{2}\mathcal{H}^{n-1}}_{\text{Adams–Bashforth}} + \underbrace{\frac{1}{2}\Delta\left(u^{n+1}+u^n\right)}_{\text{Crank–Nicolson}}, \tag{12.80}$$

where in this case, the term $\mathcal{H}^n = \mathcal{H}^{n-1} = f(x, y)$ does not depend on time. We finally get the Helmholtz equation

$$\left(I - \frac{\delta t}{2}\,\Delta\right)\delta u = \delta t\,(f + \Delta u^n), \quad \text{with} \quad \delta u = u^{n+1} - u^n, \tag{12.81}$$

which is solved using the ADI method with the following steps:

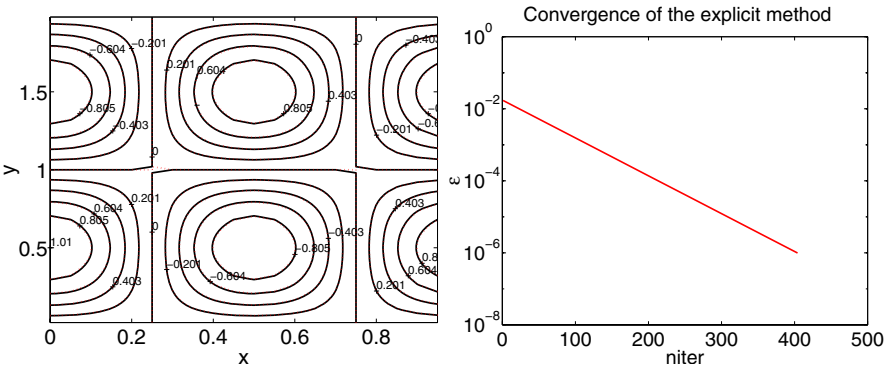

Fig. 12.4. Test of the explicit solver for the unsteady heat equation. Superposition of isocontours of the steady numerical and exact solutions (left) and convergence history (right) for $\varepsilon = \|u^{n+1} - u^n\|_2$.

$$\begin{cases} \left(I - \dfrac{\delta t}{2}\dfrac{\partial^2}{\partial x^2}\right)\overline{\delta u} = \delta t\,(f + \Delta u^n) + \text{periodicity along } x, \\ \left(I - \dfrac{\delta t}{2}\dfrac{\partial^2}{\partial y^2}\right)\delta u = \overline{\delta u} \qquad\qquad + \text{periodicity along } y. \end{cases} \tag{12.82}$$

Using second-order centered finite differences to discretize second derivatives, we obtain two linear systems with tridiagonal, periodic matrices. These systems are solved using the function `NSE_trid_per_c2D` written for the previous exercise.

Remark 12.2. The semi-implicit solver defined in this section is unconditionally stable, allowing arbitrarily large time steps δt. Compared to the explicit solver, it requires much less computational time to reach the steady solution (more work per time step but very few time steps to converge).

Exercise 12.3. Resume Exercise 12.2 and implement the implicit solver. The time step will be computed using (12.79) taking cfl = 100. Evaluate the necessary computing time to reach the steady solution and compare to the explicit solver. Hint: noticing that the coefficients of the matrices involved in the ADI steps are constant in time, optimize the function `NSE_trid_per_c2D` by:
• storing the coefficients of the matrices in vectors and not in two-dimensional arrays;
• computing all the quantities not depending on the right-hand side only once, before the `while` loop.
A solution of this exercise is proposed in Sect. 12.9 at page 277.

Exercise 12.4. Consider now the following nonlinear convection–diffusion equation:

$$\frac{\partial u}{\partial t} + \frac{\partial u^2}{\partial x} - \Delta u = f(x,y), \quad \text{for} \quad (x,y) \in [0, L_x] \times [0, L_y], \tag{12.83}$$

with periodic boundary conditions and initial condition $u^0(x, y) = 0$.

1. Choose the analytical form of the right-hand-side function $f(x, y)$ such that (12.75) is the steady solution of (12.83).
2. Use the implicit scheme (12.80) to solve this equation. Compare the results to the exact solution. Hint: use the previous program and modify only the function computing $\mathcal{H}$ (be careful, for this equation $\mathcal{H}$ varies in time, and consequently, $\mathcal{H}^n \neq \mathcal{H}^{n-1}$).
3. The time step is considered as constant and given by (12.79). Find the stability limit ($\text{cfl}_{\max}$) for a given space discretization.

A solution of this exercise is proposed in Sect. 12.9 at page 278.

12.8.3 Solving the Steady Heat Equation Using FFTs

We now write and test the necessary functions for solving the Poisson equation (Algorithm 12.4). We use as a test case the heat equation (12.73).

Exercise 12.5. 1. Solve the steady heat equation (12.73) with the right-hand side (12.74) using the Poisson solver described in Sect. 12.5 (i.e., FFT along x and finite differences along y). Compare to the exact solution.[16] Input parameters: $L_x = 1, L_y = 2, n_x = 65, n_y = 129$.
2. Optimize (see Exercise 12.3) the function solving the tridiagonal system.
3. Solve numerically the same equation using two FFTs.

A solution of this exercise is proposed in Sect. 12.9 at page 278.

12.8.4 Solving the 2D Navier–Stokes Equations

We are now ready to assemble all the modules previously developed to solve the Navier–Stokes equations and simulate the flows described in Sect. 12.7.

Exercise 12.6. Write a Navier–Stokes solver for two-dimensional periodic flows.
Hints for the structure of the program:

- define the global variables,
- set the input parameters,
- build the 2D grid and related arrays,
- define the arrays to store the flow variables and initialize them to zero,
- set the initial condition corresponding to the simulated flow (see below the parameters for the suggested run cases),
- visualize the initial field,

[16] As we have already seen, the numerical solution u_{num} is computed up to an additive constant. To compare to the exact solution u_{ex}, we have to calculate this constant by imposing that the two solutions be identical at a chosen point ($i = j = 1$, for example). We then compare u_{ex} to $u_{\text{num}} + (u_{ex}(1, 1) - u_{\text{num}}(1, 1))$.

- compute the time step,
- compute the variables for the optimization of the ADI method and Poisson solver (i.e., all variables or coefficients not depending on time),
- start the time loop:
  - solve the momentum equation for u,
  - solve the momentum equation for v,
  - compute the divergence of the nonsolenoidal field,
  - solve the Poisson equation,
  - correct the velocity field,
  - compute the pressure,
  - update the pressure gradient for the next step,
  - solve the equation for the passive scalar,
  - check that the divergence of the velocity field is zero,
  - visualize the flow field by plotting the isocontours of vorticity and passive scalar.
- end of the time loop.

A solution of this exercise is proposed in Sect. 12.9 at page 278.

Run cases. The expected results are illustrated in the figures at the end of the chapter.

1. 2D jet: Kelvin–Helmholtz instability; input parameters

$$L_z = 2, L_y = 1, n_x = 65, n_y = 65, \text{cfl} = 0.2,$$

$$Re = 1000, Pe = 1000, U_0 = 1, P_j = 20, R_j = L_y/4, A_x = 0.5, \lambda_x = 0.5L_x.$$

   The initial field for the passive scalar is identical to the field of u.
2. Same configuration, but changing $\text{cfl} = 0.1, \lambda_x = 0.25L_x$.
3. Vortex dipole:

$$L_z = 1, L_y = 1, n_x = 65, n_y = 65, \text{cfl} = 0.4, Re = 1000, Pe = 1000;$$

   vortex 1:

$$\psi_0 = +0.01, x_v = L_x/4, y_v = L_y/2 + 0.05,$$
$$l_v = 0.4\sqrt{2}\min\{x_v, y_v, L_x - x_v, L_y - y_v\};$$

   vortex 2:

$$\psi_0 = -0.01, x_v = L_x/4, y_v = L_y/2 - 0.05,$$
$$l_v = 0.4\sqrt{2}\min\{x_v, y_v, L_x - x_v, L_y - y_v\}.$$

   The initial field for the passive scalar is set to a large stripe, placed in the middle of the computational domain. For example, take

$$\begin{cases} \chi(i,j) = 1, \text{ if } n_{xm}/2 - 10 \le i \le n_{xm}/2 + 10, \\ \chi(i,j) = 0, \text{ otherwise.} \end{cases}$$

4. Add to the previous configuration a second dipole propagating in the opposite direction.
5. Imagine other flow configurations with several dipoles in the computational domain.

12.9 Solutions and Programs

The MATLAB scripts for this project are organized in two directories:

- **NSE_QP** containing the solution scripts for all preliminary questions (Exercises 12.1 to 12.5),
- **NSE_QNS** containing the Navier–Stokes solver (Exercise 12.6).

There is also a third directory named **NSE_INTERFACE** in which a different programming philosophy is illustrated. All the solution scripts of the project are called from a graphical user interface (GUI) and the results are displayed interactively. A supplementary Navier–Stokes run case is computed in this version. To launch the interface, just run the script *Main* from the subdirectory **Tutorial**.

Solution of Exercise 12.1 (Solving a Tridiagonal, Periodic System)

The MATLAB script *NSE_trid_per_c2D.m* contains the function that solves simultaneously m linear systems with tridiagonal, periodic matrices of size n. Numerous comments in the script are intended to guide the reader through the steps of Algorithm 12.6. Memory storage was optimized using a minimum number of arrays for computing intermediate coefficients. Note also the vectorial programming of the algorithm.
We recall that this function is called (and tested) by the script *NSE_test_trid.m*.

Solution of Exercise 12.2 (Explicit Solver for the Unsteady Heat Equation)

The script *NSE_Qexp_lap.m* is straightforward to read and execute. Nevertheless, it is useful to indicate the specialized functions called by this program:

- `NSE_calc_lap`: computes the Laplacian Δu;
- `NSE_fsource`: computes the right-hand term (or source term) f;
- `NSE_fexact`: computes the exact solution;
- `NSE_norm_L2`: computes the norm $\|u\|_2$;
- `NSE_visu_isos`: plots in the same figure the isocontours of the numerical and exact solutions.

Solution of Exercise 12.3 (Implicit Solver for the Unsteady Heat Equation)

The script *NSE_Qimp_lap.m* inherits the structure of the program implementing the explicit solver. Since the implicit method requires to solve tridiagonal, periodic systems, two functions optimizing this part were added: `NSE_ADI_init` and `NSE_ADI_step`. The optimization starts from the observation that in the general solver `NSE_trid_per_c2D` all the computations not

depending on the right-hand side `fi` can be done only once, outside the time loop. This is the role of the function `NSE_ADI_init`, returning the vectors `ami, api, alph, xs2`, which do not change during the time integration; these vectors are used in `NSE_ADI_step` (called inside the time loop) to compute the solution of the linear system for a given (time-dependent) vector `fi`.

Solution of Exercise 12.4 (Implicit Solver for the Nonlinear Convection–Diffusion Equation)

The script solution *NSE_Qimp_lap_nonl.m* for the nonlinear problem inherits the structure of the previous program (*NSE_Qimp_lap.m*). The only difference is the computation of the term $\mathcal{H}$ for every time step by calling inside the time loop the function `NSE_calc_hc` (file *NSE_calc_hc.m*). It goes without saying that the expression of the source term f was modified in *NSE_fsource_nonl.m* to take into account the new nonlinear term in the equation.

Solution of Exercise 12.5 (Solving the Steady Heat Equation Using FFTs)

Algorithm 12.4 is implemented in the script *NSE_Qfft_lap.m*. The script solving a tridiagonal system is optimized by splitting the algorithm into two parts, corresponding to the functions `NSE_Phi_init` and `NSE_Phi_step`. This is similar to the optimization of the ADI method, with the difference that this time the coefficients of the matrix change from one system to another (because of the dependence on the wave number), and consequently, they are stored in two-dimensional arrays. The script *NSE_Q2fft_lap.m* solves the same problem using two FFTs (along the x and y directions).

Solution of Exercise 12.6 (Solving the 2D Navier–Stokes Equations)

The main program *NSE_QNS.m* allows one to choose between the four suggested run cases. Comments in the program body identify each step of the numerical algorithm. The program calls the main functions written for the preliminary questions (`NSE_ADI_init`, `NSE_ADI_step`, `NSE_Phi_init`, `NSE_Phi_step`) and the following specific functions:

- `NSE_init_KH`: initializes the flow field for the Kelvin–Helmholtz (2D jet) run cases;
- `NSE_init_vortex` builds the flow field corresponding to an individual vortex; the vortex dipoles are obtained by superimposing the individual vortex fields;
- `NSE_visu_vort` visualizes the vorticity field (color images of isocontours);
- `NSE_visu_sca` visualizes the passive tracer leading to images similar to experimental ones;

- `NSE_print_div` prints the divergence of the velocity field to verify whether the computation is stable. The divergence must be close to the *machine zero* value, which is 10^{-15} for double-precision computations; if this is not the case, run the same computation with smaller time steps.

It is beyond the scope of this project, which focuses essentially on numerics, to get into a detailed physical description of the simulated flows. We discuss, however, some interesting physical features illustrated in the following figures.

The evolution of the Kelvin–Helmholtz instability is shown in Figs. 12.5 and 12.6. The Kelvin *cat eyes* vortices form progressively in the two shear regions of the jet; their spatial distribution is dictated by the wavelength (λ_x) of the initial perturbation. At this point, one might question whether a periodic simulation could be realistic. Since in real jet flows the instability progressively grows downstream of the injection point, our periodic computational box may be regarded as a fixed frame that zooms in the shear layer region while traveling downstream with the mean velocity of the flow. Periodic simulations offer useful information on the evolution of vortical structures in jet or shear-layer flows that fit very well to experimental results. The reader who wishes to pursue this study further could attempt to simulate the next stage of the Kelvin–Helmholtz instability, which consists in the pairing of neighboring vortices.

The first vortex dipole run case is illustrated in Fig. 12.7. The dipole effectively propagates along the horizontal axis towards the right boundary; it could be interesting to continue the simulation and see how the periodicity makes the dipole reenter the computational box from the left. The velocity induced by the dipole triggers the movement of the passive scalar (initially at rest), with a nice mushroom pattern forming. This kind of structures has been reported in studies of flow dynamics in oceanography, meteorology, and combustion.

The last run case (see Fig. 12.8) shows the head-on interaction between two dipoles of the same intensity. The result is the *partner interchange* with the formation of two new dipoles propagating in the perpendicular direction. The simulation may be performed for larger values of the final integration time to see a second collision (due to the periodicity, a dipole leaving the domain reenters through the opposite boundary). The reader may wonder whether this is a never-ending evolution!

Other interesting run cases could be imagined and simulated with this Navier–Stokes solver. We refer to many existing fluid mechanics books as an obvious source of inspiration.

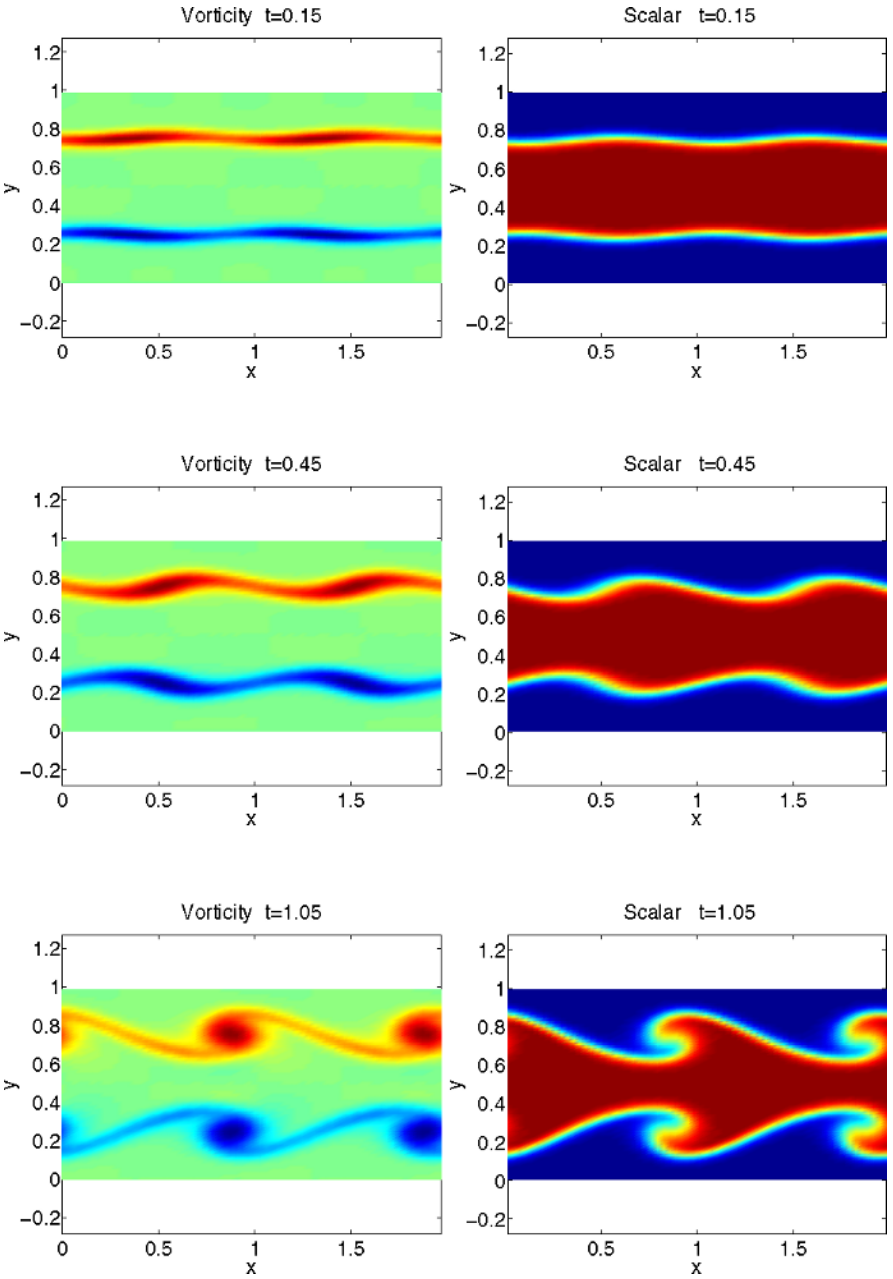

Fig. 12.5. Run case 1. Evolution of the Kelvin–Helmholtz instability for the perturbation wavelength $\lambda_x/L_x = 0.5$.

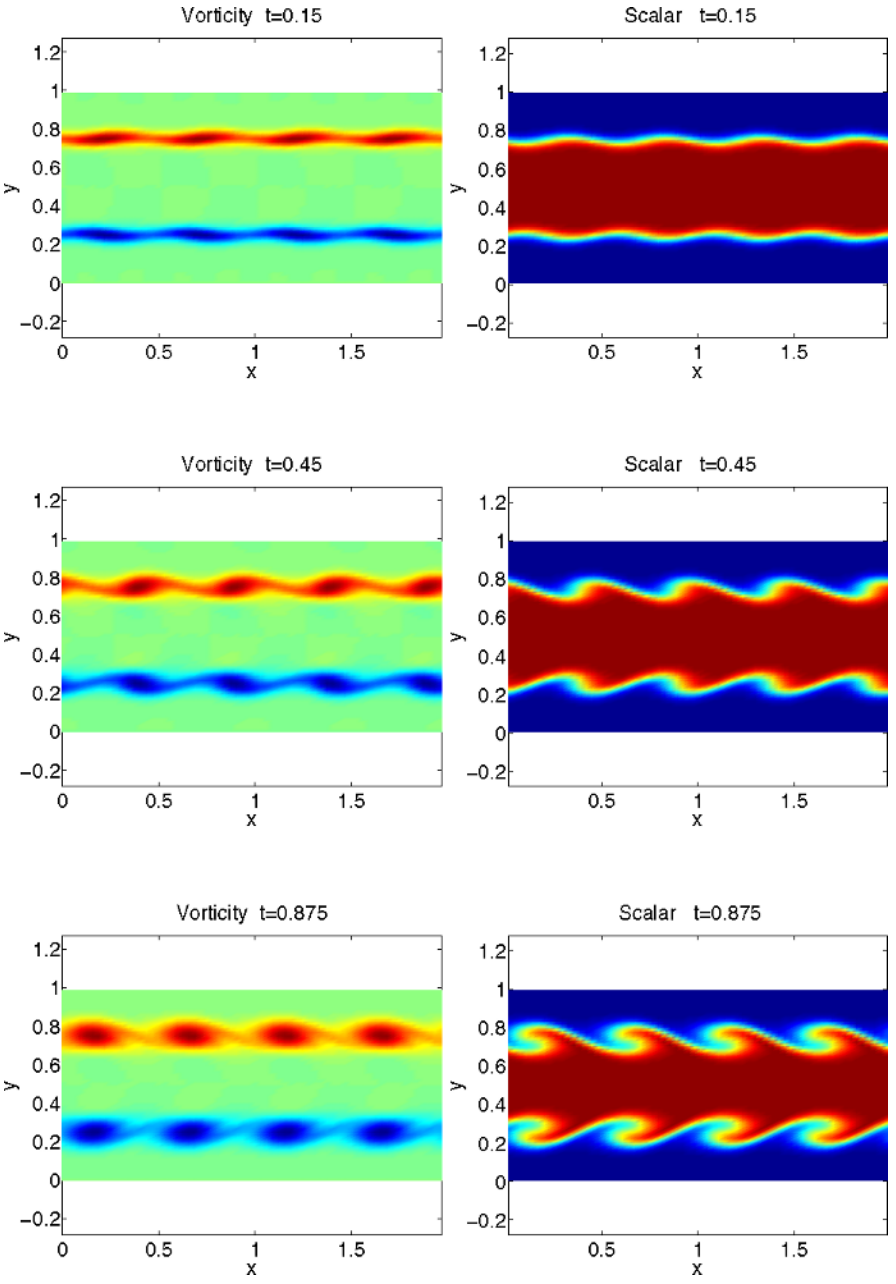

Fig. 12.6. Run case 1. Evolution of the Kelvin–Helmholtz instability for the perturbation wavelength $\lambda_x/L_x = 0.25$.

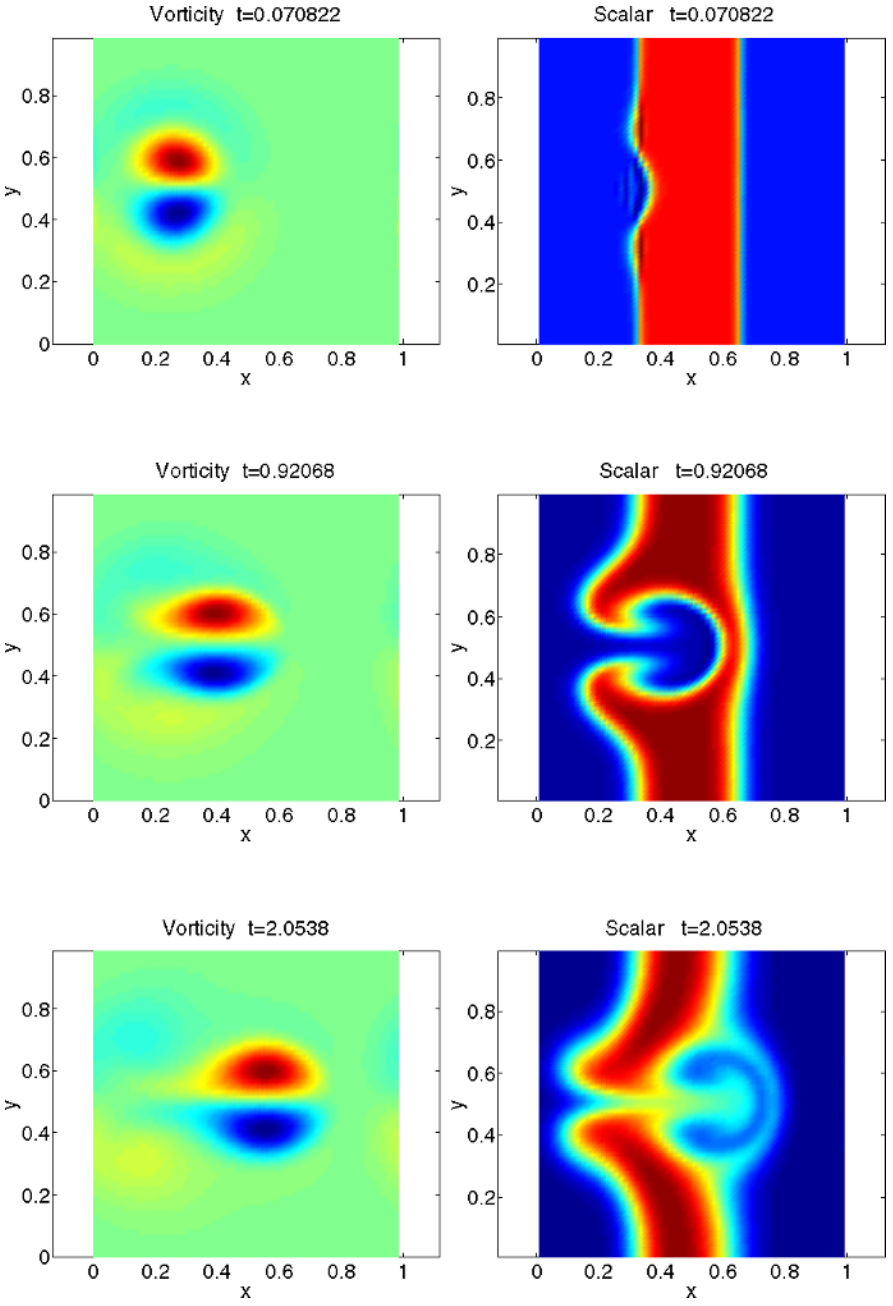

Fig. 12.7. Run case 3. Evolution of a vortex dipole.

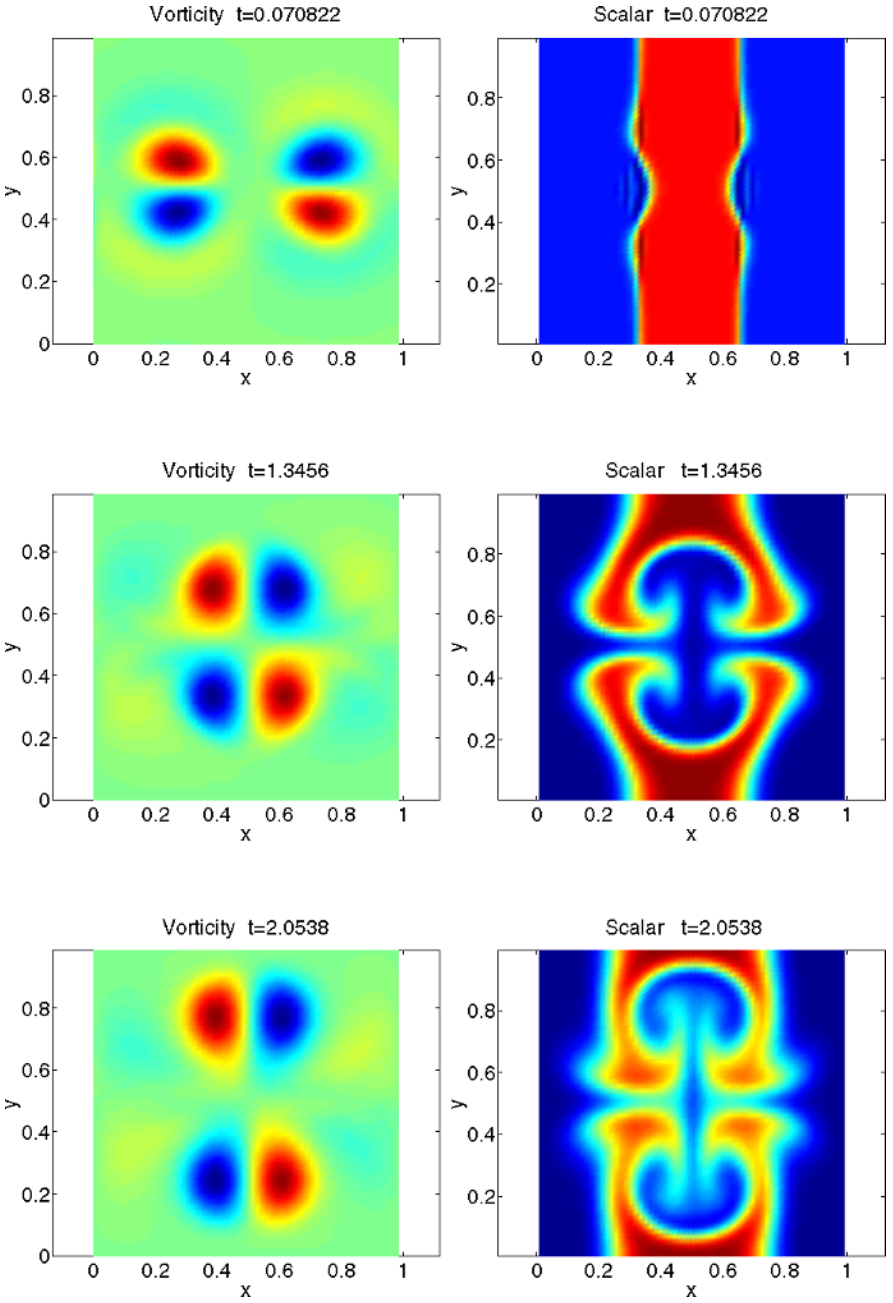

Fig. 12.8. Run case 4. Head-on collision of two identical vortex dipoles.

Chapter References

G. K. Batchelor, *An Introduction to Fluid Dynamics*, Cambridge University Press, 1988.

J. H. Ferziger and M. Perić, *Computational Methods for Fluid Dynamics*, Springer, 2002.

C. Hirsch, *Numerical Computation of Internal and External Flows*, John Wiley & Sons, 1988.

J. Kim and P. Moin, *Application of a Fractional Step Method to Incompressible Navier–Stokes Equations*, Journal of Computational Physics, **59**, p. 308, 1985.

P. Orlandi, *Fluid Flow Phenomena*, Kluwer Academic Publishers, 1999.

P. G. Saffman, *Vortex Dynamics*, Cambridge University Press, 1992.

M. Van Dyke, *An Album of Fluid Motion*, The Parabolic Press, 1982.

Bibliography

General references for all chapters

G. Allaire and S.M. Kaber, *Numerical Linear Algebra*, Springer, New York, forthcoming, 2007.

K. Atkinson and W. Han, *Theoretical Numerical Analysis*, Springer, New York, 2001.

G. K. Batchelor, *An Introduction to Fluid Dynamics*, Cambridge University Press, 1988.

A. Bellen and M. Zennaro, *Numerical Methods for Delay Differential Equations*, Numerical Mathematics and Scientific Computation. The Clarendon Press, Oxford University Press, New York, 2003.

C. Bernardi, M. Dauge, and Y. Maday, *Spectral Methods for Axisymmetric Domains. Numerical Algorithms and Tests Due to Mejdi Azaiez*, Series in Applied Mathematics, 3. Gauthier-Villars, North-Holland, Amsterdam, 1999.

C. Bernardi and Y. Maday, *Spectral Methods* in Handbook of numerical analysis, vol. V, North-Holland, Amsterdam, 1997.

C. Bernardi, Y. Maday, and F. Rapetti, *Discrétisations variationnelles de problèmes aux limites elliptiques, collection S.M.A.I. Mathématiques et Applications*, vol. 45, Springer, Paris, 2004.

P. Bézier, *Courbes et surfaces*, Mathématiques et CAO, vol 4, Hermes. Paris, 1986.

F. Brezzi and A. Russo, *Choosing Bubbles for Advection–Diffusion Problems.*, Math. Models and Meth. in Appl. Sci., vol. 4, no. 4, 1994.

J. C. Butcher, *The Numerical Analysis of Ordinary Differential Equations*, Wiley, 1987.

P. de Casteljau, *Formes à pôles*, Mathématiques et CAO, vol 2, Hermes, Paris, 1985.

P. G. Ciarlet, *The Finite Element Method for Elliptic Problems*, North Holland, Amsterdam, 1978.

P. G. Ciarlet, *Mathematical Elasticity, Volumes I, II, III*, North Holland. Amsterdam, 2000.

A. Cohen, *Wavelet Methods in Numerical Analysis*, Handbook of Numerical Analysis, vol. VII, P.G. Ciarlet and J.L. Lions eds., Elsevier, Amsterdam, 2000.

A. Cohen, *Numerical Analysis of Wavelet Methods*, North-Holland, Amsterdam, 2003.

A. Cohen and R. Ryan, *Wavelets and Multiscale Signal Processing*, Chapman and Hall, London, 1995.

S. A. Coons, *Surface Patches and B-Splines Curves*, CAGD, 1974.

M. Crouzeix and A. Mignot, *Analyse numérique des équations différentielles*, Masson, Paris, 1989.

I. Danaila, F. Hecht, and O. Pironneau, *Simulation numérique en C++*, Dunod, Paris, 2003.

I. Daubechies, *Ten Lectures on Wavelets*, Society for Industrial and Applied Mathematics. Philadelphia. Pennsylvania, 1992.

P. J. Davis, *Interpolation and Approximation*, Dover Publications, Inc., New York, 1975.

S. Delabrière and M. Postel, *Méthodes d'approximation, Equations différentielles, Applications Scilab*, Ellipses, Paris, 2004.

J. P. Demailly, *Analyse numérique et équations différentielles*, Presses Universitaires de Grenoble, 1996.

R. A. DeVore and G. G. Lorentz, *Constructive Approximation*, Springer-Verlag, Berlin, 1993.

G. Farin, *Curves and Surfaces for CAGD : A Practical Guide*, Academic Press, 4th ed., New York, 1996.

G. Farin and D. Hansford, *The Essentials of CAGD*, AK Peters, 2000.

J. Ferguson, *Multivariable Curve Interpolation*, Journal of the Association for Computing Machinery, 1964.

J. H. Ferziger and M. Perić, *Computational Methods for Fluid Dynamics*, Springer, 2002.

C. A. J. Fletcher, *Computational Techniques for Fluid Dynamics*, Springer-Verlag, 1991.

E. Godlewski and P.-A. Raviart, *Numerical Approximation of Hyperbolic Systems of Conservation Laws*, Springer-Verlag, 1996.

E. Hairer, S. P. Norsett, and G. Wanner, *Solving Ordinary Differential Equations I, Nonstiff Problems*, Springer Series in Computational Mathematics, 8, Springer-Verlag, 1987.

C. Hirsch, *Numerical Computation of Internal and External Flows*, John Wiley & Sons, 1988.

J. Hoschek and D. Lasser, *Fundamentals of Computer Aided Geometric Design*, Peters. Massachusetts, 1997.

A. Iserles, *A First Course in the Numerical Analysis of Differential Equations*, Cambridge Texts in Applied Mathematics. Cambridge University Press, Cambridge, 1996.

P. Joly, *Mise en œuvre de la méthode des éléments finis, collection S.M.A.I. Mathématiques et Applications*, Ellipses, Paris, 1990.

F. John, *Partial Differential Equations*, Springer-Verlag, 1978.

J. Kim and P. Moin, *Application of a Fractional Step Method to Incompressible Navier–Stokes Equations*, Journal of Computational Physics, **59**, p. 308, 1985.

A. R. Krommer and C. W. Ueberhuber, *Numerical Integration on Advanced Computer Systems*. Lecture Notes in Computer Science, 848. Springer-Verlag, Berlin, 1994.

J. D. Lambert, *Computational Methods in Ordinary Differential Equations*, Wiley, 1973.
R. LeVeque, *Numerical Methods for Conservation Laws*, Birkhäuser, 1992.
P. L. Lions, *On the alternating Schwarz method I* . In R. Gowinski, G. H. Golub, G. A. Meurant and J. Périaux, editors. First International Symposium on Domain Decomposition Methods for Partial Differential Equations, pp. 1–42, SIAM, Philadelphia, 1988.
B. Lucquin, *Équations aux dérivées partielles et leurs approximations*, Ellipses, Paris, 2004.
B. Lucquin and O. Pironneau, *Introduction to Scientific Computing*, Willey, Chichester, 1998.
S. G. Mallat, *A Wavelet Tour of Signal Processing*, Academic Press, New York, 1997.
Y. Meyer, *Ondelettes et opérateurs. Tomes I à III*, Hermann, Paris, 1990.
A. R. Mitchell and D. F. Griffiths, *Computational Methods in Partial Differential Equations*, Wiley, 1980.
B. Mohammadi and J.-H. Saïac, *Pratique de la simulation numérique*, Dunod, 2003.
D. N. Norrie and G. de Vries, *The Finite Element Method*, Academic Press, New York, 1973.
P. Orlandi, *Fluid Flow Phenomena*, Kluwer Academic Publishers, 1999.
L. Piegl and W. Tiller, *The NURBS Book*, Springer, Berlin, 1995.
A. Quarteroni and A. Valli, *Domain Decomposition Methods for Partial Differential Equations*, Numerical Mathematics and Scientific Computation, The Clarendon Press, Oxford University Press, New York, 1999.
R. D. Richtmyer and K. W. Morton, *Difference Methods for Initial-Value Problems*, 2nd ed., Wiley-Interscience, 1967.
T. J. Rivlin, *An Introduction to the Approximation of Functions*, Dover Publications Inc., New York, 1981.
M. Saad, *Compressible Fluid Flow*, Pearson Education, 1998.
P. G. Saffman, *Vortex Dynamics*, Cambridge University Press, 1992.
L. Schwartz, *Analyse, topologie générale et analyse fonctionnelle*, Hermann, Paris, 1980.
H. A. Schwarz, *Gesammelte Mathematische Abhandlungen.* Volume 2. Springer, Berlin, 1890. First published in Vierteljahrsschrift Naturforsch. Ges. Zurich, 1870.
B. F. Smith, P. E. Bjørstad, and W. D. Gropp, *Domain Decomposition, Parallel Multilevel Methods for Elliptic Partial Differential Equations*, Cambridge University Press, Cambridge, 1996.
J. C. Strikwerda, *Finite Difference Schemes and Partial Differential Equations*, Wadsworth and Brooks/Cole, 1989.
G. Szegő, *Orthogonal Polynomials*, fourth edition, American Mathematical Society, Colloquium Publications, vol. XXIII. Providence, R.I., 1975.

L. N. Trefethen, *Finite Difference and Spectral Methods for Ordinary and Partial Differential Equations*, unpublished text, available at http//web.comlab.ox.ac.uk/oucl/work/nick.trefethen/pdetext.html, 1996.

L. N. Trefethen and D. Bau III, *Numerical Linear Algebra*, Society for Industrial and Applied Mathematics (SIAM), Philadelphia, 1997.

M. Van Dyke, *An Album of Fluid Motion*, The Parabolic Press, 1982.

B. I. Wohlmuth, *Discretization Methods and Iterative Solvers Based on Domain Decomposition*, Lecture Notes in Computational Science and Engineering, 17, Springer-Verlag, Berlin, 2001.

O. C. Zienkiewicz, *The Finite Element Method in Engineering Science*, McGraw-Hill, London, 1971.

Index

absorption equation, 8
Adams–Bashforth scheme, 7, 252, 253, 273
Adams–Moulton scheme, 7
ADI method, 259, 260, 273
algorithm
  de Casteljau, 200
  divided differences, 54
  Remez, 60
  Thomas, 252, 268
approximation
  best
    Hilbertian, 62
    uniform, 60
  piecewise
    affine, 67
    constant, 66
    cubic, 68

basis
  canonical, 52
  Haar, 131
  Hilbertian, 62
  Lagrange, 52
  Legendre, 112
Bernstein polynomial, 194
best Hilbertian approximation, 62
best uniform approximation, 60
bilaplacian, 155
boundary condition, 120, 241
  Dirichlet, 14, 17, 171, 236
  Fourier, 179, 183, 236
  homogeneous, 14
  inhomogeneous, 171
  Neumann, 179, 183, 236
  periodic, 16, 26, 251, 257
boundary layer, 98
boundary value problem, 85
Brusselator, 33
Bézier
  curve, 193
  patch, 206
  surface, 206

CAGD, 193
CFL condition, 13, 15, 23, 224, 264, 272
characteristic curve, 12, 15, 22, 217, 219
characteristic equation, 38
Chebyshev
  expansion, 79
  points, 55
  polynomial, 55
compressible fluid, 215
condensation, 95
condition number, 52
consistency, 9
contact discontinuity, 214, 220
convection
  equation, 11, 21, 216, 217, 224
  phenomenon, 30
convection-diffusion equation, 265
convergence, 9, 57, 187
  fast, 116
  slow, 116
Crank–Nicolson scheme, 7, 252, 253, 273
critical point, 34, 37

data compression, 133
Daubechies wavelet, 142
de Casteljau algorithm, 200
delayed differential equation, 37
density, 215
differences (divided –), 54
differential equation, 33, 111, 165
diffusion, 17, 18, 226, 254
  numerical, 27
  phenomenon, 29
diffusivity (thermal –), 29
Dirichlet boundary condition, 14, 17, 153, 171, 236
discontinuity, 116

contact, 214, 220
dissipation, 25
artificial, 226
divergence, 45, 252
divided differences, 53, 54
domain decomposition, 166
domain of dependence, 15

elasticity, 152
energy (total –), 215
enthalpy, 215
equioscillatory, 59
erf (error function), 18
Euler
explicit modified scheme, 6, 7
explicit scheme, 5, 7, 20, 39, 46, 272
implicit scheme, 5, 7
system of equations, 215
expansion
Chebyshev, 79
fan, 220
Fourier, 16
Legendre, 62
wave, 214
extrapolation, 49

FEM, 87, 237
FFT, 70, 252, 262
finite difference, 125, 155, 167, 171
backward, 3, 224, 226
centered, 3, 4, 224, 257
forward, 3, 224, 226
finite element, 86, 87, 90, 237
P1, 87
P2, 90
fluid
compressible, 215
incompressible, 251
flux, 215, 229
splitting, 228
formulation (variational –), 86
Fourier
boundary condition, 179, 183, 236
expansion, 16
FFT, 70, 252, 262
series, 261

Galerkin approximation, 117
Gauss quadrature, 113
Gibbs phenomenon, 116
Godunov scheme, 228
gradient, 252
Green formula, 237
grid (computational –), 172, 182, 256

Haar
basis, 131
wavelet, 137
heat
coefficient, 215, 217
equation, 17, 29, 226, 271, 275
steady equation, 171
Helmholtz equation, 252, 255, 258
Hermite, 119
interpolation, 57
polynomial, 58
Heun scheme, 7
Hopf bifurcation, 42
hyperbolic system, 216

ill-conditioned, 56
incompressible fluid, 251, 252
interpolation, 49, 51
Hermite, 57, 58
Lagrange, 51, 57
stability, 56
inverse problem, 244
isentropic flow, 217
isocontours, 274

Jacobian matrix, 35, 38, 216
jet flow, 266
junction
of curves, 197
of patches, 207

Kelvin–Helmholtz instability, 252, 265

Lagrange
basis, 52
interpolation, 51
polynomial, 51, 52
Laplacian, 152, 155, 166, 172, 252
Lax–Wendroff scheme, 223
leapfrog scheme, 5, 7
Lebesgue constant, 56
Legendre
basis, 112
coefficients, 63
expansion, 62, 115
polynomials, 62, 111
series, 62

MacCormack scheme, 223
Mach number, 215
Mallat transform, 141
matrix
exponential, 35
inverse, 233
Jacobian, 216
tridiagonal, 268
tridiagonal periodic, 260, 268, 269, 277
Vandermonde, 64, 70
mesh, 238
mother wavelet, 138
multiresolution analysis, 133
multiscale analysis, 133

Navier–Stokes
equations, 252
fractional-step method, 253
projection method, 253
Neumann boundary condition, 153, 179, 183, 236
normal equations, 65
numerical integration, 113

ODE, 1, 33, 111
orthogonal projection, 63
overlap, 166

P1 finite element, 87
P2 finite element, 90
parametric curve, 36, 43
PDE, 1, 111, 165
Peclet number, 90, 265
periodic
boundary condition, 16, 26, 251, 257
trajectory, 42, 46
phenomenon
Gibbs, 116
Runge, 57
Poisson equation, 252, 255, 261
polygon (control –), 196
polynomial
Bernstein, 194
Hermite, 119
Lagrange, 51, 52
Legendre, 62, 111
of best Hilbertian approximation, 62
of best uniform approximation, 60
projection (orthogonal), 63

quadrature, 50, 86
Gauss, 113
rule, 113
Simpson, 87
trapezoidal, 86

Rankine–Hugoniot, 219
rarefaction wave, 214
regression line, 64
Remez algorithm, 60
Reynolds number, 253
Riemann problem, 217
Roe
approximate solver, 229
average, 230
Runge–Kutta scheme, 7, 20, 37, 40
Runge phenomenon, 57

scaling function, 137
Schauder wavelet, 139, 141
scheme
13-point, 156

5-point, 155, 172
Adams–Bashforth, 7, 253, 273
Adams–Moulton, 7
centered, 19, 222
conservative, 230
Crank–Nicolson, 7, 253, 273
Euler explicit , 7
Euler implicit , 7
explicit, 5, 6, 224, 272
Godunov, 228
Heun, 7
implicit, 5, 6, 273
Lax–Wendroff, 223
leapfrog, 7
MacCormack, 223
Roe, 229
Runge–Kutta, 7
upwind, 13, 23, 25, 224, 227
Schwarz method, 166
series
Chebyshev, 79
Legendre, 62
Taylor, 3
shock
tube, 213
wave, 214, 219
Simpson quadrature, 87
smooth function, 116
Sod shock tube, 221
spectral method, 117
spline, 66
stability, 9, 34, 56
amplification function, 10
CFL condition, 13, 15, 23, 224, 264, 272
region, 10, 20, 26
steady solution, 34
stopping criterion, 169
stream-function, 267
string (vibrating –), 16

Taylor
expansion, 3, 35, 172, 224
formula, 35
thermal
diffusivity, 179
shock, 171
Thomas algorithm, 252, 268, 269
tracer (passive –), 265
trajectory, 42
periodic, 42, 46
trapezoidal quadrature, 86
triangulation, 238
tridiagonal matrix, 167, 173
two-scale relation, 128, 139, 142

upwind scheme, 13, 23, 25, 224, 227

Vandermonde matrix, 64, 70
variational formulation, 86, 237
viscosity
artificial, 226
kinematic, 253
vortex, 264, 267
dipole, 252, 267
vorticity, 264

wave
characteristic, 217, 224
elementary, 16
equation, 14
expansion, 214
number, 16, 262
rarefaction, 214
shock, 214
wavelength, 279
wavelet, 137
Daubechies, 142
Haar, 137
Schauder, 139

Index of Programs

APP_ApproxScript1.m, 70
APP_ApproxScript2.m, 71
APP_ApproxScript3.m, 72
APP_ApproxScript4.m, 73
APP_ApproxScript5.m, 73
APP_ApproxScript8.m, 77
APP_condVanderMonde.m, 71
APP_condVanderMondeBis.m, 71
APP_dd.m, 72
APP_ddHermite.m, 76
APP_equiosc.m, 79
APP_interpol.m, 73
APP_Interpolation.m, 76
APP_Lebesgue.m, 73
APP_ls.m, 80
APP_Remez.m, 79
APP_Runge.m, 76
APP_scriptHermite.m, 77
APP_spline0.m, 81
APP_spline1.m, 82
APP_spline3.m, 82

CAGD_casteljau.m, 210
CAGD_cbezier.m, 210
CAGD_coox.m, 211
CAGD_ex1.m, 210
CAGD_ex1b.m, 210
CAGD_ex1c.m, 210
CAGD_ex2.m, 211
CAGD_pbzier.m, 210
CAGD_tbezier.m, 210

DDM_f1BB.m, 183
DDM_f1CT, 183
DDM_f1Exact.m, 183
DDM_f2CT.m, 183
DDM_f2Exact.m, 183
DDM_FinDif2dDirichlet.m, 183
DDM_FinDif2dFourier.m, 183
DDM_FunSchwarz1d.m, 181
DDM_g1BB.m, 183
DDM_g1CT.m, 183
DDM_g1Exact.m, 183
DDM_g2Exact.m, 183
DDM_LaplaceDirichlet.m, 183
DDM_LaplaceFourier.m, 183
DDM_Perf.m, 187
DDM_rhs1d.m, 181
DDM_rhs2dBB.m, 183
DDM_rhs2dCT.m, 183
DDM_rhs2dExact.m, 183
DDM_RightHandSide2dDirichlet.m, 183
DDM_RightHandSideFourier.m, 183
DDM_Schwarz2dDirichlet.m, 187
DDM_Schwarz2dFourier.m, 190
DDM_TestFinDif2d.m, 183
DDM_TestSchwarz2d.m, 184, 190

ELAS_bilap_matrix.m, 162
ELAS_bilap_rhs.m, 162
ELAS_lap_matrix.m, 162
ELAS_lap_rhs.m, 162
ELAS_plate_ex.m, 162
ELAS_solution.m, 162

FEM_ConvecDiffAP1.m, 101
FEM_ConvecDiffAP2.m, 104
FEM_ConvecDiffbP1.m, 101
FEM_ConvecDiffbP2.m, 104
FEM_ConvecDiffscript1.m, 101
FEM_ConvecDiffscript2.m, 102
FEM_ConvecDiffscript3.m, 102
FEM_ConvecDiffscript4.m, 105
FEM_ConvecDiffscript5.m, 106
FEM_ConvecDiffSolExa.m, 98

HYP_calc_dt.m, 232
HYP_flux_roe.m, 233
HYP_mach_compat.m, 232
HYP_plot_graph.m, 232
HYP_shock_tube.m, 232
HYP_shock_tube_exact.m, 232
HYP_trans_usol_w.m, 232

HYP_trans_w_f.m, 232
HYP_trans_w_usol.m, 232

MRA_daube4.m, 149
MRA_daube4_ex1.m, 149
MRA_daube4_ex2.m, 149
MRA_daube4_ex3.m, 149
MRA_haar.m, 148
MRA_haar_ex1.m, 148
MRA_haar_ex2.m, 148
MRA_haar_ex3.m, 149
MRA_schauder.m, 148
MRA_schauder_ex1.m, 149
MRA_schauder_ex2.m, 149
MRA_schauder_ex3.m, 149

NSE_ADI_init.m, 278
NSE_ADI_step.m, 278
NSE_affiche_div.m, 279
NSE_calc_hc.m, 278
NSE_calc_lap.m, 277
NSE_fexact.m, 277
NSE_fsource.m, 277
NSE_fsource_nonl.m, 278
NSE_init_KH.m, 278
NSE_init_vortex.m, 278
NSE_norm_L2.m, 277
NSE_Phi_init.m, 278
NSE_Phi_step.m, 278
NSE_Q2fft_lap.m, 278
NSE_Qexp_lap.m, 277
NSE_Qfft_lap.m, 278
NSE_Qimp_lap.m, 277
NSE_Qimp_lap_nonl.m, 278
NSE_QNS.m, 278
NSE_test_trid.m, 271, 277
NSE_trid_per_c2D.m, 277
NSE_visu_isos.m, 277
NSE_visu_sca.m, 278
NSE_visu_vort.m, 278

ODE_Chemistry2.m, 42
ODE_Chemistry3.m, 44
ODE_DelayEnzyme.m, 46
ODE_Enzyme.m, 46
ODE_EnzymeCondIni.m, 47
ODE_ErrorEnzyme.m, 47
ODE_EulerDelay.m, 46
ODE_fun2.m, 42
ODE_fun3.m, 44
ODE_RungeKuttaDelay.m, 46
ODE_stab2comp.m, 41
ODE_stab3comp.m, 43
ODE_StabDelay.m, 45

PDE_absorption.m, 20
PDE_absorption_source.m, 20
PDE_conv_bound_cond.m, 24
PDE_conv_exact_sol.m, 23
PDE_conv_init_cond.m, 24
PDE_convection.m, 24
PDE_EulerExp.m, 20
PDE_heat.m, 29
PDE_heat_u0.m, 29
PDE_heat_uex.m, 29
PDE_RKutta4.m, 20
PDE_wave_fstring.m, 28
PDE_wave_fstring_exact.m, 28
PDE_wave_fstring_in.m, 28
PDE_wave_infstring.m, 26
PDE_wave_infstring_u0.m, 26
PDE_wave_infstring_u1.m, 26

SPE_AppLegExp.m, 122
SPE_CalcLegExp, 122
SPE_fbe.m, 122
SPE_LegExpLoop.m, 122
SPE_LegLinComb.m, 120
SPE_PlotLegPol.m, 120
SPE_special.m, 122
SPE_SpecMeth.m, 123
SPE_specsec.m, 122
SPE_TestIntGauss.m, 121
SPE_xwGauss.m, 121

THER_matrix_inv.m, 249
THER_oven.m, 249
THER_oven_ex1.m, 248
THER_oven_ex2.m, 249